DEPARTMENT OF CHEMICAL AND PROCESS ENGINEERING

Investigation Of Rheological Properties Of Concentrated Milk And The Effect Of These Properties On Flow Within Falling Film Evaporators

Keng Lin (Jason) Ang

December 2011

A thesis submitted in partial fulfilment of the requirements for the degree of Master of Engineering

Abstract

The falling film flow of milk was studied both analytically and experimentally. Experiments were carried out for concentrations from 19.93% to 62.09% to obtain the rheological data of milk while analytical studies were done to derive the solutions of the problem. Studies which include calculations and simulations were carried out for a typical milk flow in a falling film evaporator.

It was found that milk was non-Newtonian at high concentrations and Herschel-Bulkley model was able to model the milk flow. The typical falling film flow was able to be simulated as a two phase flow in COMSOL to gain a better understanding of the flow. It was found that there were counter-current flow between the film and air in the evaporator.

A Matlab program was also used to study the analytical solutions of the film temperature change while it flows down the tube with results showing that heat transfer was not linear as would have believed. Results from several experiments also enabled the change of milk viscosity with time to be modeled. Milk viscosity increased steadily with time and higher at higher total solids from 35.47% to 49.25% for three hours.

Calculations revealed that film thickness of milk was very thin, from 0.00116 m at the entrance of tube to 0.00146 m at the tube exit. From the use of models developed of the rheological parameters, results showed that these parameters have impacts on film flow except the yield stress. However, the viscosity and yield stress are factors that will limit the operating range available for falling film evaporator.

Acknowledgements

I wish to thank Associate Professor Ken Morison for the supervision of this thesis work. I also like to thank Dr Justin Nijdam where his teachings on the subject of Computational Fluid Dynamics (CFD) have been invaluable. Other people to acknowledge for in this research include Dr. Alex James for her help with Matlab, CAPE technical staffs and especially Mr. Tony Allen for his helps with computers.

Table of Contents

Abstract i
Acknowledgements ii
Table of Contents iii
1. Introduction 1
1.1. Film Flow Hydrodynamics 4
1.2. Factors Affecting Falling Film Evaporators 7
1.3. Objectives 13
2. Literature Review 15
2.1. Boiling Regimes 15
2.2. Boiling Point Elevation 16
2.3. Heat Transfer 17
2.6. Film Temperature Distribution 38
2.7. Wave Phenomenon 40
2.8. Protein Denaturation 41
3. Experimental Methods 47
3.1. Materials 47
3.2. Experimental Procedures 48
3.3. Calibration of condensate flask 49
3.4. Preparation of Antifoam 49
3.5. Concentrating milk 49
3.6. Viscosity measurements 50
3.7. Total solids/Moisture content measurements 52
4. Rheological Model 53
4.1. Newtonian And Non-Newtonian Fluids 53
4.2. Rheological Parameters 54
4.3. Methods 55
4.4. Results 55
4.5. Discussion 71
4.6. Conclusions 75
5. Age Thickening Model 77
5.1. Introduction 77
5.2. Method 78
5.3. Results 78
5.4. Discussion 93
5.5. Conclusions 96
6. Analytical And Numerical Solutions 97
6.1. Newtonian/Non-Newtonian Film Flow 97
6.2. Film Temperature Distribution 108
6.3. Conclusion 112
7. CFD Simulation : COMSOL Multiphysics 113
7.1. Multiphase Flow Attempts 114
7.2. Discussion 146
7.3. Conclusions 148
8. Results 151
8.1. Rheological parameters 151
8.2. Spreadsheet calculations results 154
9. Discussion 175

10. Conclusions 179
11. References 181
12. Appendices 191
Appendix A. Analytical Derivations 191
Appendix B. Newton's Method For Finding Film Thickness 198
Appendix C. VBA Codes For Physical Properties 200
Appendix D. Matlab Code For Film Temperature Distribution 203
Appendix E. Approximating Masses In Rotary Evaporator 205
Appendix F. The Spreadsheet 207
Appendix G. Sample spreadsheet 229

1. Introduction

According to the New Zealand Dairy Statistics published by the DairyNZ (2009/10), the total milk processed was 16,483 million litres corresponding to 1,438 million kg of milk solids. With the price per kg of milk solids in 2009/10 at $6.37 dollars, the value of milk to dairy farmers would be about $9,160 million dollars.

In terms of export, the dairy products earned New Zealand $4.4 billion in the 1996/97 year (NZIC, 1998a), more than $6.3 billion in 2007 (Stringleman and Scrimgeour, 2009) and $8.8 billion in 2010 (Statistics New Zealand, n.d.). Approximately 96% of total milk production is used for the manufacture of processed dairy products with the remainder being used to meet domestic requirements (NZIC, 1998a). The dairy industry is therefore a major contributor to New Zealand's economy.

Among the export products are cheese, whole milk powder, skim milk powder, creamery butter, casein products, anhydrous milkfat, whey products and buttermilk powder.

The production of milk powder has become increasingly popular. In the 1993/94 dairying season, over 450,000 tonnes of milk powder were produced and exported. Since the year 2000, the export of milk powder, specifically whole milk powder have more than doubled and reached 893 000 tonnes in the year 2009/10 (TheDairySite, 2010).

Whole milk powder (WMP), skim milk powder (SMP), milk protein concentrate (MPC) and other varieties were produced by spray drying after concentration in an evaporator. Figure 1.1 below shows the steps towards the production of various types of milk powder.

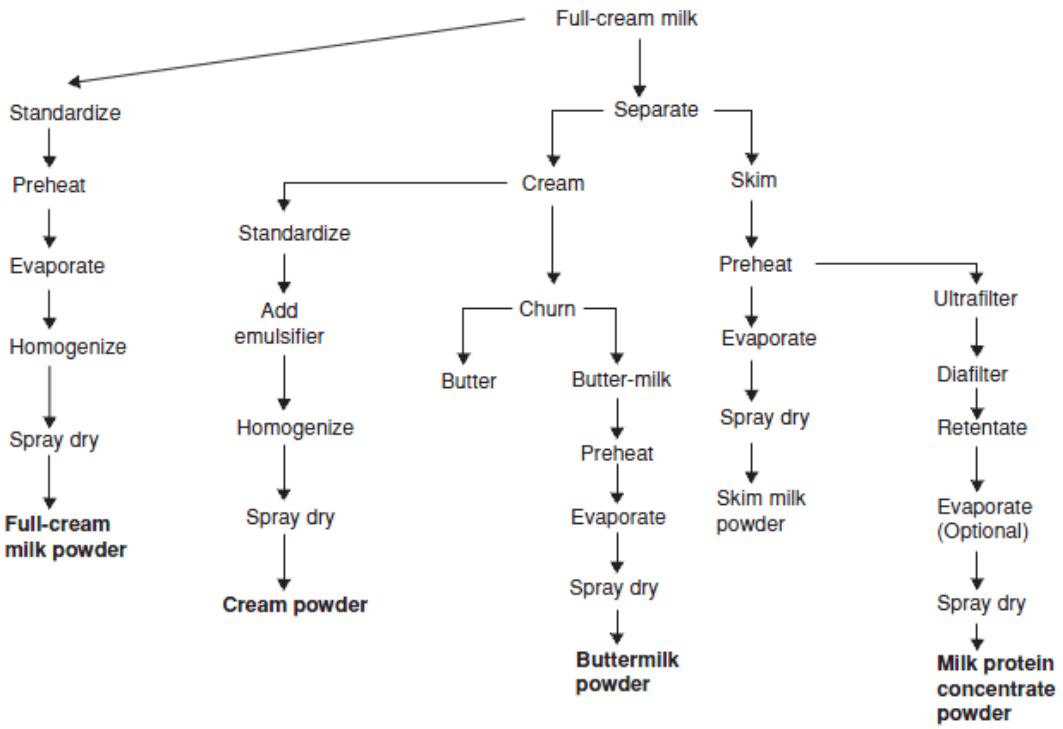

Figure 1.1: Flow chart for the production of milk powders (Augustin and Clarke, 2008).

Milk is concentrated in the evaporator from around 9% total solids content for skim milk and 13% for whole milk up to 45-52% total solids (NZIC, 1998b). A typical composition of whole milk and skim milk is given in Table 1.1 below. Because of its composition, skim milk will need to be evaporated more to reach the desired final total solids in the evaporator.

Table 1.1: Approximate composition of milk as from Deeth and Hartanto (2009).

Main composition	Whole Milk	Skimmed Milk
Water	87	90
Fat	3.7	< 0.1
Protein	3.3	3.4
Carbohydrate	4.8	4.9
Ash/Minerals	0.7	0.75

In an evaporator, milk is concentrated with the removal of water by evaporation where water changes phase from the liquid phase into the vapour phase. To minimize energy costs and maximize throughput, the amount of water removed in evaporators will need to be maximized as evaporators are up to 10 times more energy efficient than the spray driers they feed (Pohio, 2009). Bouman et al. (1993) asserted that energy consumption could be reduced by 10% by increasing the total solids from 48% to about 54%.

In the dairy industry, the falling film evaporator is normally used to concentrate milk. A falling film evaporator has many advantages as it has a short residence time for liquid; it is operable with a small temperature difference so has a small specific heat consumption and, depending on the Reynolds number, has a high heat transfer coefficient (Wiegand, 1971).

To become even more energy efficient the vapour produced in one falling film evaporator can be used to heat another evaporator. By doing this, the energy consumption of the overall system can be reduced by about 50% (GEA Wiegand, n.d.). This way of recycling the water vapour continuously in series is often termed as multi-effect evaporation (Figure 1.2). With *n* evaporators added in series to recycle the water vapour for use in the next evaporator, the energy usage can be decreased by approximately $1/n_{effects}$.

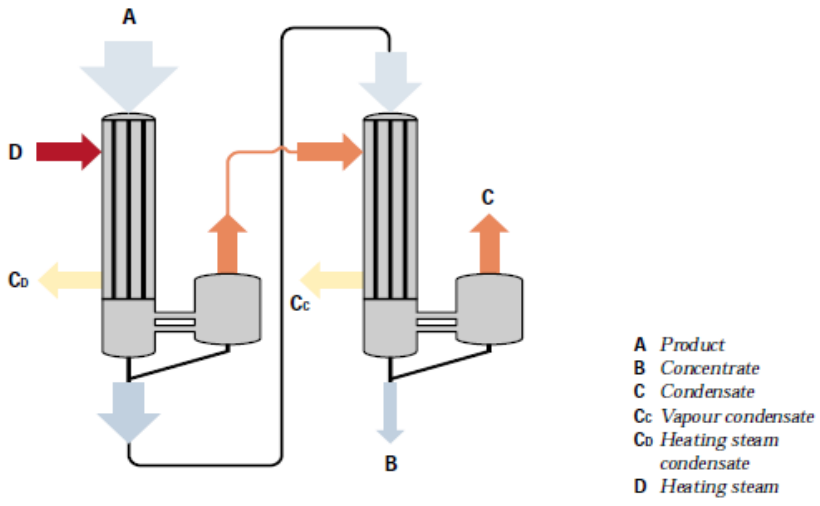

Figure 1.2: An example of multi-effect evaporation (GEA Wiegand).

Besides multi-effect evaporation, other possibilities for further energy saving can be achieved by the use of thermal or mechanical vapour recompression. Figure 1.3 shows the flow diagram of the use of the two for the falling film evaporator.

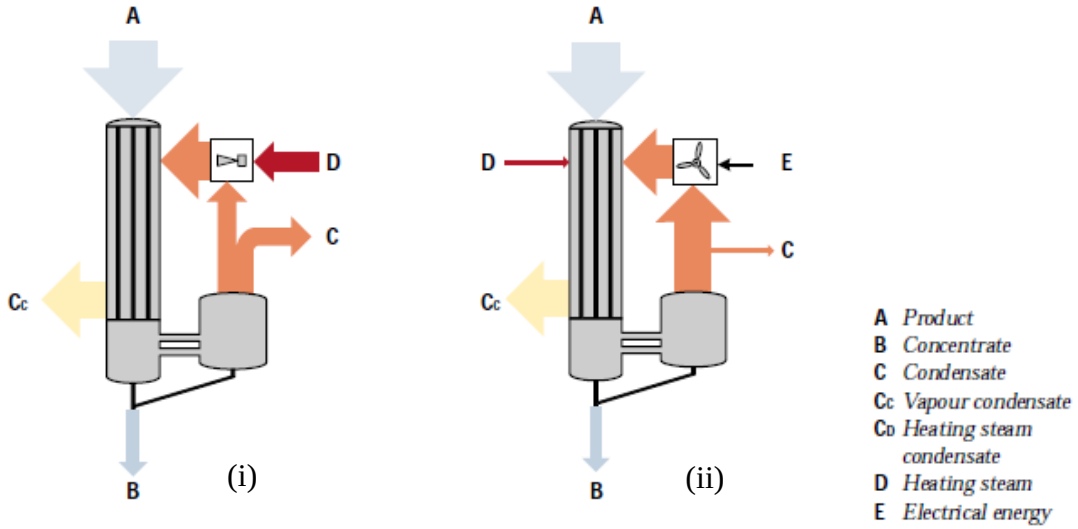

Figure 1.3: Falling film evaporator with the use of i) thermal vapour recompression, ii) mechanical vapour recompression (GEA Wiegand).

1.1. Film Flow Hydrodynamics

The flow in a falling film evaporator can be characterized by its thin film flow down the inner vertical tube wall under the influence of gravity and is sometimes referred to as gravity-driven film flow. In a falling film evaporator, liquid feed is fed at the top of the evaporator and passes through a distributor before falling evenly as a film into the tubes (Figure 1.4).

Immediately after distribution the film surface accelerates or thins down until it reaches a fully developed flow profile where its thickness becomes constant and its flow, steady and uniform (Yih, 1986). A flow is steady and uniform when its flow is constant with respect to time and constant with respect to distance in the direction of flow (Fulford, 1964). However, as water evaporates the flow profile continues to change down the tube.

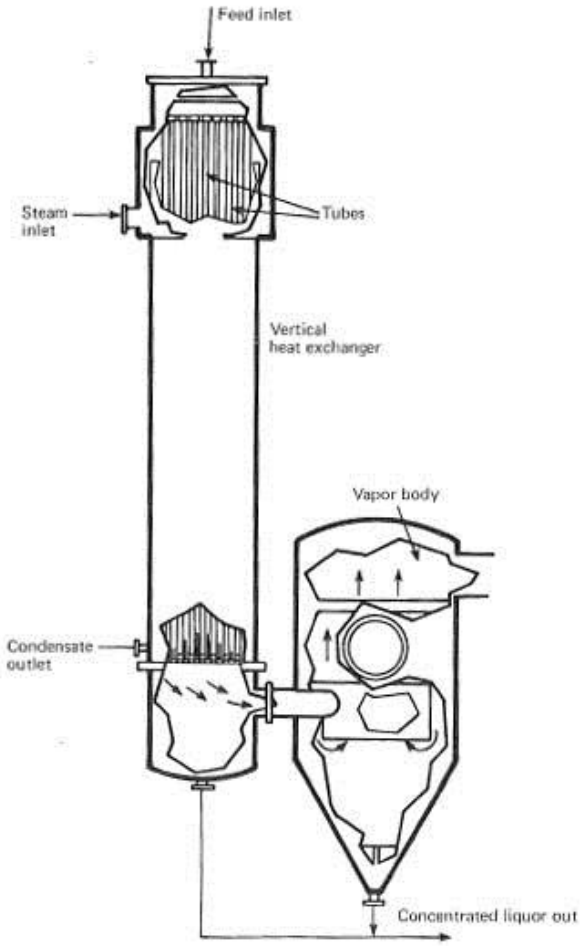

Figure 1.4: Example of a falling film evaporator (Nisenfeld, 1985).

A dimensionless Reynolds number is often used to describe flow. In film flow, the Reynolds number is

$$\mathrm{Re} = \frac{4\Gamma}{\mu} \qquad (1.1)$$

The wetting rate, Γ is the mass flow rate per unit circumference and μ is the viscosity of the liquid. However, some literatures have used the Reynolds number without the constant value 4,

$$\mathrm{Re} = \frac{\Gamma}{\mu} \qquad (1.2)$$

The wetting rate can be determined from equation (1.3) where $\dot{m}$ is mass flow rate ($kg \cdot s^{-1}$) and D_i is inner diameter of tube (m).

$$\Gamma = \frac{\dot{m}}{\pi D_i} \tag{1.3}$$

Often the minimum wetting rate is of interest and is defined as the minimum flow rate required to continuously maintain a film in the tube.

A film flow can be further classified into three regimes based on the Reynolds number:

- Smooth laminar
- Wavy laminar
- Turbulent

Several researchers have provided different values of Reynolds number for different regimes. Some of these are in Table 1.2 as below,

Table 1.2: Flow regimes.

Laminar	Wavy Laminar	Turbulent	Authors
0 - 30	30 - 500	> 500	Fulford (1964) and Halstrom (1985) cited in Jebson and Chen (1997)
< 20	20 - 1500	> 1500	Bird et al. (2002)
4 - 25	(4 - 25) - (1000 - 2000)	> (1000 - 2000)	Adib and Vasseur (2008)
< 4	4 – 400	> 400	Brauer (1956) cited in Weise and Scholl (2009)

Other dimensionless numbers used in relating film flow are Prandtl and Kapitza numbers. Prandtl number relates the liquid film's physical properties: viscosity, μ (Pa·s), specific heat capacity, c_p (J·kg^{-1}·K^{-1}) and thermal conductivity, k (W·m^{-1}·K^{-1}).

$$\mathrm{Pr} = \frac{\mu c_p}{k} \tag{1.4}$$

The Kapitza number instead relates the surface tension, σ (N·m^{-1}) with gravitational acceleration, g (m·s^{-2}), density, ρ (kg·m^{-3}) and viscosity, μ (Pa·s).

$$Ka = \frac{\mu^4 g}{\rho \sigma^3} \tag{1.5}$$

1.2. Factors Affecting Falling Film Evaporators

There are many factors that may be involved contributing to the dynamics of the operation of falling film evaporators. In general, the operation of a falling film evaporator involved heat transfer and with evaporation, mass transfer. These factors together with others, some of which are relevant to the research are highlighted.

1.2.1. Heat Convection

A falling film evaporator is a type of heat exchanger where heat is transferred from the wall to the falling film. The type of heat transfer is heat convection. As the mode of heat transfer is heat convection, the fluid motion, fluid nature and surface geometry play important roles in the heat transfer (Jiji, 2009). The stated fluid motion refers to the film flow while the fluid nature, be of any fluid, could be a Newtonian or a non-Newtonian. The surface geometry of relevance is the physical geometry of the falling film evaporator. This type of heat transfer will be the primary factors to the heat transfer in a falling film evaporator.

1.2.2. Flow

One of the important aspects in the falling film evaporator is the flow of the fluid. The flow of the fluid has the function to flow down the inner wall of the tube and in the process gets heated. The flow of the fluid therefore serves to convect the heat away from the wall.

However, in most of the application of the dairy falling film evaporators, the flow of the fluid was for the purpose of concentration. The milk flows into the evaporator to achieve a greater concentration in the end.

Furthermore, an adequate flow is important for the maintenance of a complete film in the evaporator. Insufficient flow will lead to film breakdown which causes the undesired exposure of evaporator tubes. This decreases the efficiency of heat transfer and may cause fouling (Paramalingam et al., 2000). The fouling referred to is the *viscous fouling* that arises due to the formation of dry patches from insufficient wetting. Rivulets flowing down these dry patches later gets concentrated and become very viscous (Figure 1.5). Eventually it hardens and blocks the tube.

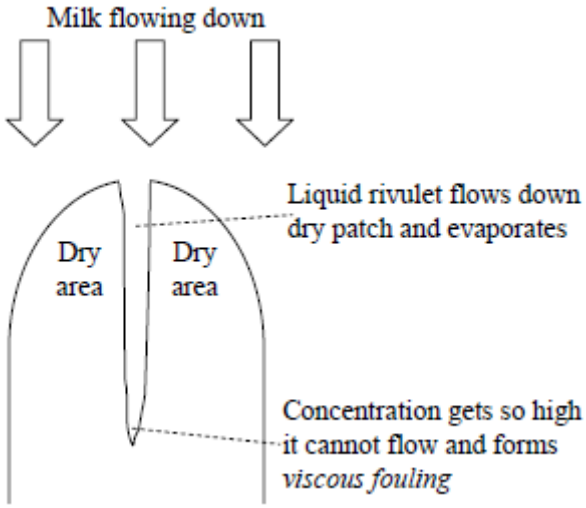

Figure 1.5: A rivulet flowing down a dry patch (Broome, 2005).

Another type of fouling that may occur in a falling film evaporator is *mineral fouling* and occurs when proteins/minerals remained attached to the inside of the tube and not due to insufficient wetting.

Because of the importance of the flow in the falling film evaporator, many research relating to film flow were carried out and the literatures in this area are vast.

1.2.3. Velocity

The falling film flow under the influence of gravitational force has a downward velocity. With the conditions that the film does not slip at the wall (i.e, velocity is zero) and a free surface at the interface, a velocity profile exists across the film thickness. For a laminar steady state flow, the velocity changes across the film thickness are greater than the changes down the tube. This velocity profile depends on the Newtonian or non-Newtonian behavior of the liquid. The velocity profile mentioned with reference to milk film flow was developed in the later chapters.

1.2.4. Viscosity And Rheological Properties

One physical property that changes as the film flows down in the falling film evaporator is the viscosity of the fluid. For the evaporation of milk, the milk film is concentrated and this change causes the viscosity of milk to increase. The change in viscosity may perhaps have the most significant impact and will become the limit to the operating range of the evaporator (Morison and Hartel, 2007).

This relationship can be seen when the viscosity increased, the film flow decreases as is the Reynolds number. The viscosity is closely related to the type of rheological models and the rheological properties that it depends on. To understand how the viscosity changes, the rheology of milk was further investigated in this research.

1.2.5. Heat Transfer Mechanisms

Essentially, heat is transferred from the wall to the falling film. The heat transfer depends on feed rate, temperature difference and percentage of feed that has been evaporated (Billet, 1989). The higher the value of the temperature difference and or

the heating rate, the greater the percentage of feed evaporated and thus the better the heat transfer.

Chen (1992) mentioned four possible mechanisms of heat transfer where evaporation could occur: at the liquid-vapour interface, at low rate nucleate boiling, at high rate nucleate boiling and lastly evaporation of vapour film.

The nucleate and non-nucleate boiling regimes will be reviewed later in the literature review chapter.

1.2.6. Distribution

In a falling film evaporator the fluid flows into a distributor at the top before flowing into the evaporator tubes. The distribution device fulfils the need for a uniform and even distribution of the fluid into all the tubes. Figure 1.6 shows a typical setup of a distributor.

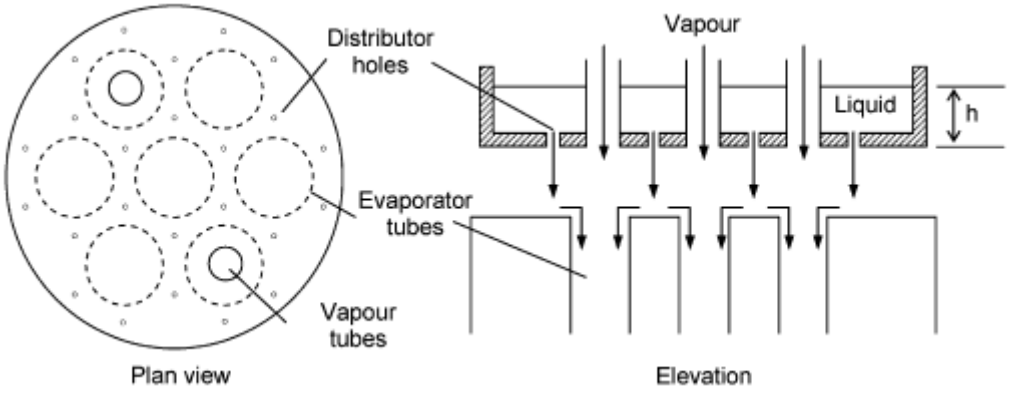

Figure 1.6: A distribution system where h shown is liquid height (Morison et al., 2006).

In working with real industrial scale evaporators, Broome (2005) found that warped distribution plates and with incorrectly sized holes led to poor liquid distribution and caused some tubes to foul and blocked.

Morison et al. (2006) defined a distribution rate that is the minimum mass flow rate per unit circumference of tube required to achieve full liquid distribution into the top entrance of the evaporator tubes.

Morison et al. (2006) concluded that the minimum distribution rate is nearly always higher than the minimum flow rate required to wet the inside of a vertical tube. The distribution system and distribution rates will need to be given consideration and not just the tube wetting rates.

1.2.7. Temperature

Assuming the falling milk film evaporating into a vacuum at the liquid-vapour interface, the evaporating temperature will be the saturation temperature provided the vapour pressure is constant. With the wall temperature constant, the temperature difference provides the driving force for heat transfer.

The heat transfer may depend on the flow of the fluid as well as the nature of the fluid or in particular the viscosity of the fluid. Due to the no slip condition, the film is stationary at the wall and the heat transfer will be by heat conduction (Holman, 2002). With the changing velocity profile further away from the wall, the temperature profile will more likely to change from being a straight line due to heat conduction.

This change in the film temperature profile with the effect of the downward flow of the falling film will be looked into detail.

1.2.8. Physical Properties

The other physical properties besides the viscosity (μ) that are involved are density (ρ), surface tension (σ), thermal conductivity (k), heat capacity (C_p) and boiling point elevation (ΔT_b). These properties are a function of temperature and concentration. In addition, the local viscosity may depend on the velocity profile.

1.2.9. 2D Problem

A study of the falling film evaporator will be a two dimensional problem as the variables and properties are changing in two directions (Figure 1.7): horizontal through the film and vertical down the tube. With some assumptions, the problem can be simplified into a one dimensional problem.

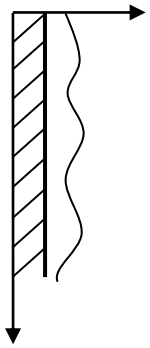

Figure 1.7: Two-dimensional problem.

1.2.10. Wave

At some Reynolds number, wave phenomena starts to occur at the free surface of the film. The incipience of waves may alter the physics of the falling film. Faghri and Zhang (2006) stated that because of the greater interfacial surface area and mixing action, wavy laminar flows gives higher heat transfer coefficients than smooth thin films.

Chun and Seban (1971) cited in Alhusseini et al. (1998) suggested that the onset of wavy laminar flow can be predicted by the empirical correlation:

$$\mathrm{Re}_{\mathrm{wavy}} = 2.43 Ka^{-1/11} \qquad (1.6)$$

1.2.11. Two Phase

The evaporation of the falling film produces vapour. The vapour generated can flow co-currently or counter-currently with the falling film and would exert a shear stress

on the film surface. Jebson and Iyer (1991) cited in Broome (2005) reported having a co-current vapour flow improved evaporation. Jebson and Chen (1997) further proved that vapour flow have a 'wind over water' effect on liquid film and the vapour momentum have a positive effect on heat transfer coefficient.

A study from Asad and Lampinen (2002) for a counter-current vapour flow revealed that the presence of the interfacial shear stress has a negative effect on the evaporator performance. However this is only for the case of the counter-current vapour flow.

1.2.12. Simulations

Several attempts were made in using COMSOL multiphysics modeling and simulation software to model the flow and temperature profile of the falling film. The results and outcomes were supplied in the later section. When all the phenomena are combined in a model, software such as COMSOL (see Chapter 7) is required to obtain a numerical simulation of the process.

1.3. Objectives

The primary aim for this thesis work was the investigation of how milk's rheological properties could affect film flow. A model was to be developed to provide a framework for the factors outlined in the previous section. Simulation of the model was to:

- Determine the temperature and velocity profile.
- Determine the contribution of age thickening to the viscosity of milk.
- Enable prediction of the various process dynamics of falling film evaporation.

Experimental work was to be carried out to provide data that was not available in literatures.

2. Literature Review

This chapter of the literature review encompasses the various phenomena that are falling film evaporators. It expands into details some factors highlighted previously in the introduction. It includes theories, correlations and equations relating to falling film evaporators. Some aspects pertaining to the change of the physicochemical properties of milk was also included.

The review is divided into the following sections:

- Boiling Regimes
- Boiling Point Elevation
- Heat Transfer
- Mixture Effect
- Film Flow
- Film Temperature Distribution
- Wave Phenomenon
- Protein Denaturation

2.1. Boiling Regimes

In a falling film evaporator, evaporation could occur with or without nucleate boiling. Boiling occurs when a solution/liquid is exposed to a surface and maintained at a temperature above its saturation temperature (Holman, 2002). Wall superheat is defined as that temperature difference between the surface/wall temperature (T_{wall}) and saturation temperature (T_{sat}) of the milk film.

$$\Delta T_w = T_{wall} - T_{sat} \qquad (2.1)$$

When the wall superheat is less than 5 °C water evaporates at the liquid-vapour interface without nucleate boiling. Nucleate boiling normally starts at a slightly higher temperature difference. Nucleate boiling is said to begin at a ΔT_w = 5 °C for water. In the nucleate boiling regime, bubbles can be seen forming and leaving the heated wall to the liquid-vapour interface.

Figure 2.1 below shows the relationship between the heat flux and wall superheat that may influence the various boiling regimes.

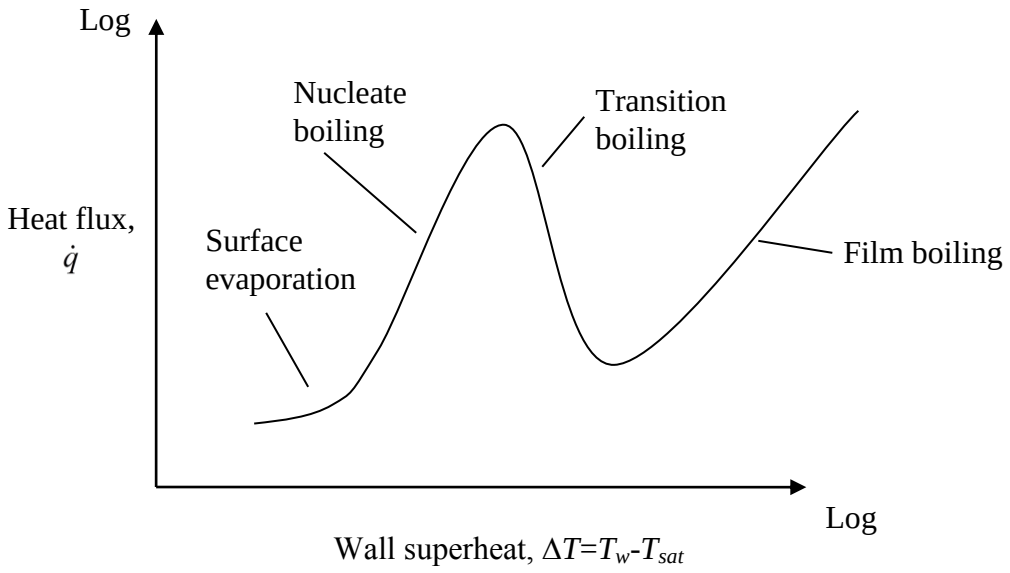

Figure 2.1: Boiling curve.

For milk the wall superheat at which nucleate boiling starts was found to be about 0.5 K (Bouman et al., 1993).

2.2. Boiling Point Elevation

Due to the presence of solutes/dissolved solids in milk, the milk film temperature is not constant throughout the evaporator length. The temperature of milk film will be slightly higher than its saturation temperature and will increase as the milk film gets more concentrated down the tube. This elevation of boiling temperature caused by solutes/dissolved solids is a property of all solute-solvent systems and is known as boiling point elevation (Roos 2007).

The boiling point elevation is given by equation (2.2),

$$\Delta T_b = \frac{-RT_{wb}^2 \ln a_w}{\Delta h_v} \qquad (2.2)$$

where R = gas constant (8.314 J·mol^{-1}·K^{-1})

T_{wb} = boiling temperature of water in Kelvin.

a_w = water activity

Assuming activity coefficient of milk is one, the water activity can be replaced by mole fraction of water, x_w (Morison and Hartel, 2007). The equation for boiling point elevation becomes,

$$\Delta T_b = \frac{-RT_{wb}^2 \ln x_w}{\Delta h_v} \qquad (2.3)$$

The molar latent heat of vaporization, Δh_v (J·mol^{-1}) can be calculated by the equation:

$$\Delta h_v = 57{,}222 - 44.3T_{wb} \qquad (2.4)$$

The milk temperature is the sum of its saturation temperature and boiling point elevation.

$$T_{milk} = T_{sat} + \Delta T_b \qquad (2.5)$$

Evaporation of milk in a falling film evaporator is normally done under vacuum. This enables evaporation of milk at a lower temperature (< 100 °C).

2.3. Heat Transfer

The heat transfer can be determined from the heat transfer equation,

$$q = UA\Delta T \qquad (2.6)$$

From the equation, U is the overall heat transfer coefficient and A is the total surface area. The overall temperature difference, ΔT is the temperature difference from the steam saturation temperature and milk saturation temperature with boiling point elevation accounted for.

2.3.1. Heat Transfer Coefficients

A dimensionless heat transfer coefficient takes the form,

$$h^+ = \frac{h_l}{k}\left(\frac{\nu^2}{g}\right)^{1/3}$$

$$h^+ = h_l \frac{l_v}{k} \qquad (2.7)$$

where $l_v = \left(\frac{\nu^2}{g}\right)^{1/3}$

h_l = liquid side heat transfer coefficient

ν = kinematic viscosity

k = thermal conductivity

The dimensionless heat transfer coefficient is related to dimensionless Reynolds and Prandtl numbers by the general expression,

$$h^+ = a\,\mathrm{Re}^b\,\mathrm{Pr}^c \qquad (2.8)$$

where a, b and c are constants. It is also sometimes expressed by the Nusselt number, Nu^* ($Nu^* = h^+$).

In some literature, the heat transfer coefficient is related to the Nusselt number by,

$$Nu = \frac{h\delta}{k} \qquad (2.9)$$

where h = heat transfer coefficient ($W \cdot m^{-2} \cdot K^{-1}$)

δ = film thickness (m)

k = thermal conductivity ($W \cdot m^{-1} \cdot K^{-1}$)

The overall heat transfer coefficient in a falling film evaporator can be determined by experiment or calculated from the equation (Mackereth, 1992):

$$\frac{1}{U} = \frac{1}{h_c} + \frac{S_s}{k_s} + \frac{S_w}{k_w} + \frac{S_f}{k_f} + \frac{1}{h_e} \qquad (2.10)$$

where U = overall heat transfer coefficient ($W \cdot m^{-2} \cdot K^{-1}$)

h_c = heat transfer coefficient of condensate film($W \cdot m^{-2} \cdot K^{-1}$)

h_e = heat transfer coefficient of product film ($W \cdot m^{-2} \cdot K^{-1}$)

S_s = steam-side scale thickness (m)

S_w = wall thickness (m)

S_f = product side foulant's thickness (m)

k_s = thermal conductivity of scale ($W \cdot m^{-1} \cdot K^{-1}$)

k_w = thermal conductivity of wall ($W \cdot m^{-1} \cdot K^{-1}$)

k_f = thermal conductivity of foulant ($W \cdot m^{-1} \cdot K^{-1}$)

2.3.2. Correlations And Equations

i. Adib et al. (2009)

The correlations obtained by Adib et al. (2009) considered that the limiting resistance was the value of the heat transfer coefficient on the product side between the wall and the evaporated liquid ($1/h=1/h'+R_f$). This includes the resistance from fouling (R_f) and the boiling liquid ($1/h'$).

Two types of models for heat transfer coefficient were presented, a logarithmic model and a linear model.

Logarithmic model: $$h = 30.37\phi^{0.19} X_{DM}^{-0.29} \Gamma^{0.17} \theta_L^{1.14} \qquad (2.11)$$

Linear model: $$h = 218 + 24\phi - 37X_{DM} + 1090\Gamma + 32\theta_L \qquad (2.12)$$

where ϕ, heat flux (kW·m^{-2}), X_{DM}, dry matter concentration (kg solid/kg solution), Γ, mass flow rate per unit perimeter length (kg·m^{-1}·s^{-1}), θ_L, boiling termperature (°C).

Adib et al. (2009) also presented two equations for the non-nucleate regime and the nucleate regime.

Non-nucleate regime ($2 \leq \phi \leq 10$ kW·m^{-2})

$$h = 33\phi^{0.05} X^{-0.27} \Gamma^{0.14} \theta_L^{1.2} \qquad (2.13)$$

An alternative equation was provided without heat flux, ϕ, as heat flux was found to have little effect on heat transfer coefficient in this regime,

$$h = 30.6 X^{-0.25} \Gamma^{0.14} \theta_L^{1.22} \qquad (2.14)$$

Nucleate regime ($20 \leq \phi \leq 80$ kW·m^{-2})

$$h = 28.34\phi^{0.34} X^{-0.53} \Gamma^{0.2} \theta_L^{1.24} \qquad (2.15)$$

ii. Adib and Vasseur (2008)

In this review paper, Adib and Vasseur (2008) classified the available correlations of heat transfer coefficients into a few categories. The heat transfer coefficient of interest was on the product side. The correlations were firstly sorted for use in either a pool boiling evaporator type or a falling film evaporator type.

For a falling film evaporator type, two boiling regimes and two flow regimes were considered. In a non-nucleate boiling regime, the heat transfer coefficient is a function of flow pattern and not a function of heat flux (ϕ) or temperature difference ($\Delta\theta = \theta s - \theta_L$, θ_s the surface/wall temperature and θ_L the liquid temperature). In a nucleate boiling regime, the heat transfer coefficient is a function of heat flux and temperature difference.

The list of equations was provided as sorted by Adib and Vasseur (2008):

Laminar and wavy-laminar (non-nucleate)

- Nusselt's equation
- Chun and Seban's equation

$$h^+ = 0.821\,\mathrm{Re}^{-0.22} \tag{2.16}$$

Re: 320 - 3200, Pr: 1.77 - 5.7

- Prost et al.'s equation

$$h^+ = 1.6636\,\mathrm{Re}^{-0.2648}\,\mathrm{Pr}^{0.1592} \tag{2.17}$$

Re: 15 - 3000, Pr: 2.5 – 200

ϕ : 17 – 25 kW·m^{-2}

Turbulent (non-nucleate)

- McAdams's equation
- Wilke's equation
- Ahmed and Kaparthi's equation
- Herbert and Stern's equation
- Chun and Seban's equation

$$h^+ = 3.8\times10^{-3}\,\mathrm{Re}^{0.4}\,\mathrm{Pr}^{0.65} \tag{2.18}$$

Re: 1600 - 21,000, Pr: 1.77 - 5.7

Nucleate boiling

- Krupiczka et al.'s equation

$$\frac{Nu}{Nu_z} = 1 + C\left(B_o \cdot Ka^{\frac{1}{11}}\right)^{1.6} \tag{2.19}$$

$B_o \times Ka^{1/11} > 10^{-6}$, $C = 7.05\times10^{7}$

$B_o \times Ka^{1/11} < 10^{-6}$, $C = 0 \rightarrow Nu = Nu_z$

$$B_o = \frac{\phi}{G\Delta H_v}$$

$$G = \frac{\dot{m}}{\pi D\delta}$$

- Bouman's equation

$h_L = 0.77\phi^{0.69}\eta^{-0.41}$ (skim milk) * (2.20)

ϕ : 600 - 32,700 W·m^{-2}

Concentration: 8.5% - 53.9%

$\Delta\theta$: 0.4 - 11.4 °C

$h_L = 6.05\phi^{0.47}\Gamma^{0.26}\eta^{-0.44}$ (whole milk) (2.21)

ϕ : 1200 - 27,400 W·m^{-2}

Concentration: 11.3% - 56.8 %

$\Delta\theta$: 0.6 - 11.5 °C

* The subscript L in h_L indicates an average over the length of the tube (rather than the local h).

They reviewed the effects of temperature difference and concentration on heat transfer coefficient for the case of skim milk. They found, by using Bouman et al.'s skim milk equation, heat transfer coefficient increased from 6 to 20 kW·m^{-2}·°C^{-1} when heat flux increased from 5 to 30 kW·m^{-2}. The heat transfer coefficient decreased in the range 21 - 12 kW·m^{-2}·°C^{-1} when the concentration of skim milk increased in the range 5 - 30%.

They found low heat flux at less than 2 kW·m^{-2}, the heat transfer coefficient estimated by Bouman et al. equation (for skim milk and whole milk) gave similar results to those estimated by non-nucleate falling film in turbulent flow correlations.

However, at high heat flux, 30 kW·m^{-2} the calculated values of heat transfer coefficient from nucleate boiling correlations were much higher. Generally, evaporators operate at moderate heat flux of less than 50 kW·m^{-2} (Yih, 1986).

From these findings, they mentioned that falling film evaporators have two advantages compared to pool boiling evaporators. Falling film evaporators provide high heat transfer coefficient at low evaporating temperature and at low temperature difference.

iii. Prost et al. (2006)

A correlation for the heat transfer coefficient of the evaporating side was obtained with experiments carried out using solution of sucrose in water. The operating conditions for the experiments were set to the conditions normally found in a single effect evaporator and were later changed to those as for a second and third effect evaporator.

The authors reasoned that Reynolds number and Prandtl number are related. For a given temperature, the flow behavior, residence time and concentration are defined by the viscosity. Therefore for a given concentration and temperature, the physical properties defining the Prandtl number is fixed. With these reasons, they surmised that the conditions that determine the Reynolds number also determine one value of the Prandtl number. They found the relationship between both these dimensionless numbers to be,

$$\mathrm{Pr} = 1878\,\mathrm{Re}^{-0.8204} \qquad (2.22)$$

$$15 < \mathrm{Re} < 3000$$

$$2.5 < \mathrm{Pr} < 200$$

From equation (2.22) and equation (2.17) as reviewed by Adib and Vasseur (2008), they presented a new equation,

$$h^{+} = 5.5236\,\mathrm{Re}^{-0.3854} \qquad (2.23)$$

It is unknown however if the Reynolds number was determined using equation (1.1) or (1.2).

iv. Broome (2005)

Broome (2005) found in his studies of industrial falling film evaporators in the dairy industry that the overall heat transfer coefficient can be correlated with the total solids, *TS* ($g \cdot g^{-1}$) to give equation (2.24) and (2.25).

$$\text{Skim milk: } U = -5463TS + 3247 \qquad (2.24)$$

Whole milk: $U = -5441TS + 3382$ (2.25)

Equation (2.24) is the correlation of overall heat transfer coefficient for skim milk and is valid for total solids from 11% to 50%. For whole milk, the correlation for the overall heat transfer coefficient is in equation (2.25) and is valid for total solids from 15% to 50%.

v. Uche et al. (2003)

Several correlations of heat transfer coefficient were compared for three types of evaporators usable in the desalination industry. The three types of evaporators were horizontal tube falling film evaporator, vertical tube falling film evaporator and vertical tube rising film evaporator.

Uche et al. used six correlations, which were Nusselt's, Kutateladze's, Labuntsov's, Chun and Seban's, Sandall et al.'s and Alhussieni et al.'s for comparison in a vertical tube falling film evaporator.

For flow from the wavy-laminar to turbulent regime, the correlations of Alhussieni et al.'s was selected as the calculated values were comparatively close to their experimental values.

vi. Krupiczka et al. (2002)

Results were presented of experimental studies of Krupiczka et al. (2002) with the evaporation of three liquids (water, methanol and isopropanol) under falling film condition inside a vertical tube. The operating conditions were at atmospheric pressure with heat flux varying from 2 to 31 $kW \cdot m^{-2}$ and at Reynolds number from 745 to 3300.

They found that at Boiling number, $B_0 \approx 10^{-5}$, the Nusselt number is the Nusselt number without nucleate boiling occurring ($Nu = Nu_z$). At this condition, the heat transfer coefficient can be determined from the Chun and Seban's correlation.

At Boiling number, $B_0 > 10^{-5}$, the correlation below was presented,

$$\frac{Nu}{Nu_z} = 1 + CB_o^{1.727} \qquad (2.26)$$

$$C = 8.1 \times 10^6$$

Krupicka et al. (2002) claimed that equation (2.19) was more accurate with the Kapitza number included.

vii. Wadekar (2000)

Wadekar (2000) compared Numrich's correlation with Alhussieni et al.'s data and Alhusseini et al.'s correlation with Muller's data. He also compared the HTFS (Heat Transfer and Fluid Flow Service) correlation, a correlation proprietary to HTFS, with those two data sets. The HTFS correlation is a general correlation applicable to falling film flow for all regimes from laminar to wavy to turbulent film flow. It is also applicable to fluids of low, medium and high Prandtl number fluids.

The following correlations were used:

- Chun and Seban's as from equation (2.16) and (2.18)
- ESDU (Engineering Sciences Data Unit)

$$Nu_t^* = 0.0097\,\mathrm{Re}^{0.29}\,\mathrm{Pr}^{0.63} \qquad (2.27)$$

$$Nu^* = \left[\frac{0.31}{\mathrm{Re}^{1.32}} + \frac{\mathrm{Re}^{1.73}\,\mathrm{Pr}^{3.78}}{1.2\times10^{12}}\right]^{1/6} \qquad (2.28)$$

- Alhusseini et al. as from equation (2.34) to (2.36)
- Numrich

$$Nu_t^* = 0.003\,\mathrm{Re}^{0.44}\,\mathrm{Pr}^{0.4} \qquad (2.29)$$

- HTFS

Wadekar (2000) concluded no single correlation predicted data well but the HTFS correlation predicted data with reasonable degree of success. However, the HTFS correlation was not given in the paper.

viii. Tuzla et al. (2000)

Tuzla et al. (2000) used three correlations as below:

- Nusselt's equation

$$Nu = \left(\frac{4}{3}\right)^{1/3} \mathrm{Re}^{1/3} \qquad (2.30)$$

- Chun and Seban as from equation (2.16) and (2.18)
- Alhussieni et al. as from equation (2.34)

Experiments were carried out for laminar falling film with surface evaporation only. The range of Prandtl number was from 500 to 6200. The viscosity range was from 86 to 650 mPa·s. The range of Reynolds number was from 1.9 to 149.

From comparison of the three correlations above, they found Alhussieni et al.'s correlation to give good agreement with their experimental data.

ix. Rao (1999)

Rao (1999) studied the heat transfer to a falling power law fluid film using aqueous solutions of Carbopol 934 at concentrations of 250 and 500 ppm by weight. He defined a film Reynolds number,

$$\mathrm{Re}_f = \rho U t / \eta \qquad (2.31)$$

where U is the average velocity (m/s), t is the film thickness (m), ρ is density (kg/m^3) and η is apparent viscosity of non-Newtonian fluid (Pa·s). In the experimental work for his studies, the range of Reynolds number was from 502-4440 and Prandtl number from 14.6-19.9.

He used equations from Ueda and Tanaka (1974), Brauer (1956), Wilke (1962) and Carey (1985) for dimensionless heat transfer coefficient to compare with his experimental results. He said that these equations usable for Newtonian fluids under predicted the heat transfer coefficient in the laminar region and over predicted in the turbulent region.

He proposed a new correlation for fully developed h* for falling power-law liquid films valid over the range of $502 \le \mathrm{Re}_a \le 5400, 5 \le \mathrm{Pr}_a \le 20$ and $0.7 \le n \le 1$:

$$h^* = 0.009\,\mathrm{Re}^{0.32}\,\mathrm{Pr}^{1/3}\,f(n) \tag{2.32}$$

$$f(n) = A + Bn + Cn^2 \tag{2.33}$$

where A, B and C are 0.6, 0.4 and 0.8 respectively and *n* is flow behavior index.

x. Alhussieni et al. (1998)

Experiments were carried out to study the falling film evaporation of single component liquids. The Prandtl number range was from 1.7 to 47. The Reynolds number range was from 124 to 15,600. Correlations or models were developed for the wavy laminar and turbulent regimes. A model was also developed for heat transfer coefficient for any Reynolds number.

Wavy-laminar regime

$$h_l^+ = 2.65\,\mathrm{Re}^{-0.158}\,Ka^{0.0563} \tag{2.34}$$

Turbulent regime

$$h_t^+ = \frac{\mathrm{Pr}\cdot\delta^{+1/3}}{\left(A_1\,\mathrm{Pr}^{3/4} + A_2\,\mathrm{Pr}^{1/2} + A_3\,\mathrm{Pr}^{1/4} + C_t\right) + \left(BKa^{1/2}\,\mathrm{Pr}^{1/2}\right)} \tag{2.35}$$

$$A_1 = 9.17$$

$$A_2 = 0.328\pi\left(130 + \delta^+\right)/\delta^+$$

$$A_3 = 0.0289\left(152100 + 2340\delta^+ + 7\delta^{+2}\right)/\delta^{+2}$$

$$B = 2.51\times10^6\,\delta^{+0.333}\cdot Ka^{-0.173}/\mathrm{Re}^{\left(3.49Ka^{0.0675}\right)}$$

$$C_t = 8.82 + 0.0003\mathrm{Re}$$

$$\delta^t = 0.0946\,\mathrm{Re}^{0.8}$$

All Reynolds number

$$h^+ = \left(h_l^{+5} + h_t^{+5}\right)^{1/5} \tag{2.36}$$

xi. Trela and Kornecki (1997)

Two conditions were given attention to in the paper, which were:

1) T_w = constant
2) q_w = constant

With regards to number (2) above, two possibilities were available where the heat flux at the free surface could be assumed to be as

- $q_i = 0$ *or*
- $q_i = q_w$

The heat transfer coefficient was defined as

$$h = \frac{Q_w}{A\Delta T_{\log}}$$

where Q_w is heat flux supplied to the liquid film, A is outer surface of the test section and ΔT_{log} is the mean logarithmic temperature difference.

For $q_i = 0$

$$Nu = 2.27\,\mathrm{Re}^{-1/3} \qquad (2.37)$$

For $q_i = q_w$

$$Nu = 1.76\,\mathrm{Re}^{-1/3} \qquad (2.38)$$

For $60 < \mathrm{Re} < 2000$

$$Nu = 0.025\,\mathrm{Re}^{0.2}\,\mathrm{Pr}^{0.344} \qquad (2.39)$$

xii. Moresi (1985)

In his ME thesis, Chen (1992) cited the works of Moresi (1985) and stated that with the condition that the minimum evaporation taking place at the surface of film, the heat transfer coefficient is approximately equal to the thermal conductivity, *k* divided by the film thickness, δ, as in equation (2.40),

$$h_L = \frac{k}{\delta} \tag{2.40}$$

The film thickness from equation (2.56), can then be substituted into equation (2.40) to obtain the new heat transfer coefficient as below:

$$h_L = \frac{k}{\left(\frac{3\mu\Gamma}{\rho^2 g}\right)^{1/3}} = \frac{k}{\left(\frac{3}{4}\right)^{1/2}\left(\frac{\mu^2}{\rho^2 g}\right)^{1/3}\left(\frac{4\Gamma}{\mu}\right)^{1/3}}$$

$$\frac{h_L}{k}\left(\frac{\mu^2}{\rho^2 g}\right)^{1/3} = \left(\frac{4}{3}\right)^{1/3}\frac{1}{\mathrm{Re}^{1/3}}$$

$$Nu^* = 1.1\mathrm{Re}^{-1/3} \tag{2.41}$$

xiii. Ahmed and Kaparthi (1963)

The heat transfer coefficients models were developed from experimental data. The Reynolds number range was from 3 to 10,250. The Prandtl number range was from 3.6 to 950. The liquids used were water and aqueous glycerol (concentration: 15 - 98%).

For $\mathrm{Re} < 2100$ (pseudo laminar flow)

$$Nu = 0.0911\mathrm{Re}^{0.33}\,\mathrm{Pr}^{0.4}\left(\mu/\mu_w\right)^{0.25} \tag{2.42}$$

For $\mathrm{Re} > 2100$ (turbulent flow)

$$Nu = 0.00079\,\mathrm{Re}^{0.93}\,\mathrm{Pr}^{0.4}\left(\mu/\mu_w\right)^{0.25} \tag{2.43}$$

where Nu = Nusselt number ($h\delta/k$)

h = Heat transfer coefficient

δ = Film thickness

k = Thermal conductivity

μ = Viscosity of the liquid at the bulk temperature

μ_w = Viscosity of the liquid at wall temperature

Various correlations and equations were reviewed and presented relating to heat transfer of falling film flow. These equations mostly refer to the heat transfer coefficient and the works done by different authors to find the relationship with falling film flow.

2.4. Mixture Effect

For a multicomponent liquid mixture, a phase change such as boiling or evaporation causes concentration gradients to occur near the vapour-liquid interface (Wadekar and Hills, 2001). This change in concentration induces mass transfer by diffusion.

The evaporation of the light component from the liquid phase leaves the liquid at the vapour-liquid interface depleted of the light component. This triggers the process of counter-diffusion of the light and heavy components to minimise the depletion of the light component at the interface (Wadekar and Hills, 2001).

With the depletion of the light component at the interface, the bubble point temperature at the interface rises. A study of binary mixture vaporization from Palen et al. (1994) seems to support this idea and stated that the mass transfer resistance in the liquid film is the cause to the significant elevation of the interfacial temperature.

This rise in bubble point temperature at the interface in turn leads to a reduced wall superheat and later deterioration of heat transfer. The whole effect where the heat transfer of a multicomponent liquid mixture is reduced by this is termed the *'mixture effect'*. Wadekar likened this effect for a binary liquid mixture to be similar to solution containing dissolved solids.

Wadekar and Hills (2001) described that for a solution containing dissolved solids, there exist a temperature difference of ΔT_m between the film's saturated temperature and temperature at the film's interface. Accordingly, there is a small increase in the temperature at the interface. This increase in the interface's temperature is a result of an increase in solute's concentration at the interface (dissolved solids for milk) as the solvent is evaporated.

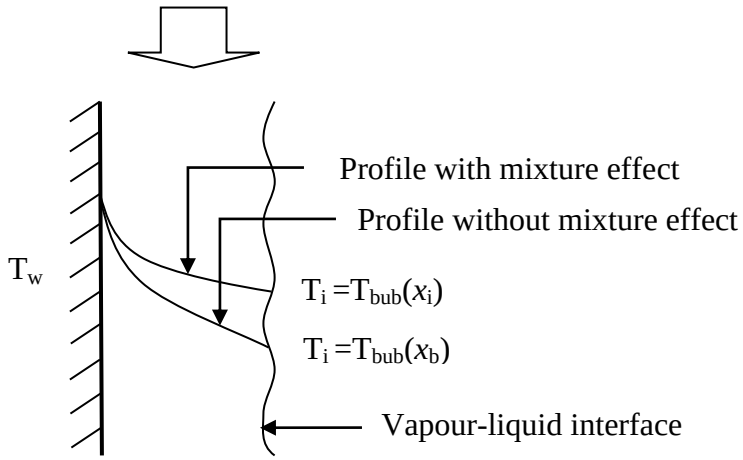

Figure 2.2: Film temperature profile as a result of with/without mixture effect (Wadekar and Hills, 2001).

Such temperature difference can be calculated by,

$$\Delta T_m = \left(T_{bub(x_i)} - T_{(x_b)}\right) \qquad (2.44)$$

where, $T_{bub(x_i)}$ = bubble point temperature at the interface

$T_{(x_b)}$ = bubble point temperature in the bulk

The temperature at the interface can be evaluated with the composition of milk at the interface. Wadekar and Hills (2001) gave the interfacial solute concentration as,

$$x_i = (1+\theta)x_b - \theta \qquad (2.45)$$

where θ = $\dot{q} / \Delta h_v \rho_l \beta_l$

$\dot{q}$ = Heat flux ($W \cdot m^{-2}$)

Δh_v = Molar latent heat of vaporization ($J\ kmol^{-1}$)

ρ_l = Molar density ($kmol\ m^{-3}$)

β_l = Mass transfer coefficient ($m \cdot s^{-1}$)

x_b = Mole fraction in the bulk

x_i = Mole fraction at the interface

Since the solute concentration at the interface is slightly higher and the temperature at the interface has increased, the available wall superheat, ΔT_w will be reduced. This increase in the interfacial temperature will be responsible for the degradation in heat transfer (Wadekar and Hills 2001). They included the interfacial temperature rise, ΔT_m, as part of the resistance to heat transfer on the product side and proposed the heat transfer resistance on the product side to be,

$$\frac{1}{\alpha_m} = \frac{1}{\alpha_{epf}} + \frac{\Delta T_m}{\dot{q}} \qquad (2.46)$$

where α_m = Mixture heat transfer coefficient ($W \cdot m^{-2} \cdot K^{-1}$)

α_{epf} = Heat transfer coefficient for equivalent pure fluid, i.e. a hypothetical fluid with the same physical properties as that of mixture but without any mixture effect ($W \cdot m^{-2} \cdot K^{-1}$)

2.5. Film Flow

Film flow studies are important to understand falling film evaporators. In the literatures, it was found that film flow can be divided into the developing region and the developed region. From here, these can further be branched out into Newtonian or non-Newtonian fluids.

Weise and Scholl (2009) from the findings of Ishigai et al. (1972) reiterated that film flow are generally smooth laminar for,

$$\mathrm{Re} \leq 0.47 \cdot Ka^{0.1} \qquad (2.47)$$

They also reiterated the works of Höhne et al. (1997) that the critical Reynolds number (Re_{crit}) without the influence of Kapitza factor as 4.42 for laminar, 19.55 - 86.43 for wavy laminar and 382.15 for turbulent flow (not specific to milk flow).

However their primary works on evaporating falling liquid film concerns with determining if Kapitza number was necessary to account for the surface tension effects. From the existing work, this was inconclusive but the experimental works from their set up proved that it was possible to increase the overall temperature difference up to 40 K without causing visible film break-up with Pr more than 50.

The following sections present reviews that are of consequence to film flow.

2.5.1.Analytical Studies

This section reviews some of the analytical studies available relating to falling film flow.

i. Newtonian

Chien (1966) obtained solutions to the laminar, gravitational film flow of liquid on vertical, circular, cylindrical surfaces. Two cases were investigated, flow on the inner and outer surface. From the study, a new dimensionless number, ζ, was introduced which characterizes film flow corresponding with the dimensionless film thickness (δ/R, δ is film thickness and R is radius).

For the case of film flow down a vertical wall in the accelerating region, Hassan (1967) worked the solution for the laminar flow by neglecting the surface tension. The relation between the film thickness and its distance traveled was given. Its velocity profile was also obtained.

ii. Non-Newtonian

Many analytical studies of non-Newtonian falling films used the power law model such as Andersson and Shang (1998) and Shang and Gu (2004).

Skelland and Popadic (1974) did an experimental and analytical study for a non-Newtonian pseudoplastic wavy falling film down a vertical plate. The paper compares the experimental results with the analytical results they derived.

Yang and Yarbrough (1980) on the other hand studied the falling film flow inside a vertical pipe in the accelerating region using the power law equation for the liquid film. This analytical study of power law fluids was also covered in a chapter devoted to falling film flow in a book by Shang (2006).

2.5.2. Milk viscosity

Milk, skim milk, cheese whey and whey permeate are dilute solutions and are usually considered to be Newtonian fluids (Kailasapathy, 2008). The viscosity of milk is around 2.2 - 2.5 mPa·s at 20 °C and depends on the metabolism and state of nutrition of the individual cow (Kailasapathy, 2008).

Milk becomes non-Newtonian at higher concentration and its viscosity increases in a non-linear fashion as concentration increases. Bienvenue et al. (2003) claimed that milk is non-Newtonian at concentration above 40% total solids.

Being non-Newtonian, the viscosity of milk is affected by its total solids, protein content, preheat treatment, milk composition, temperature and storage time (Bienvenue et al., 2003)

Vélez-Ruiz and Barbosa-Cánovas (1998) showed that whole milk behaves as a non-Newtonian fluid above 22.3% total solids. A power law model is well fitted for concentrates between 22.3% and 30.5% total solids. Later, for concentrates at 42.4% and 48.6% solids content was well described by the Herschel-Bulkley model. They also showed that rheological properties of whole milk are a function of its concentration, temperature and storage time.

Trinh et al. (2007) used reconstituted whole milk concentrates in their studies and revealed the concentrates exhibit Newtonian (< 30% TS), then power law (> 30% TS), Herschel-Bulkley (> 40% TS) and later into time-dependent rheological behaviour at (> 44% TS).

Snoeren et al. (1982) expressed viscosity of skim milk concentrate as a function of volume fraction of casein, Φ_c, native whey protein, Φ_{nw}, denatured whey protein, Φ_{dw} and viscosity of medium, η_{ref}. The relationship was expressed in the equation,

$$\eta = \eta_{ref}\left(1+\frac{1.25\left(\Phi_c+\Phi_{nw}+\Phi_{dw}\right)}{1-\left(\Phi_c+\Phi_{nw}+\Phi_{dw}\right)/\Phi_{\max}}\right)^2 \qquad (2.48)$$

Bloore and Boag (1981) found that viscosity for skim milk is a factor of temperature, total solids, age, protein content and preheat treatment. They provided various equations relating these factors.

Jebson and Chen (1997) gave a simpler equation of Bloore and Boag (1981) for condition when total solids > 45%.

$$\ln\mu = 3.911+0.0202S'-0.1291T' \qquad (2.49)$$

The μ in the equation is the dynamic viscosity, Pa·s; S' = (S - 482.5)/0.85; *T'* = (T - 52.5)/7.5; S is the concentrate total solids, g/kg; T is the absolute temperature, K.

Reddy and Datta (1994) conducted experiments to determine the thermophysical properties of reconstituted milk over the range of concentrations from 40% to 70% at temperatures from 35 °C to 65 °C. They found temperature did not have an effect on flow behavior index, *n*, and that it is a function of concentration, *X* (%) only. The consistency coefficient, *b* (Pa·s^n), was found to be a function of the inverse of the absolute temperature, *T* (K) and concentration, *X* (%).

$$n(X) = -0.008962X+1.17021 \qquad (2.50)$$

$$b(X,T) = 2.367\times10^{-6}\exp\left(2279.11/T\right)1.25^X \qquad (2.51)$$

$$\eta_a = 2.367\times10^{-6}\exp\left(2279.11/T\right)1.25^X\left(\dot{\gamma}\right)^{-0.008962X+1.17021} \qquad (2.52)$$

The equation for viscosity was determined from measurements of concentrations at 45%, 50%, 55%, 60% and 65% at temperatures of 40 °C, 50 °C, 60 °C and 65 °C.

Other properties such as thermal conductivity, specific heat and their relations with temperature and concentration were also given as equations in the paper.

Vélez-Ruiz and Barbosa-Cánovas (2000) from experiments using whole milk, determined the relationship between the flow behaviour index, *n*, and concentration, *X* (%) by a linear (eq. 2.53) and an exponential equation (eq. 2.54). They found the consistency coefficient, *K* (mPa·s^n) and concentration, *X* (%), can be described by an exponential equation.

$$\text{Linear: } n = 1.11 - 0.0072X \tag{2.53}$$

$$\text{Exponential: } n = 1.13e^{-0.0079X} \tag{2.54}$$

$$\text{Exponential: } K = 0.224e^{0.148X} \tag{2.55}$$

2.5.3. Physical properties

Equations relating to physical properties were provided by Dr Ken Morison. These equations were already encoded in Visual Basic and were used in Excel spreadsheet for calculations.

2.5.4. Film thickness

A falling Newtonian film has a film thickness that can be obtained from the equation,

$$\delta = \left(\frac{3\mu\Gamma}{\rho^2 g} \right)^{1/3} \tag{2.56}$$

The equation can be derived from the Navier-Stokes equation. The equations showed that the film thickness is related to the wetting rate, density, gravitational acceleration and viscosity of the falling film.

In Yih (1986), various equations for film thickness of the form,

$$\delta = a\left(\nu^2 / g\right)^{1/3} \left(4\Gamma / \mu\right)^b \tag{2.57}$$

were provided and were tabulated as below.

Table 2.1: Various values of a and b.

a	b	Region	Author*
0.91	1/3	Laminar	Nusselt
0.8434	1/3	Wavy laminar	Kapitza
0.805	0.368	Wavy laminar	Lukach et al.
0.0682	2/3	Turbulent	Brotz
0.2077	8/15	Turbulent	Brauer
0.266	1/2	Turbulent	Feind
0.141	7/12	Turbulent	Zhivaikin
0.1373	7/12	Turbulent	Ganchev et al.
0.1364	7/12	Turbulent	Kosky
0.2281	0.526	Turbulent	Takahama and Kato
0.1721	0.562	Turbulent	Mostofizadeh

* Full references are given by Yih (1986)

The film thickness of a non-Newtonian falling film, in particular to this studies were derived in Section 4.

2.5.5. Film breakdown

From equation (2.56), the film thickness can be seen to be directly proportional to the wetting rate of film flow. The equation indicated that an increase in wetting rate increases the film thickness.

The film thickness is an important factor in falling film flow and attention may be given to this area. One reason was that information about film thickness could give an indication of the tube being completely wetted. Conversely, the wetting rate can help to determine the film thickness that maintains the wetting of the tube.

A study on minimum wetting rate for falling film under constant temperature and with some heat transfer was conducted by Tandon (2004). The study includes many literature reviews in the area of film thickness, wetting rate as well as heat transfer.

Many correlations and equations for heat transfer coefficients, film thickness and wetting rate were reviewed as a result.

His results from experimentally determined wetting rates using distilled water, aqueous 50% sucrose solution, aqueous 10% reconstituted skim milk and aqueous 40% reconstituted skim milk were later compared with the literature results.

His results showed decreasing trends of minimum wetting rates with increasing film temperatures. Also, the minimum wetting rates decreases and increases with increasing film temperatures at constant temperature difference, ΔT.

A study by Morison et al. (2006) on the minimum wetting and distribution rates, showed that the minimum wetting rate is more dependent on surface tension and contact angle and that the viscosity have very little influence on it. This is an improvement on the works of Paramalingam et al. (2000) which earlier stated that the minimum wetting rate is depended on liquid density, viscosity, surface tension and contact angle.

2.6. Film Temperature Distribution

The interest in the temperature distribution lies in the falling film thickness and not length wise down the evaporator tube. Knowledge about the film temperature distribution could reveal how the temperature changes across the film thickness with the constant and steady flow flowing downwards.

Presented in this review are solutions/expressions obtained for the problem using mathematical approaches.

Saouli and Aiboud-Saouli (2004) derived a mathematical model for determining temperature distribution of falling liquid film along an inclined heated plate. Using the method of separation of variables, they gave the following solution for the Newtonian falling film with heat transfer,

$$\Theta(X,Y)=\frac{3}{2}X+\frac{3}{2}\left(\frac{Y}{2}-1\right)Y-\frac{1}{8}(1-Y)^4+\frac{63}{120} \qquad (2.58)$$

where, $\Theta(X,Y)=\frac{T(x,y)-T_0}{\Delta T}$, $X=\frac{ax}{u_m\delta^2}$, $Y=\frac{y}{\delta}$, $a=\frac{k}{\rho C_p}$, $\Delta T=\frac{\phi\delta}{k}$ and u_m $=\frac{1}{2}\left(\frac{\rho g\sin\theta}{\mu}\right)\delta^2$.

The solution was based on the conditions that the inlet temperature was $T_0=T(0,y)$ and flowing along the wall with constant heat flux, ϕ ($W\cdot m^{-2}$). The film surface was adiabatic and the entrance effect was neglected. The θ is the inclination angle in radian and μ is the dynamic viscosity.

Zhang et al. (2008) studied the temperature distribution of heated falling liquid films using water, ethanol aqueous solutions and glycerol aqueous solutions. They did this both experimentally and theoretically. Their studies involved the surface temperature distribution of the flowing film along the distance downstream from the inlet and across the thickness of the film.

They mentioned that the surface temperature of the film gradually rises as the film flows downwards and that a lower flow rate of the film or larger wall temperature generally causes higher surface temperature of the film.

Their solution for a Newtonian falling film is given by equation (2.59). This was solved for by assuming the film surface at the film incipience was smooth and the entrance effect neglected. Further, the flow have an initial temperature of $T_0=T(0,y)$ and wall temperature of $T_w=T(x,0)$ where *x* and *y* are the vertical and horizontal axis respectively. The μ in the equation is the dynamic viscosity.

$$\Theta(X,Y)=\frac{1}{e^{-1}-e^{\frac{1}{2}}}\cdot\left(e^{-X-\frac{1}{2}Y^2+Y}-e^{\frac{1}{2}}\right) \qquad (2.59)$$

where $\Theta(X,Y) = \frac{T(x,y)-T_0}{T_w-T_0}$, $X = \frac{ax}{u_m\delta^2}$, $Y = \frac{y}{\delta}$, $a = \frac{k}{\rho C_p}$, $T_w = T(x,0)$, $T_0 = T(0,y)$, $u_m = \frac{\rho g\delta^2}{2\mu}$.

Lockshin and Zakharov (2001) worked the exact solutions for a laminar Newtonian falling film with consideration of a shear stress at the interface and with heat transfer from the wall. A dimensionless parameter, Ω, relating the strength of traction of film surface to mass forces was introduced. The physical properties were assumed constant and no evaporation occurred. With these assumptions, the strong dependence of viscosity with temperature was neglected.

2.7. Wave Phenomenon

Although the wave effect was neglected in the current studies, waves are present in a falling film. Philipp et al. (as cited in Storch, Philipp and Gross, 2008) provided various characteristics of wave shapes possible for a falling film inside vertical tubes.

The formation of waves has attracted many studies on the hydrodynamics of the wave phenomena alone (Karimi and Kawaji, 1998, Moran, Inumaru and Kawaji, 2002). Such studies later incorporated the effects of waves on heat transfer as well as to mass transfer (Park and Nosoko, 2003, Park et al., 2004).

A notable study by Jayanthi and Hewit (1997) proved that the recirculation effect brought about by waves does not enhance heat transfer and that it is the effective thinning of the film that does so. They concluded that the overall heat transfer coefficient is primarily determined by conduction through the film.

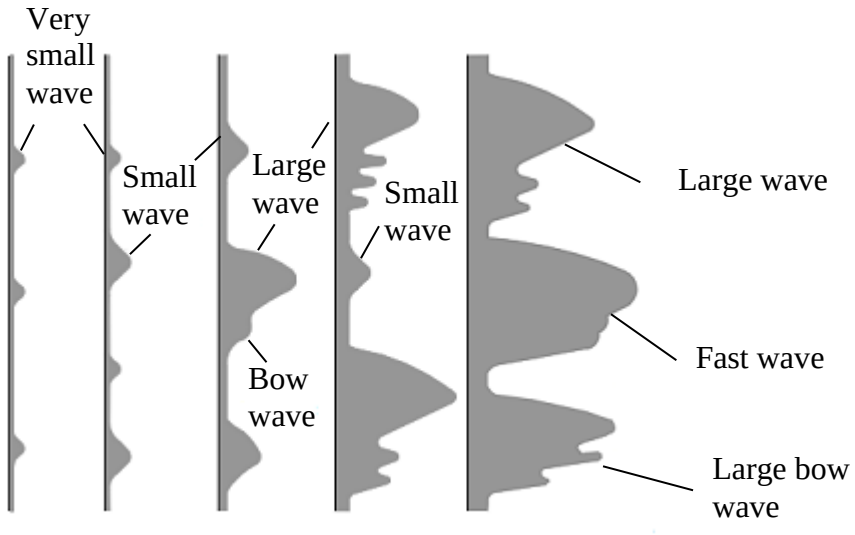

Figure 2.3: The various types of waves.

2.8. Protein Denaturation

2.8.1. Milk Proteins

Milk proteins that are present in milk consist of about 80% caseins and 20% whey proteins. The caseins in milk proteins are made up of:

- κ-casein
- α_{s1}-casein
- α_{s2}-casein
- β-casein

While whey proteins are made up of:

- β-lactoglobulin
- α-lactalbumin
- Immunoglobulin G
- Bovine serum albumin (BSA)

Whey proteins can be further classified into major or minor whey proteins. The bovine serum albumin (BSA) and immunoglobulin G are the minor whey proteins while α-lactalbumin and β-lactoglobulin are the major whey proteins.

At high temperatures, whey proteins denatured. Minor whey protein begins to denature at about 65 °C while major whey protein denatures at temperatures more than 70 - 75 °C. When denatured, whey proteins are unfolded from their native state.

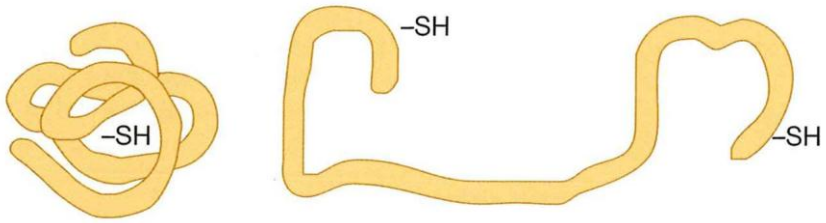

Figure 2.4: Whey protein before and after denaturation (Bylund, 2003).

The sensitivity to heat induced denaturation of whey protein is in the order of immunoglobulin G, bovine serum albumin (BSA), β-lactoglobulin and α-lactalbumin.

In the process of skim milk powder manufacture, irreversible whey protein denaturation occurs during the preheating stage. Evaporation and spray drying has little effect on whey protein denaturation (Oldfield et al., 2005).

2.8.2. Age Thickening

The physical and chemical properties of milk proteins are manifested in the functional properties of milk powders (Singh, 2007). These functional properties include viscosity, emulsification, foaming, water absorption, solubility, gelation and heat stability.

Heating milk at high temperatures of about more than 70 °C causes whey proteins to denature and to form κ-casein/whey protein complexes in milk. The formation of

these κ-casein/whey protein complexes has been associated with the increased in casein micelle size.

At any temperatures of 75 to 100 °C and time of up to 60 minutes, the size of casein micelles increased with heat treatment, holding times and increased in temperatures (Anema and Li, 2003).

It was found later that the increase in micelle size also relates to the increase in milk viscosity. The relationship between viscosity and particle volume was correlated by Anema et al. (2004) to be linear. This gave an indication of the change in viscosity was related to the change in volume fraction of casein micelles as a consequence of heating.

It is uncertain if the result above is the mechanism for age thickening. It is also uncertain the pathways that led to the formation of the κ-casein/whey protein complexes. In a recent review by Donato and Guyomarc'h (2009), the possible pathways were suggested to be either by formation of primary aggregates or partition of soluble and micelle-bound complexes.

However, it is mostly believed that the interactions involved thiol-disulphide exchange reactions between denatured β-lactoglobulin and κ-casein at the micelle surface to form the κ-casein/whey protein complexes.

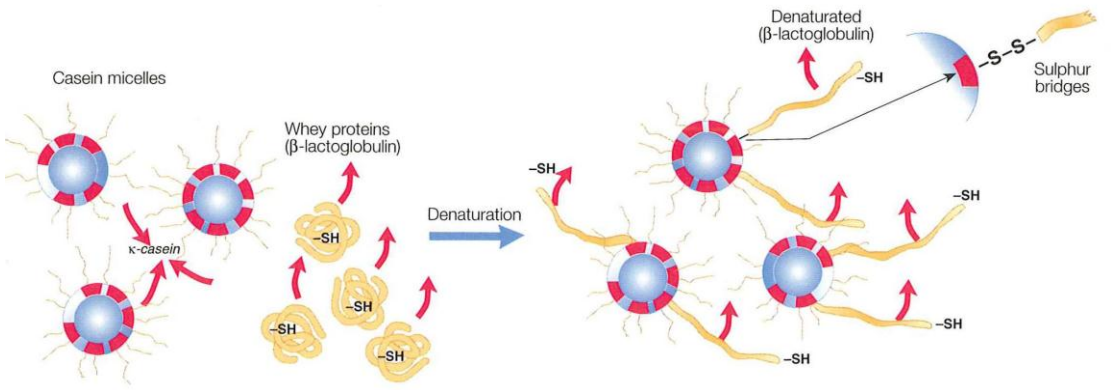

Figure 2.5: Diagrammatic formation of disulphide linkages between κ-casein and β-lactoglobulin (Bylund, 2003).

Despite the increase in viscosity from the denaturation of whey proteins due to heating, the age thickening phenomena is also influenced by the solids content and will be more so the higher the solids content in the concentrate (Figure 2.6).

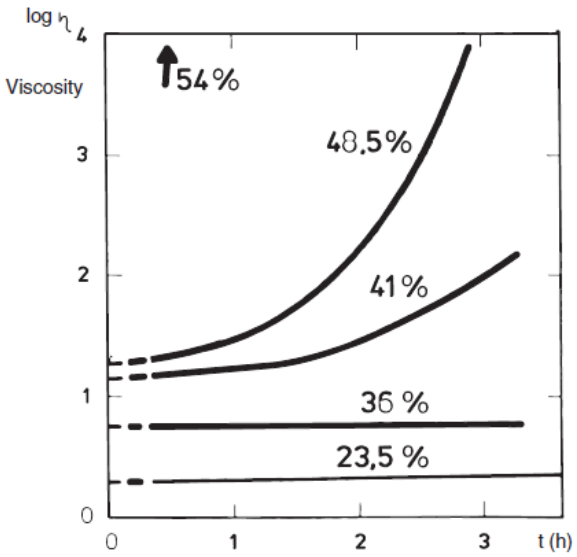

Figure 2.6: The changes of viscosity with time at different total solids for skim milk at 55 °C (Westergaard, 2004).

The trends depicting the change in viscosity with time depending on temperature are shown as below from Westergard.

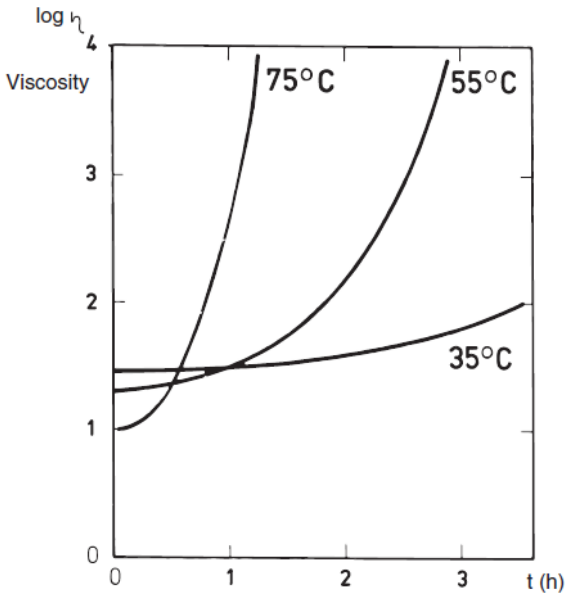

Figure 2.7: The changes of viscosity with time at different temperatures for skim milk at 48.5% solids (Westergaard, 2004).

Westergaard (2004) stated that when milk is heated the viscosity drops with time as a natural result of the temperature increase, but as the age thickening becomes more pronounced at higher temperatures, the viscosity will soon increase to the same level and further on as time passes.

3. Experimental Methods

3.1. Materials

Experimental data obtained was of the total solids in the range from 19.93% - 62.09% and at viscosity measurement temperatures 25 - 50 °C (see Table 3.1). Various types of milk were used:

- FTM - Klondyke Fresh Trim Milk (99.5% fat free pasteurised & homogenized skim milk);
- MFTM - Meadow Fresh Trim Milk (99.6% fat free fresh homogenized low fat milk);
- BM - Klondyke Fresh Blue Milk (pasteurized & homogenized milk).

Table 3.1: The milk type and temperature of viscosity measurement for each total solids.

Total Solids	Milk Type	Temperature of viscosity measurement
19.93%	MFTM	40 °C
22.60%	MFTM	40 °C
23.34%	FTM	25 °C
35.47%	MFTM	45 °C
36.60%	MFTM	45 °C
36.66%	MFTM	40 °C
38.27%	MFTM	45 °C
41.00%	MFTM	45 °C
42.50%	MFTM	45 °C
45.40%	MFTM	45 °C
46.23%	MFTM	40 °C
48.61%	BM	25 °C
49.25%	MFTM	45 °C
57.71%	BM	50 °C
62.09%	BM	40 °C

The compositional information available for the different types of milk used is listed in the table below.

Table 3.2: Compositional information for corresponding milk type used.

	Klondyke Fresh Trim (Quantity per 100ml)	**Meadow Fresh Trim (Quantity per 100ml)**	**Klondyke Fresh Blue (Quantity per 100ml)**
Protein	3.9g	3.7g	3.3g
Fat - Total	0.5g	0.4g	3.4g
- Saturated	0.3g	0.2g	2.1g
Carbohydrate - Total	4.9g	4.9g	4.5g
- Sugars	4.9g	4.9g	4.5g
Sodium	45mg	45mg	43mg
Calcium	150mg	130mg	116mg

3.2. Experimental Procedures

The steps in carrying out the experiments were as follow:

1. Meadow Fresh Trim milk, Klondyke Fresh Trim milk, Klondyke Fresh Blue milk and Meadow Fresh Original milk were used for the experiments.
2. The Lot number for 1 L milk was recorded. The expiration date on the milk was also noted as identification.
3. For each particular milk, the initial total solids were determined as mentioned in Section 3.7.
4. The amount of milk required to concentrate to the desired total solids was determined using the Excel spreadsheet as mentioned in Section 3.5.
5. The milk was concentrated as mentioned in Section 3.5.
6. After step 5, a sample was taken for viscosity measurements. The viscosity measurements were described in Section 3.6.

7. After step 5, a sample was taken for total solids/moisture content measurements. The total solids/moisture content measurements were described in Section 3.7.
8. Steps 4-7 repeated for other required total solids.

For age thickening experiments,

a. The NV viscometer cylinder to be used was preheated in the oven at 45 °C for two hours before starting the experiments.
b. Steps 1 - 6 above were carried out
c. The openings around the NV sensor and M5 system was covered using cling wrap.
d. The Haake water bath temperature was set to 45 °C.
e. After viscosity measurements were taken, sample was left in the viscometer for 15 minutes. Measurements were then repeated with the same shear rate settings and temperature.
f. Step e was repeated 12 times (a total of 3 hours).

3.3. Calibration of condensate flask

The condensate flask that collects condensed vapour was calibrated so that the volume collected could be seen. Water was used for the calibration. The weighing scale, Sartorius CP4202S was used.

3.4. Preparation of Antifoam

One drop of Dow Corning Antifoam 1520-US was added into 1 ml of distilled water and stirred. Two drops from this was added into milk that was to be concentrated.

3.5. Concentrating milk

The total solids of milk after concentration in the rotary evaporator could not be determined until the moisture content/total solids tests were performed.

A spreadsheet calculation was made available to predetermine the approximate total solids to be obtained from the rotary evaporator before concentrating the milk. For the calculations, the initial total solids were obtained and amount of milk determined.

The spreadsheet and the sample calculations were attached in the Appendices.

Milk was concentrated using a BUCHI rotary evaporator (BUCHI, Switzerland). This enabled milk to be concentrated under vacuum and low temperature. The BUCHI rotary evaporator consists of Heating bath, B-491, Vacuum controller, V-850 and Rotavapor, R-210. A 1 L round bottom flask was used.

The operating conditions used in the experiments:

- Pressure: 110 mbar
- Water bath temperature: 65 °C
- Rotation: 2 rpm

3.6. Viscosity measurements

The viscosity of concentrated milk was measured using the Haake viscometer with the M5 system (HAAKE, Germany). The Haake viscometer consists of Rotovisco (RV20), Rheocontroller (RC20), temperature controller (Haake F3) and water bath (Haake C). The shear stress - shear rate data can be obtained from this viscometer with a small amount of sample. The coaxial cylinder sensor was used. Two types of sensors, NV and MV sensors were used. The MV sensor was used when the sample of milk concentrate was high.

The sample volume required for the NV and MV sensors were 9 mL and 40 mL respectively. The sample volume was inserted into the sensor cup using a 10 ml syringe.

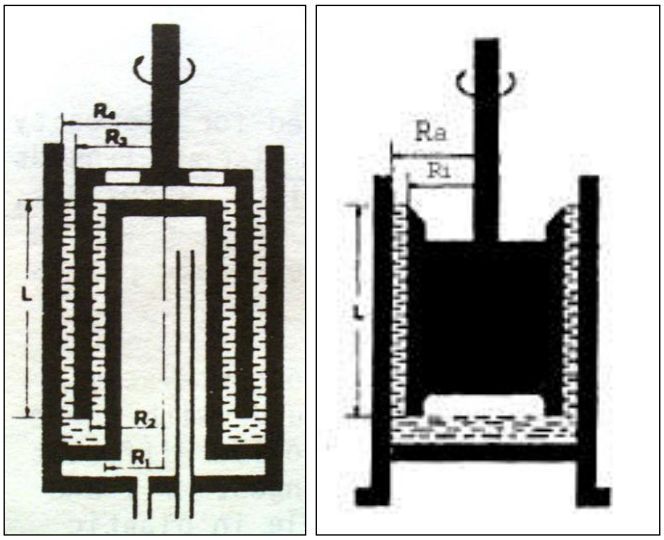

(a) (b)

Figure 3.1: (a) – NV sensor, (b) - MV sensor.

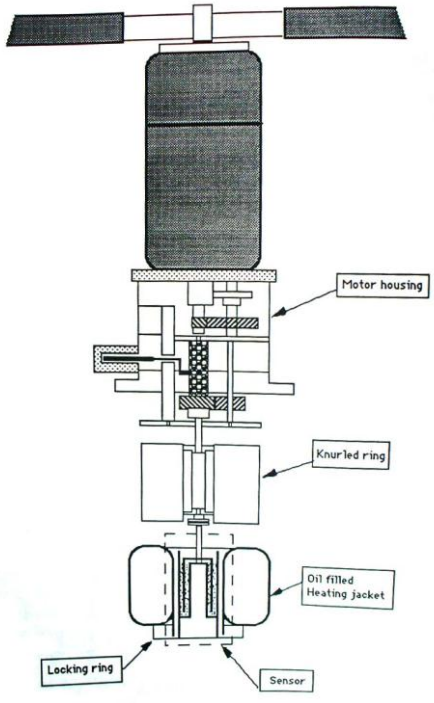

Figure 3.2: Haake M5 system.

The temperature controller, Haake F3 was used to adjust the temperature the measurements were taken. Measurements were taken at 25 °C, 30 °C, 40 °C, 45 °C and 50 °C.

The range of shear rates used was from 0.87 s^{-1} to 2709 s^{-1}. In some cases, the torque on display exceeded 100% and the viscometer automatically stopped. New shear rate settings were then introduced and measurements repeated.

All shear stress values obtained were applied with a correction using equation (3.1), which had been obtained using standard viscosity calibration oils.

$$\tau_{haake} = \tau - A\exp\left(\frac{\dot{\gamma}}{B}\right) \qquad (3.1)$$

where A is 0.04, B is 1/0.0012, τ is experimental shear stress values and $\dot{\gamma}$ is experimental shear rate values. The Haake Viscometer operating procedure was followed.

3.7. Total solids/Moisture content measurements

The sample taken after evaporation was transferred to a clean, dried and cooled aluminium dish. The total solids measurements were done in triplicates. The sample was dried in the Labserv oven for 5 hours at 105 °C.

The mass of the dish, before drying and after drying was recorded. The moisture and total solids content were calculated with the following equation:

$$Moisture\ Content = \frac{wet\ mass - dry\ mass}{total\ wet\ mass} \qquad (3.2)$$

$$Solids\ Content = \frac{dry\ mass}{total\ wet\ mass} \qquad (3.3)$$

4. Rheological Model

4.1. Newtonian And Non-Newtonian Fluids

A fluid of which the viscosity is constant with various shear rates is said to be a Newtonian fluid. Newtonian fluids are fluids that can be described by the Newton's law of viscosity. It can be denoted by the formula,

$$\tau = \mu\dot{\gamma} \tag{4.1}$$

The constant of proportionality, μ is the viscosity of Newtonian fluid and relates shear stress, τ with shear rate, $\dot{\gamma}$. A fluid that is not Newtonian is called non-Newtonian fluid. Its viscosity is not constant and changes with shear rate. The term 'apparent viscosity' is used for non-Newtonian fluids and given as,

$$\eta_a = \frac{\tau}{\dot{\gamma}} \tag{4.2}$$

Non-Newtonian fluids have flow curves that deviate from a straight line through the origin. Several non-Newtonian fluids can be classified by their flow curves in a plot of shear stress versus shear rate (Figure 4.1).

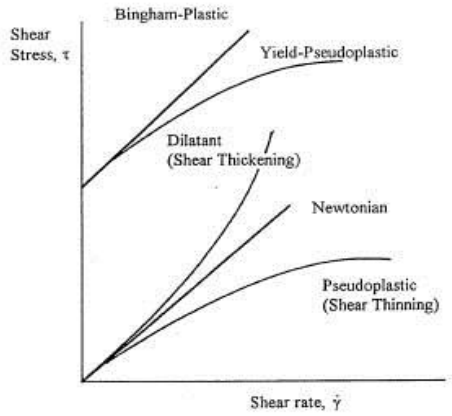

Figure 4.1: Flow curves for Newtonian and non-Newtonian fluids.

Each of these fluids can be described by models. A Bingham-Plastic fluid can be modeled by the Bingham equation,

$$\tau - \tau_y = \eta_b \dot{\gamma} \tag{4.3}$$

A pseudoplastic fluid can be modeled by either the power law equation,

$$\tau = K\dot{\gamma}^n \tag{4.4}$$

the Herschel-Bulkley equation,

$$\tau = \tau_y + K\dot{\gamma}^n \tag{4.5}$$

or Casson equation to name a few,

$$\sqrt{\tau} = \sqrt{\tau_y} + \sqrt{\eta_c \dot{\gamma}} \tag{4.6}$$

There are several more equations for a pseudoplastic fluid as well as for a dilatant fluid that are not mentioned here.

4.2. Rheological Parameters

The rheological model chosen to model the rheological changes of milk was the Herschel-Bulkley model and it has three parameters:

- Yield stress, τ_y (Pa)
- Consistency factor, K (Pa·s^n)
- Flow behavior index, n

The Herschel-Bulkley model can transpose into a power law model when the yield stress, τ_y, is zero, and for when $n = 1$ and $\tau_y = 0$ it transposes into the Newton's law of viscosity. Therefore, it is a suitable model for the Newtonian nature of milk at low concentrations and the pseudoplastic nature of milk at high concentrations.

In order to gain a better understanding of the non-Newtonian nature or *pseudoplasticity* of milk at higher concentrations, experiments were carried out to obtain the shear stress - shear rate data at various concentrations. The relationships of the three parameters (τ_y, K and n) with concentrations were then developed.

4.3. Methods

The methods outlined in Chapter 3 were followed.

4.4. Results

4.4.1. Shear Stress - Shear Rate

The experimental data was plotted as a shear stress - shear rate curve in Figures 4.2 to 4.4. Also included in the figures were the temperatures at which the shear stress - shear rate data were measured.

The method of least squares was used to fit the Herschel-Bulkley model with the experimental data. It was found that the Herschel-Bulkley model (HB-Model) fitted well to all data points.

The concentrated milk exhibited both Newtonian and non-Newtonian type fluids. At low concentrations of 19.93% - 36.66% total solids (*TS*), milk was Newtonian. A strange result was obtained for milk at 19.93% TS where it exhibited higher shear stress than milk at 22.6% TS.

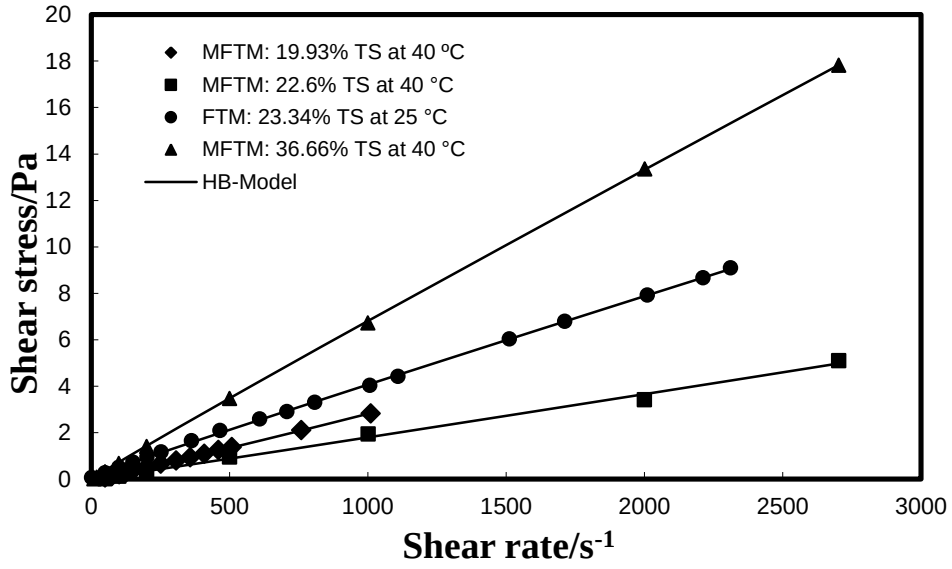

Figure 4.2: Flow curves of milk from 19.93% to 36.66% total solids.

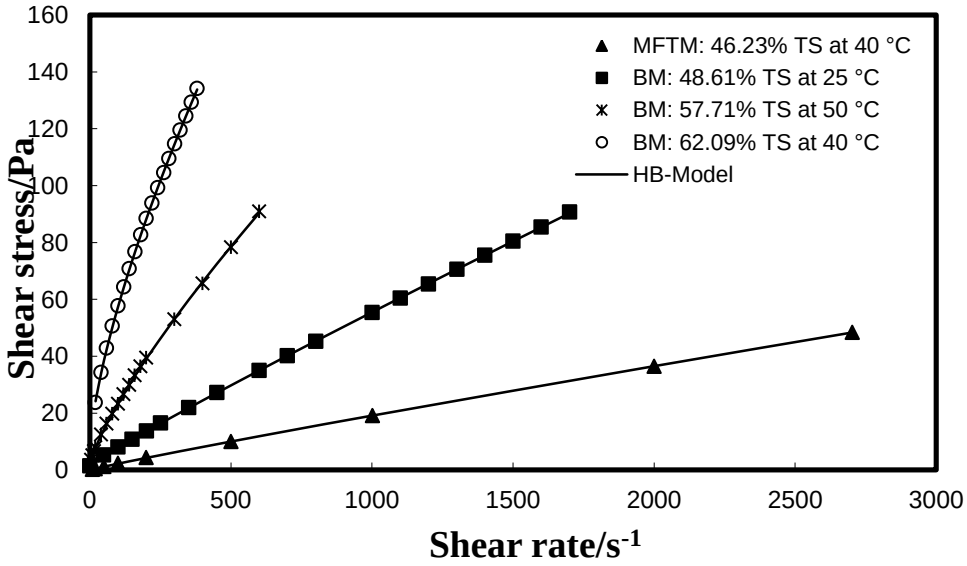

Figure 4.3: Flow curves of milk from 46.23% to 62.09% total solids.

Table 4.2 further showed the results of the rheological parameters for milk at various total solids. The rheological parameters were obtained from the least square method using Excel Solver.

As the table showed, the flow behavior index, *n*, for 19.93% TS and 22.6% TS are 1.073 and 1.025 respectively. These values of *n* are unlikely to be more than 1.0 for a Newtonian fluid and would constitute as experimental errors. This is the same for the

small yield stress, τ_y = 0.09 Pa that was detected at 23.34% *TS*. However the uncertainties that arise from these were small.

At 36.66% TS the flow behavior index, *n*, remained quite close to 1.0 showing that milk is still Newtonian. At 46.23% TS, the value of n was significantly below 1.0 and at 48.61% *TS* and above, yield stress was detected showing that at these concentrations, milk was no longer Newtonian.

Table 4.1: The results of Yield Stress, Consistency Factor and Flow Behaviour Index at different total solids.

Total Solids (***TS*/g·g^{-1}**)	**Yield Stress** (**τ_y/Pa**)	**Consistency Factor** (***K*/Pa·s^{n}**)	**Flow Behaviour Index** (***n***)
0.1993	0	0.00170	1.073
0.2260	0	0.00151	1.025
0.2334	0.090	0.00495	0.969
0.3666	0	0.00780	0.979
0.4623	0	0.0303	0.933
0.4861	1.83	0.0801	0.942
0.5771	1.72	0.582	0.786
0.6209	8.13	1.96	0.701

The results from Figure 4.4 showed that at the same shear rate, a temperature of 30 °C does not have significant effect on the milk's shear stress. However, an increase of temperature from 30 °C to 40 °C and later to 50 °C has the effect of increasing the shear stress of milk at the particular concentration of 62.09% *TS*. At the particular temperature of 40 °C, for the same shear rate, the shear stress can be seen to drop below those at 30 °C. This drop in shear stress meant that the viscosity also dropped when temperature increased from 30 °C to 40 °C. The significant increase in yield stress at 50 °C could signify the effect of age thickening was present.

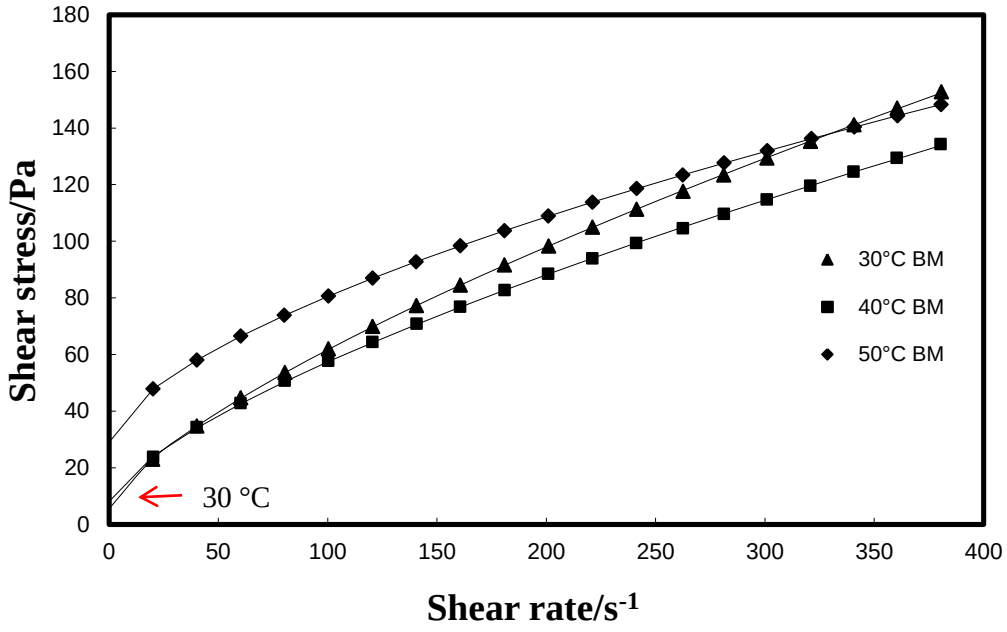

Figure 4.4: Homogenised whole milk at 62.09% total solids at different temperatures.

4.4.2. Viscosity

The same shear stress - shear rate data was recalculated as viscosity and Figure 4.5 showed the changes in viscosity at different shear rates. This result is not particular to a specific type of milk as it was taken from the same shear stress - shear rate data from different milks obtained earlier.

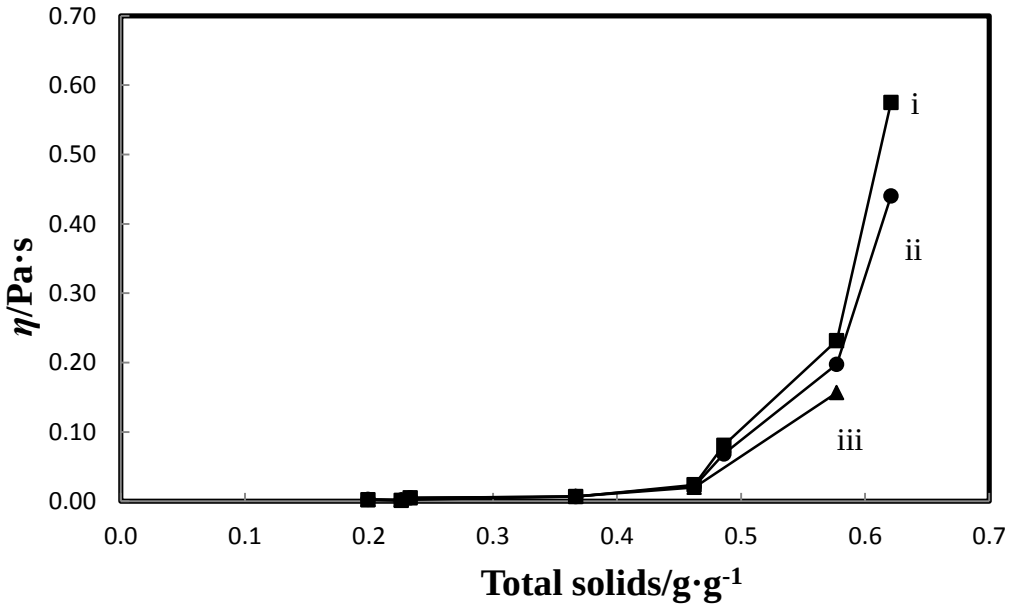

Figure 4.5: Milk viscosity at different total solids and shear rates of i) 100 s-1, ii) 200 s-1 and iii) 500 s-1.

The results showed that at higher concentrations, milk viscosity increases exponentially. At a high shear rate milk viscosity was reduced while at lower shear rates milk viscosities were high.

4.4.3. Rheological Parameters

A rheological model was required later for falling film modeling work. It was decided to use empirical modeling and not focusing on the physical mechanisms underlying a model.

Three models were developed relating the changes of the three parameters with concentrations. The model developed for the yield stress uses experimental data from 46.23% to 62.09% *TS*. The sum of the squares of the differences between the model and experimental values was calculated. The constants in the equation model, a_{yield} and b_{yield} were obtained following the use of Excel Solver to minimize the sum of squares.

$$\tau_y = MAX\left[0, \frac{a_{yield}}{\left(1-\frac{TS}{TS_{\max}}\right)^{b_{yield}}} - 0.5\right] \qquad (4.7)$$

where a_{yield} = 0.187

b_{yield} = 1.26

TS_{max} = 0.653

Figure 4.6 showed the model closely predicting the yield stress. While more data would reduce the uncertainty, the model obtained was significant to allow subsequent flow modeling.

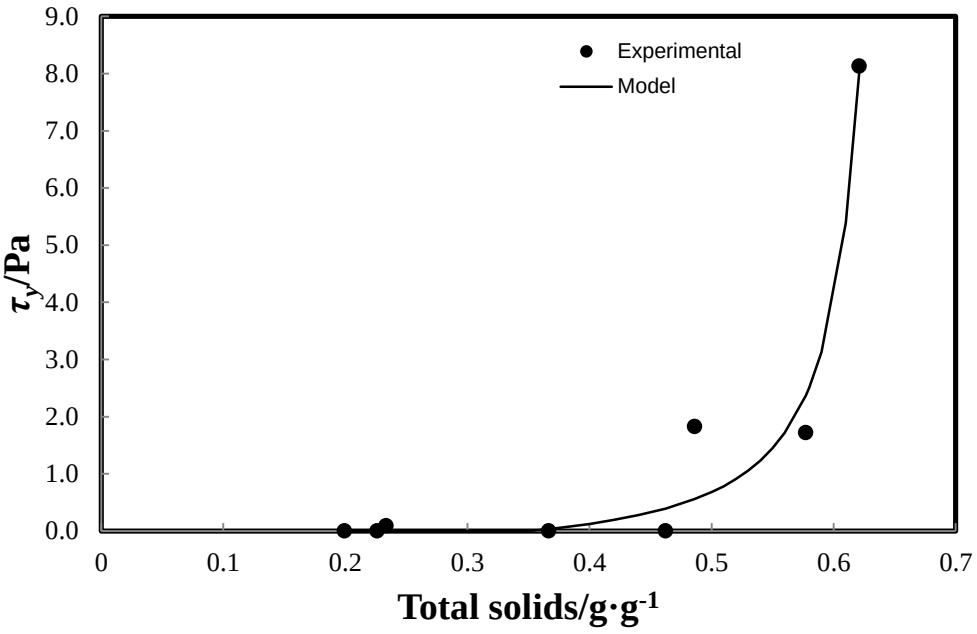

Figure 4.6: Fitting a model to the experimental yield stress results.

Table 4.2: Yield Stress values from experiments and model.

Total Solids (TS/g·g^{-1})	**Experimental Yield Stress (τ_y/Pa)**	**Yield Stress Model (τ_{ymodel})**
0.4623	0	0.39
0.4861	1.83	0.56
0.5771	1.72	2.4
0.6209	8.13	8.0

The flow behaviour index model was developed based on experimental data from 46.23 - 62.09% *TS*. The curve from the equation model was plotted with all experimental data and constants a_{index}, b_{index} and c_{index} determined by best fit to the experimental data (Figure 4.7).

$$n = \left(\left(\frac{1}{a_{index} - b_{index} TS} \right)^{c_{index}} + 1 \right)^{-1/c_{index}} \qquad (4.8)$$

where a_{index} = 1.88

b_{index} = -1.9

c_{index} = 15

The exponent c_{index} was introduced to enable a smooth transition from n = 1 to lower values.

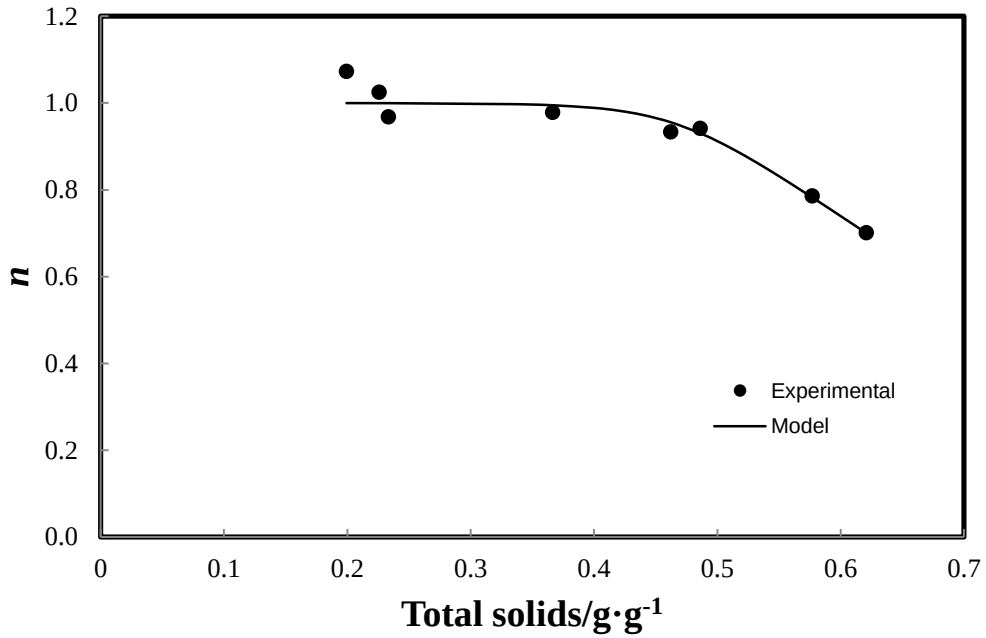

Figure 4.7: Fitting a model to the experimental flow behavior index results.

To develop the model for the consistency factor, K, equation (4.5) was rearranged to,

$$K = \frac{\left(\tau - \tau_y\right)}{\dot{\gamma}^n} \qquad (4.9)$$

so that the consistency factor, K, was a function of yield stress, τ_y, flow behaviour index, n, shear rates, $\dot{\gamma}$ and shear stress, τ.

$$K = \frac{\left(\tau - \tau_{y\text{model}}\right)}{\dot{\gamma}^{n_{\text{model}}}} \qquad (4.10)$$

The yield stress model and flow behaviour index model were substituted into equation (4.7) together with shear stress and shear rates from experimental data to form equation (4.8). The model to be developed will be based against this equation. The consistency factor from equation (4.8) was calculated at shear rate, $\dot{\gamma}$ = 100 s^{-1} as this is a typical value for falling film flow.

Table 4.3: Consistency Factor values from equation and model.

Total Solids (TS/g·g^{-1})	**Consistency Factor Equation 4.8 (K/Pa·s^n)**	**Consistency Factor Model (K_{model})**
0.1993	0.00197	0.0018
0.226	0.00119	0.0022
0.2334	0.00501	0.0024
0.3666	0.0065	0.0095
0.4623	0.024	0.039
0.4861	0.103	0.061
0.5771	0.57	0.50
0.6209	1.97	1.99

The sum of the squares of the differences was used to calculate the difference between the model and the consistency factor calculated from equation (4.8). The Excel Solver then used to minimize the sum of the squares to determine the constant a_k in the model from an initial guess.

$$K = e\left(\frac{a_k TS}{1-TS}\right)\mu_{water} \qquad (4.11)$$

where a_k = 5.06

μ_{water} = Viscosity of water at the measurement temperature.

The experimental values for consistency factor were determined from equation (4.7) and at shear rate, $\dot{\gamma}$ = 100 s^{-1}. These calculated experimental results and results from model were plotted in Figure 4.8.

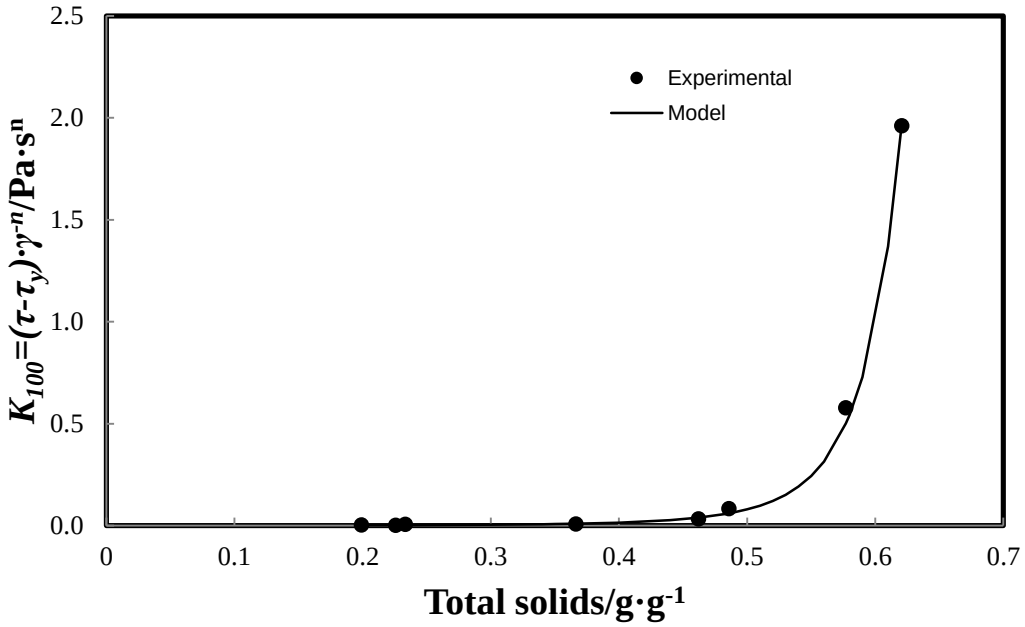

Figure 4.8: Fitting a model to the experimental Consistency Factor results.

These three models that were developed, the yield stress, consistency factor and flow behaviour index models were purely empirical models.

4.4.4. Comparison With Literature

Flow Behaviour Index (*n*)

The experimental results and the developed model were compared with results from literature (equations 2.50 and 2.54). Figure 4.9 shows that over the range of the total solids in this current experiment, the present results do not agree well with results from Reddy and Datta (1994) and Vélez-Ruiz and Barbosa-Cánovas (2000).

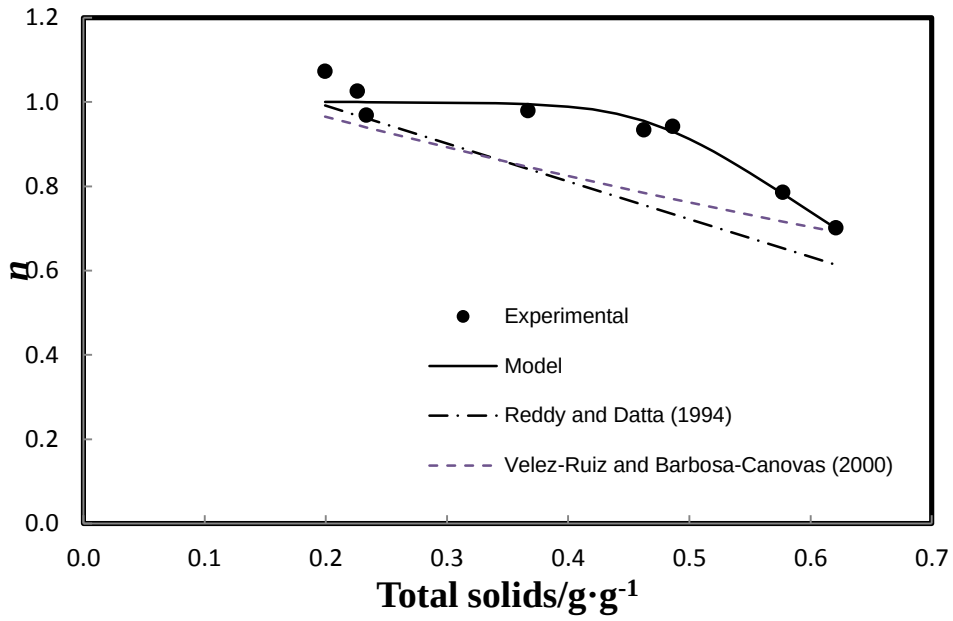

Figure 4.9: Comparison of experimental results and model with Reddy and Datta (1994) and Vélez-Ruiz and Barbosa-Cánovas (2000).

Consistency Factor (*K*)

The present results (Figure 4.10) of the Consistency Factor, *K*, were comparable with equation (2.55) from Vélez-Ruiz and Barbosa-Cánovas (2000).

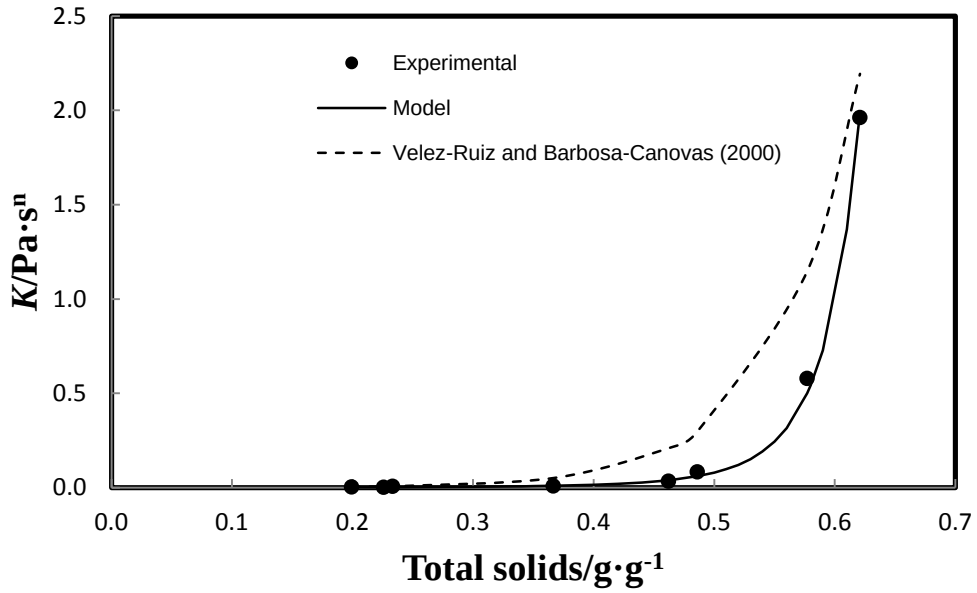

Figure 4.10: Comparison of experimental results and model with Vélez-Ruiz and Barbosa-Cánovas (2000).

Yield Stress (τ_y)

No literature giving yield stress equations for milk were found.

Viscosity (η)

Chong et al. (2009) from their experiments with four different types of skim milk, proposed the viscosity profile for high solids content to be modeled by the equation (4.12) with *A*, *B* and *C* fitting constants (see Table 4.5) and *X*, total solids (%).

$$\mu = A + \left(B \exp\left(CX\right)\right) \qquad (4.12)$$

The model proposed does not consider into effect the non-Newtonian behavior of milk at high concentration and was modeled from experimental viscosity measurements of total solids at more than 40%.

Table 4.4: The values of constants relating to different types of skim milk (Chong et al., 2009).

	Reconstituted skim milk	**Fresh skim milk**	**UHT skim milk**	**Factory skim milk**
A	9.9536	8.6212	-9.4636	2.6955
B	1.7989×10^{-4}	1.7675×10^{-6}	3.8260×10^{-2}	1.3759×10^{-4}
C	2.3848×10^{-1}	3.536×10^{-1}	1.4801×10^{-1}	2.5088×10^{-1}

The viscosity model for fresh skim milk was not used for comparison as they gave quite high values. Figure 4.11 shows the comparison between the models given by Chong et al. (2009) with experimental results. The models were fitted to the range of total solids obtained from the experiments. The experimental results used for comparison were from shear rate of 200 s^{-1}.

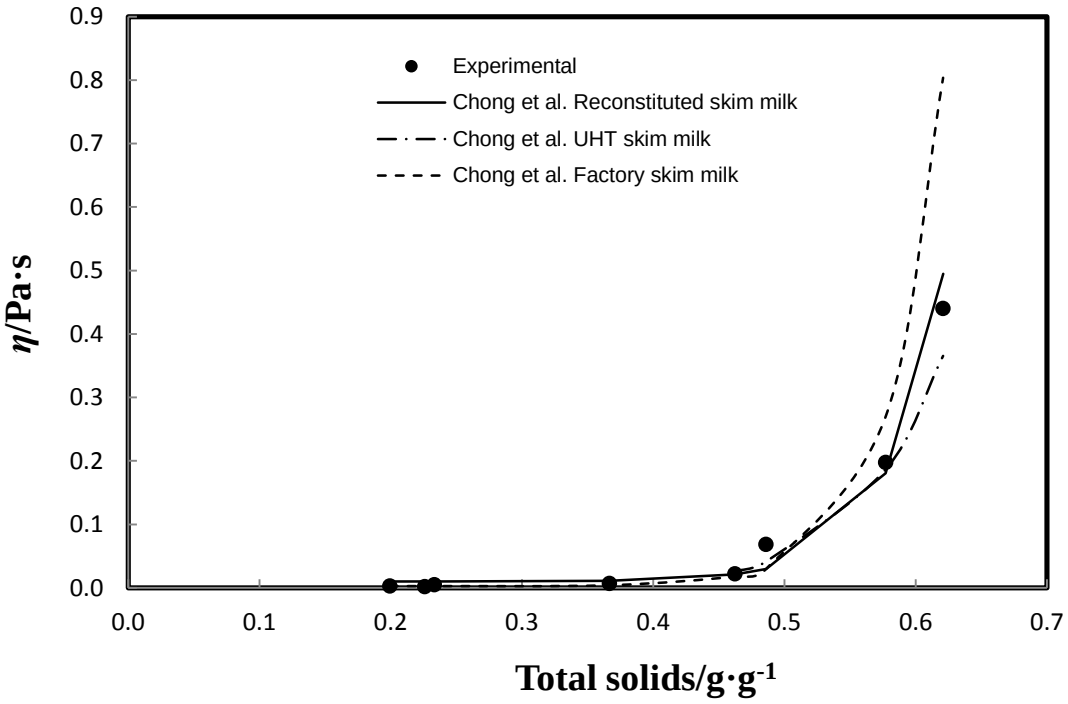

Figure 4.11:Comparison of experimental results with Chong et al. (2009) equation for reconstituted skim milk, UHT skim milk and factory skim milk.

4.4.5. Effects of Constants in Models

The constants in models were changed and their effects on the models developed were presented.

Yield stress model

The yield stress model consists of the constants a_{yield} and b_{yield}. The TS_{max} was fixed at 0.653. The a_{yield} and b_{yield} used in model were 0.188 and 1.267. Figure 4.12 shows the effects when the constant a_{yield} was changed. Table 4.6 displays the changes in a_{yield} while b_{yield} and TS_{max} remained the same.

Table 4.5: The changes in a_{yield} values.

	I	II	III
a_{yield}	0.150	0.188	0.210
b_{yield}	1.267	1.267	1.267
TS_{max}	0.653	0.653	0.653

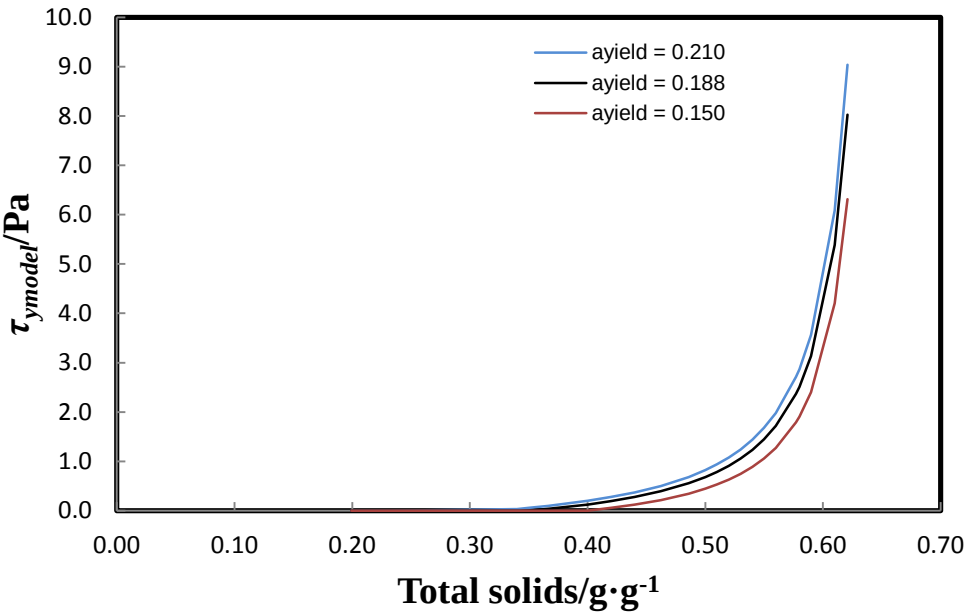

Figure 4.12: The effect of a_{yield} on yield stress model.

Figure 4.13 shows the effects when the constant b_{yield} was changed. Table 4.7 displays the changes in b_{yield} while a_{yield} and TS_{max} remained the same.

Table 4.6: The changes in b_{yield} values.

	I	II	III
a_{yield}	0.188	0.188	0.188
b_{yield}	1.160	1.267	1.360
TS_{max}	0.653	0.653	0.653

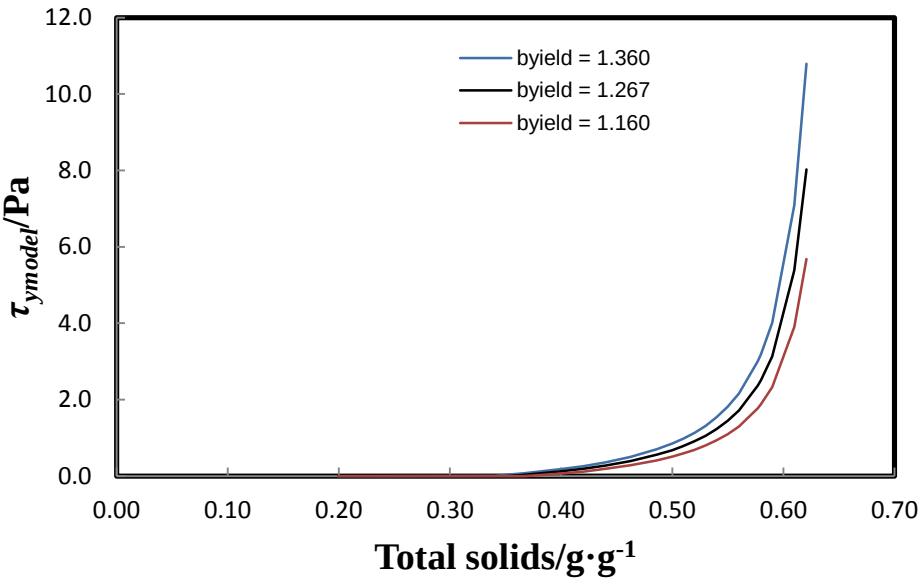

Figure 4.13: The effect of b_{yield} on yield stress model.

Flow behavior index model

The flow behaviour model consists of the constants a_{index}, b_{index} and c_{index}. The a_{index}, b_{index} and c_{index} used in model were 1.88, -1.9 and 15. Figure 4.14 showed the effects when the constant a_{index} was changed. Table 4.8 displayed the changes in a_{index} while b_{index} and c_{index} remained the same.

Table 4.7: The changes in a_{index} values.

	I	**II**	**III**
a_{index}	1.5	1.88	2.1
b_{index}	-1.9	-1.9	-1.9
c_{index}	15	15	15

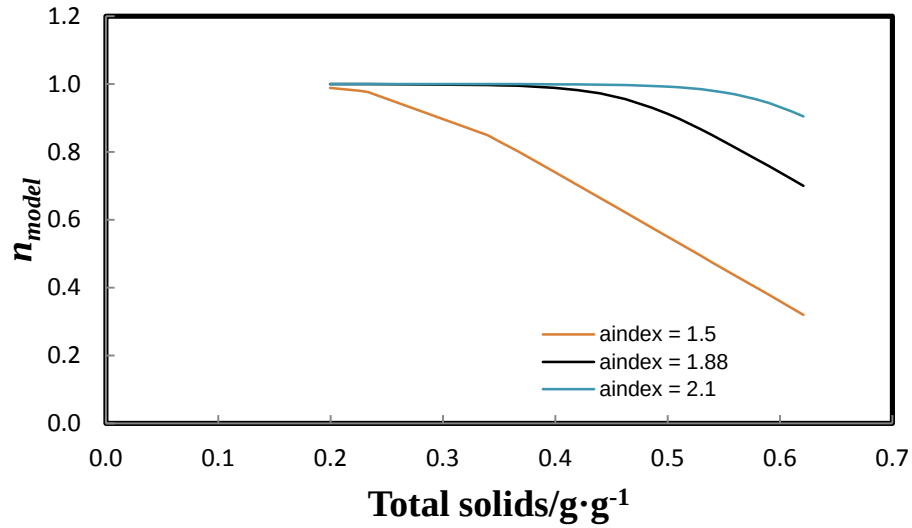

Figure 4.14: The effect of a_{index} on flow behavior index model.

Figure 4.15 shows the effects when the constant b_{index} was changed. Table 4.9 displays the changes in b_{index} while a_{index} and c_{index} remained the same.

Table 4.8: The changes in b_{index} values.

	I	II	III
a_{index}	1.88	1.88	1.88
b_{index}	-2.2	-1.9	-1.6
c_{index}	15	15	15

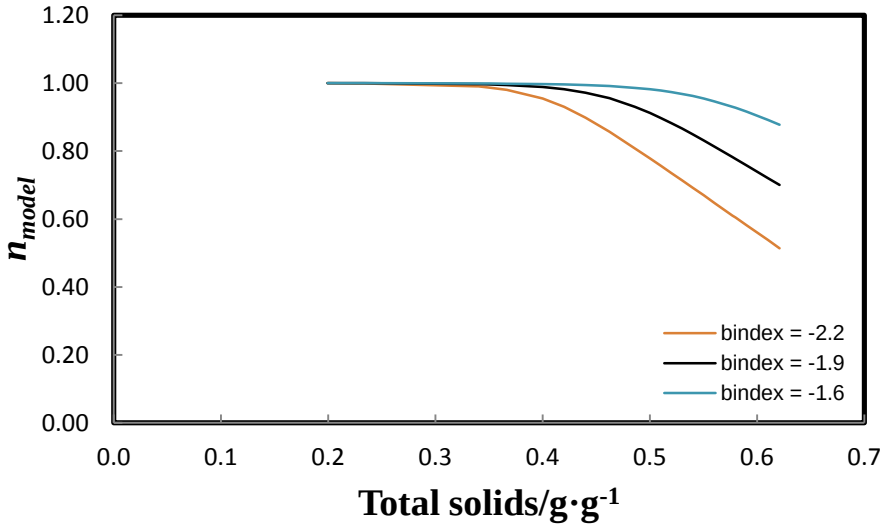

Figure 4.15: The effect of b_{index} on flow behavior index model.

Figure 4.16 shows the effects when the constant c_{index} was changed. Table 4.10 displays the changes in c_{index} while a_{index} and b_{index} remained the same.

Table 4.9: The changes in c_{index} values.

	I	II	III
a_{index}	1.88	1.88	1.88
b_{index}	-1.9	-1.9	-1.9
c_{index}	10	15	25

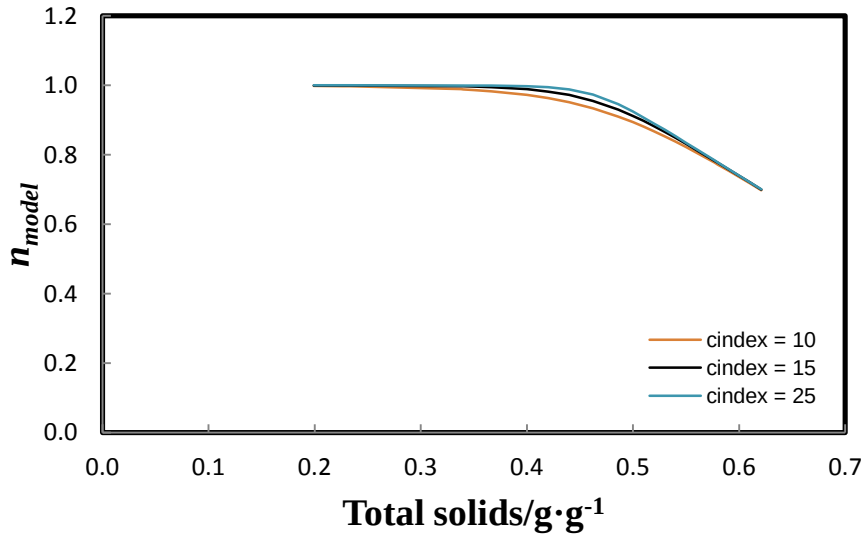

Figure 4.16: The effect of c_{index} on flow behavior index model.

Consistency factor model

The consistency factor model consists of the constant a_k. The a_k used in model was 5.066. Figure 4.17 shows the effects when the constant a_k was changed. Table 4.11 displays the changes in a_k.

Table 4.10: The changes in a_k values.

	I	II	III
a_k	4.7	5.066	5.3

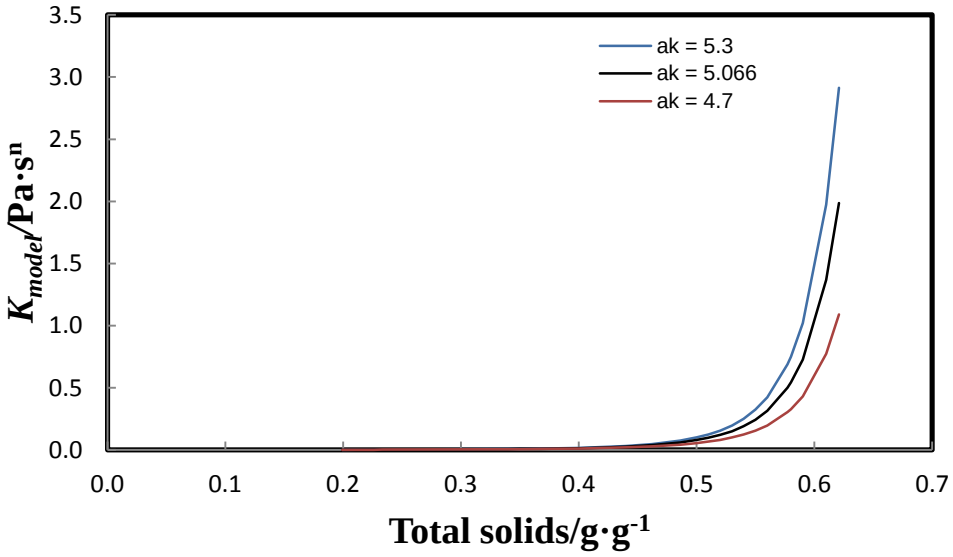

Figure 4.17: The effect of a_k on consistency factor model.

4.5. Discussion

Experimental works were done to collect the shear stress - shear rate data of milk from 19.93% to 62.09% total solids. The Herschel-Bulkley model was able to model well the experimental shear stress for all the total solids obtained. Table 4.11 shows the differences between the experimental results and the model were small.

Table 4.11: Differences in experimental and Herschel-Bulkley shear stress.

Total solids TS (%)	Sum of squares differences of experimental shear stress with Herschel-Bulkley shear stress
19.93%	0.0085
22.60%	0.11
23.34%	0.034
36.66%	0.019
46.23%	0.049
48.61%	0.62
57.71%	1.2
62.09%	1.1

Experimental results showed that the shear stress of milk increases as the total solids increased. The viscosity of milk has also showed to have increased together with the increased in total solids.

Milk viscosity increased exponentially starting from about 36.66% total solids. For the range of total solids from 19.93% to 46.23%, there was no significant change in milk viscosity with the change in shear rates. A departure from this trend was seen to occur starting at 46.23% total solids and higher.

For three different shear rates (100 s^{-1}, 200 s^{-1} and 500 s^{-1}), experimental results start to give three different milk viscosities at 46.23% total solids. This separation shows that the milk viscosity starts to be shear rate dependent. This dependency on shear rate starting at 46.23% total solids meant that the viscosity of milk was becoming non-Newtonian.

The rheological parameters for milk at different total solids were obtained with the use of Herschel-Bulkley model. From the model, the shear stress is clearly dependent on these rheological parameters. Any changes on the rheological parameters will consequently be imparted onto the shear stress.

For the different milks used, the yield stress increased exponentially as the total solids increased. Similarly, this can be said about the consistency factor. The flow behavior index decreases gradually to *n* less than 1 as the total solids increased, indicating that milk was less and less Newtonian with increasing total solids and was pseudoplastic.

Based on the results of the rheological parameters, milk began to have a yield stress starting at 48.61% total solids and above. The consistency factor increased in a similar way as the yield stress. The flow behavior index was clearly decreasing starting at 48.61% from 0.942 to 0.701 at 62.09% total solids.

It was clear that milk was Newtonian from 19.93% up to 46.23% total solids. Milk was non-Newtonian from 46.23% to 62.09% total solids. Since there were no yield stress from the results obtained for total solids between 36.66% and 48.61% TS, a

power law behavior could be possible. Therefore, milk can be Newtonian from 19.93% to 36.66% TS, Power law from 36.66% to 48.61% TS and Herschel-Bulkley from 48.61% to 62.09% TS. This is consistent with the results from Bienvenue et al. (2003) and Vélez-Ruiz and Barbosa-Cánovas (1998).

The results so far showed that with increasing total solids, the yield stress and consistency factor increased exponentially as is milk viscosity. This reveals that the yield stress and consistency factor are as much important to viscosity as is the total solids when milk is non-Newtonian.

A viscosity model was developed by Chong et al. (2009) that describes the changes of milk viscosity with total solids for more than 40%. They found milk viscosity changes exponentially for total solids more than 40% (Figure 4.18) which is consistent with present experimental results.

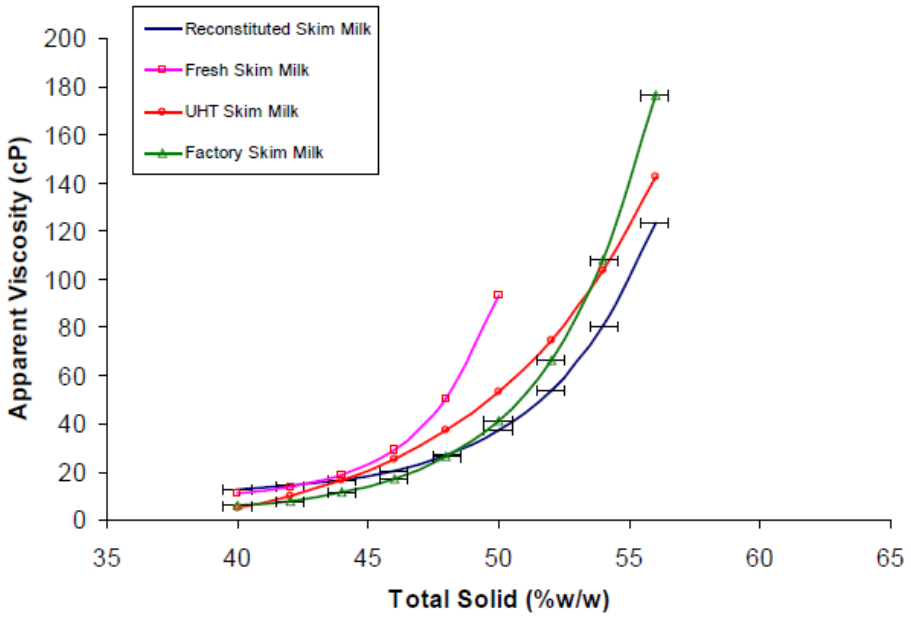

Figure 4.18: Viscosity of milk at higher total solids (Chong et al., 2009).

Their proposed equation was used to compare with the current results available. For the range of total solids applicable in the experiments, the equation predicted the viscosity quite closely for shear rate at 200 s^{-1}. The authors stated that the shear rate their equation was based on was fixed at 60 rpm. It is unknown if this translate to the current experimental shear rate of 200 s^{-1}.

The models developed for the rheological parameters were a function of total solids only. These models developed were based on experimental results and were empirical. It described the respective changes of the models with total solids.

The consistency factor model and the flow behavior index model developed were compared with results from literatures. It was found that while the consistency factor model compares well with literature the flow behavior index does not.

Various constants introduced into the models were added so that it would fit into the experimental results. The effects of these various constants on the models were evaluated.

The yield stress model contains three constants which were a_{yield} (0.188), b_{yield} (1.267) and *TSmax* (0.653). The constant *TSmax* is the maximum total solids estimated for milk before its yield stress increase indefinitely. It was shown that any small increase in a_{yield} or b_{yield} increases the yield stress.

Table 4.12: The effects of a_{yield} and b_{yield} on yield stress.

Total solids ($g \cdot g^{-1}$)	**a_{yield}**			**b_{yield}**		
	(I)	**(II)**	**(III)**	**(I)**	**(II)**	**(III)**
	0.15	**0.188**	**0.21**	**1.16**	**1.267**	**1.36**
0.4861	0.34	0.56	0.68	0.41	0.56	0.70
0.5771	1.79	2.37	2.71	1.78	2.37	3.00
0.6209	6.32	8.03	9.04	5.68	8.03	10.79

The flow behavior index model consists of three constants, a_{index}, b_{index} and c_{index}. Increasing the constant a_{index}, brings the model closer to $n = 1$ (a straight line). Increasing the constant b_{index} (towards negative) lowers the model to *n* less than 1 with negative slope. The constant c_{index} adds curvature between the transition of the influence of the two constants, a_{index} and b_{index}. Increasing the constant c_{index} increases the curvature.

The consistency factor model has but one constant, a_k. An increase in the constant a_k increases the consistency factor.

Table 4.13: The effects of a_k on consistency factor.

Total solids ($g \cdot g^{-1}$)	**a_k**		
	(I)	**(II)**	**(III)**
	4.7	**5.066**	**5.3**
0.4861	0.043	0.060	0.075
0.5771	0.30	0.50	0.69
0.6209	1.09	1.99	2.91

4.6. Conclusions

The conclusions up to this point were:

- The viscosity of milk increased exponentially with total solids after 36.66%. The equation proposed by Chong et al. (2009) could be used to predict milk viscosity with the uncertainty of the shear rate that it applies to.
- The Herschel-Bulkley model can be used to model milk regardless if it is Newtonian or non-Newtonian.
- The rheological trend of milk can be summed up as: Newtonian from 19.93% - 36.66% TS, Power law from 36.66% - 48.61% TS and Herschel-Bulkley from 48.61% - 62.09% TS.
- Empirical models developed for the three rheological parameters can be used for further calculations in the future that relates to the non-Newtonian nature of milk.

5. Age Thickening Model

5.1. Introduction

Experiments were carried out to study the age thickening of skim milk. The experiments were based on measuring the change of milk viscosity with time. A reaction based model was used to model the age thickening phenomena.

Two known reaction orders were the first order and second order reactions. The first order reaction can occur for when reactant, *A* proceeds to product, *P* as follows:

$$A \rightarrow P$$

The equation that describes the change of *A* (in concentration) with time, *t*, is

$$A = A_0 \cdot e^{-kt} \qquad (5.1)$$

The second order reaction can occur when reactant, *A* proceeds to product, *P* (possibly) via,

$$2A \rightarrow P$$

The equation that describes the change of *A* with time, *t*, for this reaction is

$$\frac{1}{A} = -kt + \frac{1}{A_0} \qquad (5.2)$$

The rate constant and the initial concentration were denoted by the terms, *k* and A_0. Here, the *A* and A_0 in equations (5.1) and (5.2) were later replaced by the viscosity, η and initial viscosity, η_0.

5.2. Method

The milk used for these experiments was Meadow Fresh Trim milk (MFTM). The temperature the shear stress - shear rate were measured was at 45 °C. The experimental method in Chapter 3 for age thickening was followed.

5.3. Results

The range of total solids obtained from the experiments performed was from 35.47% to 49.25% TS. Experiments from this will also include the shear stress - shear rate results and its rheological parameters.

5.3.1. Shear stress - Shear rate

The new shear stress - shear rate data was collected for the range of total solids from 35.47% to 49.25% at time, t = 0 hours until time, t = 3 hours. The shear stress was plotted with shear rate for time, t = 0 hours, that is, the first data to be obtained after the sample was loaded into the viscometer. This was presented in Figure 5.1.

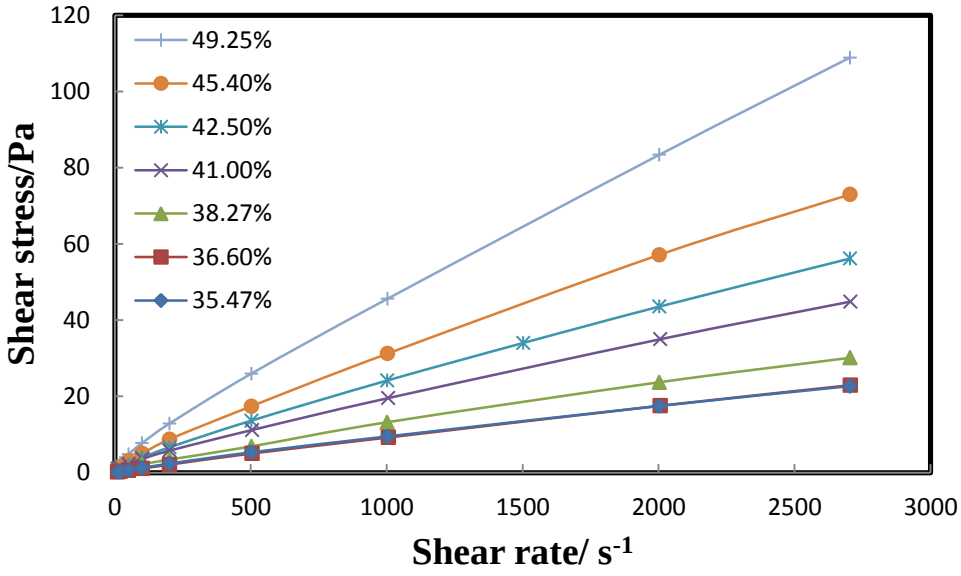

Figure 5.1: Flow curves of milk at various total solids at time, t = 0 hours.

The range of shear rates used initially for the first few intervals of measurements was from $10s^{-1}$ to $2700s^{-1}$. However as the viscosity increased with time, it exceeded the

maximum torque allowed for the viscometer and new range of shear rates was introduced. This occurred when measuring the data for 45.4% and 49.25% TS.

5.3.2. Viscosity vs Time

From the shear stress - shear rate measurements, viscosity was calculated and plotted against time. Figures 5.2 and 5.3 represent the plot of viscosity - time at shear rate of $50s^{-1}$ and $500s^{-1}$ respectively.

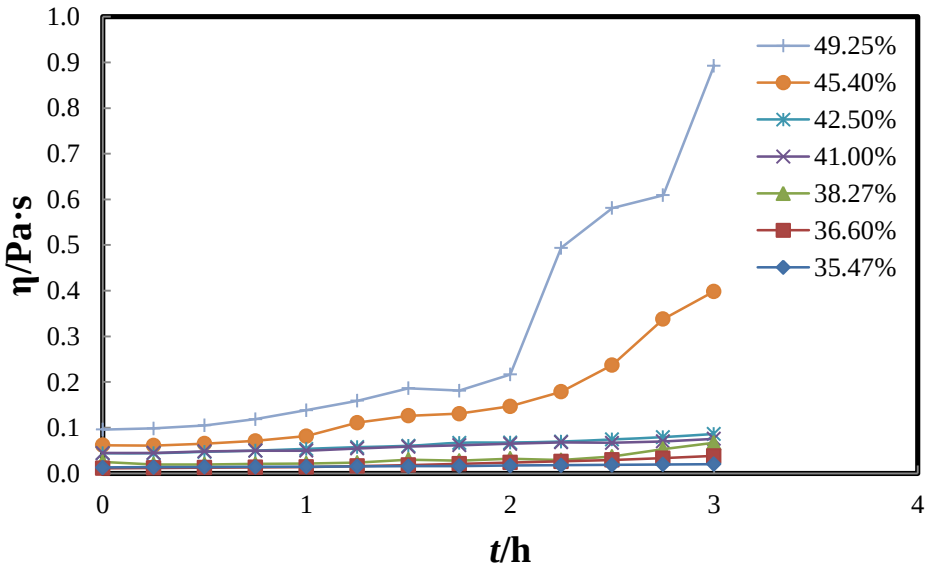

Figure 5.2: Milk viscosities at shear rate of 50 s^{-1} at different total solids.

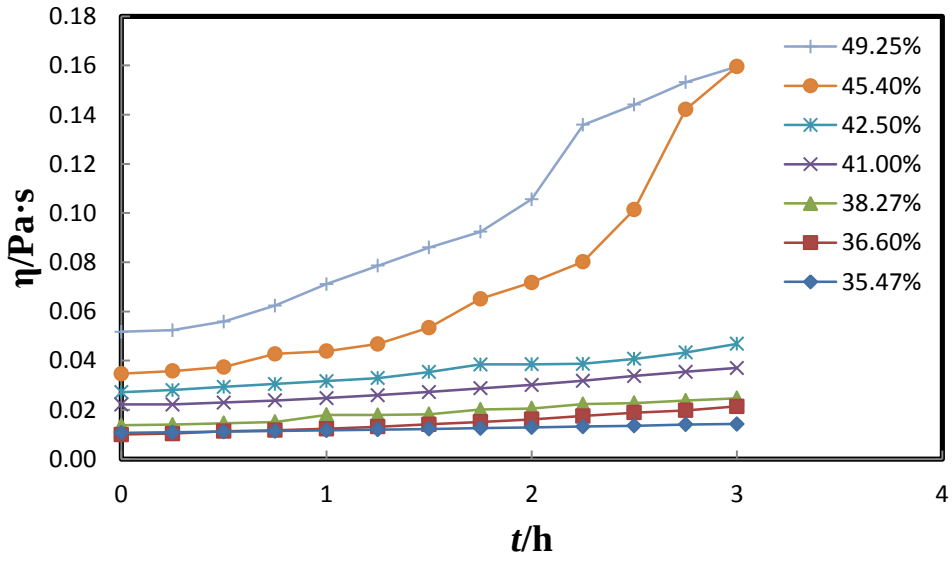

Figure 5.3: Milk viscosities at shear rate of 500 s^{-1} at different total solids.

In measuring the shear stress - shear rate, the NV sensor of the viscometer was not preheated at 45 °C for the 36.60% and 41% TS samples. This was found to have not affected the viscosity much.

From the figures, milk viscosities increased with time at temperature of 45 °C. The viscosities were also higher with higher concentration (total solids) and proceed to increase further with time. At higher total solids (45.4% and 49.25%) the viscosity can be seen to increase at an hourly interval.

To compare with Figure 2.6 from Westergaard (2004), the calculated viscosities were converted to mPa·s (cP) unit from Pa·s unit. A logarithmic of these (viscosity at 500 s^{-1}) was then plotted with time (Figure 5.4).

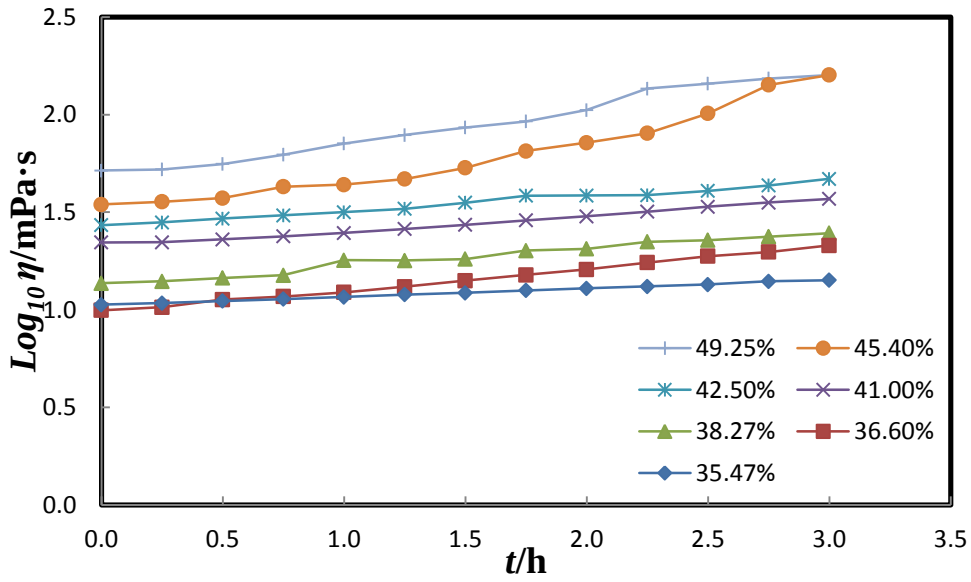

Figure 5.4: Skim milk concentrate viscosity versus time at 45 °C.

5.3.3. Rheological parameters

The Herschel-Bulkley model was used as before to obtain the rheological parameters of the yield stress, consistency factor and flow behavior index. This was applied to each set of shear stress - shear rate data and for each of the 15 minutes interval where the shear stress - shear rate data was taken.

Table 5.1: Rheological parameters at time, t = 0 hours.

Total solids (***TS***/g·g^{-1})	**Yield Stress** (τ_y/Pa)	**Consistency Factor** (***K***/Pa·s^{n})	**Flow Behaviour Index** (***n***)
0.3547	0.0000	0.0232	0.872
0.3660	0.0000	0.0175	0.909
0.3827	0.323	0.0318	0.867
0.4100	0.787	0.0485	0.862
0.4250	0.237	0.0689	0.848
0.4540	0.651	0.0766	0.867
0.4925	1.52	0.0969	0.886

The first set of data for the yield stress, consistency factor and flow behavior index as from Table 5.1 were then plotted in Figures 5.5 to 5.7 over the range of total solids measured.

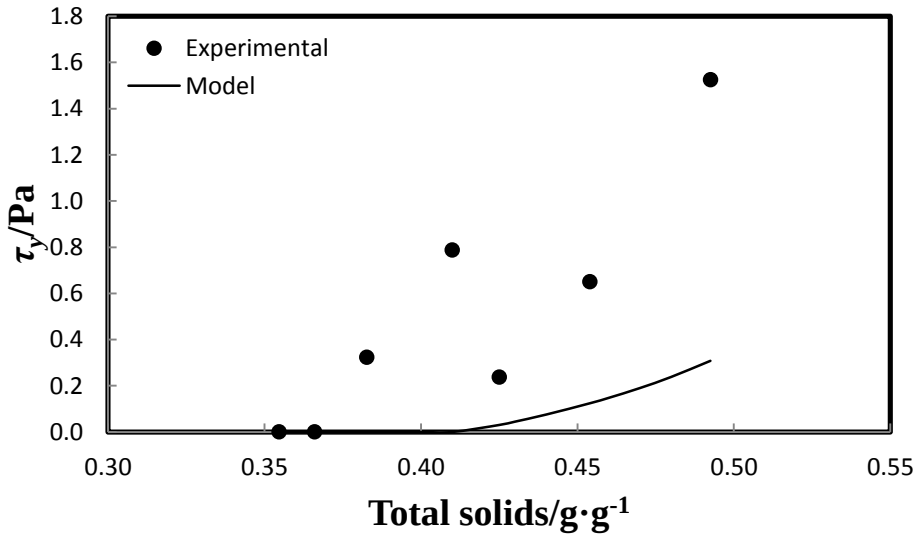

Figure 5.5: Model predicting experimental yield stress.

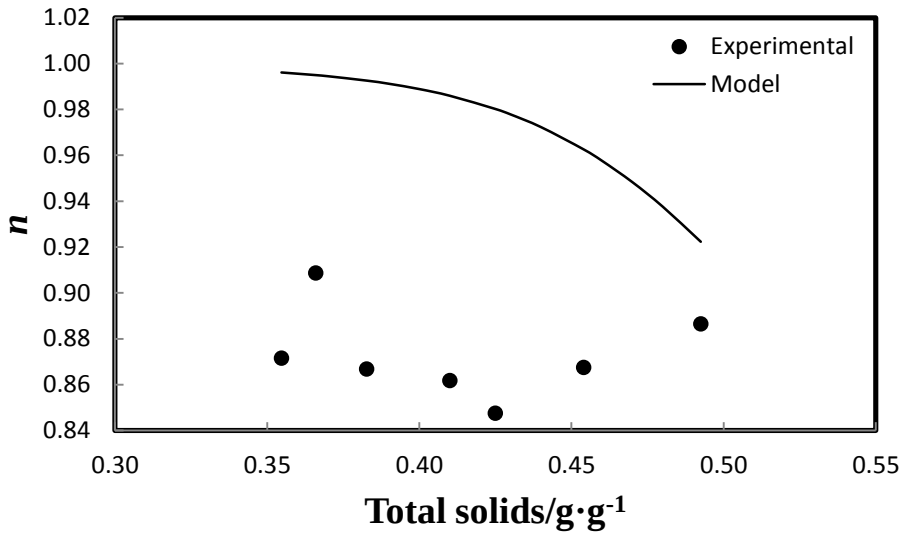

Figure 5.6: Model predicting experimental flow behavior index.

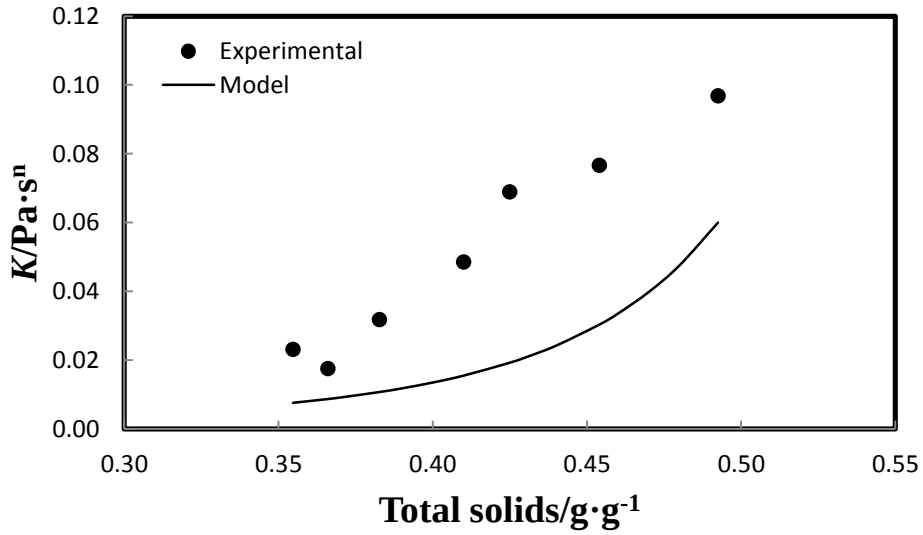

Figure 5.7: Model predicting experimental consistency factor.

These experimental results of the yield stress, flow behavior index and consistency factor presented were the experimental data when time was t = 0 hours when the experiment started. Therefore these set of results were the results without the influence of the age thickening phenomena.

Throughout the time the experiments were running to collect the shear stress - shear rate data, the experimental yield stress, flow behavior index and consistency factor were also obtained in the process and were plotted in Figures 5.8 to 5.10.

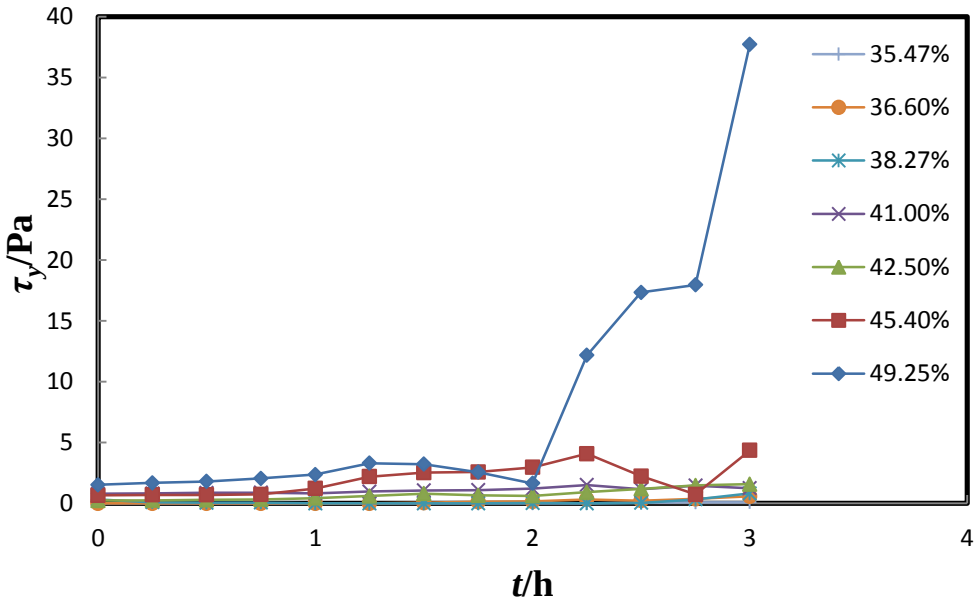

Figure 5.8: The changes of yield stress with time at different total solids.

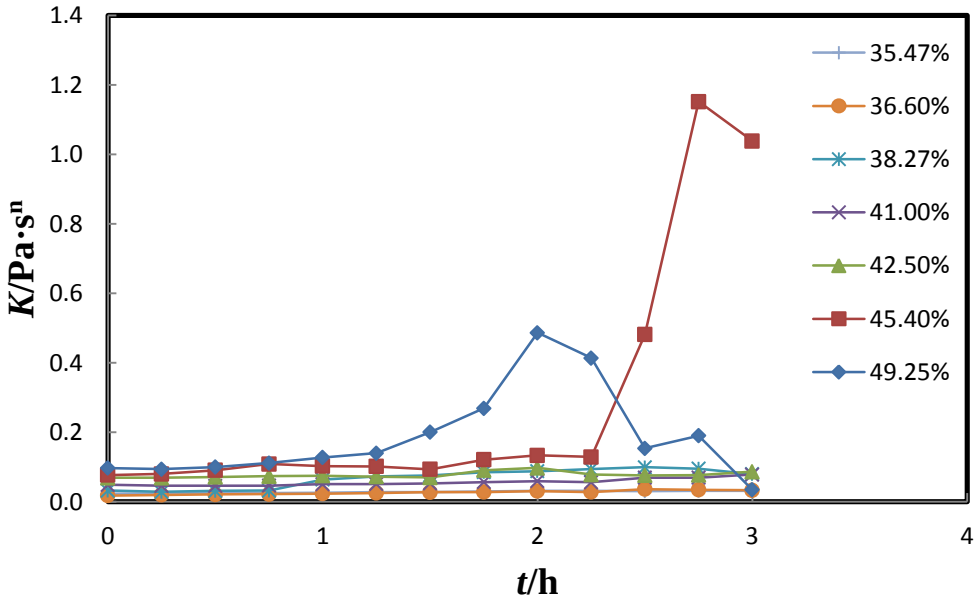

Figure 5.9: The change of consistency factor with time at different total solids.

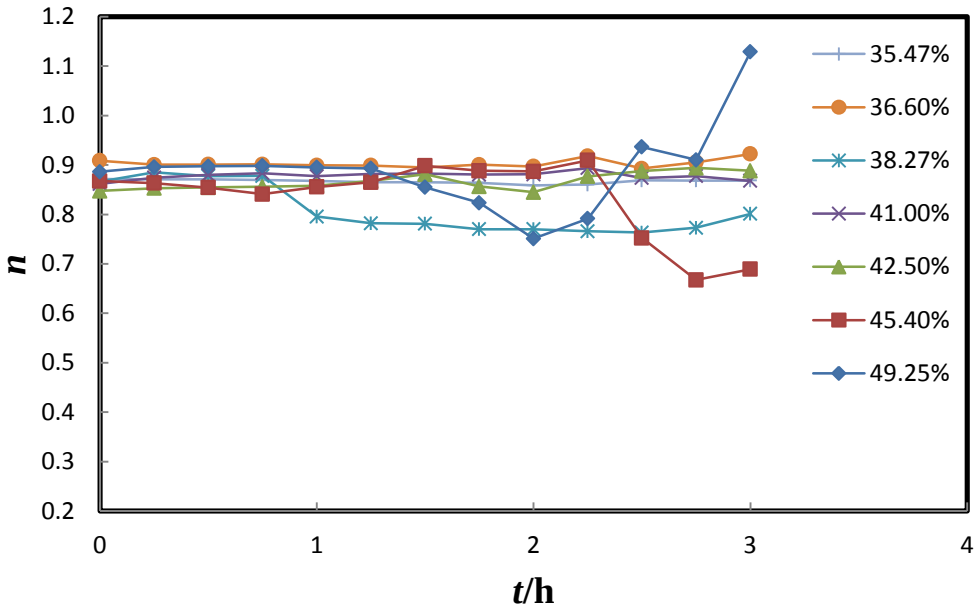

Figure 5.10: The change of flow behavior index with time at different total solids.

These results are discussed further in Section 5.4.

5.3.4. First and second order reaction models

The viscosities calculated from experimental shear stress - shear rate and at the shear rate, $\dot{\gamma} = 500\ s^{-1}$ were plotted with time. A trendline was added and the rate constant, k and initial viscosity, η_0 or $1/\eta_0$ were then determined from the equation displayed. The exponential trendline was chosen for the first order reaction and the linear trendline for the second order reaction.

The values of the k, η_0 and $1/\eta_0$ obtained were then substituted into equations (5.1) and (5.2) to calculate the viscosity based on those equations.

The sum of squares was used to calculate the difference of the column '1st order model' with the column 'Experimental $\eta_{\gamma=500}$' (see Table 5.2). Similarly, this was also done for the column '2nd order model' with the column 'Experimental $1/\eta_{\gamma=500}$'. This process was then repeated for the other total solids.

Table 5.2: The experimental and calculated viscosity at 35.47% *TS*.

Time	Experimental $\eta_{\gamma=500}$	1st order model $\eta_{\gamma=500}$	Experimental $1/\eta_{\gamma=500}$	2nd order model $1/\eta_{\gamma=500}$
0.00	0.0106	0.0106	94.2	94.1
0.25	0.0108	0.0109	92.4	92.1
0.50	0.0111	0.0111	90.1	90.1
0.75	0.0113	0.0114	88.1	88.0
1.00	0.0116	0.0117	85.9	86.0
1.25	0.0120	0.0120	83.6	84.0
1.50	0.0122	0.0123	81.9	82.0
1.75	0.0126	0.0126	79.7	79.9
2.00	0.0129	0.0129	77.7	77.9
2.25	0.0132	0.0132	75.9	75.9
2.50	0.0135	0.0136	74.2	73.9
2.75	0.0140	0.0139	71.4	71.8
3.00	0.0142	0.0143	70.5	69.8

Figures 5.11 to 5.17 show the plot of viscosity - time and 1/viscosity - time curves. The corresponding exponential and linear trendlines were added with equations displayed to these figures. The k and η_0 values from these equations were tabulated in Tables 5.3 to 5.9 according to their respective first order and second order type.

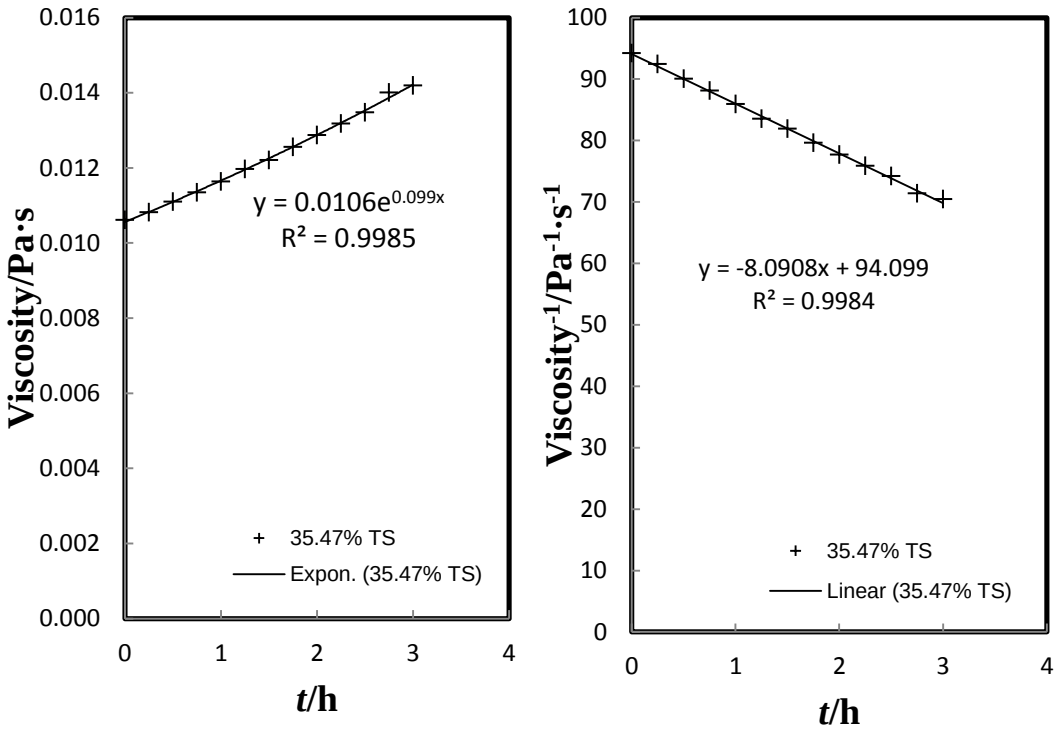

Figure 5.11: Viscosity versus time at 35.47% TS.

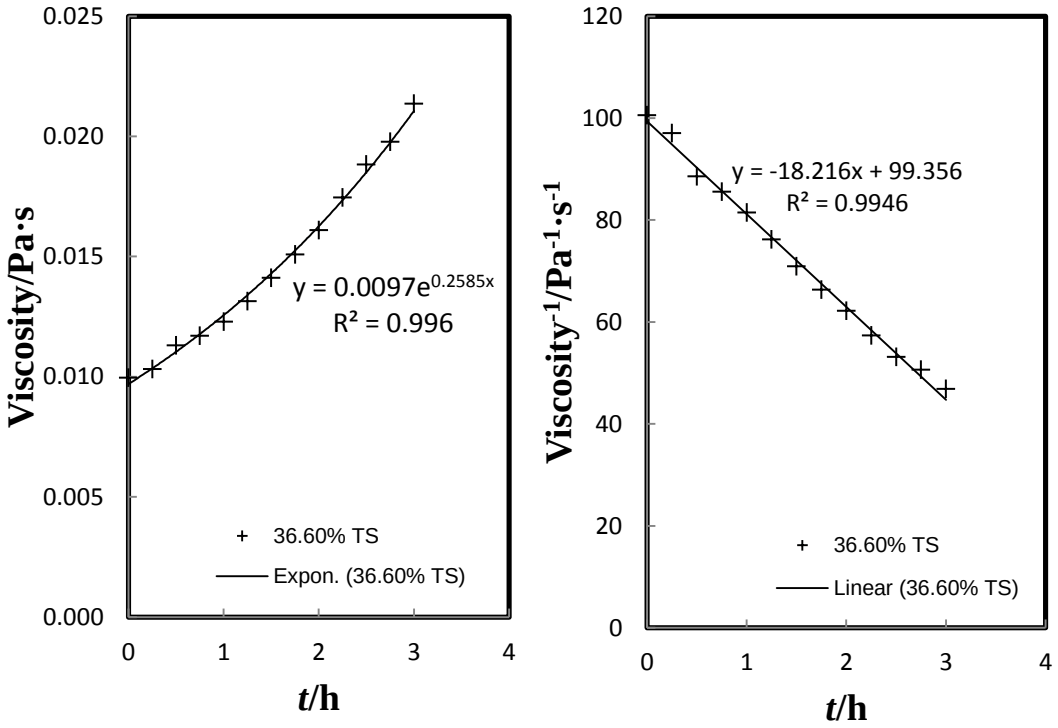

Figure 5.12: Reciprocal of viscosity with time at 36.60% TS.

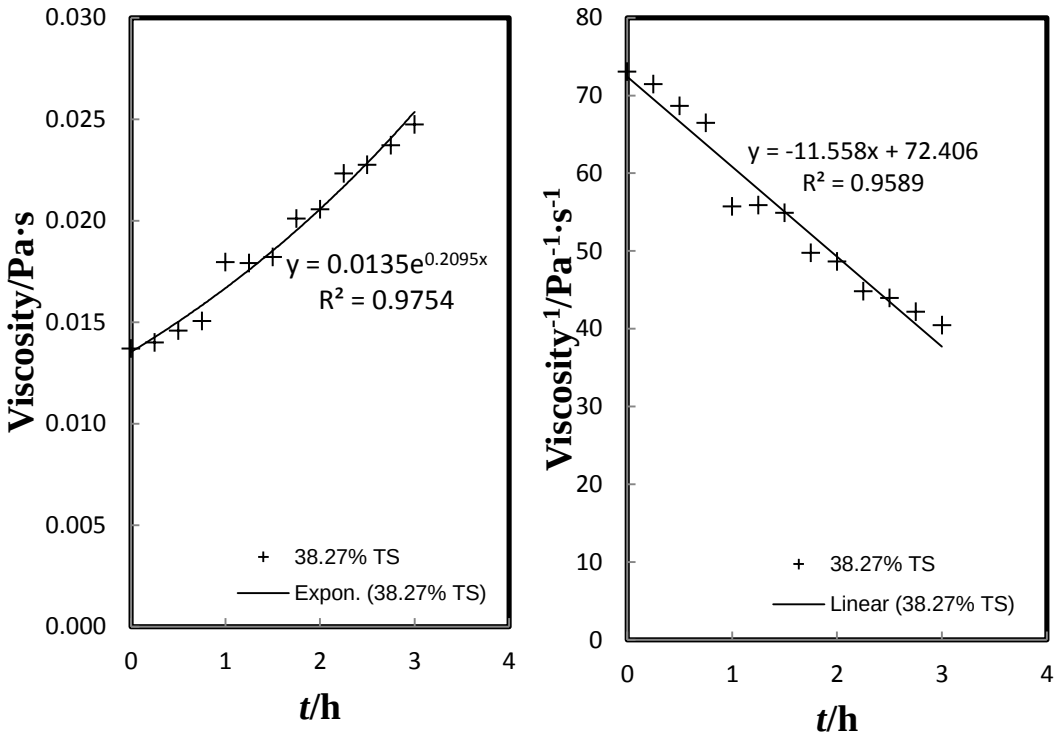

Figure 5.13: Viscosity versus time at 38.27% TS.

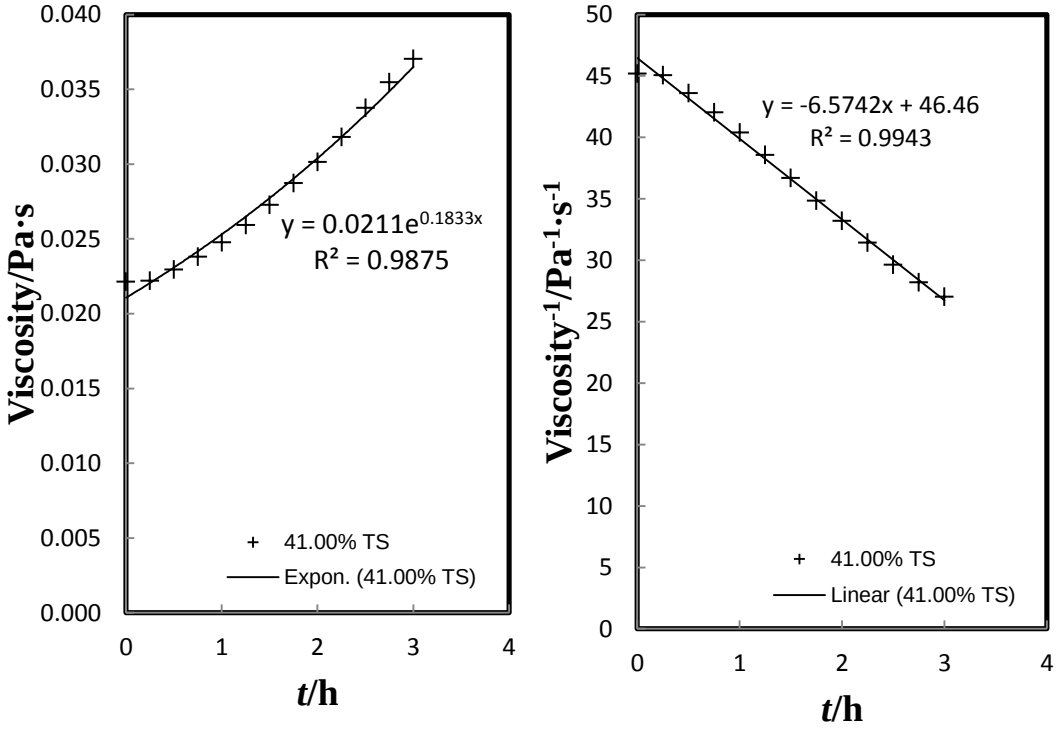

Figure 5.14: Reciprocal of viscosity with time at 41.00% TS.

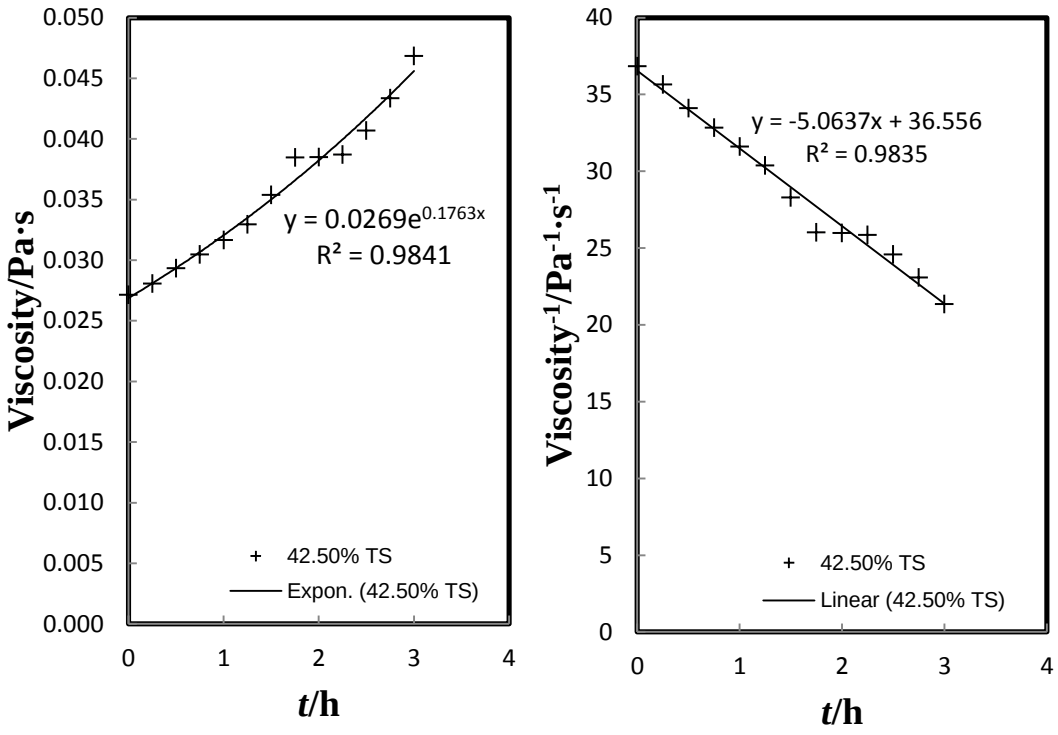

Figure 5.15: Viscosity versus time at 42.50% TS.

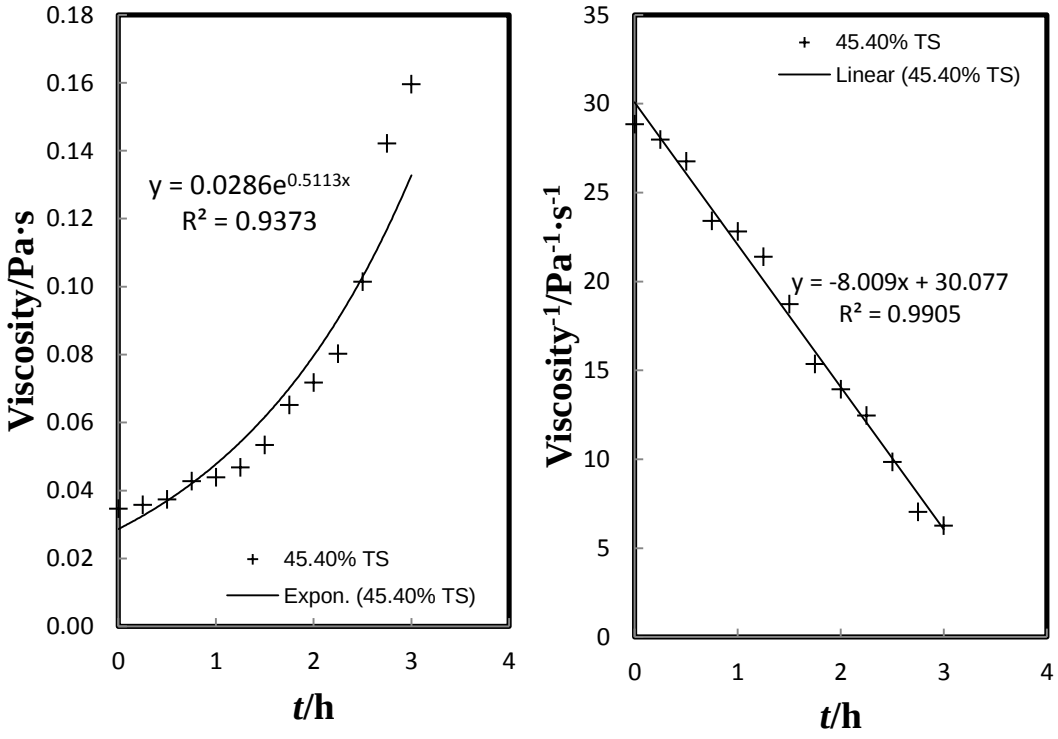

Figure 5.16: Reciprocal of viscosity with time at 45.40% TS.

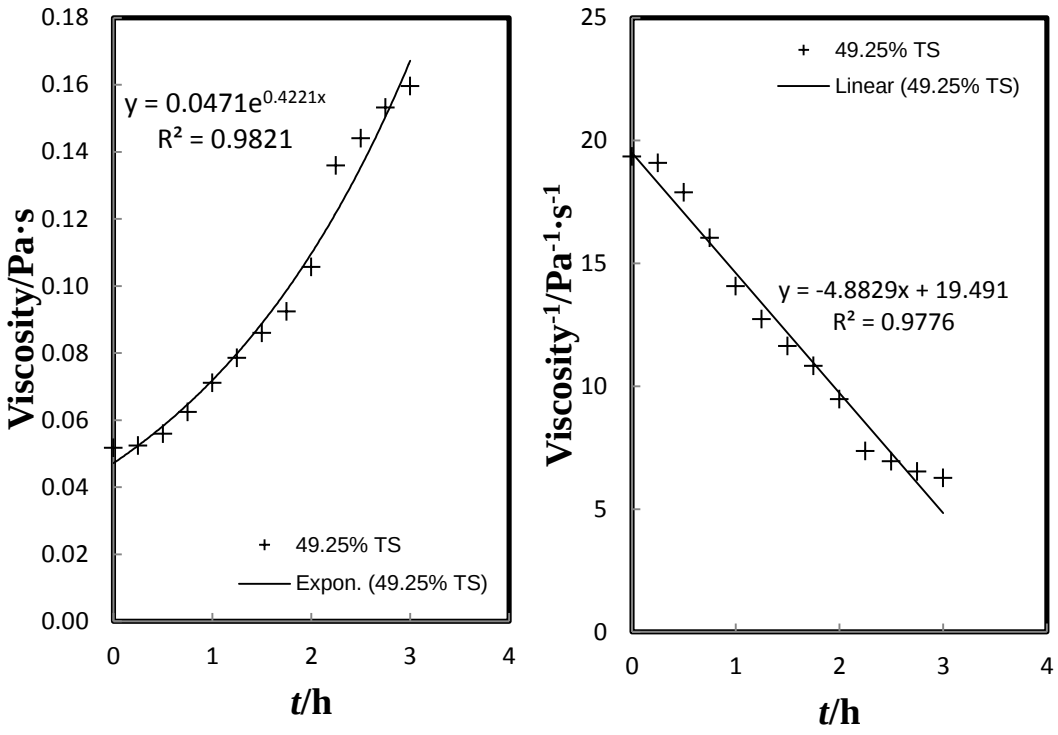

Figure 5.17: Viscosity versus time at 49.25% TS.

5.3.5. Developing a model

It was found the first order reaction model has the smallest difference with the viscosity calculated from the experimental shear stress - shear rate. Therefore, the model chosen to model the age thickening phenomena of skim milk was the first order reaction model. However the second order model was found to be adequate too. There is potential to investigate this reaction model further.

Table 5.3: Summaries of the first and second order results.

Total solids	First order			Second order		
	k	η_o	R-squared	k	$1/\eta_o$	R-squared
35.47%	0.099	0.0106	0.9985	-8.0908	94.099	0.9984
36.60%	0.2585	0.0097	0.996	-18.216	99.356	0.9946
38.27%	0.2095	0.0135	0.9754	-11.558	72.406	0.9589
41.00%	0.1833	0.0211	0.9875	-6.5742	46.46	0.9943
42.50%	0.1763	0.0269	0.9841	-5.0637	36.556	0.9835
45.40%	0.5113	0.0286	0.9373	-8.009	30.077	0.9905
49.25%	0.4221	0.0471	0.9821	-4.8829	19.491	0.9776

The first order model is an exponential type equation and after replacing the concentration, *A*, with viscosity, the model becomes,

$$\eta(t) = \eta_0 \cdot e^{kt} \qquad (5.3)$$

Table 5.4: The k and η_0 values at different total solids for a first order model.

***TS*(g·g^{-1})**	**0.3547**	**0.366**	**0.3827**	**0.41**	**0.425**	**0.454**	**0.4925**
k	0.099	-	0.2095	0.1833	-	0.5113	0.4221
η_0	0.0106	0.0097	0.0135	0.0211	0.0269	0.0286	0.0471

The values of *k* and η_0 obtained were compiled together for different total solids. Figures 5.18 and 5.19 show the changes of *k* and η_0 with total solids. To further develop the model of equation (5.3), trendline was added to the graphs to obtain equations that describe the changes of *k* and η_0 with total solids.

For the total solids at 0.366 and 0.425, the rate constant, *k* was omitted so that the trendline can be close to most of the other data points. It can be seen that the changes of *k* and η_0 with total solids were exponential. The equations were,

$$\eta_0 = 0.00017 \cdot e^{11.5TS} \qquad (5.4)$$

$$k = 0.0025 \cdot e^{10.9TS} \qquad (5.5)$$

However, the constants in equations (5.4) and (5.5) can be arbitrary. Later, in comparison with experimental data, the constants 0.00017 and 11.5 in equation (5.4) were changed to 0.0002 (exactly) and 11.101 (exactly) respectively to give a new equation (5.6). This was to give a better overall fit from minimizing the sum of squares between the model and experimental results.

$$\eta_0 = 0.0002 \cdot e^{11.101TS} \qquad (5.6)$$

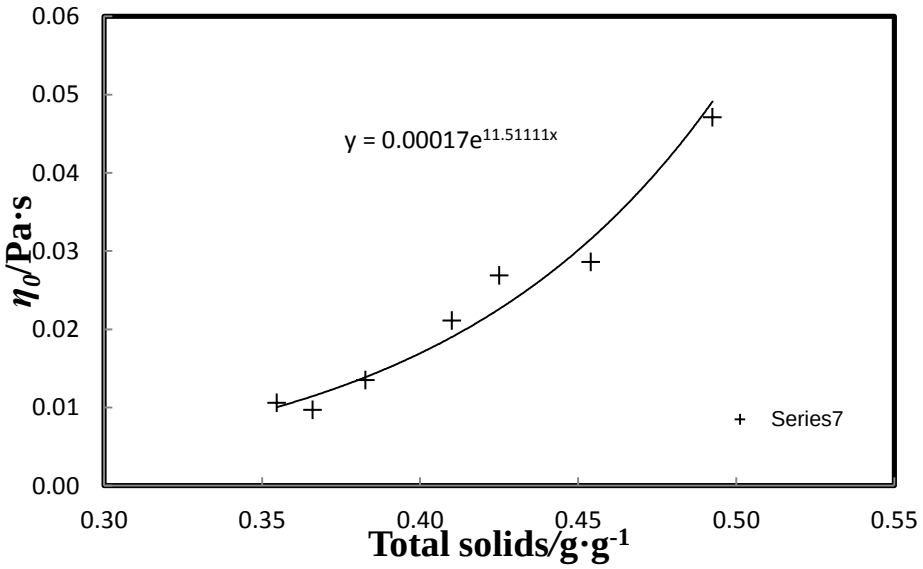

Figure 5.18: The initial viscosity, η_0, versus total solids.

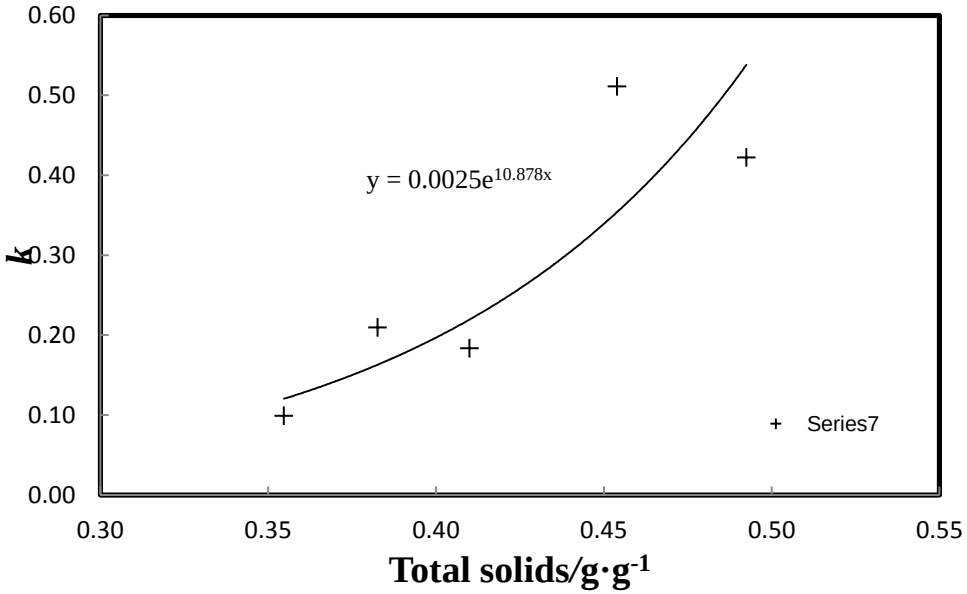

Figure 5.19: The rate constants, k versus total solids.

Figure 5.20 show the comparison between the experimental results with model developed from equation (5.3) for various type of total solids, TS ($g \cdot g^{-1}$). The straight line in the figure depicts the model developed.

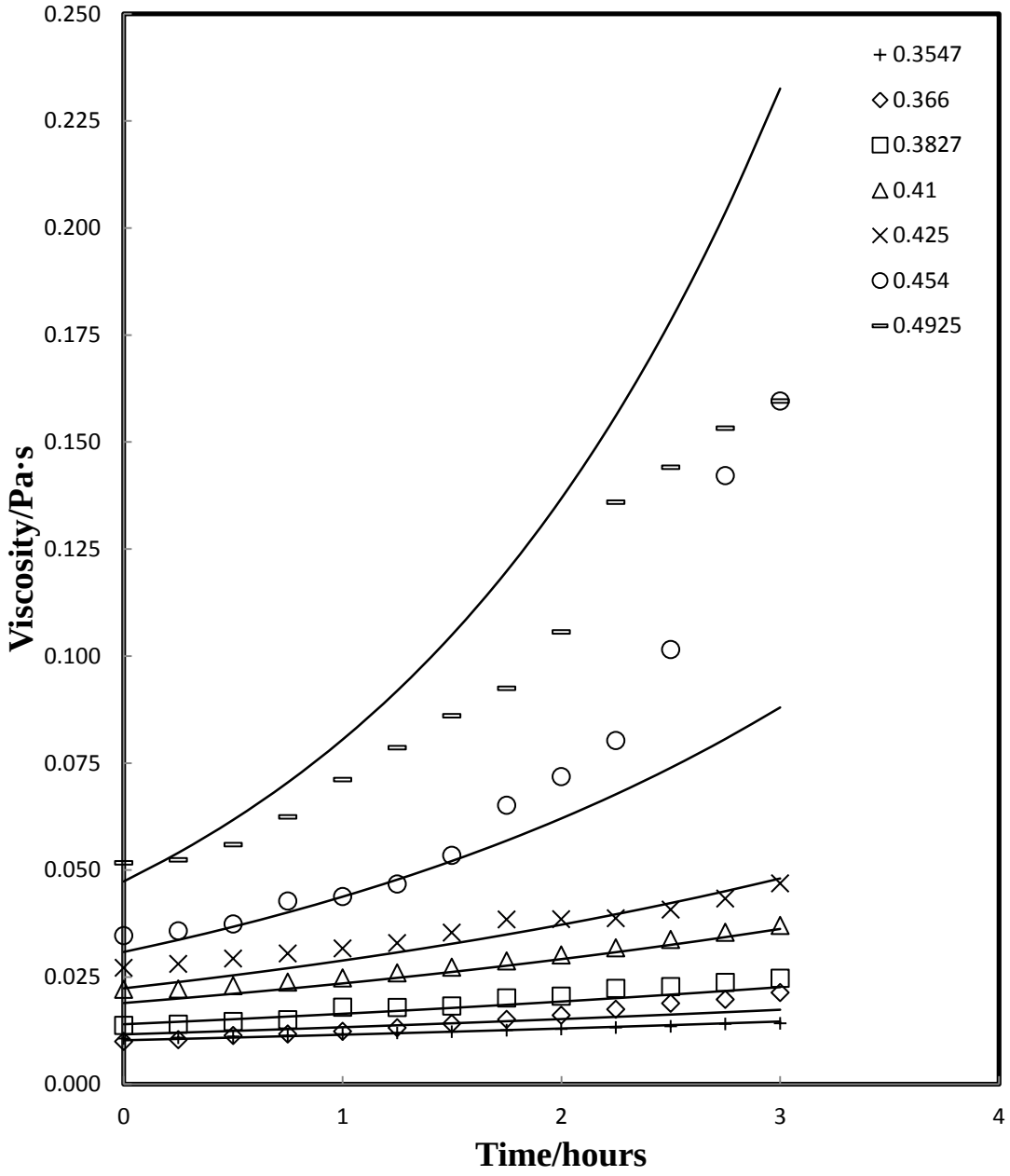

Figure 5.20: The developed model predicting the viscosity over time at various total solids (equations 5.3, 5.5 and 5.6).

5.4. Discussion

The viscosity-time results from experiments showed discrepancy with that reported by Westergard (2004). The milk viscosity at 45.4% TS and 49.25% TS does not increase as dramatically as reported by Westergaard (2004).

The highest value obtained was around 2.2 for 45.4% TS and 49.25% TS while that reported by Westergaard was about 2 for 41% TS and 3.8 for 48.5% TS. The results however showed that for the duration of 3 hours, milk viscosity does increase.

There are a number of reasons for the discrepancy, to which the composition and previous heat treatment can be some of the reasons. The viscosity used for comparison could be calculated at a different shear rate from Westergaard. As can be seen before, viscosities measured at different shear rates can have very different values. The temperature the viscosity was measured was at a higher temperature of 55 °C compared to the current experimental works which was at 45 °C.

For the range of total solids the experimental data was taken, the Herschel-Bulkley was used to obtain the rheological parameters as was done in Chapter 4. For this particular range of total solids (35.47% - 49.25%), results showed that the yield stress occurred earlier from 38.27% TS.

From Figure 5.1 and Table 5.1, it is possible that milk exhibits Power law behavior earlier from 35.47% to 38.27% TS rather than from 36.66% as mentioned in Chapter 4.

A comparison was made in this range of total solids for the experimental rheological parameters with the models developed earlier from Chapter 4. It was found that the models were not comparable with current experimental results. The yield stress occurred earlier and higher than the model would have predicted. The consistency factors were under predicted by the model while the flow behavior indexes were over predicted.

The deviations were surprising considering that the models developed earlier were from experiments using mostly Meadow Fresh Trim Milk (MFTM) which was the milk used for the current experiments. The only exceptions from earlier experiments were that Klondyke Fresh Trim Milk (FTM) and Klondyke Blue Milk (BM) were used at 23.34% TS and 48.61% - 62.09% TS respectively.

The main difference between the current and previous experiments was the temperature the shear stress - shear rate measurements were taken. The temperature used in the current experiments was 45 °C while that used in previous experiments were 25 °C, 40 °C and 50 °C. Other factors also include the time of year the milk was produced.

Because these experiments were about age thickening, the change of the rheological parameters with time was obtained following the consecutive shear stress - shear rate data that was taken every 15 minutes interval.

The yield stress was found to increase slowly with time. There were small incremental increases in yield stress with time at higher total solids. A significant difference occurred after two hours where the yield stress increased sharply for 49.25% TS from 1.6 to 37.7 Pa.

The consistency factor has the same trend and increases steadily with time except at higher total solids of 45.4% TS and 49.25% TS where the increases were more. Unusual results occurred for 49.25% TS where the consistency factor gradually decreases starting from t = 2 hours where it should be increasing. This could be because of the increased in yield stress which automatically causes the consistency factor to be lowered.

The flow behavior index on the other hand does not change much and has average values between 0.8 – 0.95. For 38.27%, 45.4% and 49.25% TS, the flow behavior index does not follow any obvious trend. These unusual results that occurred can be explained by some errors in shear stress-shear rate measurements.

A model was successfully developed, relating the changes of the viscosity with time. The model developed was a first order reaction type. This model was based on the experimental data for the range of total solids from 35.47% TS to 49.25% TS.

The equation model is a function of initial viscosity, η_0, that is, the viscosity at time, t = 0 hours, rate constant, k, and time, t. The main interest with developing the model was in predicting the changes of viscosity with time. In doing so, it was found that milk at different concentration (total solids), the viscosity changes differently with time.

Hence, instead of being able to describe the changes of viscosity with time for just one particular concentration (total solids), the model must be able to predict the changes of viscosity with time for milk at any concentration.

For any milk at any concentration, the milk starts off with an initial viscosity at time, t = 0, before its viscosity increases. This type of increase in viscosity is known as age thickening. Based on the equation model, this increase in viscosity is governed by a rate constant. It is important then to find the relationship between the initial viscosity and rate constant with concentration.

From experimental results, the change in the initial viscosity and rate constant with concentration were found to be exponential. This was incorporated into the equation model which would then be able to predict the changes of viscosity with time and also at any concentration of milk. Implicitly, the final equation model is a function of concentration or total solids as well.

This final model is valid for the range of total solids mentioned above. The results showed the model closely predicting experimental results with the exceptions of the last two concentrations at 45.4% TS and 49.25% TS.

The important factors affecting the accuracy of the model are the initial viscosity equation and rate constant equation which are functions of total solids. The results available where these equations were developed may not be sufficient.

The rate constant equation which describes the rate the viscosity is changing with time was developed from the shear stress - shear rate data. Experimental errors from the shear stress - shear rate measurement could be compounded and led to inaccurate development of the rate constant equation.

5.5. Conclusions

The conclusions that can be made from all the above are:

- The rheological trend of milk could be revised to be as Newtonian from 19.93% - 35.47%, power law from 35.47% - 48.61% and pseudoplastic from 48.61% - 62.09%.
- A separate experiment should be carried out for whole and skim milk.
- Rheological parameters should be temperature dependent and not just concentration dependent.
- A model was developed that describes the changes of viscosity with time and was found to be a function of time, *t*, and total solids, *TS*.
- More experiments will need to be carried out for a wider range of total solids to get a better model.

6. Analytical And Numerical Solutions

6.1. Newtonian/Non-Newtonian Film Flow

6.1.1. Non-Newtonian Film Flow

Analytical expressions were derived for falling film flow of milk on a flat plane rather than a falling film flow in a tube. This was done on the basis that the film thickness is small compared to the tube dimension so the expressions obtained will be close to those for falling film flow in a tube.

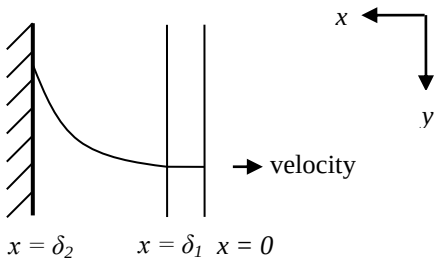

Figure 6.1: Falling film on a flat plane.

The corresponding orientation of the x - and y - axis was as depicted in Figure 6.1 above. For a Herschel-Bulkley fluid when the shear stress, τ, is less than the yield stress, τ_y, the shear rate is zero. This is shown in the region from $0 < x < \delta_1$ in Figure 6.1.

The derivations showed that by letting the milk rheological behavior to take the form of the Herschel-Bulkley model, the film flow velocity and its average velocity can be expressed as,

$$v = \frac{n}{n+1}\frac{K}{\rho g}\left[\left(\frac{\rho g \delta_2 - \tau_y}{K}\right)^{\frac{n+1}{n}} - \left(\frac{\rho g x - \tau_y}{K}\right)^{\frac{n+1}{n}}\right] \qquad (6.1)$$

$$v_{ave} = \frac{1}{\delta_2}\frac{n}{n+1}\frac{K}{\rho g}\left[\left(\frac{\rho g\delta_2 - \tau_y}{K}\right)^{\frac{n+1}{n}}\delta_2 - \frac{n}{2n+1}\frac{K}{\rho g}\left(\frac{\rho g\delta_2 - \tau_y}{K}\right)^{\frac{2n+1}{n}}\right] \qquad (6.2)$$

By substitution of the average velocity into the equation, $\Gamma = \rho v_{av}\delta_2$, the equation (6.3) was derived for the wetting rate. It is a function of density, ρ, flow behavior index, n, yield stress, τ_y, consistency factor, K and film thickness δ_2.

$$\Gamma = \rho\frac{n}{n+1}\frac{K}{\rho g}\left[\left(\frac{\rho g\delta_2 - \tau_y}{K}\right)^{\frac{n+1}{n}}\delta_2 - \frac{n}{2n+1}\frac{K}{\rho g}\left(\frac{\rho g\delta_2 - \tau_y}{K}\right)^{\frac{2n+1}{n}}\right] \qquad (6.3)$$

This equation was solved for its film thickness, δ_2, given the wetting rate, Γ, density, ρ, flow behavior index, n, yield stress, τ_y and consistency factor, K. Newton's method was used and was coded into VBA to obtain the film thickness, δ_2.

Full derivations are included in Appendix A.

6.1.2. Newtonian Film Flow

Newtonian falling film flow can be derived similarly from the Navier-Stokes equation. Based on Jiji (2009), the Navier-Stokes equation can be reduced to obtain equation (6.4) assuming the changes in the film thickness with y are negligible.

$$\rho g + \mu\frac{\partial^2 v}{\partial x^2} = 0 \qquad (6.4)$$

By assuming constant viscosity and density, the equation can be solved with the boundary conditions that the velocity is zero at the wall and the change in velocity at the interface is zero. The velocity was expressed as,

$$v = \frac{\rho g \delta^2}{2\mu}\left[1-\left(\frac{x}{\delta}\right)^2\right] \qquad (6.5)$$

The maximum velocity and the average velocity can then be obtained as in equation (6.6) and (6.7).

$$v_{\max} = \frac{\rho g \delta^2}{2\mu} \qquad (6.6)$$

$$v_{av} = \frac{\rho g \delta^2}{3\mu} \qquad (6.7)$$

The wetting rate can be solved for by substituting the average velocity into the equation, $\Gamma = \rho v_{av} \delta$, to give equation (6.8).

$$\Gamma = \frac{\rho^2 g \delta^3}{3\mu} \qquad (6.8)$$

The equation (6.8) can be re-arranged to obtain the film thickness for the Newtonian falling film.

$$\delta = \left(\frac{3\mu\Gamma}{\rho^2 g}\right)^{1/3} \qquad (6.9)$$

Full derivations are included in Appendix A.

6.1.3. Analysis

Film Velocity Profile

The velocity profile for a steady Newtonian falling film was derived as equation (6.5) while that of the pseudoplastic non-Newtonian falling film was derived as equation (6.1). The derived equation for the non-Newtonian type showed that the velocity

profile is a function of flow behavior index, n, consistency factor, K, yield stress, τ_y, density, ρ, film thickness, δ_2 and position, x.

The effect of viscosity was already incorporated into the velocity profile by the rheological parameters (flow behavior index, consistency factor and yield stress). Hence, the changes in the rheological parameters will reflect the changes in viscosity.

The velocity profile for Newtonian type however is simpler and is a function of density, ρ, viscosity, μ, film thickness, δ and position, x.

To inspect the effects of the available variables, all calculations were done in an Excel spreadsheet. A few other related variables were given a hypothetical value in order to initiate the calculations.

Although the equations were derived from falling film flow on a flat plane, the calculations in the spreadsheet was that of the falling film flow in a tube.

Figure 6.2 show the velocity profile down the length of tube for the Newtonian and non-Newtonian type. The velocity profiles from the figure were extracted from the spreadsheet calculation for when the following variables were:

- Total solids in at top of tube, TS_{in} = 0.45 g·g^{-1}
- Wetting rate, Γ = 0.3 kg·m^{-1}·s^{-1}
- Temperature difference, ΔT = 6 °C
- Temperature of milk, T_{milk} = 54 °C + ΔT_b
- Total length of tube, L = 15 m
- Inner diameter of tube, D_i = 0.0478 m.
- Overall heat transfer coefficient, U, extrapolated from U_{50} = 1 kW/m^2°C at 50% TS and U_{60} = 0.5 kW/m^2°C at 60% TS.

The figure is presented with their axes inverted to give an orientation consistent with Figure 6.1. At length, L = 0 m from top of tube, the Newtonian and non-Newtonian

type velocity profiles were almost identical. However as film flows down the tube, differences can be seen but were not that great.

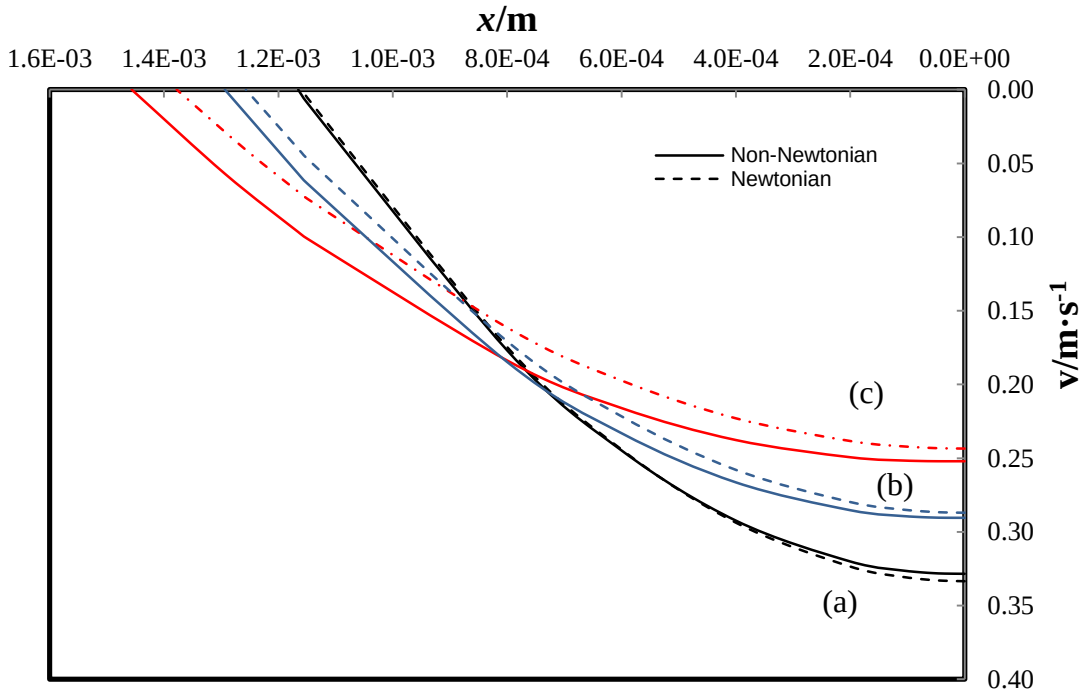

Figure 6.2: Velocity profile for Newtonian (---) and non-Newtonian (—) film flow at (a) Length of tube, L = 0 m, (b) Length of tube, L = 7 m, (c) Length of tube, L = 15 m.

The film velocity profiles were parabolic. The velocity gradually decreases as the film flows down the tube and its profiles becoming flatter for both the case of Newtonian and non-Newtonian type film flow.

This is consistent with the increased in viscosity as the total solids increased down the tube. Figure 6.3 shows the changes in the calculated viscosity with total solids at the wetting rate of 0.3 $kg \cdot m^{-1} \cdot s^{-1}$ and 45% total solids feed.

The viscosity used in Newtonian type velocity profile was that from derived shear stress - shear rate equations and was therefore not fixed.

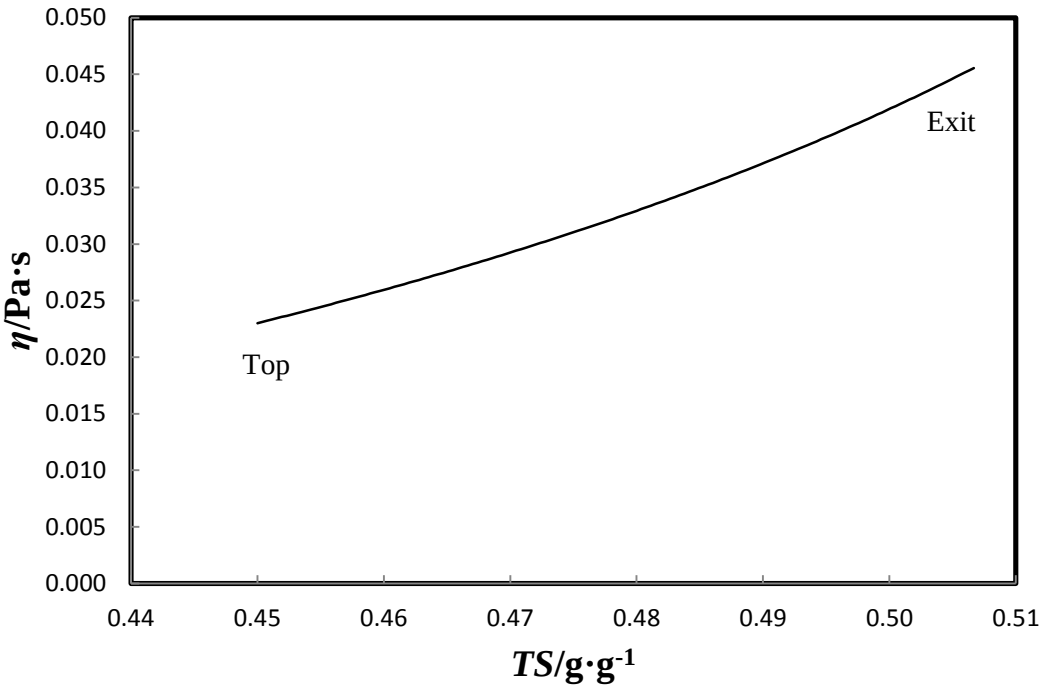

Figure 6.3: The viscosity profile from top-to-exit of tube.

The parabolic velocity profiles shown would be accurate and can be inspected from the equations derived. From equation (6.5) of the Newtonian type, the velocity reaches a maximum as in equation (6.6) when $x \to 0$ and zero when $x \to \delta$.

From equation (6.1), it can be seen that the non-Newtonian velocity profile has two separate profiles divided by the film thickness, δ_1. For $x \le \delta_1$, the velocity profile is plug flow type and for $\delta_1 < x < \delta_2$, the velocity profile is parabolic. This theory is consistent with Šutalo et al. (2006), where they derived similarly for the velocity profile with the substitution of the Herschel-Bulkley model into their derivations.

From the equation (6.1) of the non-Newtonian type, the velocity reaches a maximum when $x \to \delta_1$ and zero when $x \to \delta_2$. Based on the conditions stated earlier, the film has a thickness δ_1 = 9.59E-06m at length of 0m and δ_1 = 3.45E-05 m at length of 15 m.

Film thickness

The equation for a Newtonian film thickness iss presented in equation (6.9). The VBA code for calculating the non-Newtonian film thickness was added into Excel and can be called upon as a function in Excel. The function was named ‘FindDelta2’.

The Newtonian film thickness was calculated as in equation (6.9). The viscosity, η, density, ρ and wetting rate, Γ, were not taken to be constant as they would be changing down the length of evaporator tube.

The wetting rate substituted into equation (6.9) was of the form of equation (1.3). The density substituted into equation (6.9) can be called upon from the function ‘MilkDensity’ in Excel. For viscosity, the derived shear stress and shear rate was used and substituted into equation (6.9) for calculations

A comparison of the film thickness between the Newtonian and non-Newtonian is shown in Figure 6.4. The figure shows that there was a small difference between the Newtonian and non-Newtonian film thicknesses resulting in an almost linear straight line relationship. The conditions the film thicknesses were calculated were the same as those mentioned above for film velocity profile.

Figure 6.5 shows the effects of varying wetting rate on the non-Newtonian film thickness that was calculated using the function ‘FindDelta2’ coded from VBA into Excel.

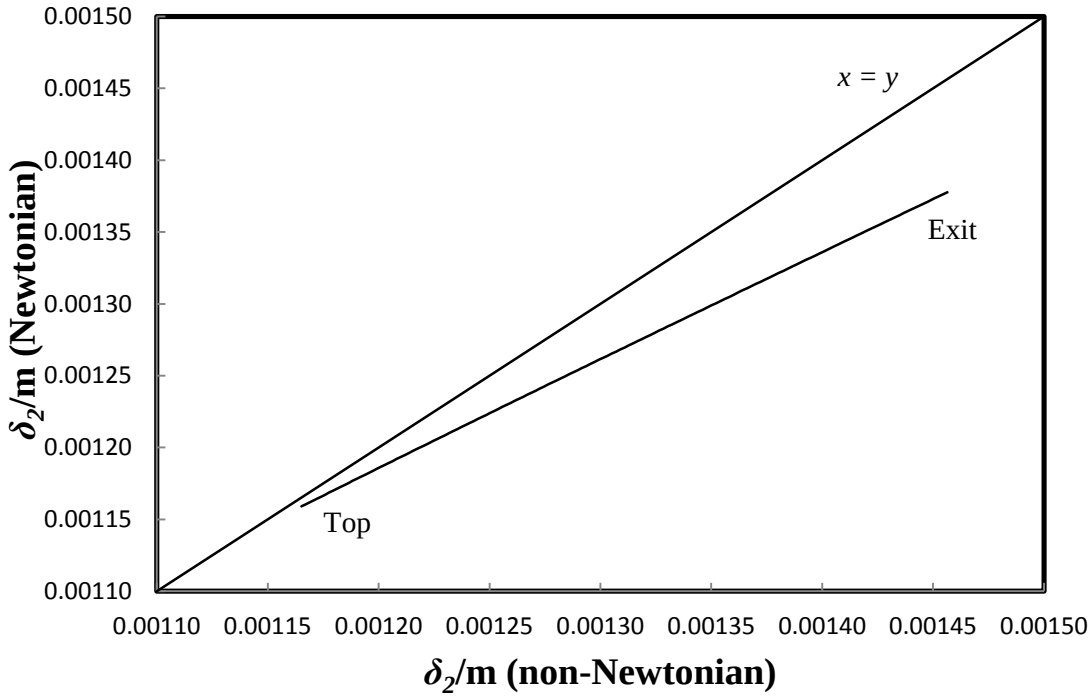

Figure 6.4: Newtonian versus non-Newtonian film thicknesses from top to the exit of tube.

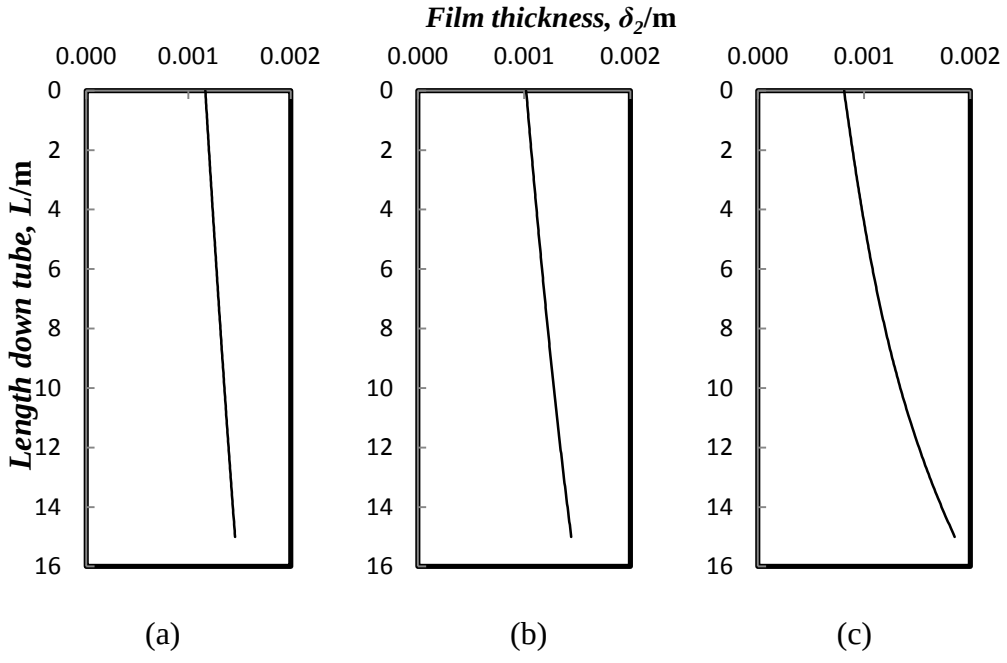

Figure 6.5: Film thickness profile along length of tube with 45% TS feed at (a) Γ = 0.3 kg•m^{-1}•s^{-1}, (b) Γ = 0.2 kg•m^{-1}•s^{-1} and (c) Γ = 0.1 kg•m^{-1}•s^{-1}

At wetting rate of Γ = 0.0585 kg·m^{-1}·s^{-1} and 45% *TS* feed, Figure 6.6 shows the film thickness becomes increasingly thick with a final film thickness of 0.0267 m and have clogged the tube which has inner diameter of 0.0478 m (= radius of 0.0239 m).

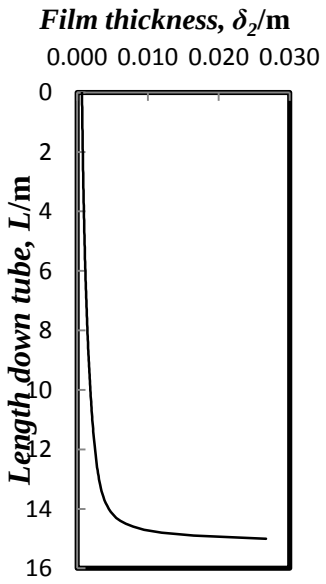

Figure 6.6: Film thickness profile along length of tube with 45% TS feed at Γ = 0.0585 kg•m^{-1}•s^{-1}.

This blockage of the tube can be explained by the yield stress which, at this low wetting rate, was increasing rapidly at an exponential rate. The final yield stress the model calculated was 318.5 Pa which was very high. Therefore, for the film to continue to flow, the film thickness will have to continue to increase at a rate as fast as the yield stress was increasing.

In addition, the milk film also spends approximately a total of 13.5 minutes in the tube before it blocks the tube. However, at such a high yield stress as the above, it is likely that the film would have stopped flowing and eventually fouling would have occurred and this would have contributed to the blocking of the tube.

Figure 6.7 shows the effects of varying wetting rate on the non-Newtonian film with a 50% *TS* feed.

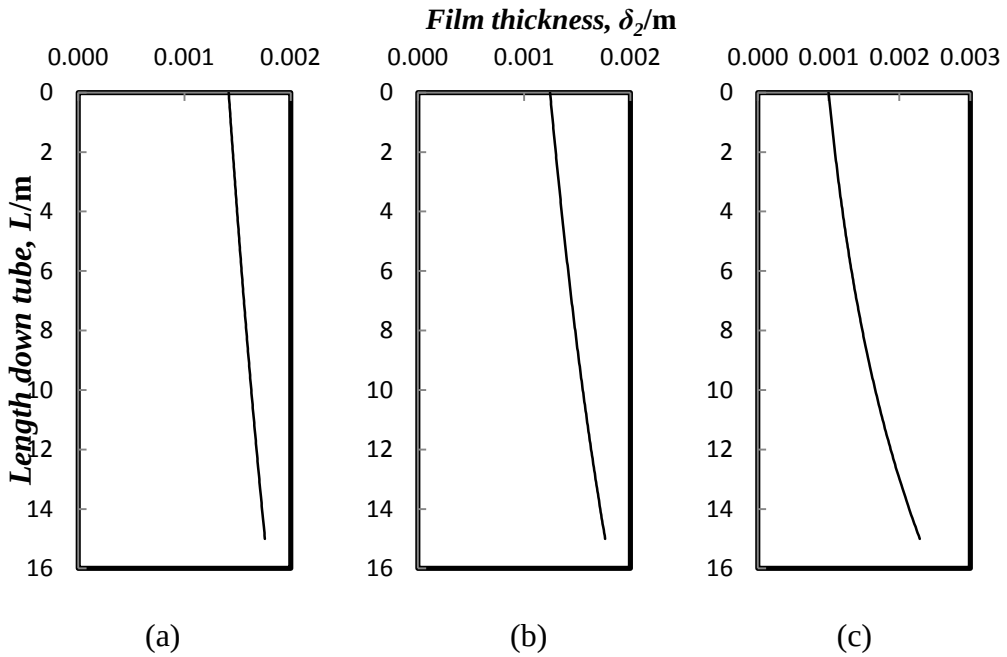

Figure 6.7: Film thickness profile along length of tube with 50% TS feed at (a) Γ = 0.3 kg•m^{-1}•s^{-1}, (b) Γ = 0.2 kg•m^{-1}•s^{-1} and (c) Γ = 0.1 kg•m^{-1}•s^{-1}.

The film thickness δ_1 is defined when the term $\rho g x = \tau_y$, that is, when the stress is equal to the yield stress. Hence, δ_1 is dependent on the yield stress. Because of the yield stress, τ_y, the film will need to have a thickness greater than δ_1 for the film to move (Šutalo et al., 2006).

Figures 6.8 and 6.9 show the respective changes of the film thickness δ_1 and δ_2 with total solids. Comparison of these two film thicknesses shows that δ_1 was very small compared to δ_2 but the trends with increasing total solids were the same.

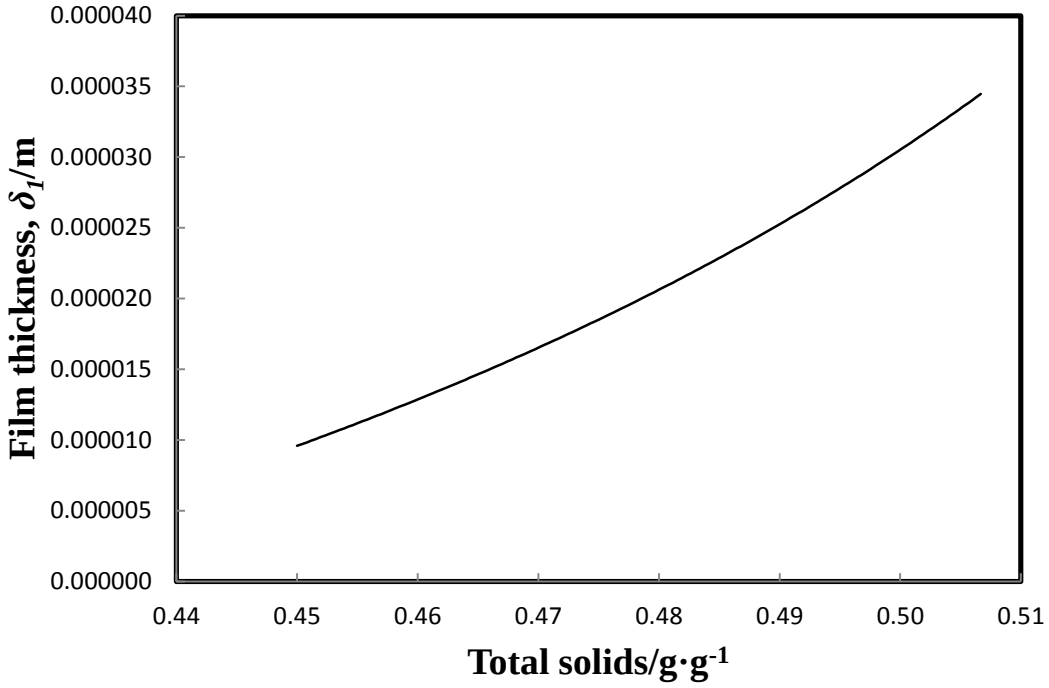

Figure 6.8: The change of film thickness δ_1 with total solids.

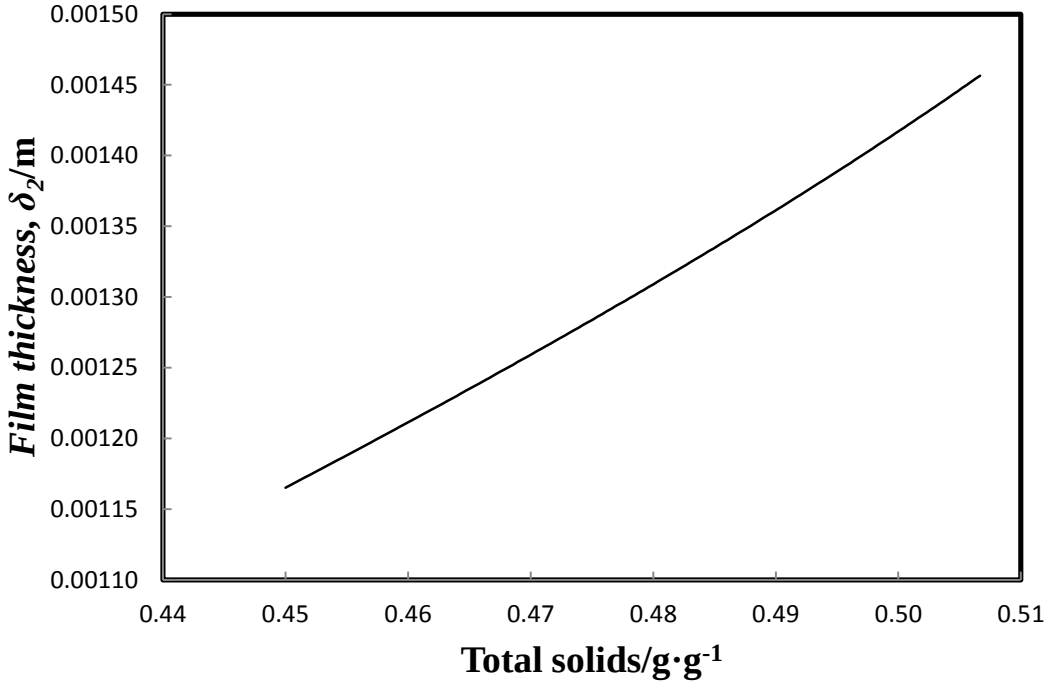

Figure 6.9: The change of film thickness δ_2 with total solids.

6.2. Film Temperature Distribution

In this section, the aim was in determining the temperature distribution of the falling film. The falling film is heated at the wall at temperature, T_w, which is assumed to be constant. At the film surface it is exposed to a uniform and constant pressure, P. The falling film evaporates at the surface only with the surface temperature T_s. The surface temperature is equal to the saturation temperature of water at pressure P plus the boiling point elevation.

The governing equation to solve for,

$$v\frac{\partial T(x,y)}{\partial x} = \alpha\frac{\partial^2 T(x,y)}{\partial y^2}$$

$$T(0,y) = T_0$$

$$T(x,0) = T_w$$

$$T(x,\delta) = T_s$$

where v is defined as the velocity profile previously derived for the falling film. Depending on the type of flow, the substituted velocity profile could be the Newtonian or non-Newtonian type.

A number of authors have derived expressions for the temperature distribution in a Newtonian falling film with the assumption of constant viscosity. These authors (Saouli and Aiboud-Saouli, 2004, Zhang et al., 2008) both used the Newtonian type velocity profile of equation (6.5) to arrive at the final solutions.

A code was written in Matlab with the help from Dr. Alex James to solve the equations above. The full descriptions of the code are attached in Appendix D.

6.2.1. Results and Discussion

Figures 6.10 to 6.12 below showed results as solved for by Matlab. The results also include analytical solutions from Saouli and Aiboud-Saouli (2004) and Zhang et al. (2008). From the figures, analytical-1 refers to solution from equation (2.58) and analytical-2 refers to solution from equation (2.59).

The blue coloured solution as shown in the figures refers to the numerical solution from Matlab using the function *pdepe*. The *x* and *y* axis in the figures are the non-dimensionalized temperature, Θ and film thickness, Y as listed in Section 2.6.

The 'Solution at distance down' as mentioned in the figures refers to the non-dimensionalized X as listed in Section 2.6. As opposed to Saouli and Aiboud-Saouli (2004) and Zhang et al. (2008), the horizontal and vertical axis was coded as *x* and *t* (instead of *y*) respectively in Matlab.

Comparisons of these three solutions showed there were some inconsistencies. The solution from Matlab does not satisfy the initial condition when X = 0. From this, Matlab implies that the temperature at the entrance was T = 0.

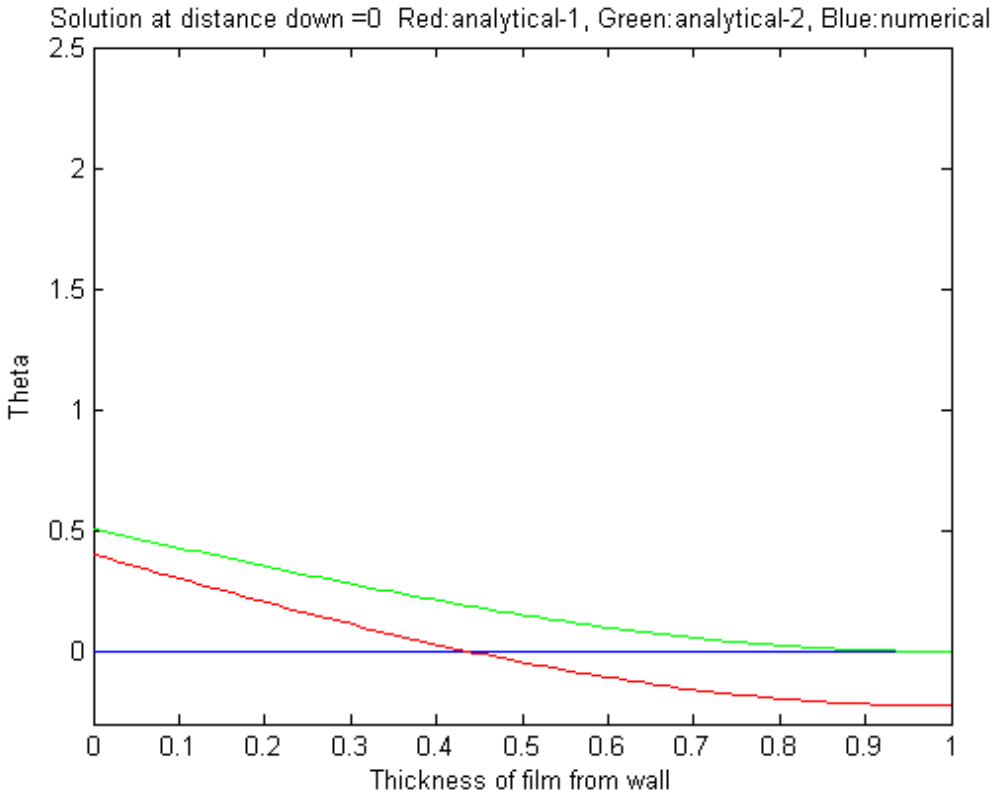

Figure 6.10: Temperature, Θ, distribution across film thickness, Y, at X = 0.

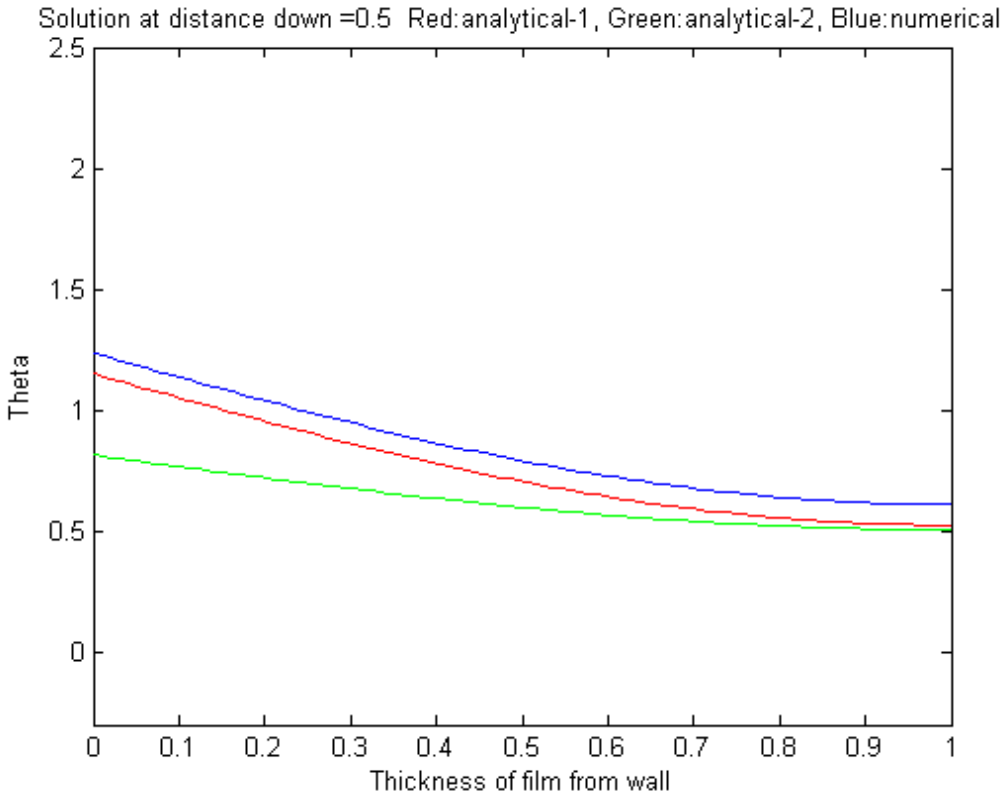

Figure 6.11: Temperature, Θ, distribution across film thickness, Y, at X = 0.5.

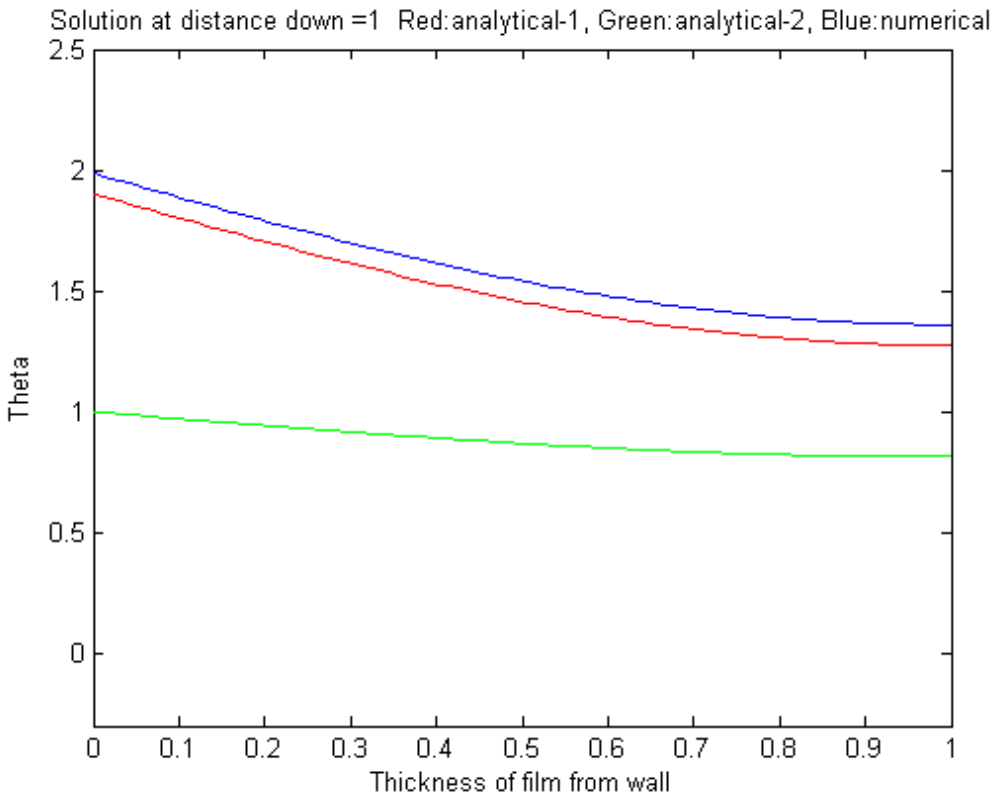

Figure 6.12: Temperature, Θ, distribution across film thickness, Y, at X = 1.

However, both solutions from literatures satisfy the initial condition. From the results, the temperature of film increased with more distance traveled down the length of the tube.

From comparisons, the analytical solution from Zhang et al. (2008) does not change much with the distance down the tube and proves to be inadequate for describing the temperature distribution at after length X = 0.6. However the solutions from Matlab and Saouli and Aiboud-Saouli (2004) continue to change with X.

The results also gave indication that the temperature distribution from the wall to the falling film was not linear.

Hence, the flow of the film has an influence on the heat transfer.

6.3.Conclusion

- Analytical equations were derived for Newtonin/non-Newtonian type velocity profiles and its corresponding film thicknesses.
- Brief analyses of these equations were made. It was found there were differences with the velocity profiles between the Newtonian and non-Newtonian type while that the film thicknesses between the two was little.
- The analytical equations derived for the non-Newtonian type also found use with the rheological models derived earlier. Further discussion can be made with more investigation.
- Matlab was used to obtain the film temperature profile under conditions mentioned above.
- Analytical solutions provided by Saouli and Aiboud-Saouli (2004) and Zhang et al. (2008) were compared together with the numerical solution from Matlab.
- The analytical solution from Saouli and Aiboud-Saouli (2004) was quite closely comparable with the numerical solution from Matlab.

7. CFD Simulation : COMSOL Multiphysics

Several attempts were made to use commercial CFD package COMSOL Multiphysics version 4.0 to simulate the falling film flow. The modules that came with the software were the Chemical Engineering Module, Heat Transfer Module and AC/DC Module.

In the modules, several physics interfaces were available for use. Some predefined multiphysics interfaces for coupled physics such as *Non-Isothermal Flow* and *Free and Porous Media Flow* were included.

It was thought that COMSOL would be the best software to use for simulating the falling film flow with its ability to couple two different physics together. It was hoped that through COMSOL, a final model for a falling film could be obtained which would not just be able to simulate the heat, flow and mass transfer but also the thickness and position of the liquid-vapour interface.

The initial attempts with the use of COMSOL began with the single phase flow physics type using the *Laminar Flow* physics interface and later the *Nonisothermal Laminar Flow* physics interface for coupled physics between fluid flow and heat transfer.

Later attempts focused on mass transfer using the *Transport of Diluted Species* physics interface from the Chemical Species Transport physics type. All these attempts were not satisfactory as a fixed geometry was used and not necessarily reflect the actual falling film flow.

Other methods were sought that would account for the changing film thickness. The moving mesh method available in COMSOL was attempted. However this method was complicated and not appropriate for a constant flow with changing interface.

Another method involving the simulation of the flow of two different phases under the multiphase flow physics type was chosen.

7.1. Multiphase Flow Attempts

COMSOL provide two methods to track a fluid-fluid interface of a two phase flow:

- The phase field method
- The level set method

In this simulation study, the phase field method was chosen. The *Laminar Two-Phase Flow, Phase Field* physics interface available in COMSOL was used. The physics interface enables modeling of laminar two-phase flow of two immiscible fluids separated by a moving interface. With the phase field method, the interface between the two fluids is governed by the phase field variable, ϕ. The moving interface can then be tracked from the phase field variable.

For two phase flow of this type, the interface solves the incompressible Navier-Stokes equation and the fourth-order PDE Cahn-Hilliard equation. In COMSOL, the Navier-Stokes equation is recognized as,

$$\rho\frac{\partial u}{\partial t}+\rho(u\cdot\nabla)u=\nabla\cdot\left[-pI+\mu\left(\nabla u+\nabla u^{T}\right)\right]+F_{g}+F_{st}+F_{ext}+F$$

$$\nabla\cdot u=0$$

The fourth-order PDE Cahn-Hilliard equation can be decomposed into two second-order PDEs

$$\frac{\partial\phi}{\partial t}+u\cdot\nabla\phi=\nabla\cdot\frac{\gamma\lambda}{\varepsilon^{2}}\nabla\psi$$

$$\psi=-\nabla\cdot\varepsilon^{2}\nabla\phi+\left(\phi^{2}-1\right)\phi+\left(\frac{\varepsilon^{2}}{\lambda}\right)\frac{\partial f_{ext}}{\partial\phi}$$

These two equations were added together with the Navier-Stokes equation to solve the two phase flow.

7.1.1. Geometry

The geometry consists of two rectangles which were Domain 1 and Domain 2. Domain 1 has the dimension of 0.01 m × 0.1 m. Domain 2 has the dimension of 0.0012 m × 0.002 m.

The layout of the geometry was depicted in Figure 7.1. In the figure, the *x* and *y* axis are the grid coordinates. The boolean *Union* operation was used to combine Domain 1 and Domain 2 together.

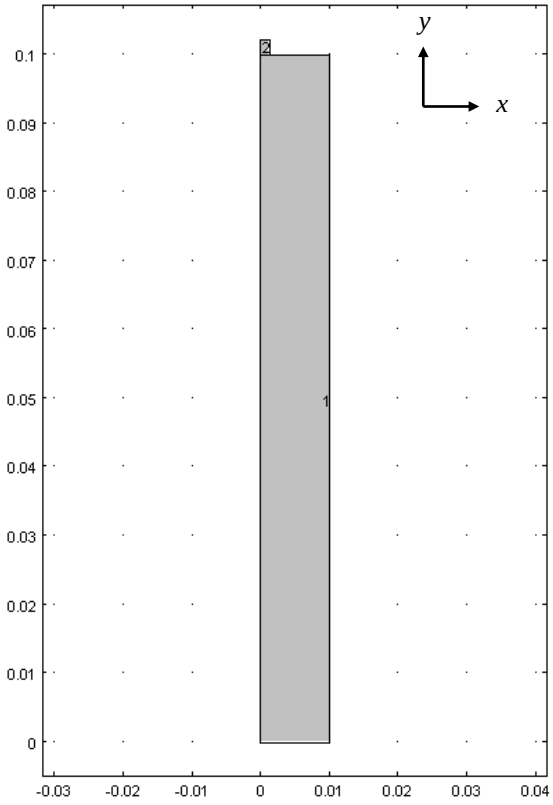

Figure 7.1: Layout of geometry.

7.1.2. Materials

The materials used in the simulation were water and air (not water vapour). Domain 1 was selected as initially containing air and Domain 2 as initially containing water. The properties for water and air were readily available from COMSOL and were

automatically integrated to the materials selected. Options were available for a *user defined* properties.

7.1.3. Mesh

A few meshes were created for this simulation. Figures 7.2 to 7.5 shows the different meshes used. The statistics to the meshes created were tabulated in the corresponding Tables 7.1 to 7.4. Unless otherwise stated, the element type used for the meshes was triangular type.

Table 7.1: Domain element statistics of mesh A generated from COMSOL.

Number of elements	8954
Minimum element quality	0.8254
Average element quality	0.9773
Element area ratio	0.02793
Mesh area	0.001002 m^2

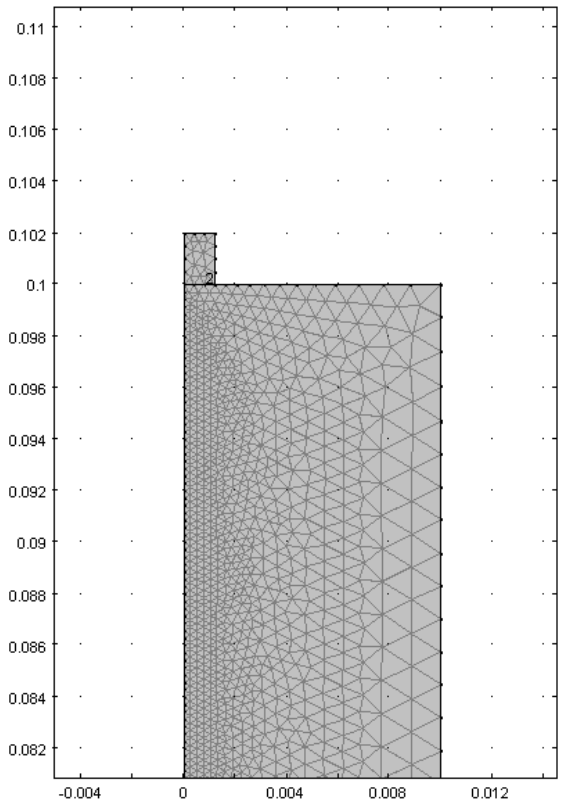

Figure 7.2: Mesh A.

Mesh A was created with more elements distributed to the left side of the wall boundaries in Domain 1. It has maximum element size of 0.0014 m in Domain 1 and 0.0006 m in Domain 2.

Table 7.2: Domain element statistics of mesh B generated from COMSOL.

Number of elements	15615
Minimum element quality	0.8566
Average element quality	0.9967
Element area ratio	0.3914
Mesh area	0.001002 m^2

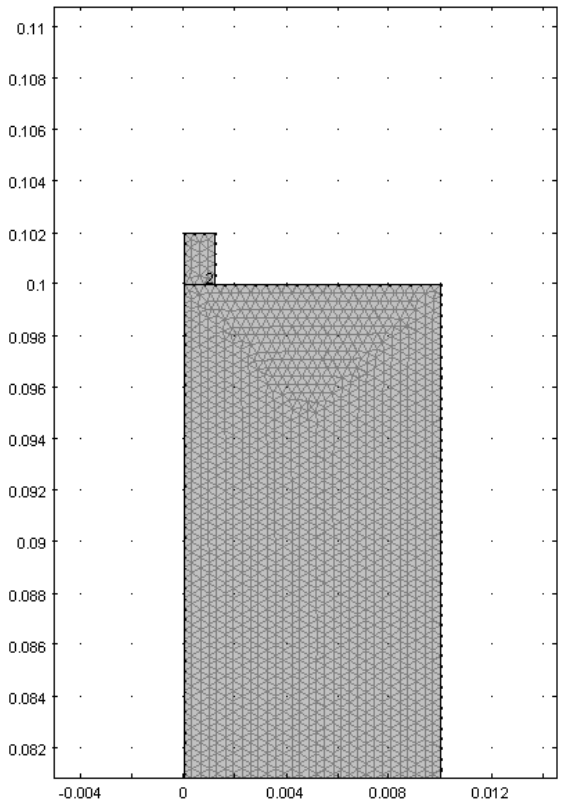

Figure 7.3: Mesh B.

Mesh B was created with the elements' size smaller than mesh A. The maximum element size was 0.0005 m in Domain 2 and 0.0004 m in Domain 1. Mesh C was created on a smaller geometry than those of mesh A and mesh B where the width of Domain 2 was smaller by half of that used for mesh A and mesh B. In mesh C, a structured mesh (mapped) was applied to Domain 2. The element's size in Domain 2 was 0.0003 m while in Domain 1 was 0.0004 m.

In mesh C, the elements were distributed slightly more on the left side of the wall boundary of Domain 2.

Table 7.3: Domain element statistics of mesh C generated from COMSOL.

Number of elements	10213
Minimum element quality	0.8362
Average element quality	0.9906
Element area ratio	0.1999
Mesh area	0.0005024 m^2

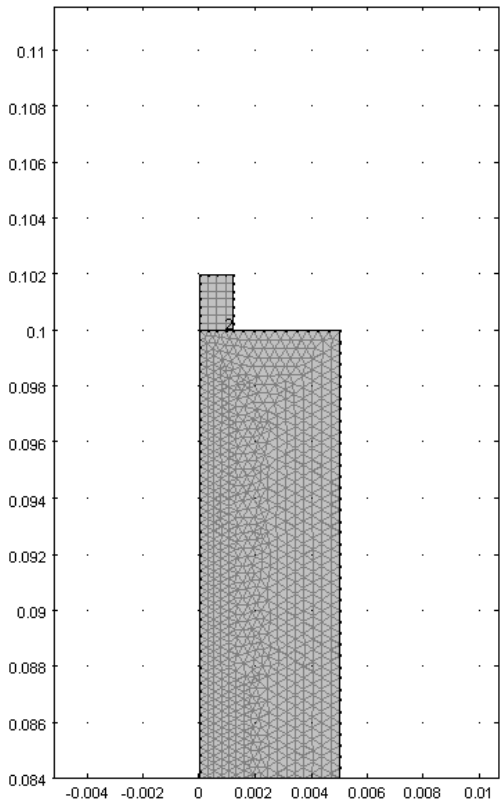

Figure 7.4: Mesh C.

The final mesh used, mesh D has the smallest element size compared to mesh A, B and C. It is therefore the finer of the finer mesh B. It has the maximum element size of 0.0002 m for Domain 1 and Domain 2. It uses the same element type which is the triangular type for its Domain 1 and Domain 2.

Table 7.4: Domain element statistics of mesh D generated from COMSOL.

Number of elements	62238
Minimum element quality	0.8515
Average element quality	0.9971
Element area ratio	0.4029
Mesh area	0.001002 m^2

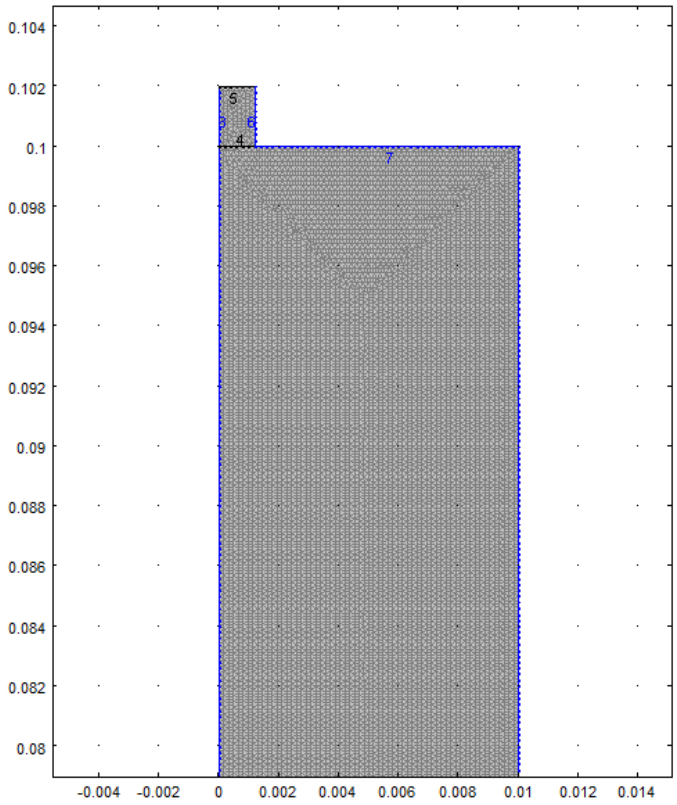

Figure 7.5: Mesh D.

7.1.4. Physics of Simulations

In these attempts, water and air were used as the materials for the simulation of the falling film flow. The initial attempts considered only a falling film flow with no heat transfer and therefore no evaporation involved.

The simulations using mesh C was done with the use of only the Laminar Two-Phase Flow, Phase Field physics interface alone.

To simulate a falling film flow, geometries were designed so that the flow begins from the top and exits at the bottom with no addition of a distributor.

From Figure 7.1, the flow enters at the top from Domain 2 and flows out at the bottom from Domain 1. The rectangular Domain 2 was made small so that the flow will flow into Domain 1 as a film.

The boundaries assigned to the geometries were designated as follows (Figure 7.6 and Figure 7.7):

- Wall - 1, 3, 6, 7 and 8
- Outlet - 2
- Interface - 4
- Inlet - 5

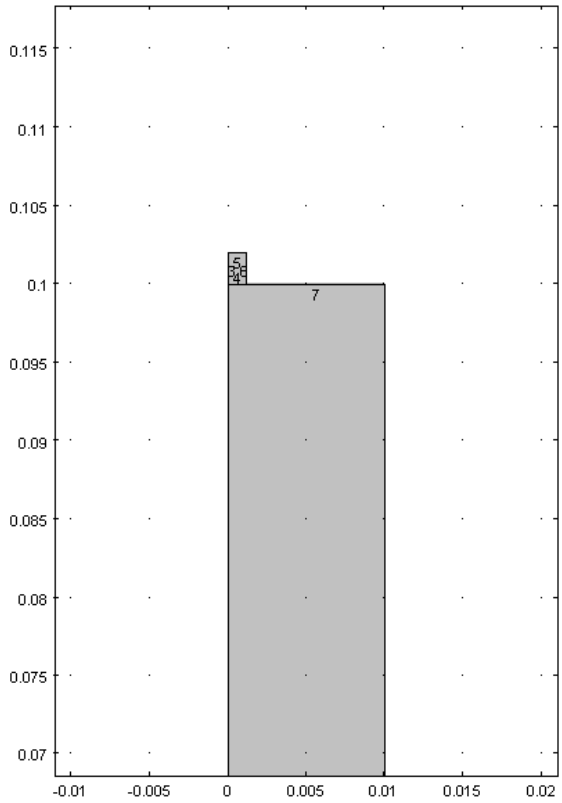

Figure 7.6: The designated boundaries for the top part of the geometry.

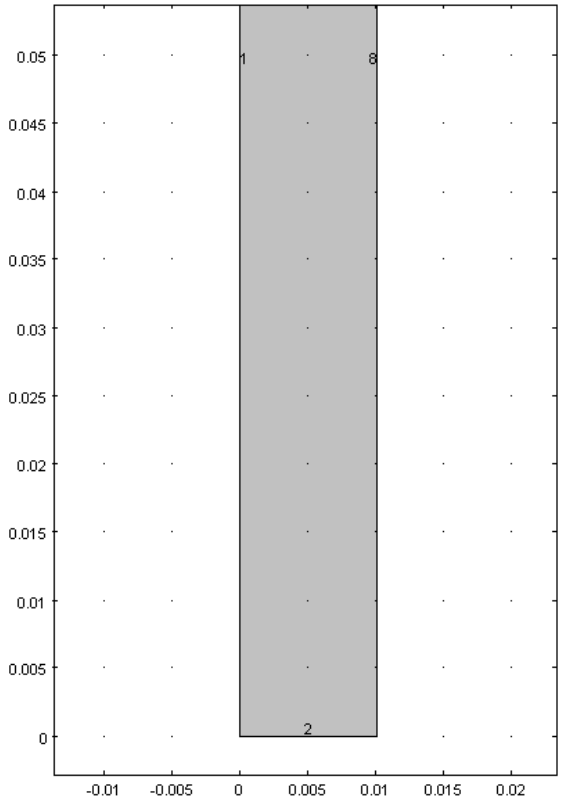

Figure 7.7: The designated boundaries for the lower part of the geometry.

A *no slip* condition was added to the wall boundaries. A gravity force was added to all domains. The initial conditions were set where water was initially in Domain 2 and air initially in Domain 1. A volume fraction of 1 was assigned to water initially in Domain 2. The simulations were in 2D and were time dependent studies.

7.1.5. Results

Mesh A

In using mesh A, the surface tension was defined as 0.045 $N \cdot m^{-1}$ (chosen because it was pre-calculated as in Appendix F) while the viscosities were as from COMSOL library. An inlet velocity of 0.5 $m \cdot s^{-1}$ was used.

Volume fraction

Figure 7.8 shows the development of film flow (designated by the volume fraction) with time using mesh A.

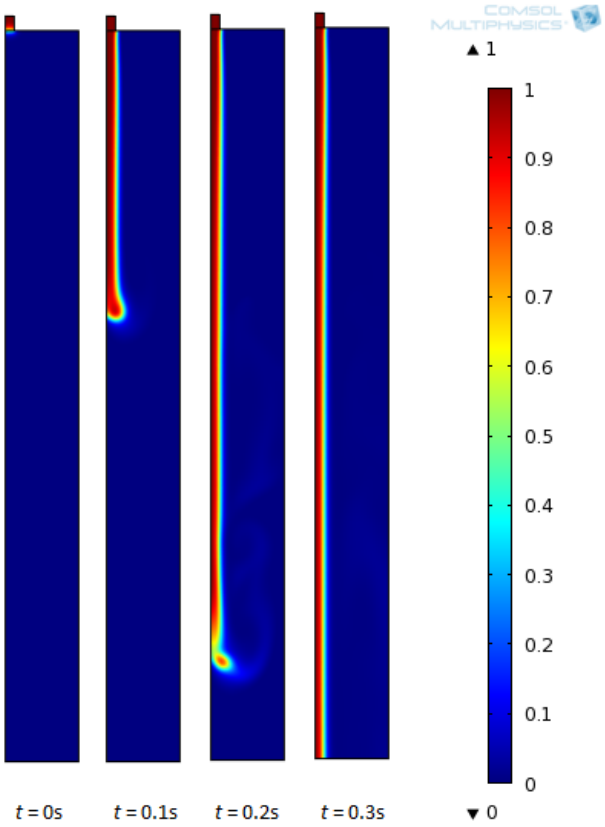

Figure 7.8: Changing volume fraction of water with time using mesh A.

The distinctive interface can be seen from this method of simulation. The volume fraction of 1 indicated by the color dark red represents water while the color blue represents air. This will be so for the remaining figures relating to volume fraction.

The present results showed that after time, t = 0.3 s there were no visible changes in the profile.

Velocity profile

Figures 7.9 to 7.12 show the development of velocity profiles of water and air with time using mesh A. An arrow surface plot was added to the figures for indicating the direction of flows.

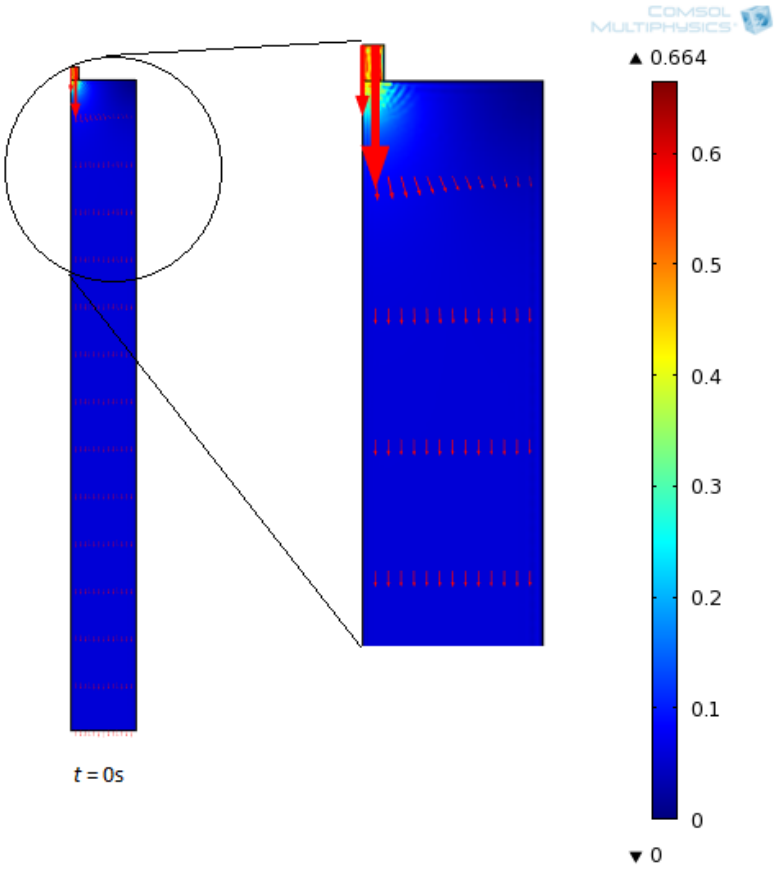

Figure 7.9: Velocity profile at time, t = 0 s using mesh A.

Figure 7.9 showed the velocity profile at time, t = 0 s. The arrows were pointing downwards in the direction of flow giving indication the direction of the velocity profile. The figure also shows the velocity has a maximum velocity of 0.664 $m \cdot s^{-1}$ at this point.

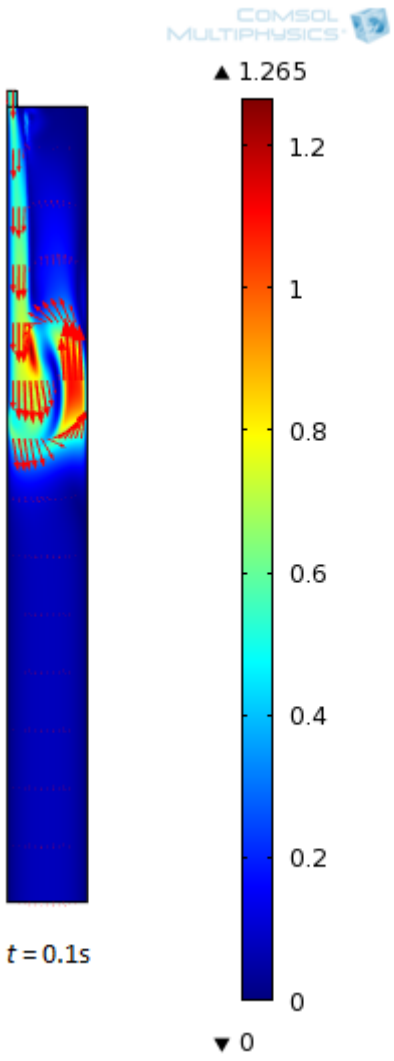

Figure 7.10: Velocity profile at time, t = 0.1 s using mesh A.

The velocity profile in Figure 7.10 shows that there seems to be a recirculation of flows. As few figures later will show, this is not true and that the two different directions of the velocity profiles shown were actually two different velocity profiles from two different materials of water and air.

Figure 7.11 continue to show the developing trend of the falling film and the developing trend of the velocity profile of air that is flowing upwards.

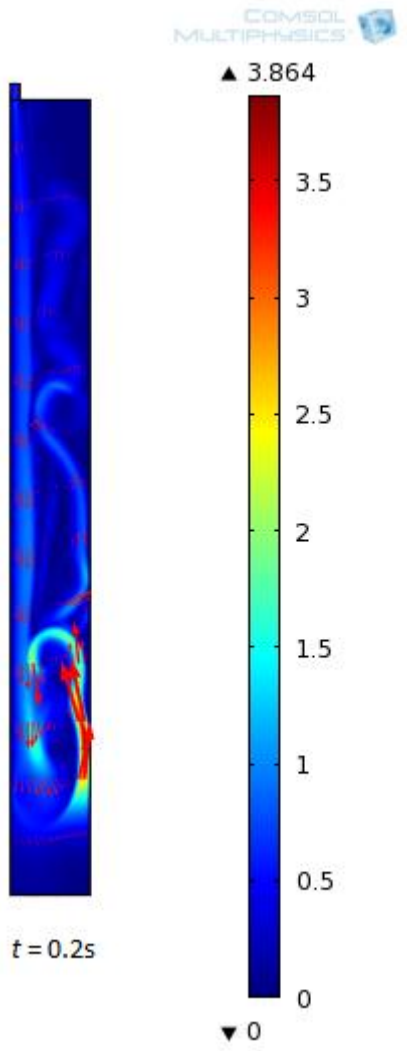

Figure 7.11: Velocity profile at time, t = 0.2 s using mesh A.

The development of the velocity profiles from time, t = 0.3 s to t = 5 s were collected together for comparison in Figure 7.12.

It can be seen from Figure 7.12 that starting from time, *t* = 1 s, there were no significant changes to the velocity profiles.

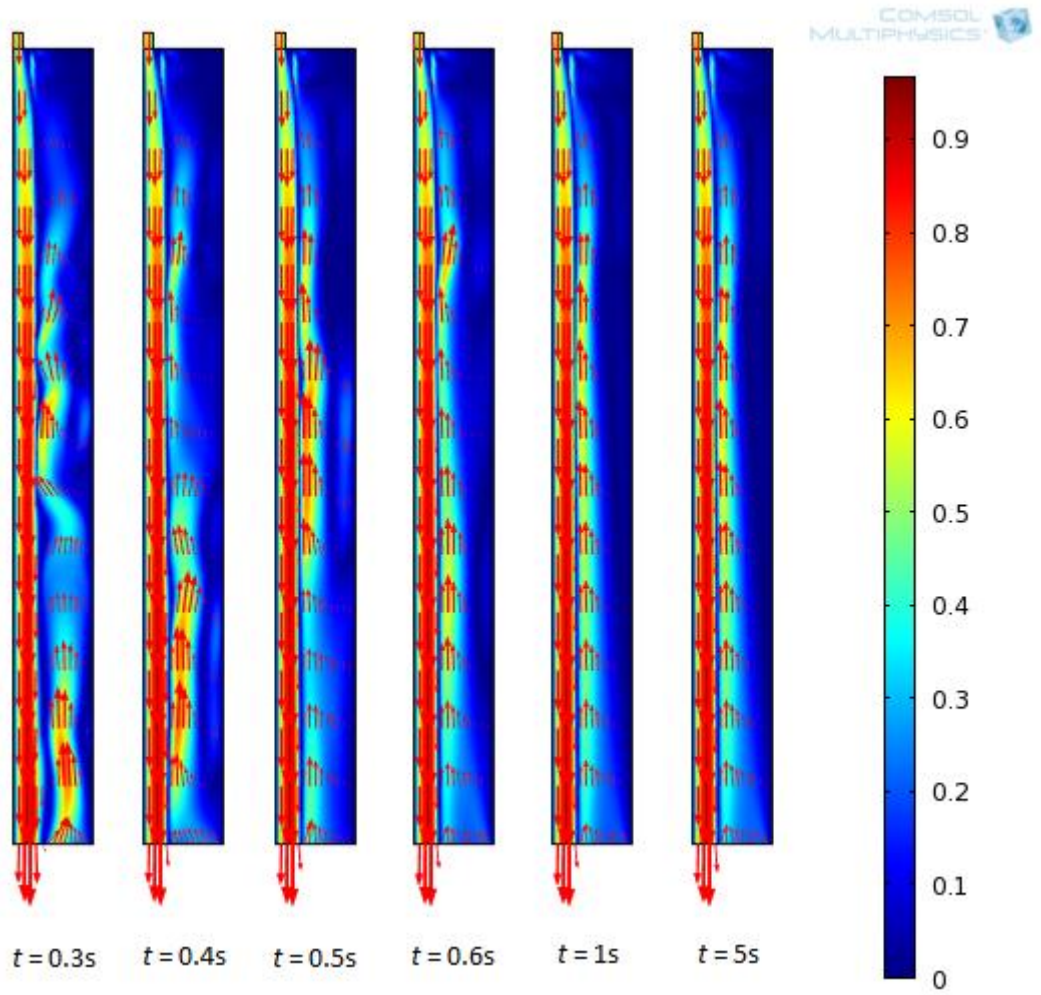

Figure 7.12: Changing velocity profile from time, t = 0.3 s to 5 s using mesh A.

Mesh B

In using mesh B, the physics settings were the same as mesh A with the surface tension defined as 0.045 $N \cdot m^{-1}$ while the viscosity was as from COMSOL library. An inlet velocity of 0.5 $m \cdot s^{-1}$ was used.

Volume fraction

Figure 7.13 show the development of film flow (designated by the volume fraction) with time using mesh B.

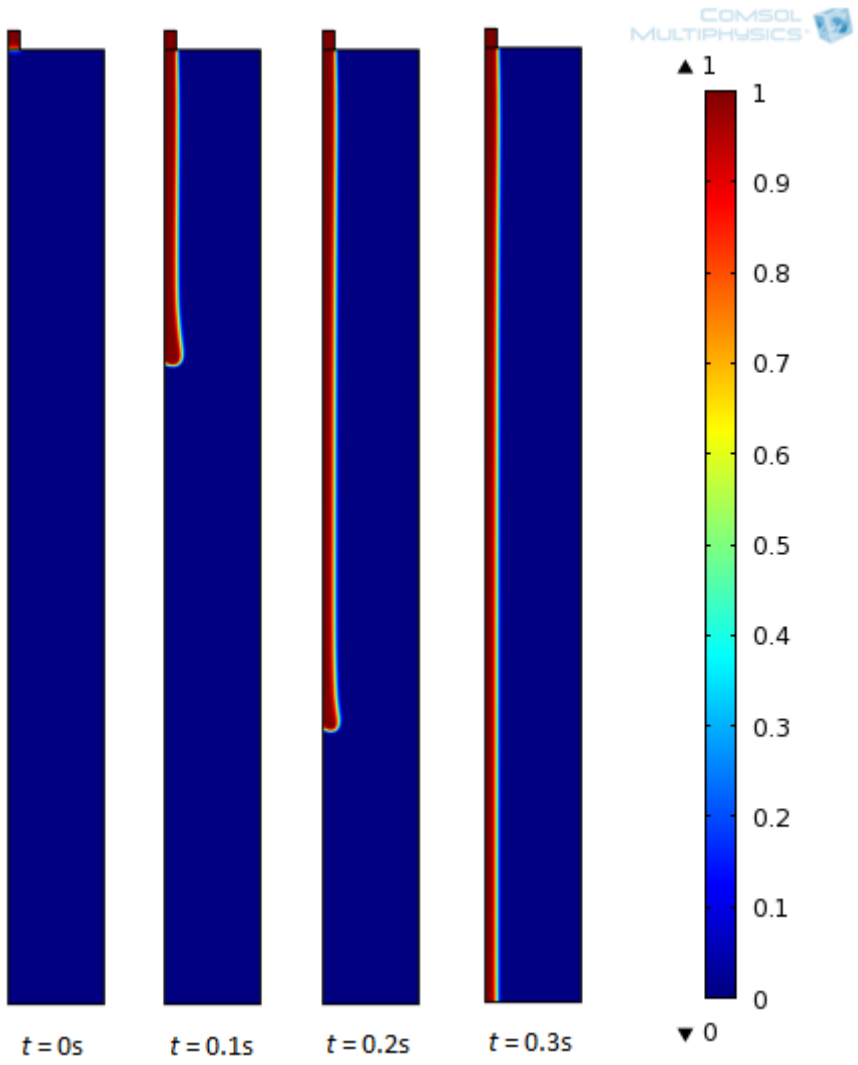

Figure 7.13: Changing volume fraction of water with time using mesh B.

The interface can be seen to be more distinctive with the use of mesh B which was the finer mesh of mesh A and C. The result from the use of mesh B indicated that there were no waves and the interface was smooth with the current conditions used. After time, t = 0.3 s, no further visible changes in the profile were observed.

Velocity profile

Figures 7.14 to 7.16 show the development of velocity profiles of water and air with time using mesh B. An arrow surface plot was added to the figures as before for indicating the direction of flows.

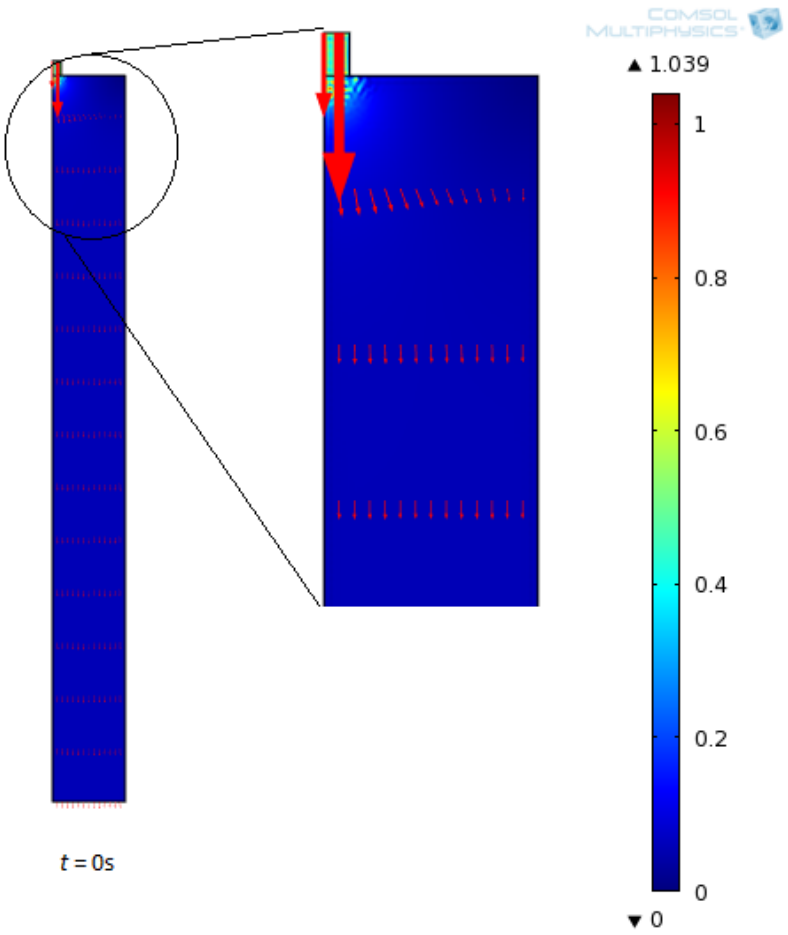

Figure 7.14: Velocity profile at time, t = 0 s using mesh B.

Figure 7.14 shows the velocity profile as the water initially from Domain 2 enters into Domain 1 initially filled with air.

Figure 7.15 further shows the development of the velocity profiles from time, t = 0.1 s to t = 0.2 s once the water already entered into Domain 1. The figure also illustrates the development of the upwards air velocity profile as a result of the falling water film.

This result from the use of mesh B further supports the result earlier from mesh A of the two different velocity profiles in Figures 7.10 and 7.11.

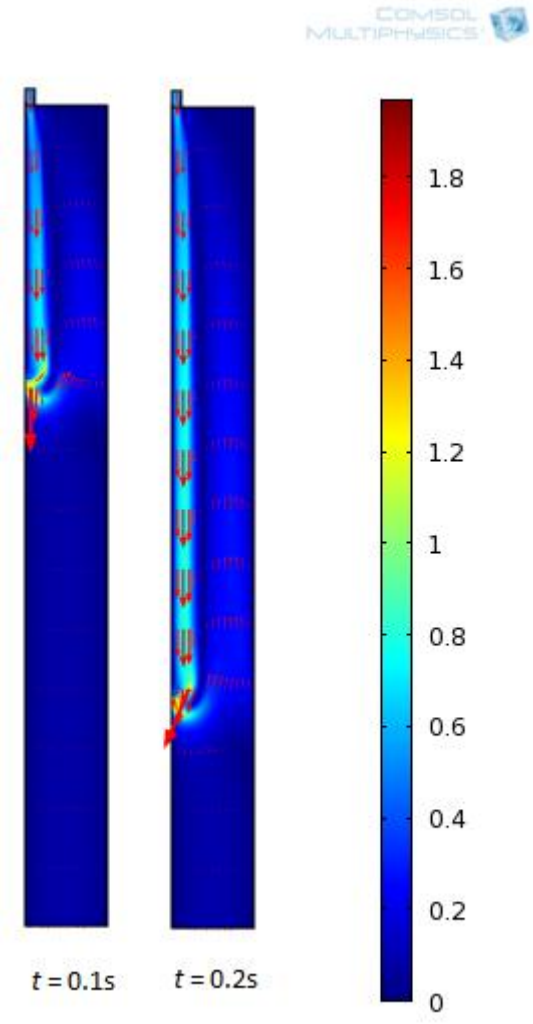

Figure 7.15: Velocity profile at time, t = 0.1 s and 0.2 s using mesh B.

In addition, Figure 7.15 depicts the changes of velocities in terms of magnitude and direction providing further descriptions of the film flow in Figure 7.13 of the same time at t = 0.1 s and t = 0.2 s.

Further comparison of the velocity profiles from time, t = 0.3 s to t = 5 s were made in Figure 7.16. The figure reveals that two different velocity profiles in opposite directions exist in the current simulations.

After time, t = 1 s, no visible change in the profile was observed.

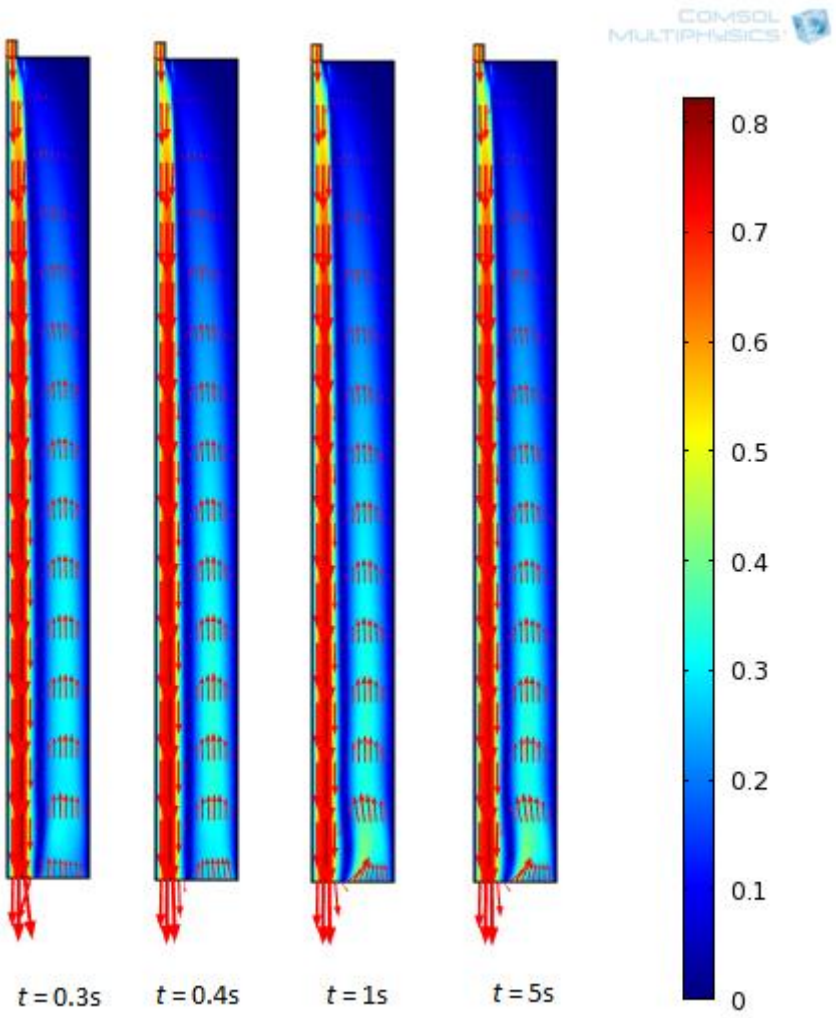

Figure 7.16: Velocity profiles from time, t =0.3 s to 5 s using mesh B.

Mesh C

In using mesh C, the surface tension and the viscosity was as from COMSOL library. An inlet velocity of 0.5 $m \cdot s^{-1}$ was used. The geometry that comes with mesh C was slightly smaller where the width of Domain 1 was reduced by half to 0.01 m.

Volume fraction

Figure 7.17 shows the development of film flow (designated by the volume fraction) with time using mesh C in a smaller geometry.

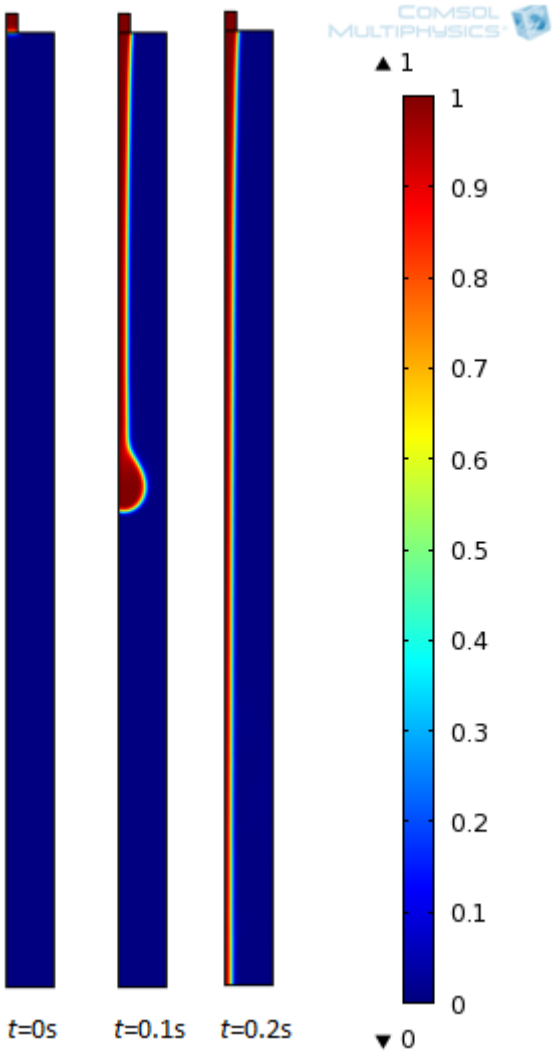

Figure 7.17: Changing volume fraction with time using mesh C.

The results from mesh C gave similar results as from mesh A and B. This shows that the reduced dimension of geometry does not affect the overall solutions. A thinning effect of the film was observed from this result.

After time, t = 0.2 s there was no visible change in the profile.

Velocity profile

Figures 7.18 to 7.20 show the development of velocity profiles of water and air with time using mesh C in a smaller geometry. Again, arrow surface plot was added to the figures for indicating the direction of flows.

The structured mesh in Domain 2 from mesh C gave a slightly different velocity profile in the beginning compared to mesh A and B when time, t = 0 s.

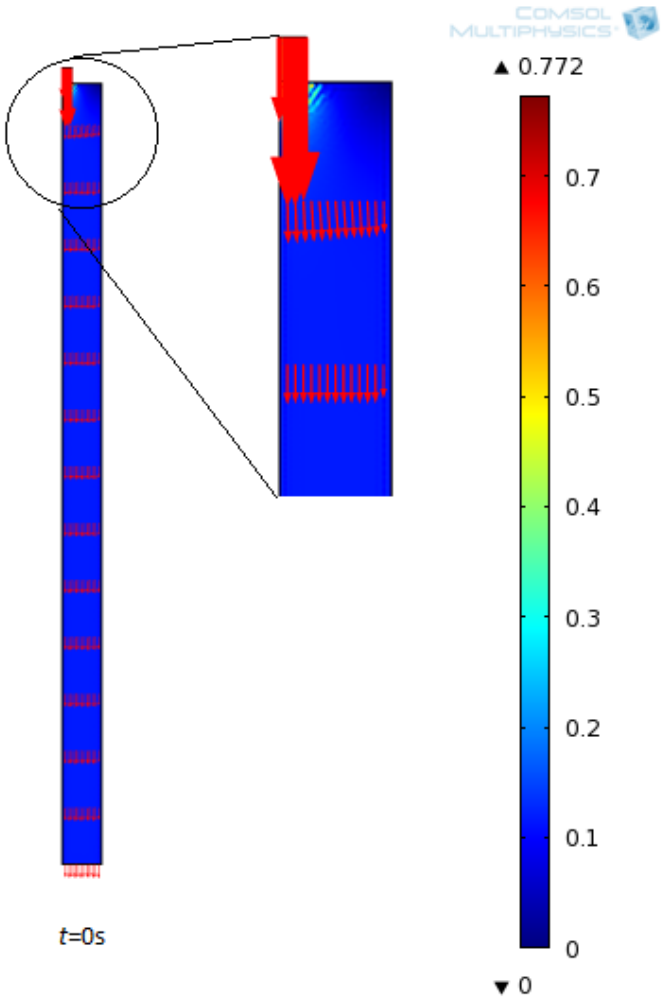

Figure 7.18: Velocity profile at time, t = 0 s using mesh C.

Figure 7.19 showed the two different velocity profiles as reported earlier. This occurred starting from time, t = 0.1 s.

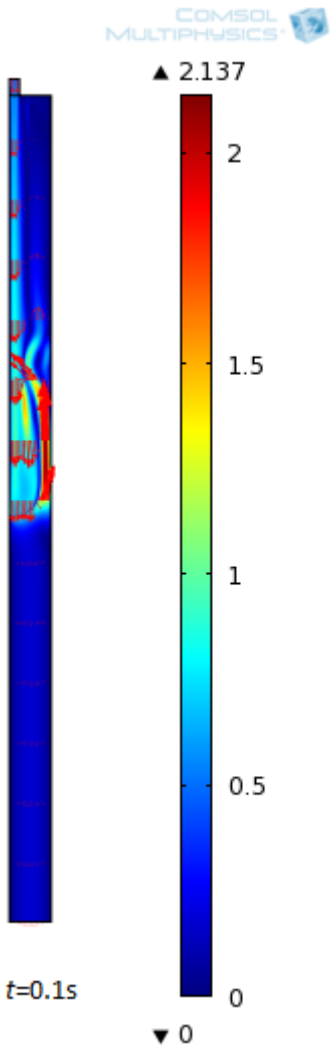

Figure 7.19: Velocity profile at time, t = 0.1 s using mesh C.

The velocity profiles for time, t = 0.2 s to 0.4 s were collected together in Figure 7.20. At time, t = 0.2 s, the falling water film have reached a steady profile while the air velocity profile continue to develop. After time, t = 0.3 s there was no visible change observed in both the water and air velocity profiles.

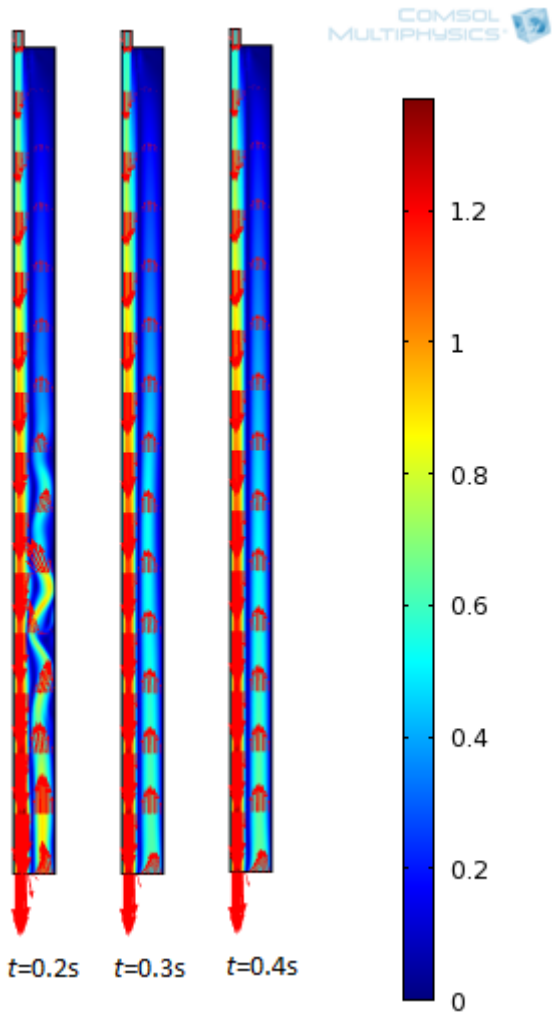

Figure 7.20: Velocity profiles from time, t = 0.2s to 0.4s using mesh C.

Mesh D

The same settings previously used for mesh A, B and C was kept the same so that comparison of the results can be made. The surface tension used was 0.045 $N \cdot m^{-1}$ with inlet velocity of 0.5 $m \cdot s^{-1}$. The viscosities used were as from COMSOL library.

The simulation using mesh D took longer to solve compared to mesh A, B and C with a solving time of 1274817.27s or 14.75 days. Of the four meshes, mesh D was the finer mesh being halved that the element size of mesh B.

Volume fraction

The phase field method with its volume fraction shows the development of the falling water film. The interface between the water and air can be clearly identified with this method.

The development of the falling film was fast that after time, t = 0.2 s there were no visible changes in the flow profile. This is consistent with earlier results from mesh A, B and C where the time the profile observed to have no changes were 0.3 s, 0.3 s and 0.2 s respectively.

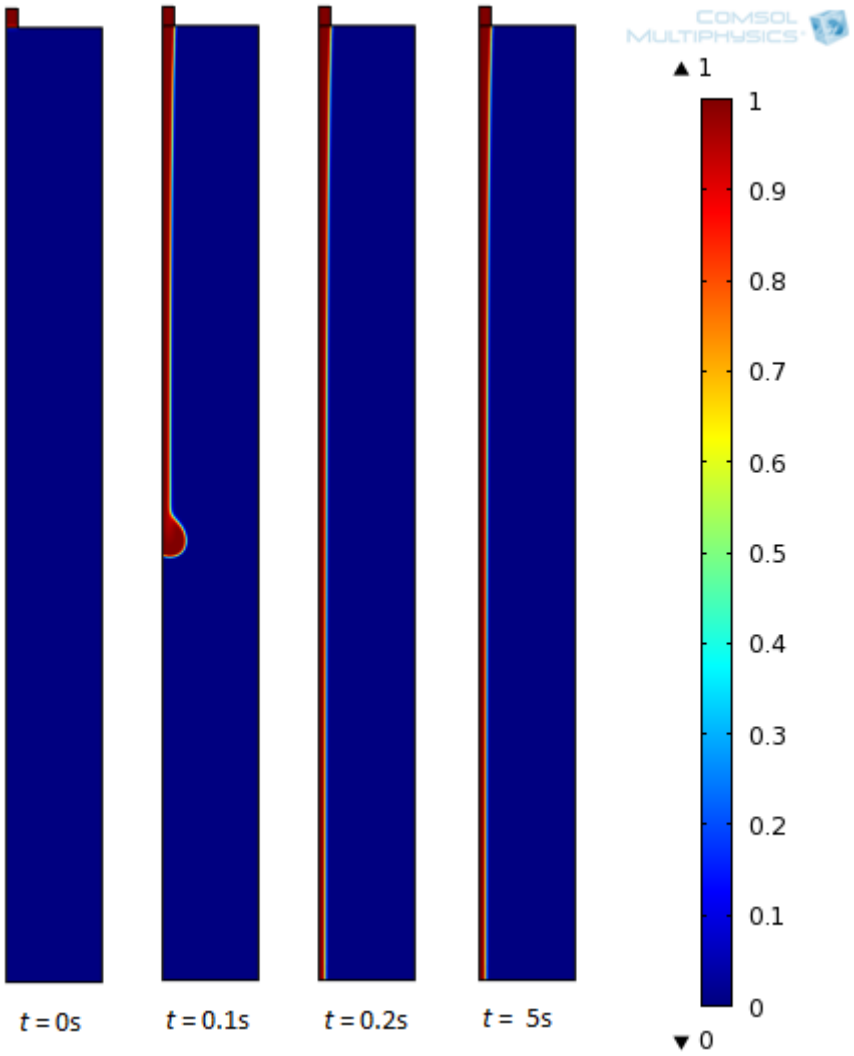

Figure 7.21: Changing volume fraction with time using mesh D.

The development of the falling film so far with the use of mesh D showed similar results from previous use of mesh A, B and C. Consistent with theory, Figure 7.21

showed there were a developing region and a developed region in the falling film, that is a thinning of the film.

Velocity profile

Figures 7.22 to 7.25 show the development of the velocity profiles from the simulation using mesh D.

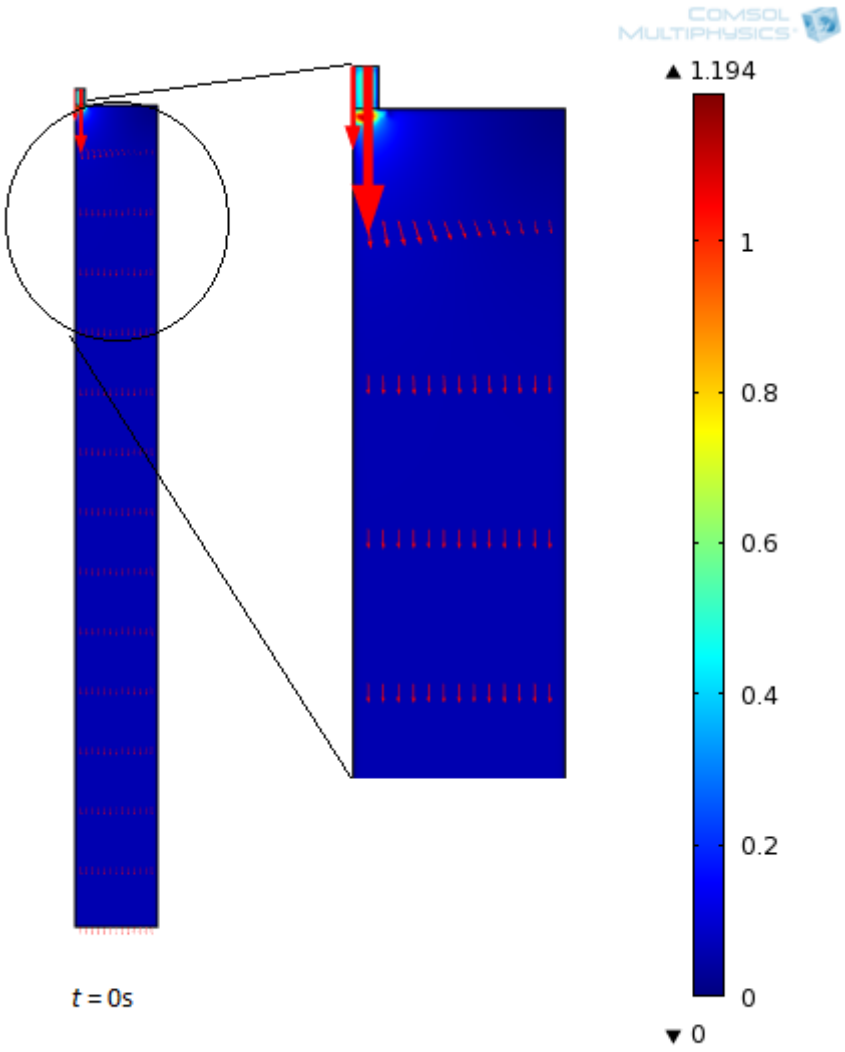

Figure 7.22: Velocity profile at time, t = 0 s using mesh D.

A magnified portion at the entrance was included in the Figure 7.22 to help with the visualization of the velocity profile.

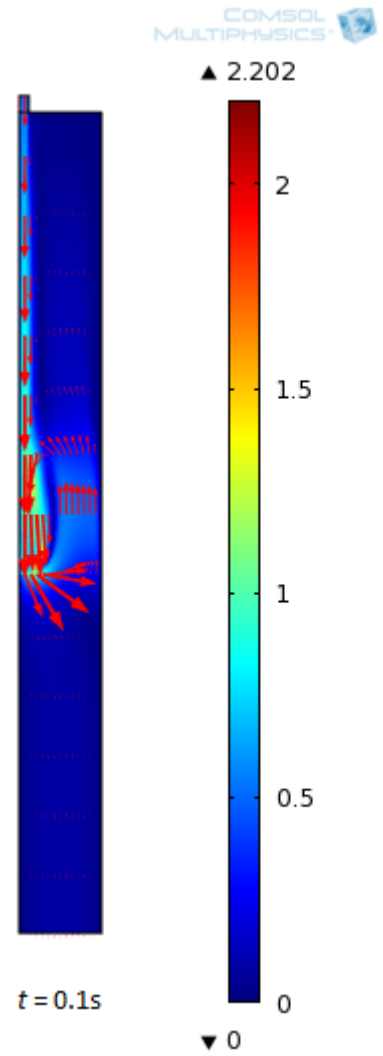

Figure 7.23: Velocity profile at time, t = 0.1 s using mesh D.

The refined mesh D provides the same result of the existence of the two different velocity profiles as previously reported. The upward air velocity profile was induced by the falling film.

Figures 7.24 and 7.25 show the progress of the velocity profiles with time. The observations of these velocity profiles were expected. However, the use of the more refined mesh D showed that the magnitude of the air velocity profile was small which differs from earlier results.

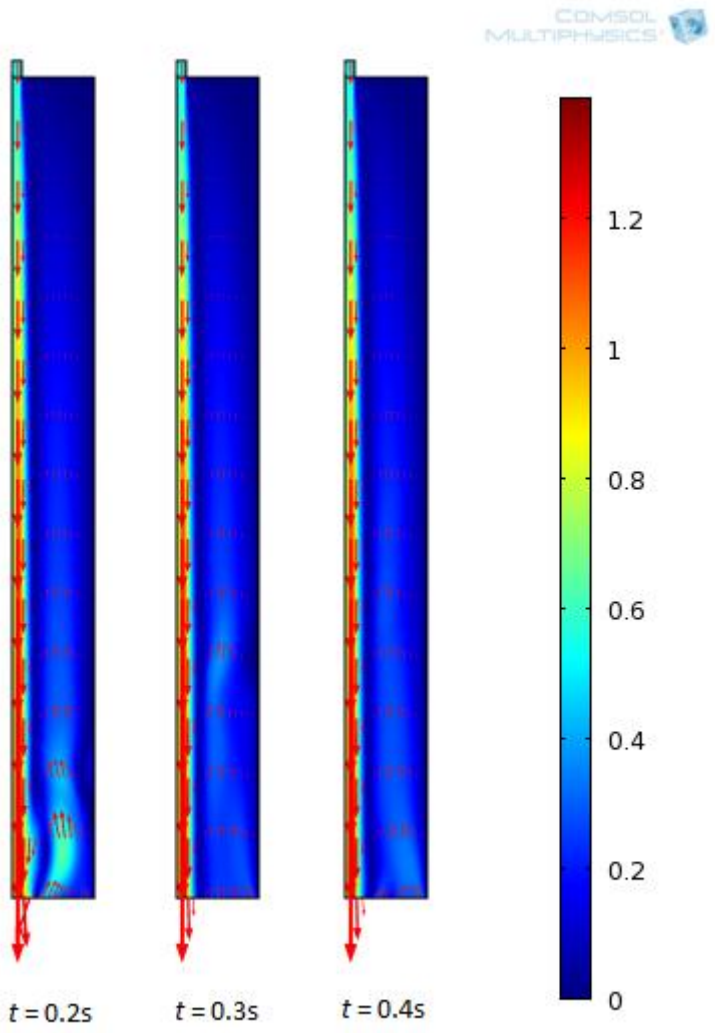

Figure 7.24: Velocity profiles from time, t = 0.2 s to 0.4 s using mesh D.

Figure 7.25 below showed the velocity profile from time, t = 0.5 s to t = 0.7 s.

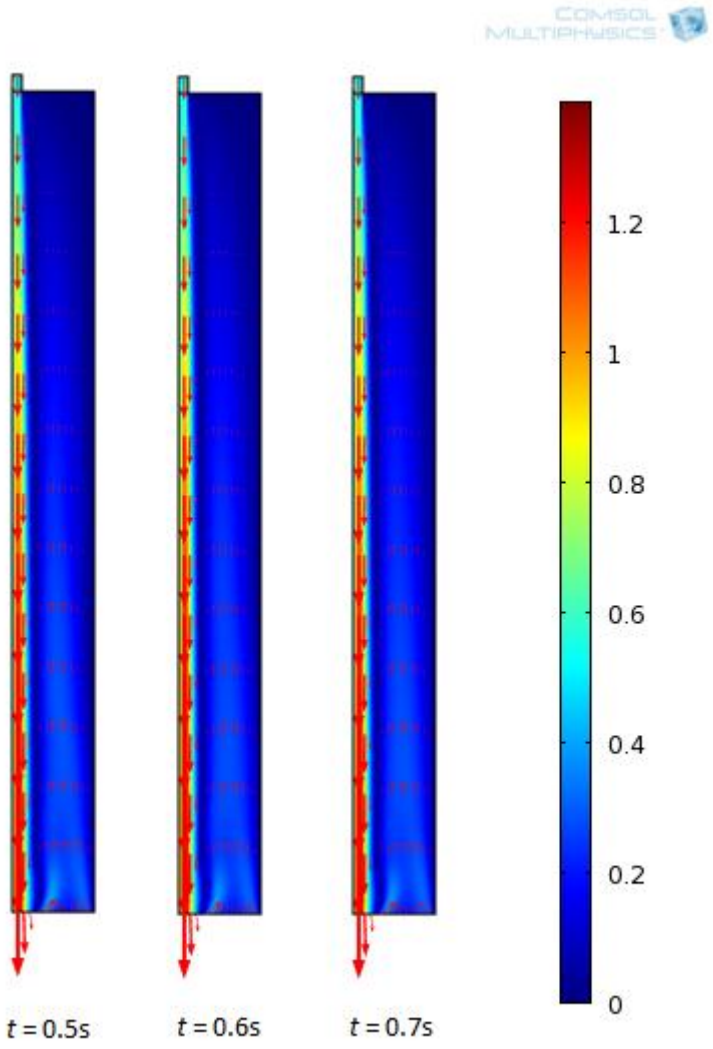

Figure 7.25: Velocity profiles from time, t = 0.5 s to 0.7 s using mesh D.

Film thickness

In the simulations, mesh B was the finer mesh while mesh D being more refined. The result from Figures 7.13 and 7.21 was chosen for measuring the film thickness predicted by the simulations using mesh B and D. This result was printed as full page on A4 size paper and the thickness measured with a ruler. The interface between the water and air was taken to be when volume fraction is 0.5. The film thickness measured this way gave a thickness of 0.001375 m from using mesh B.

The film thicknesses as measured from using mesh D are presented in the Table 7.5 below. The film thicknesses are different from each length of the Domain 1 due to the thinning of the film. The position of the length was taken to be increasing from the bottom of Domain 1 up to 0.1 m where it is near the entrance of the falling film.

Table 7.5: Film thickness as obtained from Figure 7.21 using mesh D.

Length (m)	Film thickness (m)
0.1	0.00116
0.08	0.00106
0.06	0.000833
0.04	0.000833
0.02	0.000833

These film thicknesses are just for the case of falling water film with no heat transfer and no evaporation and not indicative of the actual falling film evaporation of milk. For comparison, the calculated milk film thickness for steady state process at 10% TS and 45% TS were 0.000427 m and 0.001165 m respectively at the top/entrance of the tube.

Graphical velocity profile

A few graphical plots of the velocity were done to have a better understanding of the velocity profiles. The velocities were plotted against the horizontal distance of Domain 1 in COMSOL.

Figures 7.26 to 7.35 show the velocity profile at different length, *L*, of the geometry and at different time, *t*. The length the velocities were plotted was at L = 0.01 m, L = 0.02 m and L = 0.03 m. The interest in looking at the velocities at these lengths which were near towards the bottom of the geometry was to ascertain if a developed flow was obtained.

These plots were also presented at different time to determine if the velocities changes after a particular time.

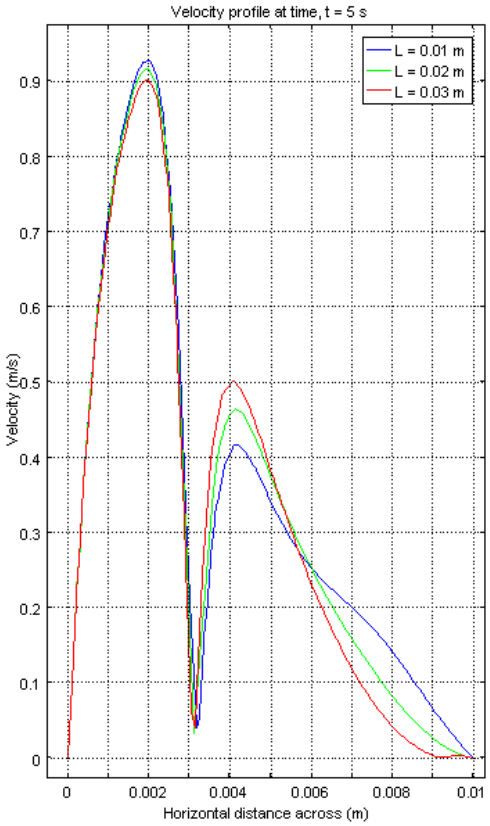

Figure 7.26: Graphical velocity profile at different lengths from mesh A.

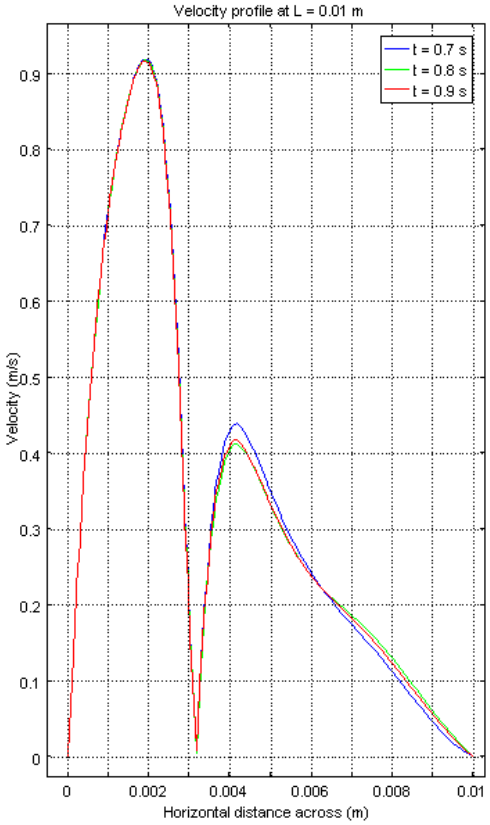

Figure 7.27: Graphical velocity profile at different study time from mesh A.

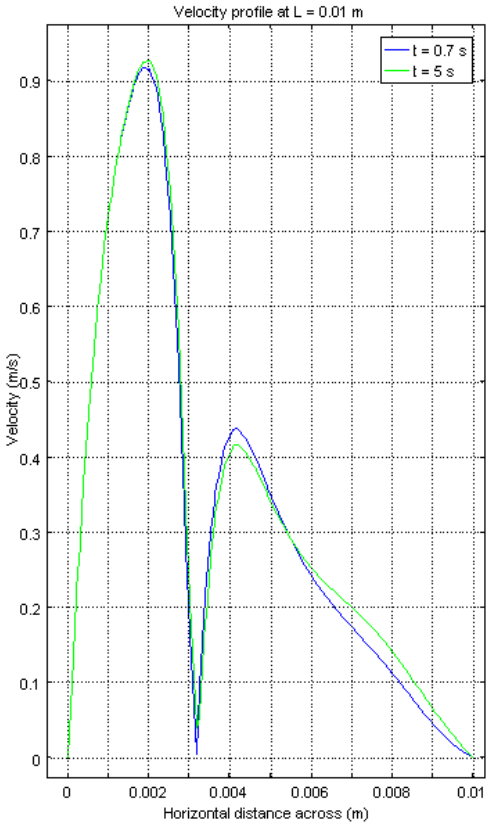

Figure 7.28: Graphical velocity profile at study time, t = 0.7 s and 5 s from mesh A.

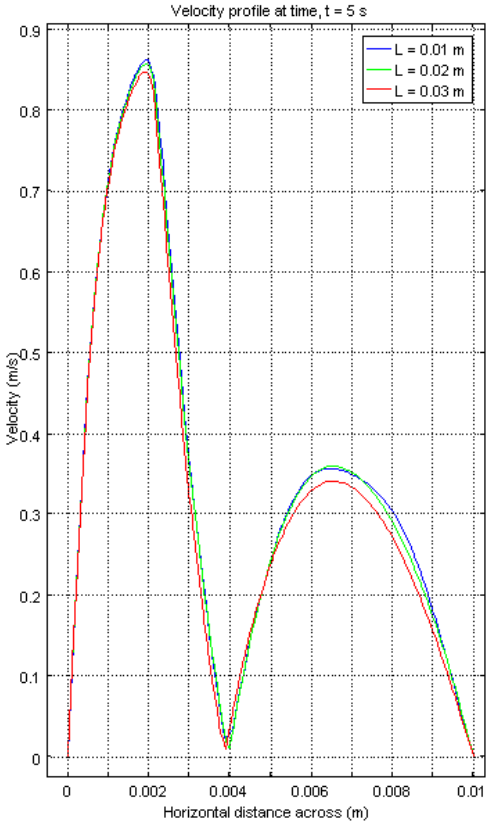

Figure 7.29: Graphical velocity profile at different lengths from mesh B.

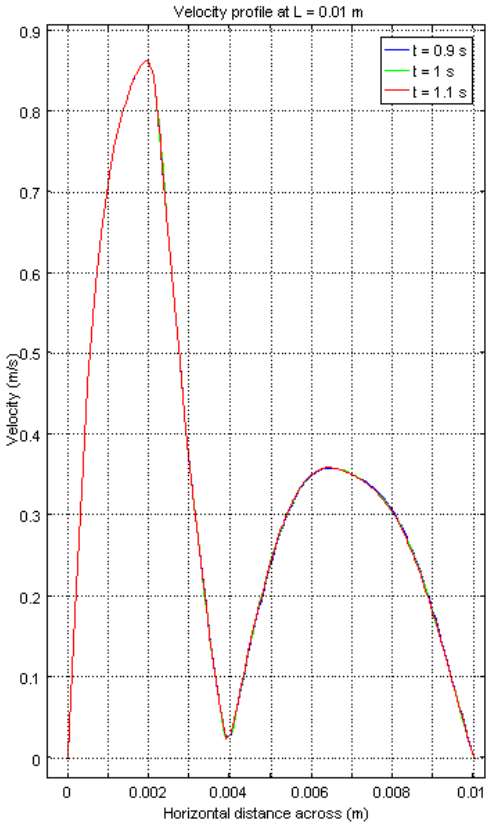

Figure 7.30: Graphical velocity profile at different study time from mesh B.

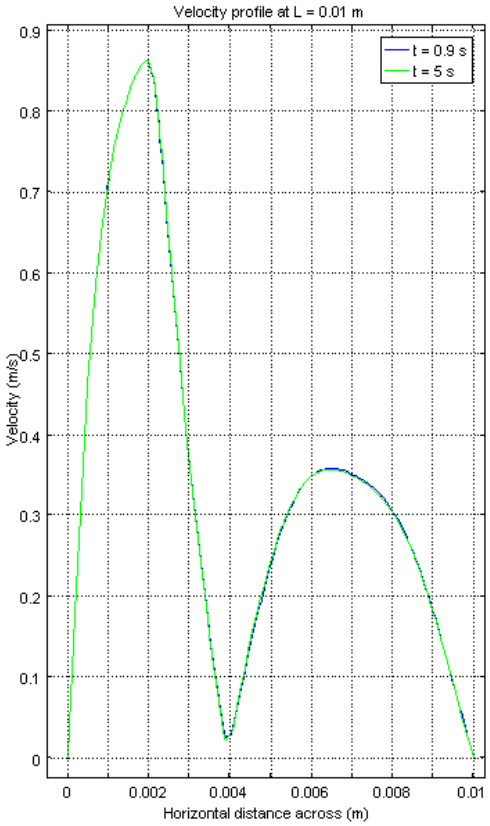

Figure 7.31: Graphical velocity profile at study time, t = 0.9 s and 5 s from mesh B.

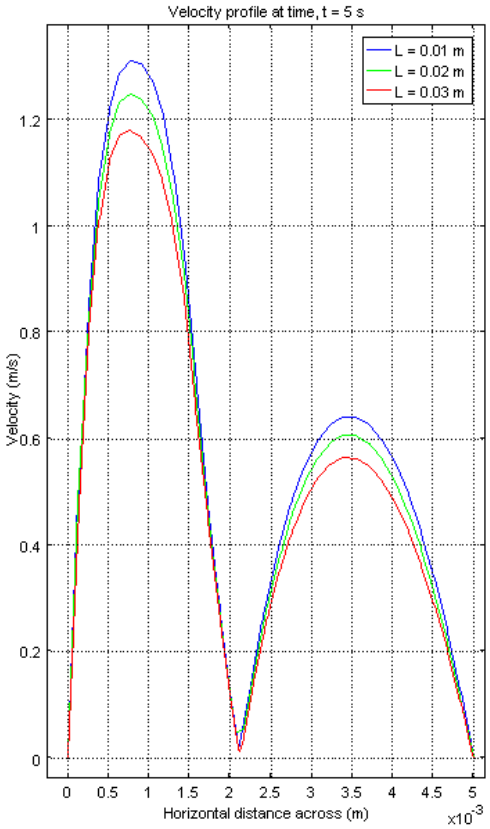

Figure 7.32: Graphical velocity profile at different lengths from mesh C.

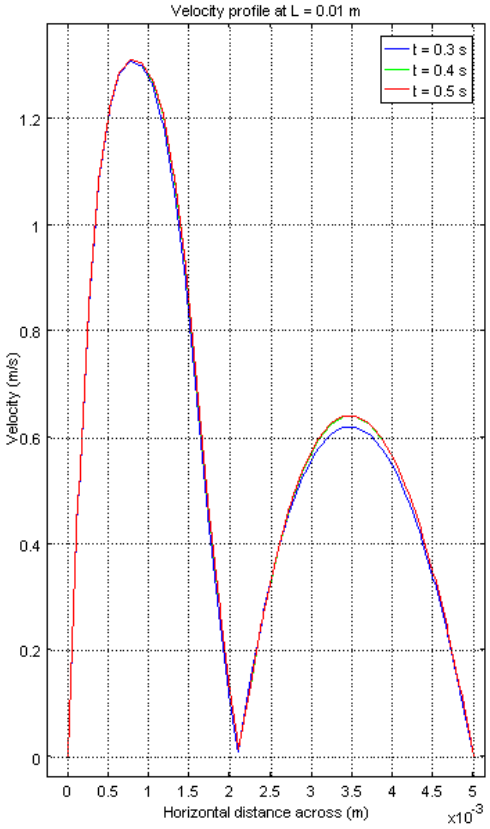

Figure 7.33: Graphical velocity profile at different study time from mesh C.

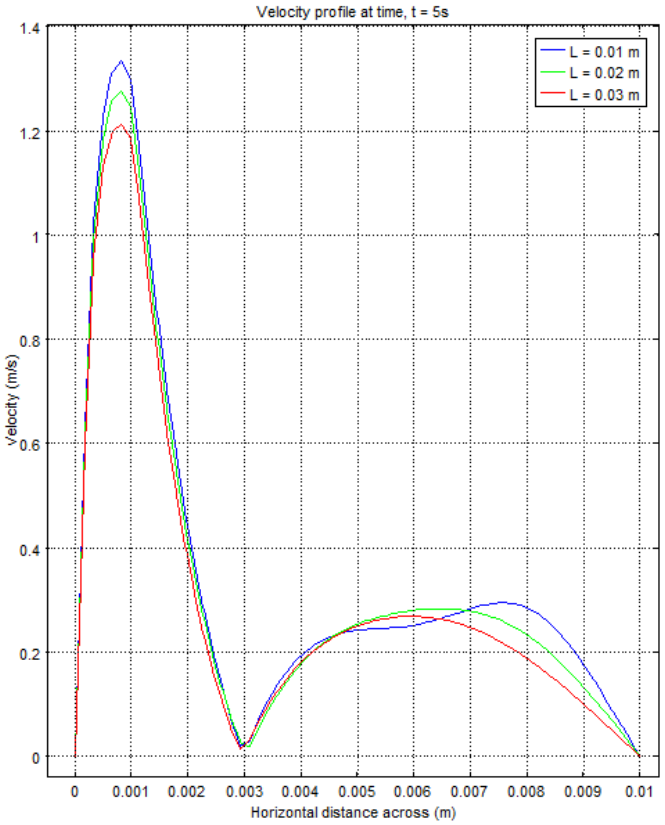

Figure 7.34: Graphical velocity profile at different lengths from mesh D.

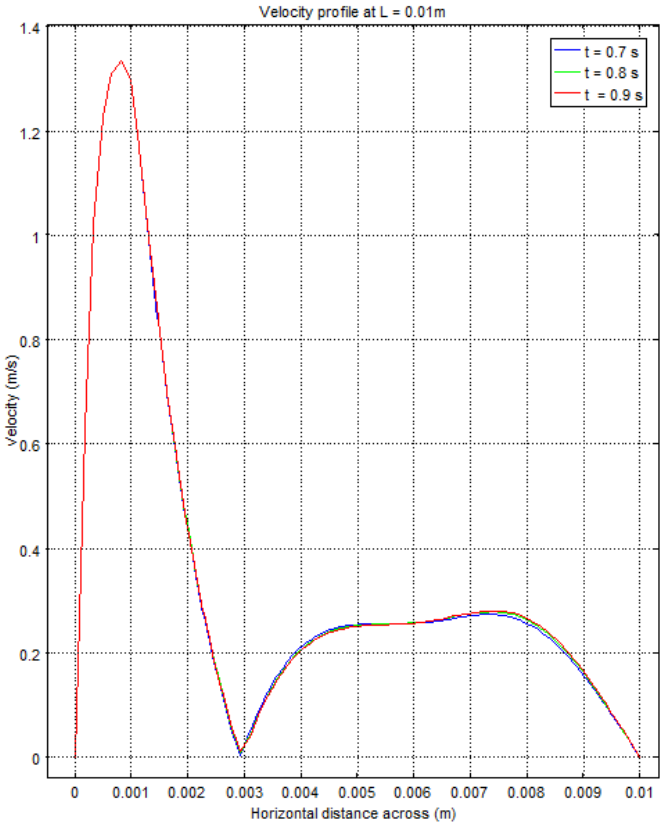

Figure 7.35: Graphical velocity profile at different study time from mesh D.

7.2. Discussion

COMSOL was used in the attempt to simulate the falling film flow of milk in a falling film evaporator. A simple 2D geometry design was used in these attempts where it consisted of two rectangles. The flow was constricted at the top in a smaller rectangle to simulate film flow and later flowed down into the larger rectangle.

The attempts made were using only water and air with their properties readily taken from COMSOL. Various meshes were used for determining the true solutions from the simulations. These various meshes used were also part of a 'grid independence test' to gauge the mesh elements' size so that the mesh used for simulations only have just the right element size. This is important to save computing time.

Altogether, four different types of meshes were used. These meshes were labeled A, B, C and D. Each of these meshes was different from each other in some way. Mesh A was the coarser of all the meshes while mesh D was the finer mesh overall.

Importance was placed in the meshes as the outcome solutions will be dictated by the meshes. Hence in some of the meshes, for example, mesh A and mesh C have more elements distributed to the left of Domain 1 as it was anticipated the complexities of the calculations will be in that vicinity.

To solve for and obtain solutions, COMSOL have to solve the various mathematical equations according to the type of physics chosen. It was decided that a two phase flow with the phase field method be used. With this method, COMSOL have to solve the Navier-Stokes equation together with the fourth-order Cahn-Hilliard equation. In solving this problem, the Cahn-Hilliard equation was broken down into two equations. In total, COMSOL will have to solve for three equations for this type of simulations.

The solving time will be greatly increased with the increased in the number of equations and with a more refined mesh. For example, mesh D which has 62,238 elements and element size of 0.0002 m overall took the longest time to solve.

The results from these simulations so far showed good agreement between the four types of meshes used. All solutions from the meshes indicated there were two types of flow occurring. The falling water film flows down into Domain 1 and induces the air initially in Domain 1 to flow upwards.

The results from using mesh A showed that the upwards air flow profile occurred near the film interface. As results from finer mesh B and C later showed this was not the case and that the air flow profile was actually parabolic just adjacent to the falling film.

Results from a more refined mesh D further showed that the air flow were actually small compared to the falling film flow. These results can be traced back to Figures 7.26 - 7.35 which showed the graphical velocity plot. These figures mentioned, showed the velocity magnitude only.

It should be mentioned that, these results arrived at were only pertaining to the physics set up in COMSOL. There was no vacuum added into the system and no heat transfer to cause evaporation of the falling film.

Other relevant properties added for defining the physics of the simulation was the surface tension (0.045 $N \cdot m^{-1}$) and the inlet velocity (0.5 $m \cdot s^{-1}$). These values were chosen because it was pre-calculated in a spreadsheet as the values likely to be for a 45% TS milk film flow into the tube of a 0.0478 m inner diameter.

One of the other important results that will be looking for from these simulations was if the velocity still changes down the length of the geometry and or changes with time. The total length of the geometry including Domain 2 was 0.102 m. For a fully developed, steady state flow, the flow velocity should not be changing with length and time when there was no evaporation.

Results from mesh C and D showed there were developing and developed flow regions where mesh A and B only able to showed a developed flow region. It was hard to justify the point where the developing region ends and the developed flow

region start from the present pen and paper calculations of the film thickness in Table 7.5.

The present simulations for all the meshes were time dependent studies. The time span of the studies was 5 seconds. It was found that the flow velocities do not change much with time. However as Figures 7.26, 7.29, 7.32 and 7.34 showed, there were changes in flow velocities with length of geometry even at L = 0.01 m. This meant that the flow was still developing.

Even with a more refined mesh such as mesh D, the solutions obtained were still quite different from the less fine or coarser meshes of A, B and C. The grid independence test will therefore still need to be carried out to determine the type of mesh where the solutions obtained no longer changes.

7.3. Conclusions

Many attempts were made to where the current results were reached. The availability of the phase field method in COMSOL provided the opportunity for simulating the falling film flow involving a moving interface.

The attempt to carry out simulation involving a moving interface was quite a difficult process. The use of the phase field method proves to be quite time consuming considering the size of the geometry used which was quite small.

A simulation into the problem involving a moving interface would present an independent research by itself. In the literatures, two papers were sighted which use the CFD approach to simulate similar problems.

Instead of using COMSOL, the authors to these papers use a different CFD package with additional algorithms. Haeri and Hashemabadi (2008) used a version of VOF family of algorithms named CICSAM to track the air-liquid interface with the

OpenFOAM 1.3 CFD package. Sutalo et al. (2006) used CFX-4 with a homogeneous multiphase model and surface-sharpening algorithm. They claimed the CFD model was able to predict the fluid film thicknesses and flow patterns accurately.

However in all of the attempts, information was obtained about a typical falling film flow with the current method of simulations. There are many opportunities available where this part of research could benefit from further improvements.

The Heat Transfer physics interface could be coupled with the Two Phase Flow physics to include the heat transfer phenomena. An equation model relating the film thickness could be added into the simulation so that the film thickness could be calculated instantaneously.

A *grid independence* test will need to be carried out to obtain consistent results from the simulation. Several other possible improvements include improving the mesh with better meshing techniques, replacing water with milk, using longer geometry or different design of geometry.

8. Results

This chapter of the results presents the various results from the research. Here, some of the results from other chapters will be compiled together to give an overall view of the results. Some results obtained from spreadsheet calculations will also be made available here.

8.1. Rheological parameters

In chapter four, several shear stress - shear rate data were obtained for different total solids of milk. As a result, the rheological parameters and the relationships with total solids were found. These relationships derived were from the experimental results and were empirical models. At that moment, the models were valid for the range of total solids from 19.93% to 62.09%.

In chapter five, the age thickening experiments were performed for milk from 35.47% to 49.25% total solids. This range of total solids supplements the lack of data in between the ranges of total solids from earlier experiments. Additional rheological parameters were obtained for this range of total solids.

All these rheological parameters were combined together and the models previously developed re-evaluated. In total there were 15 data sets and the overall range of total solids were still from 19.93% to 62.09%. A full list of the total solids and the milk used together with the temperature it was measured can be referred to in Table 3.1 of Chapter Three.

Flow behavior index

All the results obtained for the flow behavior index were plotted against the total solids. Two other models from the literatures were added. For comparison, the model previously developed was also added. This was presented in Figure 8.1.

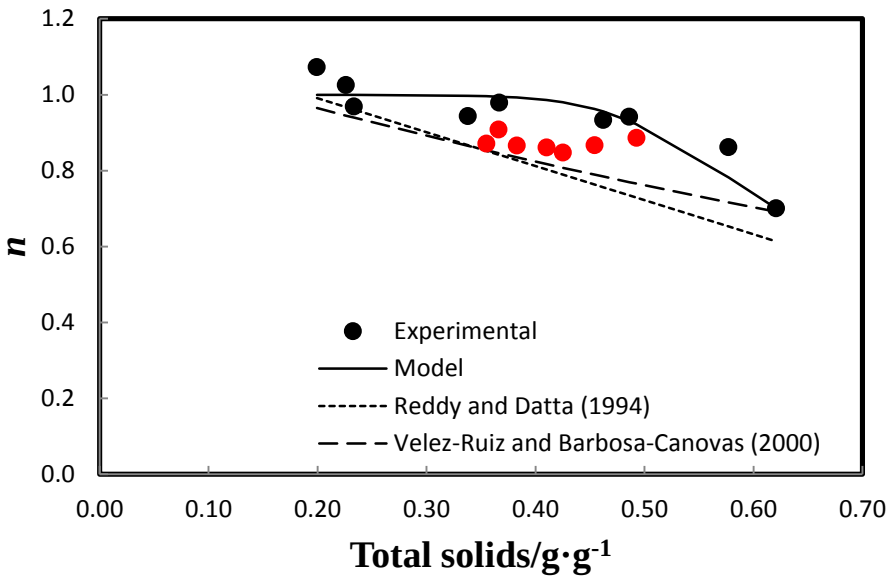

Figure 8.1: Flow behavior index for total solids in the range 19.93% to 62.09%.

With the additional data from the range of 35.47% to 49.25% total solids (coloured in red), the change in the flow behavior index with total solids was unexpectedly different from the model developed.

One difference between the data from the 35.47% - 49.25% TS range and the data from the 19.93% - 62.09% TS range was the temperature the data was measured.

The extra data showed that the flow behavior index decreases linearly with increasing total solids. However, the two models from the literatures were not in the range of the experimental results.

Consistency factor

The previous plot of consistency factor versus total solids was re-plotted again here with the extra data from the range of 35.47% to 49.25% total solids (coloured in red). It can be seen that the model previously developed for the consistency factor slightly under predicted the overall experimental results.

With the additional data, it can be seen that the consistency factor increases earlier than the model predicted (Figure 8.2).

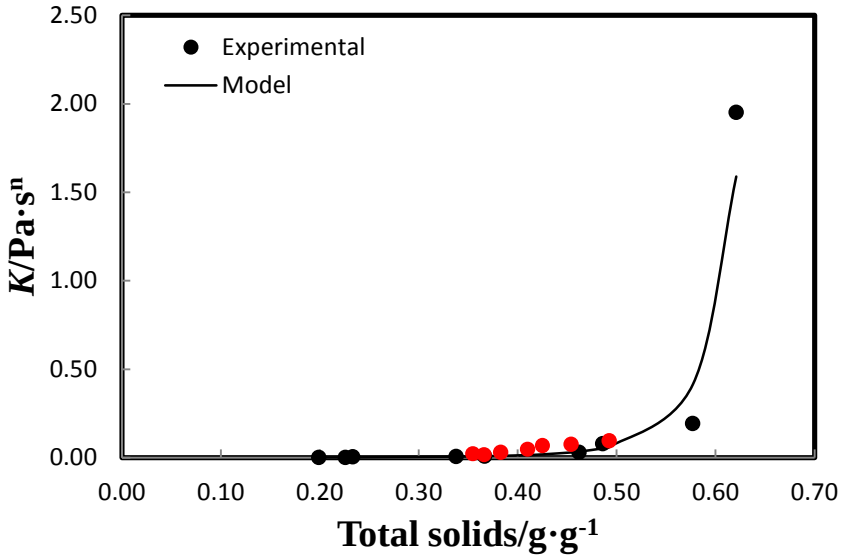

Figure 8.2: Consistency factor for total solids in the range 19.93% to 62.09%.

Yield stress

Figure 8.3 depicts the experimental as well as the model yield stress for the range of total solids from 19.93% to 62.09%. The data points coloured in red are the data from 35.47% to 49.25% total solids.

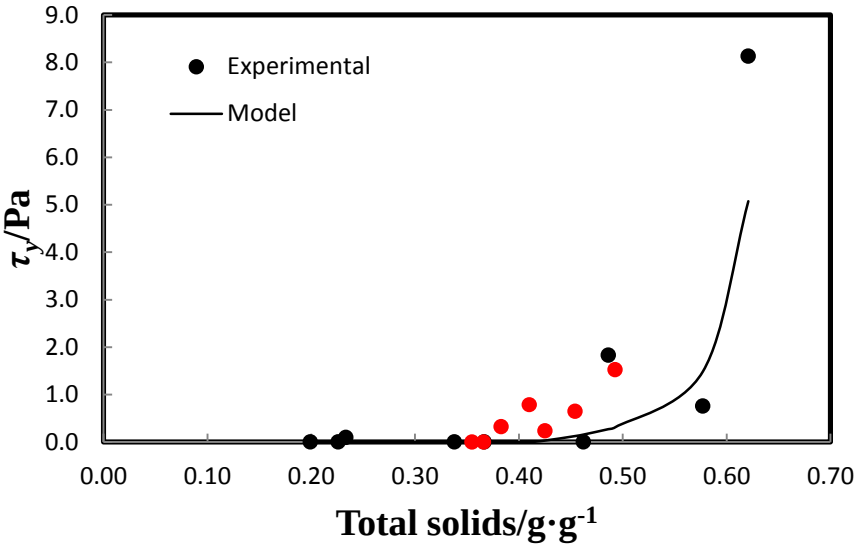

Figure 8.3: Yield stress for total solids in the range 19.93% to 62.09%.

This overall result showed that the yield stress for milk increased earlier than was predicted by the model.

8.2. Spreadsheet calculations results

Several calculations were done on Excel spreadsheets and presented in this section are the results obtained from the calculations. In performing the calculations, several factors or constants were given arbitrary values.

The results presented here unless otherwise stated are results when the arbitrary values shown in Table 8.1 were used:

Table 8.1: The arbitrary values used in spreadsheet calculations.

Total solids in (TS_{in}/g·g^{-1})	0.45
Wetting rate (Γ/kg·m^{-1}·s^{-1})	0.3
Temperature difference (ΔT /°C)	6
Temperature of milk (T_{milk}/°C) where ΔT_b is the boiling point elevation.	54 + ΔT_b
Total length of tube (L/m)	15
Inner diameter of tube (D_i/m)	0.0478

The overall heat transfer coefficient was interpolated and extrapolated from U_{50} = 1 kW/m^2°C at 50% TS and U_{60} = 0.5 kW/m^2°C at 60% TS. Each calculation down the tube length was done with element size, Δz of 0.1 m. The sample calculations done were attached in the appendices. Some of these calculations were based on the equations or formulas sought from the literatures.

8.2.1. Rheological parameters

The rheological models developed earlier were included into the spreadsheet calculations. As milk is non-Newtonian at high total solids, these models were important to help with the calculations.

Figures 8.4 to 8.6 show the changes of rheological parameters according to the change in total solids of milk as it flows down the tube. With the total solids in (TS_{in}) at 0.45, the figures show the changes from the top to bottom of the tube.

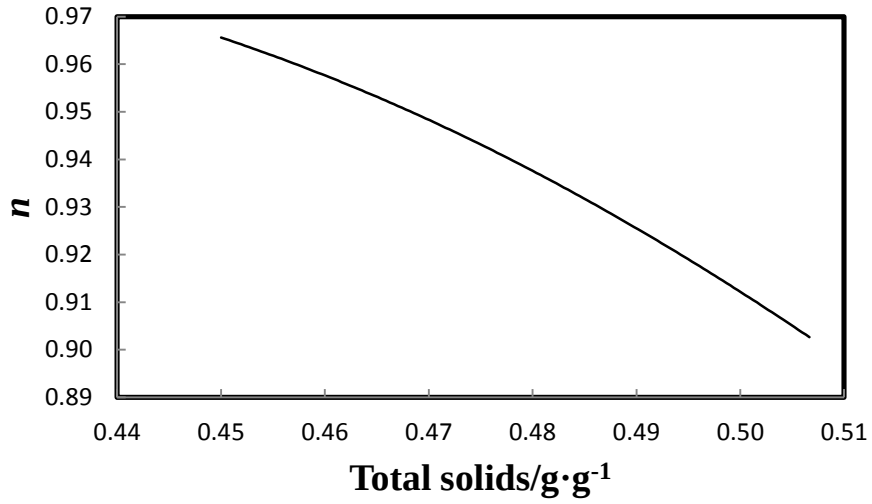

Figure 8.4: The flow behavior index model of falling milk film down the tube.

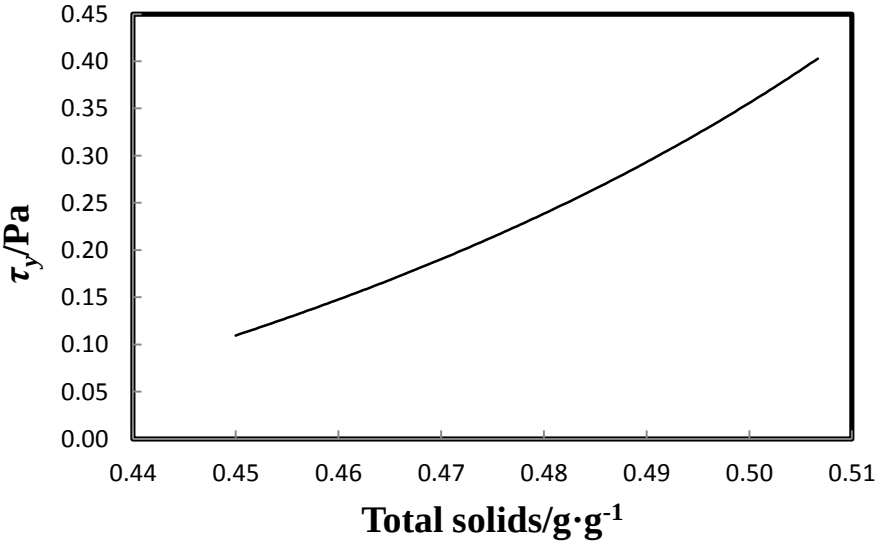

Figure 8.5: The yield stress model of falling milk film down the tube.

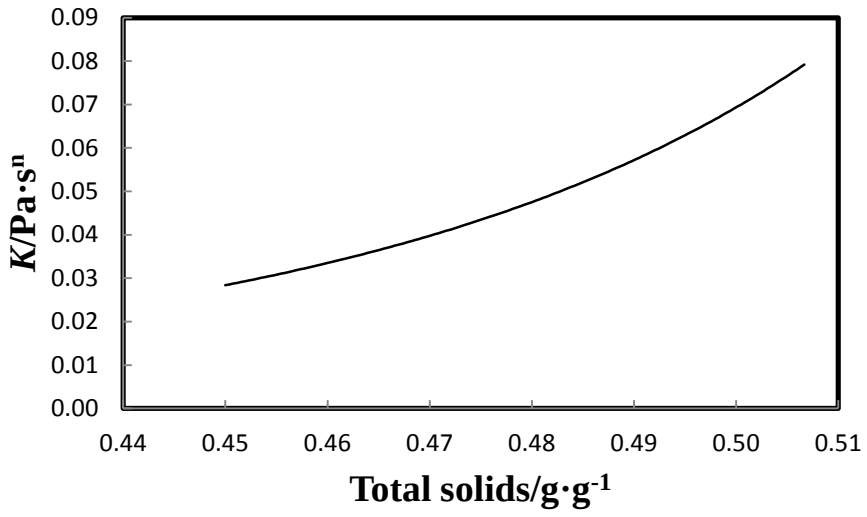

Figure 8.6: The consistency factor model of falling milk film down the tube.

A separate analysis on the yield stress and the effect of the wetting rate was presented as a result in Figure 8.7. This result show the particular yield stress at the tube exit and that at the wetting rate of less than 0.15 $kg \cdot m^{-1} \cdot s^{-1}$, a noticeable exponential increase in the yield stress was noted.

It should be noted that this yield stress was calculated from the yield stress model developed earlier and not data obtained from experiments.

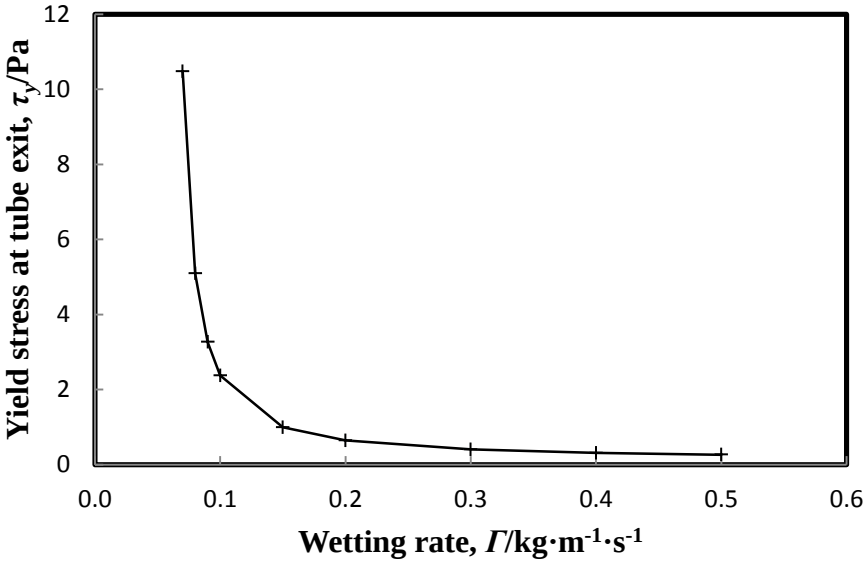

Figure 8.7: The effect of wetting rate on the yield stress at tube exit.

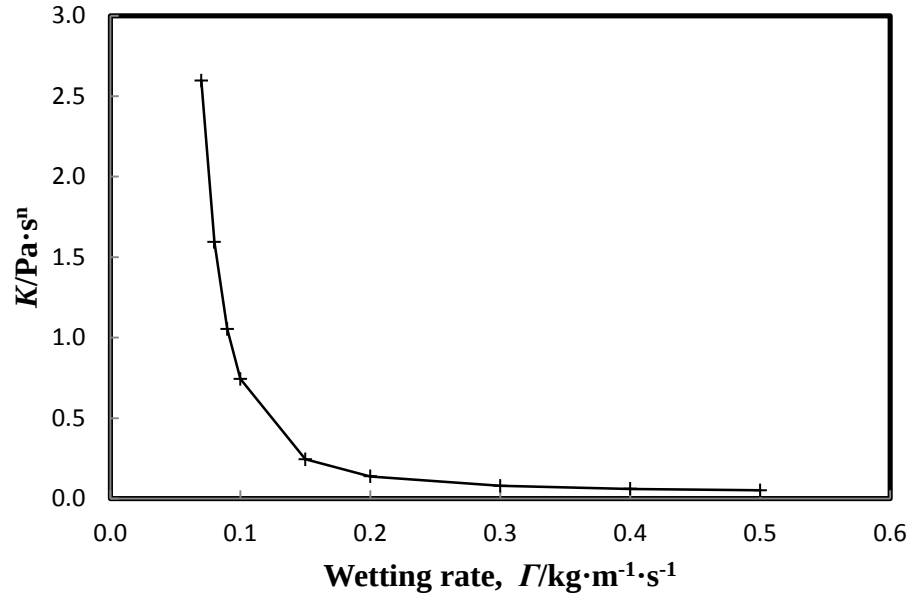

Figure 8.8: The effect of wetting rate on the consistency factor at tube exit.

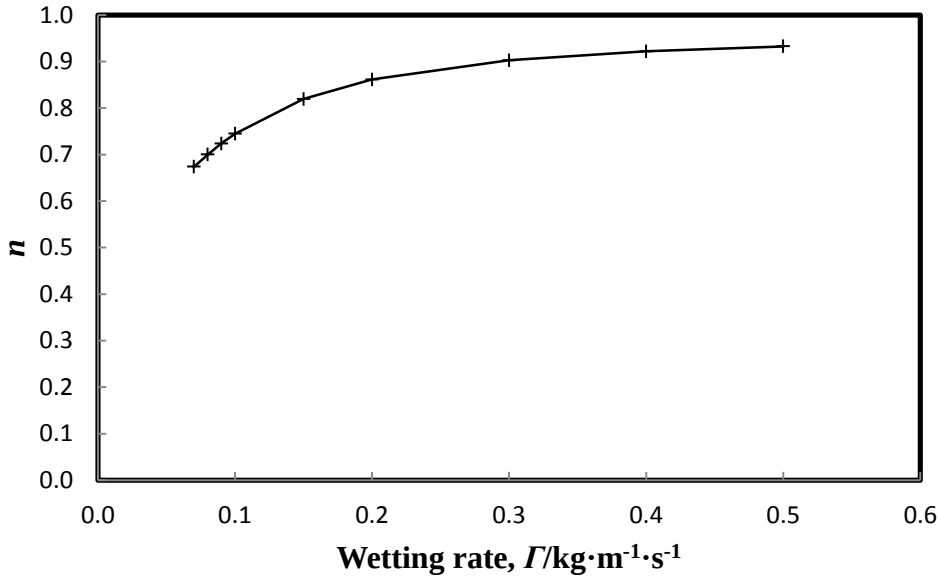

Figure 8.9: The effect of wetting rate on the flow behavior index at tube exit.

8.2.2. Wetting rate

The wetting rate was set at 0.3 $kg \cdot m^{-1} \cdot s^{-1}$ upon entering the tube. Due to evaporation, the actual wetting rate decreases as the milk continues to flow down the tube. Figure 8.7 show the decrease in the wetting rate as it would be as the milk film flows down the tube.

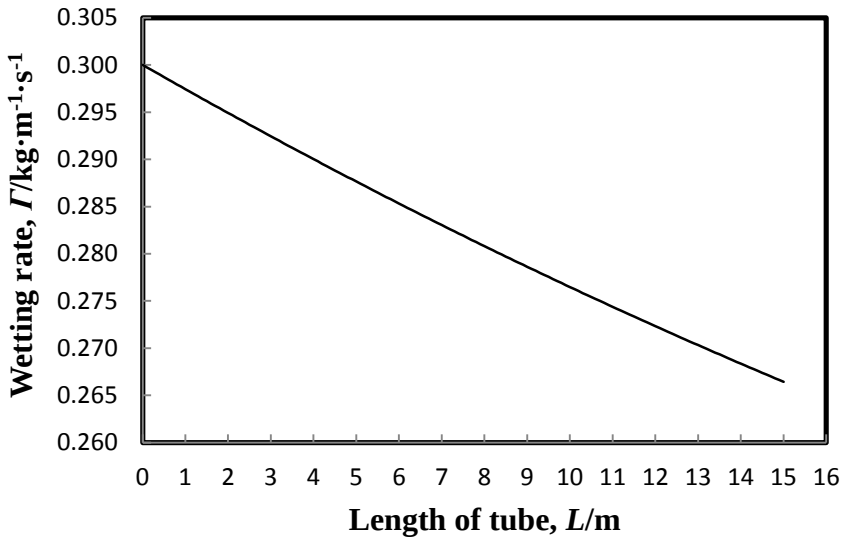

Figure 8.10: The actual changes of wetting rate down the tube.

8.2.3. Wall shear stress

The wall shear stress was calculated using the formula,

$$\tau_w = \rho g \delta_2$$

With everything else except the film thickness, δ_2, changing significantly, the wall shear stress increases as the film thickness, δ_2, increases.

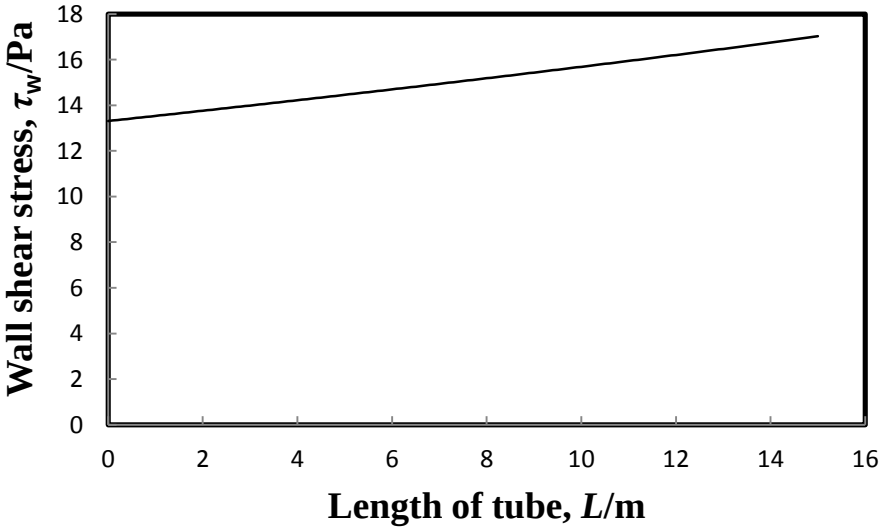

Figure 8.11: The change of wall shear stress down the tube.

8.2.4. Shear rate at $x = \delta_2$

The shear rate for the milk flow in the tube was calculated using the formula,

$$\tau_y + K\dot{\gamma}^n = \rho g x$$

$$\dot{\gamma} = \left(\frac{\rho g \delta_2 - \tau_y}{K} \right)^{1/n}$$

where K, τ_y and n are the consistency factor, yield stress and flow behavior index. The film thickness was denoted by δ_2.

The shear rate was calculated based on the position $x = \delta_2$. As the film thickness will increase down the tube, the position of x will also be changing down the tube. The shear rate calculated therefore is not fixed to a particular position.

This calculation shows that the shear rate for milk decreases down the length of tube where all other factors such as evaporation, boiling point elevation were already accounted for.

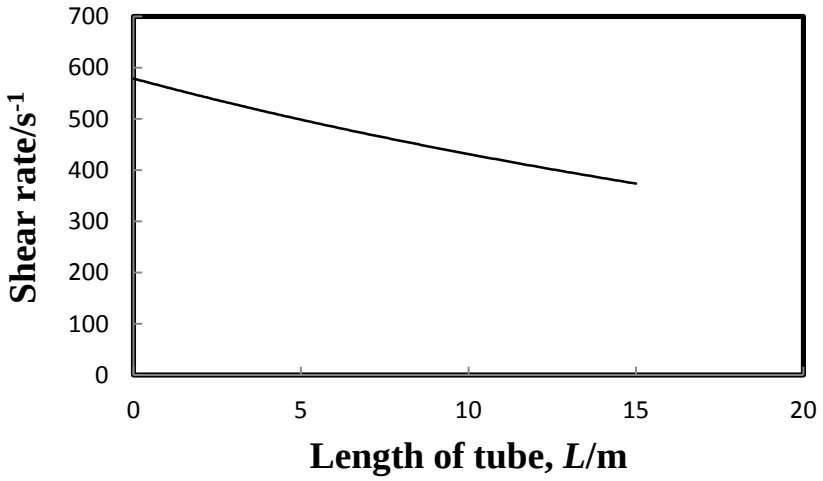

Figure 8.12: The change of shear rate down the tube.

8.2.5. Viscosity

Two methods were used to calculate the viscosity. Viscosity 1 in Figure 8.10 was calculated as

$$\eta_a = \frac{\tau}{\gamma}$$

where the shear stress and shear rate were calculated as mentioned in sections 8.2.3 and 8.2.4.

The viscosity 2 was calculated using modified equation of Bloore and Boag (1981) by Jebson and Chen (1997). This equation was equation (2.49) as reviewed in Chapter Two.

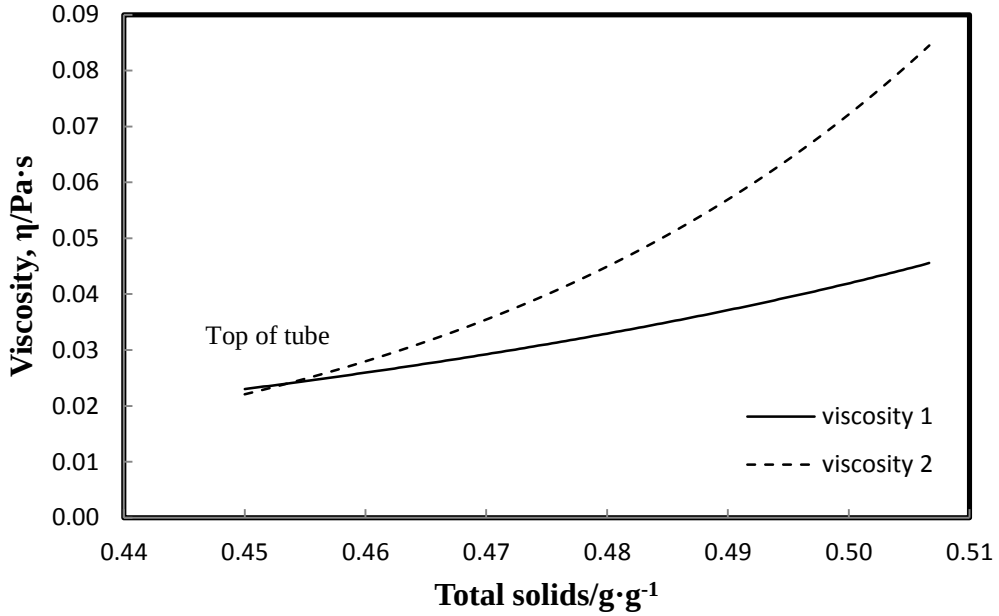

Figure 8.13: Two different calculated viscosities.

It should be noted that the viscosity calculated in viscosity 2 is dependent on the milk temperature and total solids and not dependent on the shear rate which is important for a non-Newtonian type fluids.

8.2.6. Density, Surface tension, Thermal conductivity and Specific heat

The thermal conductivity, specific heat and density were calculated using functions, 'MilkThermalConductivity', 'MilkCp' and 'MilkDensity' respectively. Figures 8.11 to 8.13 show these changes down the tube length.

The surface tension on the other hand was calculated based on the equation (see Appendix F),

$$\sigma = \left(\frac{-0.17T_{milk} + 55}{1000} \right)$$

where T_{milk} is the milk temperature in °C. Figure 8.14 show the changes of the surface tension down the tube length.

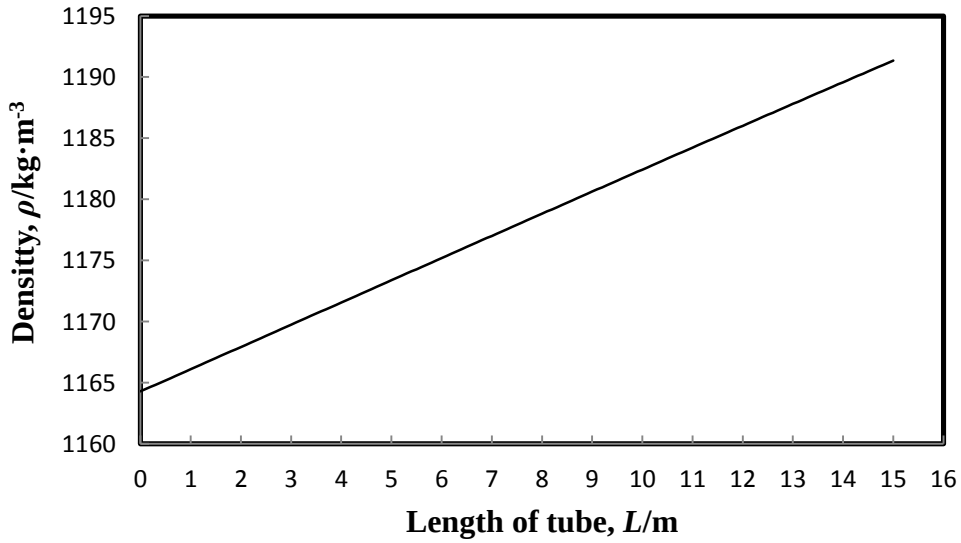

Figure 8.14: The changes of milk density down length of tube.

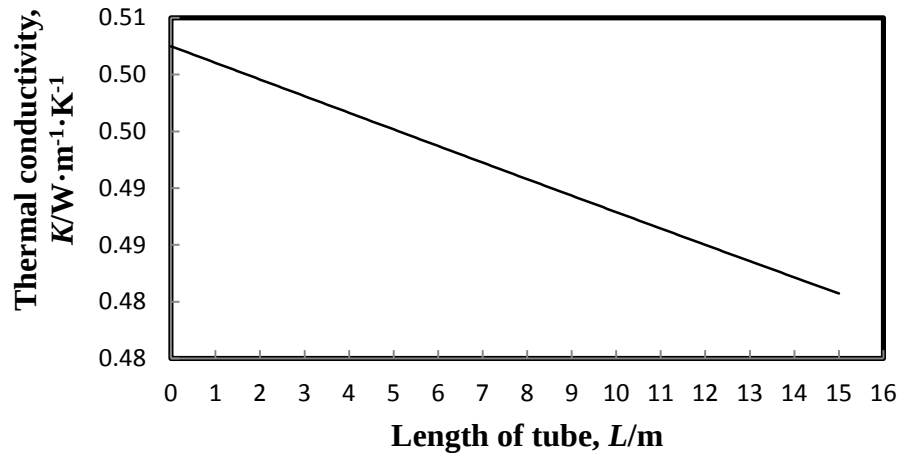

Figure 8.15: The changes of milk thermal conductivity down length of tube.

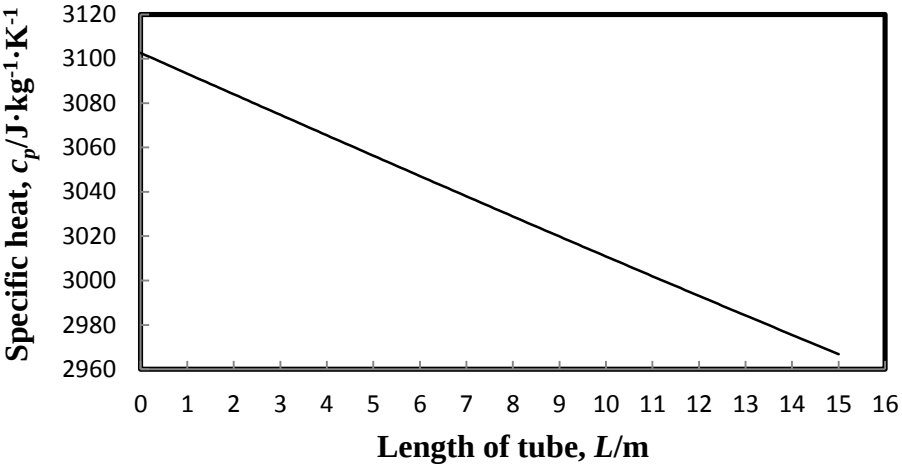

Figure 8.16: The changes of milk specific heat down length of tube.

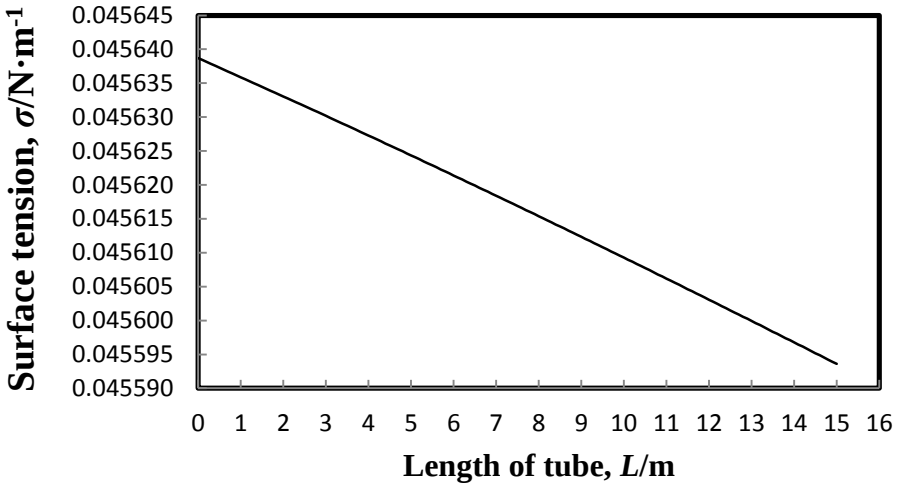

Figure 8.17: The changes of milk surface tension down length of tube.

8.2.7. Residence/retention time

The residence time was calculated based on the equation,

$$t = \frac{\Delta z}{\mathrm{v}_{ave}}, \text{ where } \mathrm{v}_{ave} = \frac{\dot{m}}{\rho A}$$

where the tube was divided into element height, Δz and v_{ave} is the average velocity in the element. For sample calculations go to Appendix F. Figure 8.18 show the residence time profile.

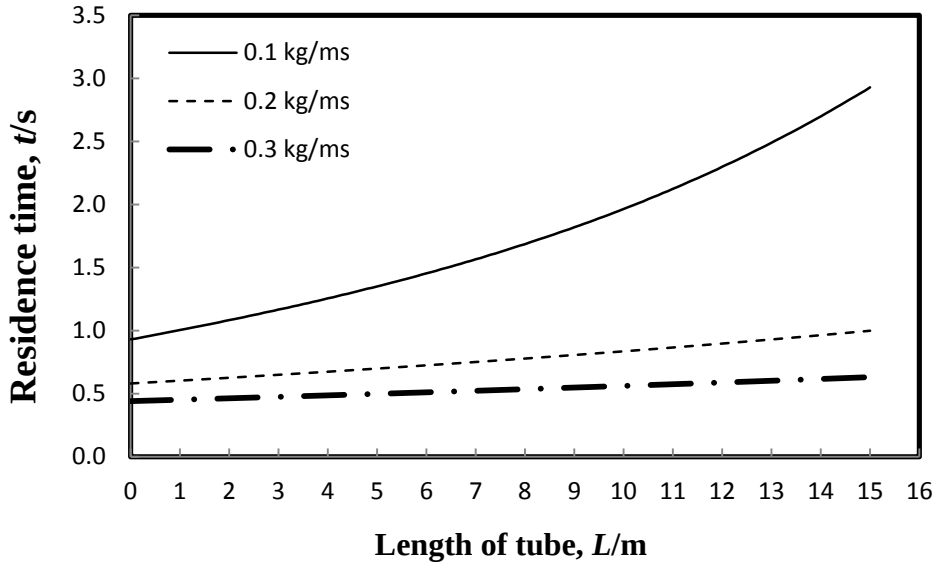

Figure 8.18: The residence time profile of milk film flow down a tube for different wetting rate.

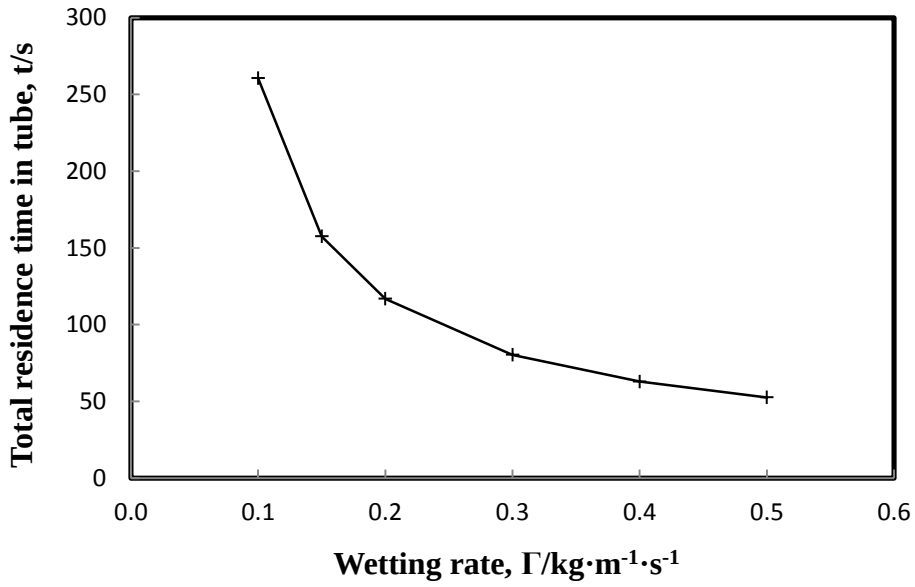

Figure 8.19: The effect of wetting rate on the overall residence time of film flow.

For a 15 m tube, the total time milk film flow in the tube was longer for any wetting rate lower than 0.5 $kg \cdot m^{-1} \cdot s^{-1}$. The time spent could increased up to 260 s (4.33 minutes) when the wetting rate is 0.1 $kg \cdot m^{-1} \cdot s^{-1}$ and could lead to tube blockage if the wetting rate reduced further.

8.2.8. Dimensionless numbers

Several dimensionless numbers were calculated for the milk film flow down the tube. These include the Reynolds number, Kapitza number, Prandtl number and Boiling number.

Figure 8.20 show the change of Prandtl number with Reynolds number while Figure 8.21, the change of Reynolds number with Kapitza number.

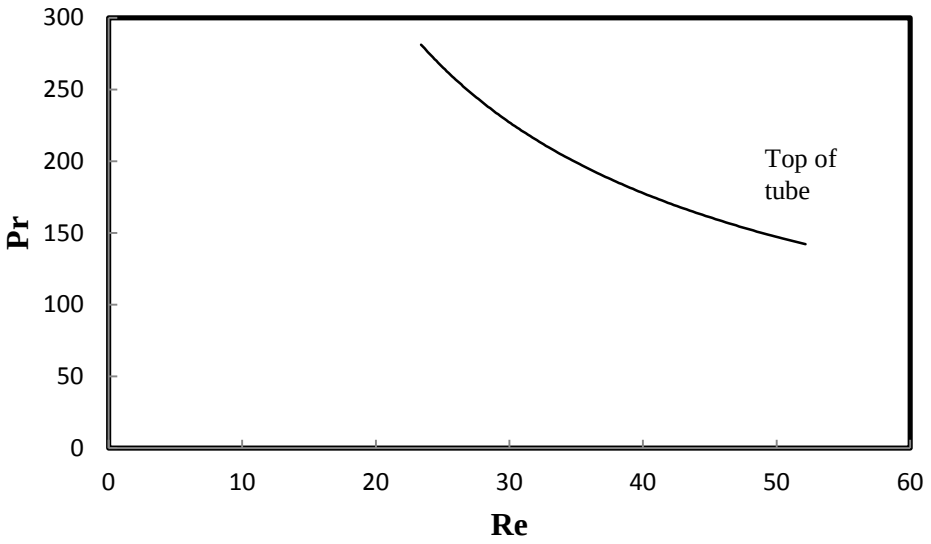

Figure 8.20: The change of Prandtl number with Reynolds number.

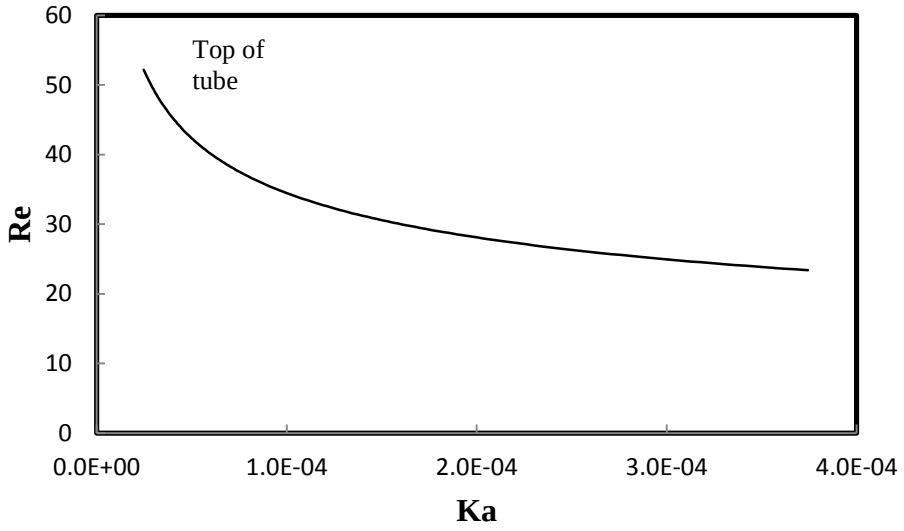

Figure 8.21: The change of Reynolds number with Kapitza number.

The equation (2.19) reviewed in Chapter Two of the Literature Review was calculated in the spreadsheet for the conditions as stated earlier. This was to determine if nucleate boiling had occurred with the present conditions. For nucleate boiling to occur, the $Bo \times Ka^{1/11}$ number needs to be 1×10^{-5} or 10^{-6}.

This calculation show that nucleate boiling does not occur at the present conditions.

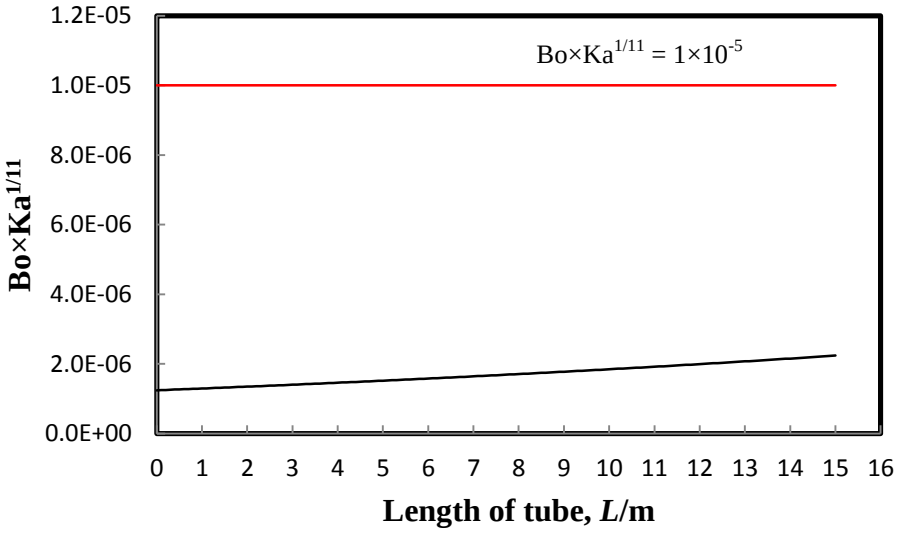

Figure 8.22: The calculated Bo×Ka1/11 number for film flow down the tube.

8.2.9. Boiling point elevation

It was anticipated that the boiling point elevation, BPE, would present some significant effect on the film flow. The boiling point elevation was calculated based on typical dry basis of skim milk composition (see Appendix G).

Figure 8.23 shows that the BPE increased up to about 1 K at about 43% total solids.

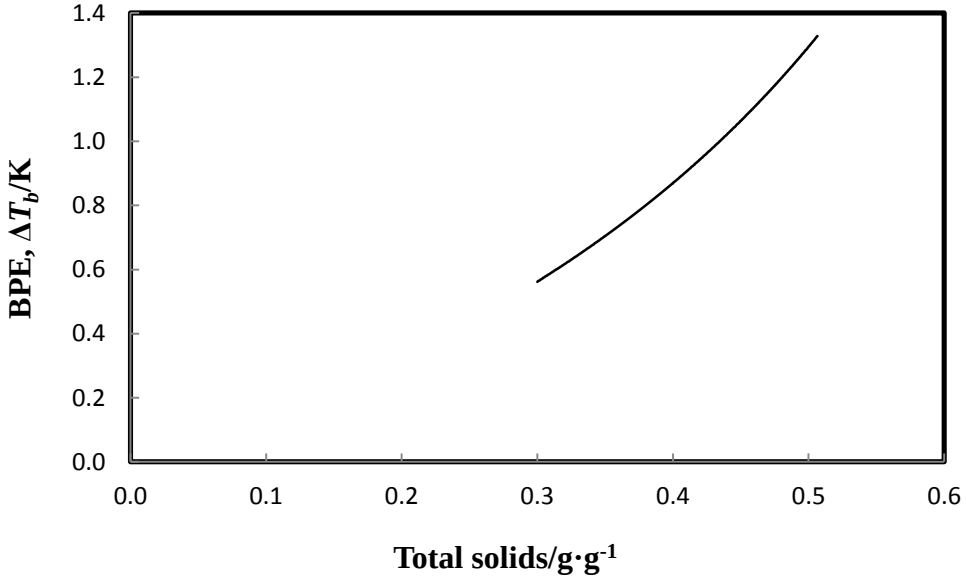

Figure 8.23: The calculated boiling point elevation of milk.

8.2.10. Total solids

The total solids for the film flow were calculated for every element size, Δz, down the tube. The total solids profile for milk and the total solids profile at the interface are presented together in Figure 8.24 for a wetting rate of 0.3 $kg \cdot m^{-1} \cdot s^{-1}$.

The total solids at the interface were calculated based on Wadekar's mixture effect with slight modification. Wadekar's equation (2.45) for solute concentration at the interface was calculated to be more accurate for water instead. The solute concentration at the interface (or total solids) was then taken to be the value of 1 minus the value calculated from equation (2.45).

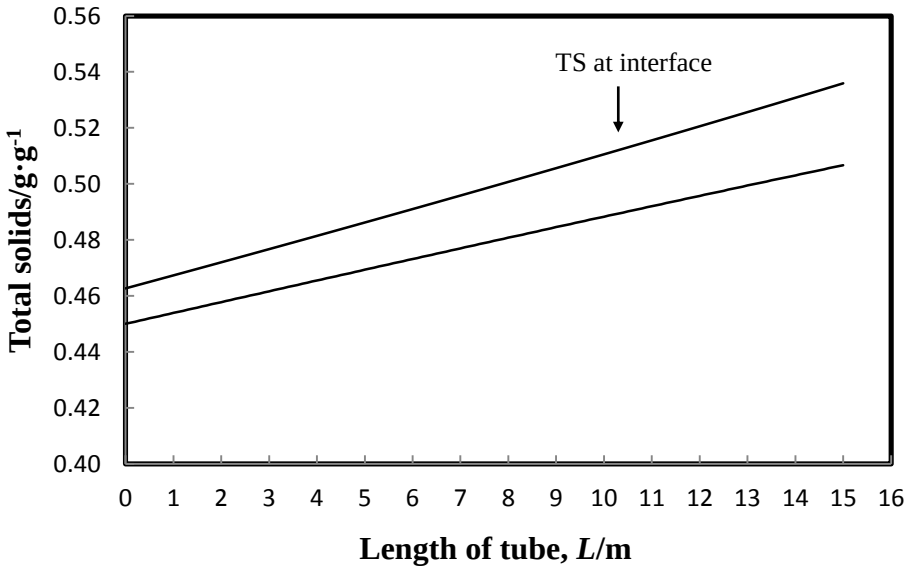

Figure 8.24: Profiles of total solids for wetting rate at 0.3 kg•m-1•s-1.

Figure 8.25 show the different total solids profile for different wetting rates while Figure 8.26 show the different total solids obtained at tube exit for different total solids in (TS_{in}) and wetting rates (Γ).

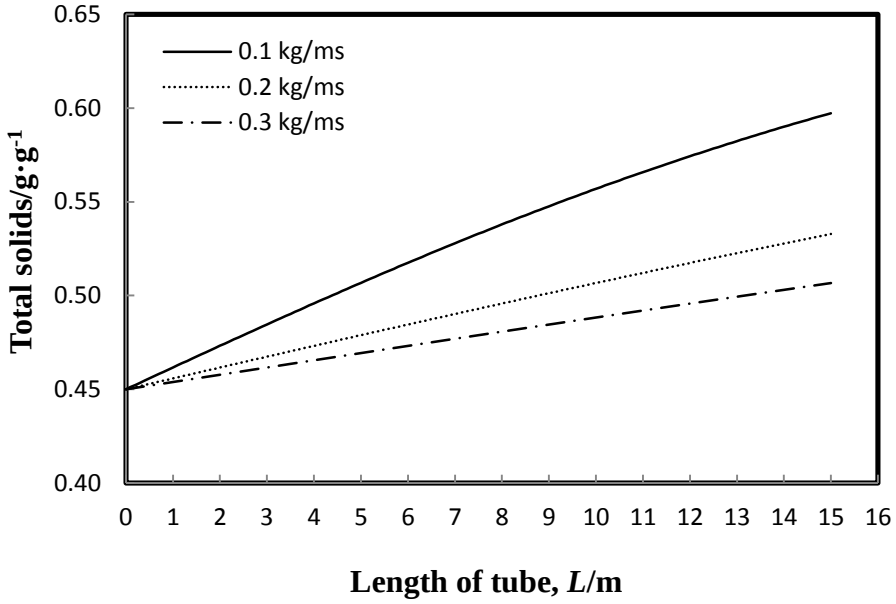

Figure 8.25: Total solids profile of milk film flow down the tube.

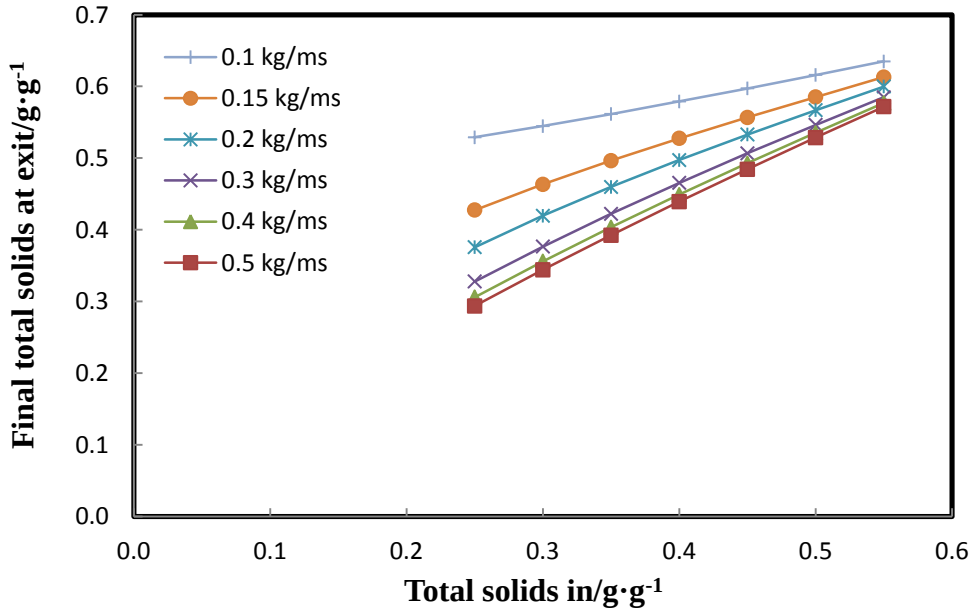

Figure 8.26: The final total solids at exit at various TS_{in} and wetting rate.

The results from Figure 8.26 showed that for any higher total solids in (TS_{in}), the final total solids out from the tube can't be increased anymore regardless of any lower wetting rates.

If the wetting rate is low the outlet solids content could be high enough to cause excessive fouling and possibly tube blockage.

8.2.11. Film thickness

For results and analysis of film thickness, see Chapter Six.

The final film thickness at the tube exit and factors affecting it were analyzed and presented in Figures 8.27 to 8.29. The final film thickness at the tube exit may be affected by the total solids in (TS_{in}) and the temperature difference, ΔT.

It was found that at a wetting rate of 0.2 $kg \cdot m^{-1} \cdot s^{-1}$ the final film thickness was at the minimum. For the range of wetting rates (Γ), temperature difference (ΔT) and total solids in (TS_{in}), the film thickness did not exceed 0.0239 m (tube radius) and therefore does not cause blockage.

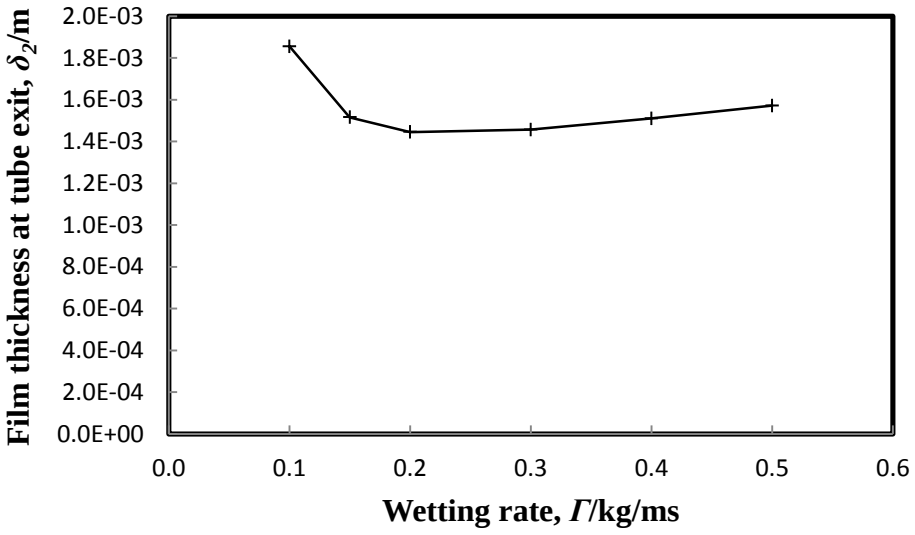

Figure 8.27: The effect of wetting rates on the film thickness, δ_2, at tube exit.

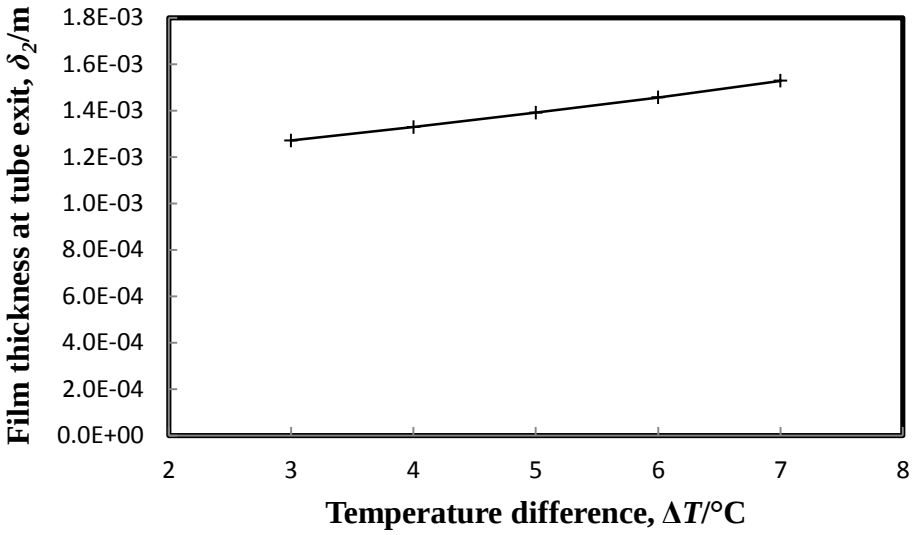

Figure 8.28: The effect of temperature difference, ΔT, on film thickness, δ_2, at tube exit.

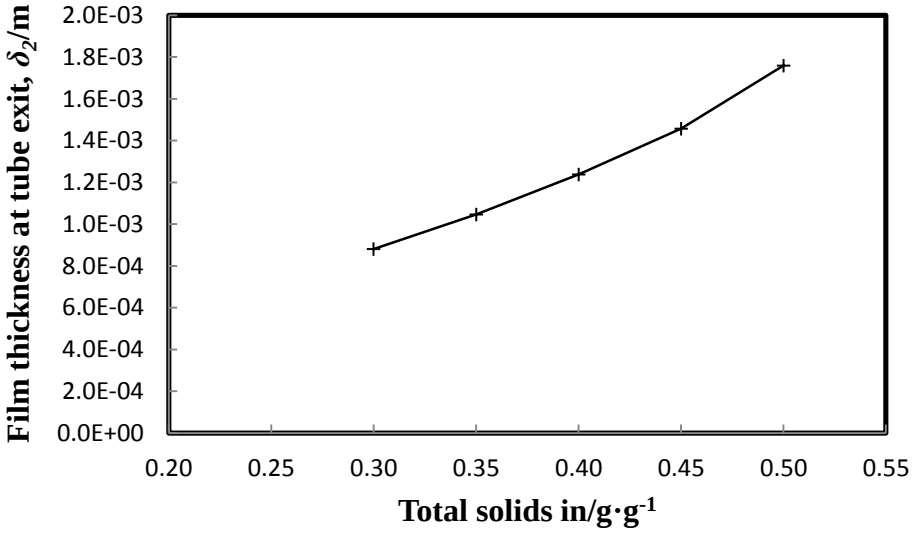

Figure 8.29: The film thickness at tube exit for various total solids in (TS_{in}).

8.2.12.Velocity

For results and analysis of velocity, see Chapter Six.

As milk is non-Newtonian at high total solids, the rheological parameters may have an important role in the film flow. To study their significance on film flow (velocity), the various rheological parameters, flow behavior index (n), consistency factor (K) and yield stress (τ_y) were each varied while others kept the same.

In the Figures 8.30 to 8.32, the velocity shown was the velocity of milk flow in the tube while it is at length, L = 7m, that is at mid-way down the tube. Both the x and y axes were inverted to give a true impression of the film flow.

The figures shown are the velocity profiles without the end boundaries such as near the wall and near the film interface.

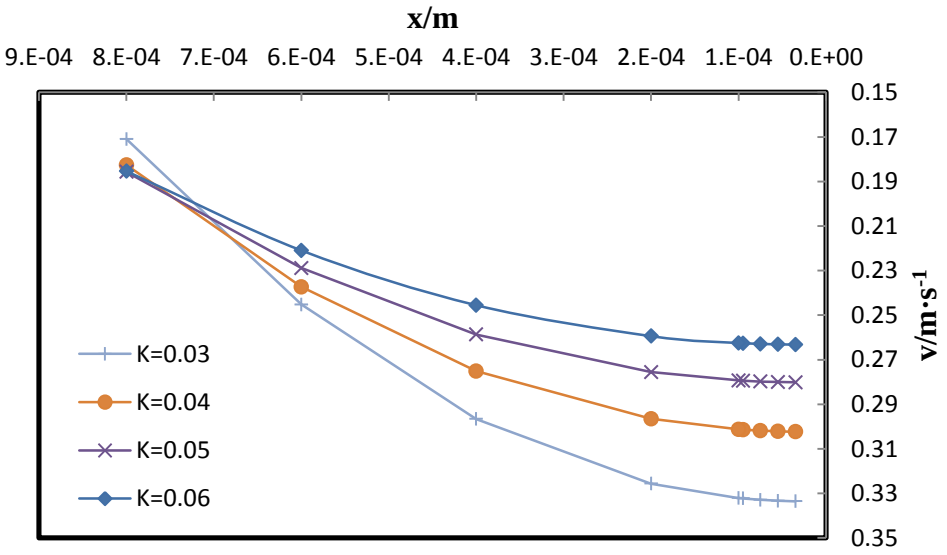

Figure 8.30: The velocity profiles when the consistency factor was varied.

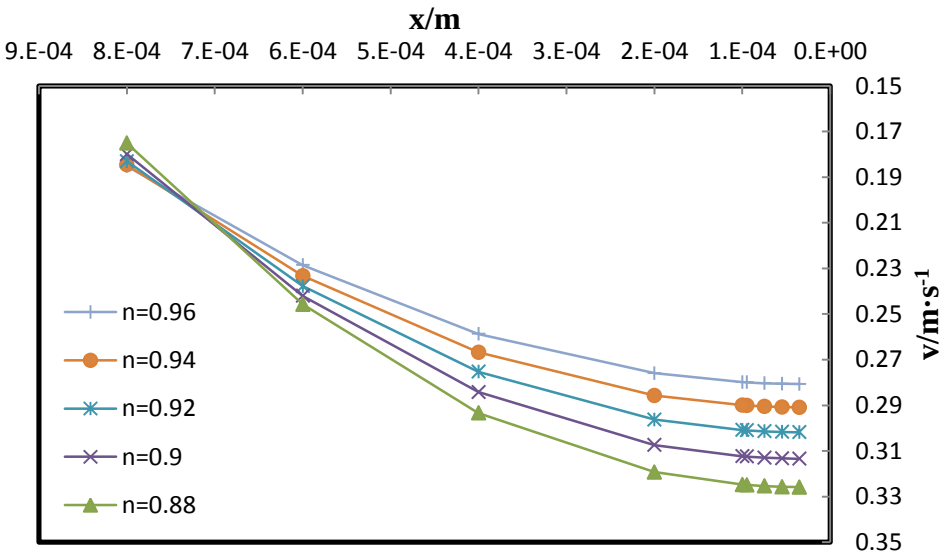

Figure 8.31: The velocity profiles when the flow behavior index was varied.

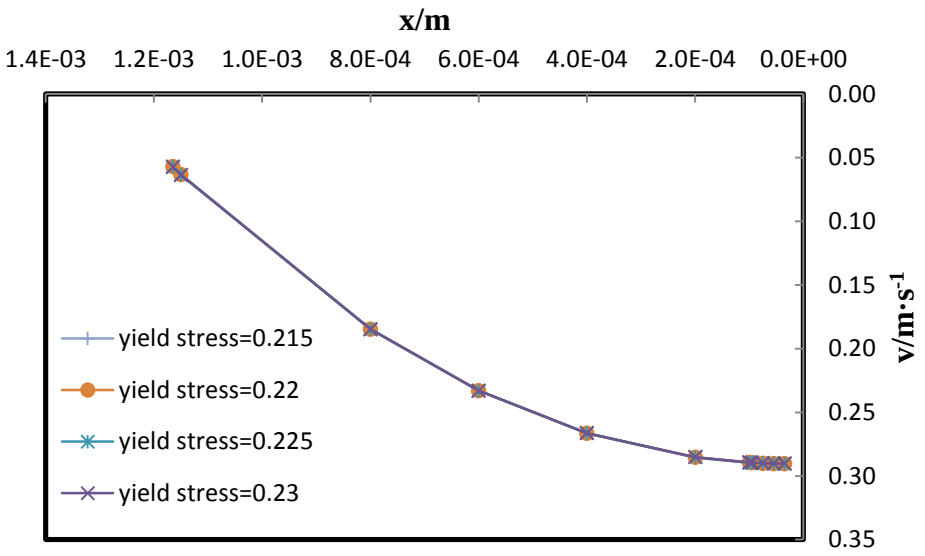

Figure 8.32: The velocity profiles when the yield stress was varied.

8.2.13. Heat transfer coefficients

Some heat transfer coefficients were calculated for the milk flow down the tube. These were calculated from the correlations available in literatures. Some of the correlations used were previously reviewed in Chapter Two of Literature Review. These equations were equation (2.16), (2.34) and (2.42).

These equations/correlations were in dimensionless form and were converted into heat transfer coefficients with units of $W \cdot m^{-2} \cdot K^{-1}$.

Wadekar and Hills (2001) proposed that if the wall temperature rather than the heat flux is known the equation below can be used in place of equation (2.46).

$$\alpha_{lm} = \alpha_{epf}\left(1 - \frac{\Delta T_m}{T_w - T_{bub(x_b)}}\right)$$

For calculations, the wall temperature was set to T_{wall} = 61°C and the heat transfer coefficient for equivalent pure fluid, α_{epf} substituted by Chun and Seban's equation. For sample calculations, go to Appendix F. Figure 8.31 show the calculated heat transfer coefficients from these equations/correlations.

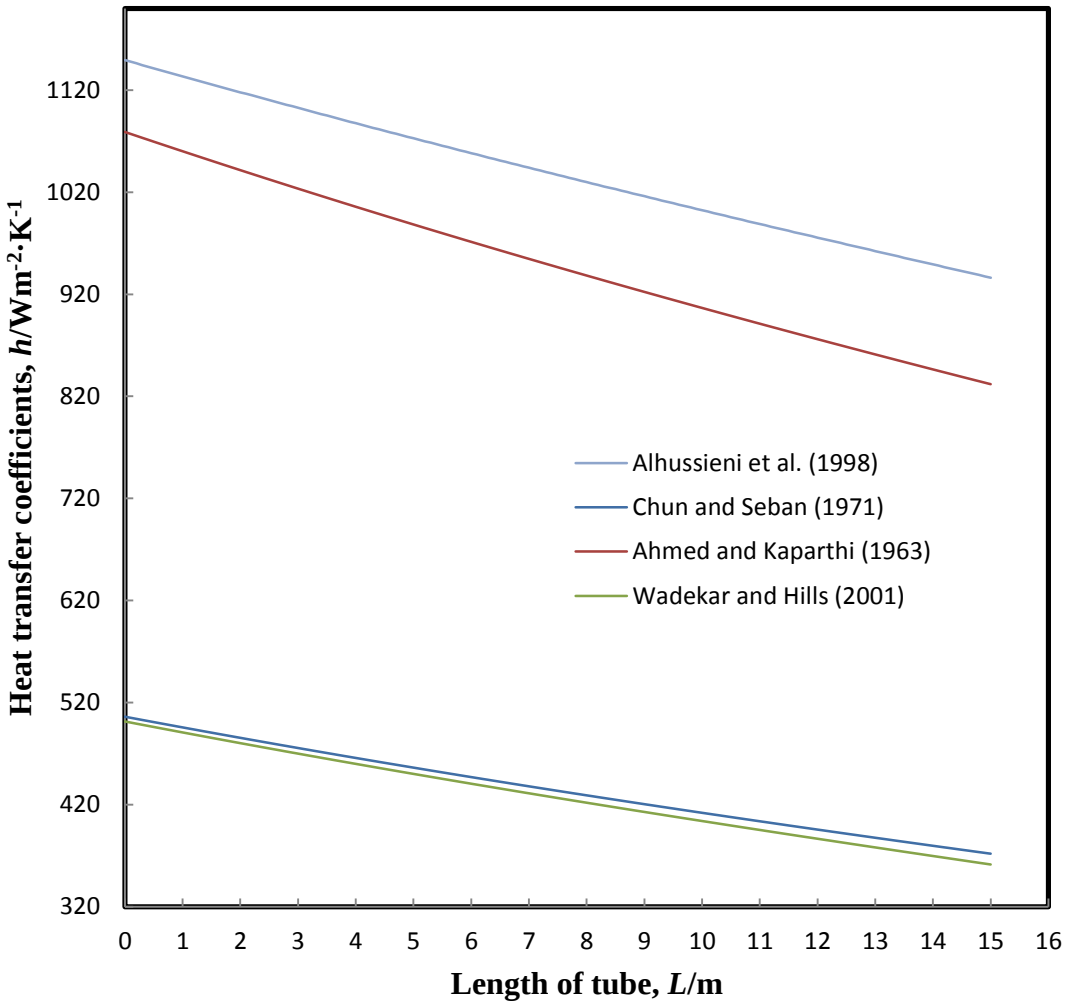

Figure 8.33: The calculated heat transfer coefficients from equations and correlations.

9. Discussion

In this final part of the discussion, the falling film of milk in a hypothetical evaporator tube will be discussed. The focus of the discussion will be the milk flow with total solids in (TS_{in}) of 45%. The discussion arises from the results that were derived from the several calculations that were made and earlier results from other experiments.

The empirical models developed for the rheological parameters were found to be inadequate for one parameter, the flow behavior index. It was found that the trend from the model does not cover most of the range of the experimental results.

Models from Reddy and Datta (1994) and Vélez-Ruiz and Barbosa-Cánovas (2000) were included for comparison. These models too were not in the range of experimental results.

It is clear that the flow behavior index of milk gradually decreases from 1.0 as the total solids content of milk increases. The results from Figure 8.1 indicated that this transition is linear.

As from Figure 8.1, it is apparent that temperature may have an effect on the flow behavior index. For the range of 35.47% to 49.25% total solids where the temperature was high, the flow behavior index was lower than the others.

For the other models, the consistency factor and yield stress were quite closely predicted. It is apparent from Figures 8.2 and 8.3 that the consistency factor and yield stress increased earlier from 35.47% total solids.

Despite these inadequacies, these models were used for present calculations in a spreadsheet. The film flow, velocity and film thickness depends on these parameters.

For calculations, the wetting rate was arbitrary and was set at 0.3 $kg \cdot m^{-1} \cdot s^{-1}$. It was assumed that no film break-up occur for all calculations. The wetting rate also indicates the film mass flow rate. A high wetting rate would indicate high film flow

and vice versa for low wetting rate. The actual wetting rate would decrease as the mass flow rate decreases due to evaporation.

For a wetting rate of less than 0.15 $kg \cdot m^{-1} \cdot s^{-1}$, the yield stress of milk was calculated to be increasing significantly to the extent that would present a limit to the range of wetting rates that can be used. This study on the effect of wetting rate was extended to the consistency factor and flow behavior index at tube exit.

The results showed that the consistency factor follow the same trend as the yield stress where it increased exponentially when wetting rate decreases. The flow behavior index however increased when wetting rate increases.

For film flow at present conditions, the shear rate was calculated to be about 500 s^{-1} with the highest shear rate at 579 s^{-1} at the entrance of the tube. Hence, the reason the viscosity at shear rate of $\dot{\gamma}$ = 500 s^{-1} was chosen for developing the age thickening model earlier. The shear rate for the film flow was found to decrease and this corresponds well with the increase of the viscosity of the milk flow. The viscosity was calculated to increase exponentially similar to previously observed in earlier results.

The time spent for the milk in the evaporator tube was not more than 117 s (~1.9 minutes) for wetting rate of 0.2 $kg \cdot m^{-1} \cdot s^{-1}$. However, when the wetting rate was reduced to 0.15 $kg \cdot m^{-1} \cdot s^{-1}$ and further the time spent was increased dramatically.

The calculations made, revealed that the milk flow have a Reynolds number of 52.2 at the start of the flow and decreases to 23.4 as it flows down to the end of the tube. For this range of Reynolds number, the flow regime was clearly a wavy laminar but this was not taken into account in the model. The Prandtl number however increases (from Pr = 142.1 to 281.2) with decreasing Reynolds number. This trend was the same when the Prandtl number was replaced with the Kapitza number although the Kapitza number was very low (2.48×10^{-5} - 3.74×10-4). With this low Kapitza number, it was found that nucleate boiling does not occur.

Earlier results revealed that the heat transfer to the film was not linear. With the heat transfer, the film temperature was found to increase as it flows down the length of the tube and to be higher where it is near most to the tube wall. Due to the boiling point elevation, the milk film has a further increased in temperature of about 1 K and more.

Because of the constant evaporation and constant heating at the tube wall, the total solids of milk will increase. Based on Wadekar's theory of 'mixture effect', calculations were performed to obtain the total solids at the interface. The equation provided by Wadekar seems to be incorrect and was modified to reflect the increase of the total solids at the interface. This increase was found to be about 1.3% – 2.9% TS.

The calculated results of Figure 8.26 showed that for low total solids in (TS_{in}), milk can be concentrated to higher final total solids. This is especially true when the wetting rate is lower than 0.5 $kg \cdot m^{-1} \cdot s^{-1}$. Results indicated that there is a limit to how much the final total solids out from the tube can be increased by lowering the wetting rates. This is because, with the amount of solids being the same for each TS_{in}, having less wetting rates means the total mass available for evaporation becomes less. With less mass to be evaporated, milk can't be concentrated any higher.

From analytical studies, it was found that there were two types of thicknesses. One in which the shear stress was less than the yield stress and the other higher than the yield stress. These two film thicknesses can be represented by δ_1 and δ_2 as previously derived. The film thickness, δ_1 was small (9.59×10^{-6}m to 3.45×10^{-5}m) compared to δ_2 (0.00117m to 0.00146m) and represents only a small portion of the overall film thickness, δ_2.

The final film thickness at the tube exit was examined when the wetting rate (Γ), temperature difference (°C) and total solids in (TS_{in}) were varied. Although the results were not unexpected, one interesting result was discovered. An increase in wetting rate leads to increasing film thickness at tube exit even though the film thickness should be decreasing. It was found that the contributing factor to the increase of the

film thickness was due to the increase of the flow behavior index, *n*, when the wetting rate increased.

The two film thicknesses also represent two different velocity profiles for the overall milk flow. The two types of velocities are visible from Figures 6.1 to 6.2 earlier. This difference starts before and after the film thickness, δ_1.

The impact of the consistency factor, flow behavior index and yield stress on the velocity profiles were analyzed in the Results chapter. The yield stress was found to have no significance effect on the velocity profiles. On the other hand, decreasing flow behavior index and consistency factor have the effects of increasing the milk film velocities.

The heat transfer coefficients of the film flow (internal) were calculated and they decreased down the length of the tube. This decrease indicates that with the increase of the total solids of milk, the heat transfer deteriorates. Four different correlations were used for the calculations, namely, Alhusseini et al. (1998), Chun and Seban (1971), Ahmed and Kaparthi (1963) and Wadekar and Hills (2001). The comparison made in Figure 8.33 showed that the correlations from Alhusseini et al. (1998) and Ahmed and Kaparthi (1963) gave higher heat transfer coefficients than those from Chun and Seban (1971) and Wadekar and Hills (2001).

These calculated heat transfer coefficients may also depend on the overall heat transfer coefficient and the arbitrary temperature difference, ΔT, used. For the Wadekar and Hills (2001) correlation, the Chun and Seban (1971) equation was used as the heat transfer coefficient for equivalent pure fluid, α_{epf}. This correlation from Wadekar and Hills (2001) which include the 'mixture effect' is dependent mostly on the equivalent pure fluid heat transfer coefficient, α_{epf}. As the result in Figure 8.33 showed, the heat transfer coefficient from Wadekar and Hills (2001) and Chun and Seban (1971) were quite close.

10. Conclusions

The research and investigations made on milk and its rheological properties clearly identified that milk can be Newtonian and non-Newtonian. At low concentration or total solids content of up to 35%, milk is Newtonian and at higher total solids of more than 35% milk is non-Newtonian.

The non-Newtonian nature of milk can be well described by the Herschel-Bulkley model. The Herschel-Bulkley model used enabled the determination of the relationships of the rheological parameters with milk.

The empirical models that were developed for the rheological parameters relates to the total solids content of milk. The properties of milk change the most when the total solids content of milk changes. Furthermore, the total solids content of milk is of interest when milk is being concentrated.

Several parts of this research have focused on investigating the rheological properties of milk, its age thickening phenomena, the analytical and simulations of the falling film flow.

These several parts of the research provided further details to the falling film of milk. The results from the research indicated there were many factors that were important to the dynamics of the falling film evaporator. These results were presented and discussed.

The overall conclusions that can be made from this research were that:

- The falling film flow is quite complex and when coupled with heat transfer, the overall process can be very complicated.
- A lot of factors or variables are involved with the evaporation process of the falling film flow. Each of these variables can be depended on each other and may have various impacts on the performance of the falling film evaporator.
- It was found from this study that one of the limiting factors to the falling film evaporation of milk starting from 45% TS was the yield stress of milk.

- Further concentration of milk already at 45% TS requires consideration of the non-Newtonian nature of milk.
- The Herschel-Bulkley model can be successfully used to describe the non-Newtonian nature of milk at high total solids.
- Calculations for the viscosity in the tube showed that it increased exponentially.
- Various experiments could be performed to validate the calculations and models further improved.

11. References

Adib, T. A. and Vasseur, J. (2008) Bibliographic analysis of predicting heat transfer coefficients in boiling for applications in designing liquid food evaporators, *Journal of Food Engineering*, 87, 149-161.

Adib, T. A., Heyd, B. & Vasseur, J. (2009) Experimental results and modeling of boiling heat transfer coefficients in falling film evaporator usable for evaporator design, *Chemical Engineering and Processing*, 48, 961-968.

Ahmed, S. Y. and Kaparthi, R. (1963) Heat transfer studies of falling film heat exchangers, *Indian J. Technol.*, 1, 377-381.

Alhusseini, A. A., Tuzla, K. & Chen, J. C. (1998) Falling film evaporation of single component liquids, *Int. J. Heat Mass Transfer*, 41(12), 1623-1632.

Andersson, H. I. and Shang, D. (1998) An extended study of the hydrodynamics of gravity-driven film flow of power-law fluids, *Fluid Dynamics Research*, 22, 345-357.

Anema, S. G. and Li, Y. (2003) Association of denatured whey proteins with casein micelles in heated reconstituted skim milk and its effect on casein micelle size, *Journal of Dairy Research*, 70, 73-83.

Anema, S. G., Lowe, E. K. and Li, Y. (2004) Effect of pH on the viscosity of heated reconstituted skim milk, *International Dairy Journal*, 14, 541-548.

Assad, M. E. H. and Lampinen, M. J. (2002) Mathematical modeling of falling liquid film evaporation process, *International Journal of Refrigeration*, 25(7), 985-991.

Augustin, M. A. and Clarke, P. T. (2008) Dry milk products in R. C. Chandan, A. Kilara & N. P. Shah (Eds.) *Dairy Processing and Quality Assurance* (pp. 319), Wiley-Blackwell.

Bienvenue, A., Jiménez-Flores, R. & Singh, H. (2003) Rheological properties of concentrated skim milk: Importance of soluble minerals in the changes in viscosity during storage, *J. Dairy Sci.*, *86*, 3813-3821.

Billet, R. (1989) *Evaporation Technology : Principles, Applications, Economics*, VCH Ellis Horwood Ltd., Chichester, England and Weinheim, Germany.

Bird, R.B., Stewart, W.E. and Lightfoot, E.N. (2001). *Transport Phenomena* (Second Edition ed.). John Wiley & Sons.

Bloore, C. G. & Boag, I. F. (1981) Some factors affecting the viscosity of concentrated skim milk, *New Zealand Journal of Dairy Science and Technology*, *16*, 143-154.

Bouman, S., Waalewijn, R., De Jong, P. and Van Der Linden, H.J.L.J. (1993) Design of falling-film evaporators in the dairy industry, *Journal of the Society of Dairy Technology*, 46(3), 100-106.

Broome, S. R. (2005) *Liquid distribution and falling film wetting in dairy evaporators*, ME Thesis, University of Canterbury, Christchurch, New Zealand.

Bylund, G. (2003) *Dairy Processing Handbook* (2nd Rev. Ed.), Lund, Sweden: Tetrapak Processing System AB.

Chen, H. (1992) *Factors affecting heat transfer in the falling film evaporator*, ME Thesis, Massey University, New Zealand.

Chien, S-F (1966) Laminar, gravitational film flow of liquid on vertical, circular, cylindrical surfaces, *J. Appl. Mech.*, 33(1), 222-224.

Chong, L. X. Q., Lin, S. X. Q. and Chen, X. D. (2009) Concentration Dependent Viscosity in Milk Evaporation Process, In Engineering Our Future: Are We up to the

Challenge?, Burswood Entertainment Complex, Barton, ACT: Engineers Australia, 1149-1158.

Deeth, H.C. and Hartanto, J. (2009) 'Chemistry of milk – Role of constituents in evaporation and drying', in A.Y. Tamine (Ed.) *Dairy powders and concentrated products* (pp.1-27), Chichester, UK: Blackwell Publishing Ltd.

Donato, L. and Guyomarc'h, F. (2009) Formation and properties of the whey protein/κ-casein complexes in heated skim milk – A review, *Dairy Sci. Technol.*, 89, 3-29.

Faghri, A. and Zhang, Y. (2006) *Transport phenomena in multiphase systems*, Amsterdam Elsevier.

Fulford, G.D. (1964) The flow of liquids in thin films. In T.B. Drew (Ed.) *Advances in chemical engineering Volume 5*. London: Academic Press Inc.

GEA Wiegand (n.d.) Evaporation Technology. Retrieved from http://www.niroinc.com/html/evaporator/evpdfs/gea_w_evap_tec.pdf.

Haeri, S. and Hashemabadi, S.H. (2009) Experimental study of gravity-driven film flow of non-Newtonian fluids, *Chemical Engineering Communications*, 196(5), 519-529.

Hassan, N. A. (1967) Laminar flow along a vertical wall, *J. Appl. Mech.*, 34(3), 535-537.

Holman, J. P. (2002) *Heat transfer* (9th Ed.), New York, NY: McGraw-Hill.

Jayanthi, S. and Hewit, G.F. (1997) Hydrodynamics and heat transfer of wavy thin film flow, *Int. J. Heat Mass Transfer*, 40(1), 179-190.

Jebson, R. S. & Chen, H. (1997) Performances of falling film evaporators on whole milk and a comparison with performance on skim milk, *Journal of Dairy Research*, 64, 57-67.

Jiji, L. M. (2009) *Heat convection (second edition)*, Berlin, Springer-Verlag.

Kailasapathy, K. (2008) Chemical composition, physical and functional properties of milk and milk ingredients in R. C. Chandan, A. Kilara & N. P. Shah (Eds.) *Dairy Processing and Quality Assurance*, Wiley-Blackwell.

Karimi, G. and Kawaji, M. (1998) An experimental study of freely falling films in a vertical tube, *Chemical Engineering Science*, 53(20), 3501-3512.

Krupiczka, R., Rotkegel, A. & Ziobrowski, Z. (2002) Heat transfer to evaporating liquid films within a vertical tube, *Chemical Engineering and Processing*, 41, 23-28.

Lockshin, J. L. And Zakharov, M. K. (2001) Exact solutions for heat and mass transfer in a falling laminar film, *International Journal of Heat and Mass Transfer*, 44, 4541-4552.

Mackereth, A. R. (1992) Inside the stainless steel – An insight into evaporation heat transfer, In Milk Powders For The Future: A symposium on Milk Powder Research, Palmerston North.

Moran, K., Inumaru, J. and Kawaji, M. (2002) Instantaneous hydrodynamics of a laminar wavy liquid film, *International Journal of Multiphase Flow*, 28, 731-755.

Morison, K. R. & Hartel, R. W. (2007) 'Evaporation and freeze concentration', in D. R. Heldman & D. R. Lund (Eds.) *Handbook of Food Engineering* (pp. 495-552), Boca Raton, FL: CRC Press.

Morison, K.R., Worth, Q.A.G. and O'Dea, N.P. (2006) Minimum wetting and distribution rates in falling film evaporators, *Food and Bioproducts Processing*, 84(4), 302-310.

NZIC (1998a) The Dairy Industry: Introduction to the New Zealand Industry. Retrieved from http://nzic.org.nz/ChemProcesses/dairy/3A.pdf.

NZIC (1998b) The Dairy Industry: Milk Powder. Retrieved from http://nzic.org.nz/ChemProcesses/dairy/3C.pdf.

New Zealand Dairy Statistics (2010/11) Retrieved from http://www.lic.co.nz/pdf/DAIRY%20STATISTICS%2010-11-WEB.pdf

Nisenfeld, A. E. (1985) *Industrial Evaporators*. North Carolina: The Instrument Society of America.

Oldfield, D.J., Taylor, M.W. and Singh, H. (2005) Effect of preheating and other process parameters on whey protein reactions during skim milk powder manufacture, *International Dairy Journal*, 15(5), 501-511.

Palen, J.W., Wang, Q. and Chen J.C. (1994) Falling film evaporation of binary mixtures, *AIChE Journal*, 40(2), 207-214.

Paramalingam, S., Winchester, J. and Marsh, C. (2000) On the fouling of falling film evaporators due to film break-up, *Food and Bioproducts Processing*, 78(2), 79-84.

Park, C.D. and Nosoko, T. (2003) Three-dimensional wave dynamics on a falling film and associated mass transfer, *AICHE Journal*, 49(11), 2715-2727.

Park, C.D., Nosoko, T., Gima, S. and Ro, S.T. (2004) Wave-augmented mass transfer in a liquid film falling inside a vertical tube, *International Journal of Heat and Mass Transfer*, 47, 2587-2598.

Pohio, K. (2009) *Total solids optimization for evaporators*, MEM Thesis, University of Canterbury, Christchurch, New Zealand.

Prost, J. S., González, M. T. & Urbicain, M. J. (2006) Determination and correlation of heat transfer coefficients in a falling film evaporator, *Journal of Food Engineering*, 73, 320-326.

Rao, B. K. (1999) Heat transfer to a falling power-law fluid film, *International Journal of Heat and Fluid Flow*, 20, 429-436.

Reddy, Ch.S. and Datta, A.K. (1994) Thermophysical properties of concentrated reconstituted milk during processing, *Journal of food engineering*, 21, 31-40.

Roos, Y. H. (2007) 'Phase transitions and transformations in food systems', in D. R. Heldman & D. R. Lund (Eds.) *Handbook of Food Engineering* (pp. 287-532), Boca Raton, FL: CRC Press.

Saouli, S. and Aiboud-Saouli, S. (2004) Second law analysis of laminar falling liquid film along an inclined heated plate, *Int. Comm. Heat Mass Transfer*, 31(6), 879-886.

Shang, D. (2006) *Free Convection Film Flows and Heat Transfer*, Berlin, Springer-Verlag.

Shang, D. and Gu, J. (2004) Analyses of pseudo-similarity and boundary layer thickness for non-Newtonian falling film flow, *Heat Mass Transfer*, 41, 44-50.

Singh, H. (2007) Interactions of milk proteins during the manufacture of milk powders, *Lait*, 87, 413-423.

Skelland, A. H. P. and Popadić, V. O. (1974) Falling films of pseudoplastic liquids, *The Chemical Engineering Journal*, 8, 235-242.

Snoeren, T.H.M, Damman, A.J. and Klok, H.J. (1982) The viscosity of skim-milk concentrates, *Netherlands Milk Dairy Journal*, 36, 305-316.

Statistics New Zealand (n.d.) New Zealand In Profile: 2011. Retrieved from http://www.stats.govt.nz/browse_for_stats/snapshots-of-nz/nz-in-profile-2011/imports-exports.aspx.

Storch, Th., Philipp, Ch. and Gross, U. (2008) Zero shear-stress experiments of falling film evaporation inside a vertical tube 5th European Thermal-Sciences Conference.

Stringleman, H. and Scrimgeour, F. (2009) Te Ara - the Encyclopedia of New Zealand : Dairying and dairy products - Dairy exports. Retrived from http://www.TeAra.govt.nz/en/dairying-and-dairy-products/11.

Sutalo, I. D., Bui, A. and Rudman, M. (2006) The flow of non-Newtonian fluids down inclines, *J. Non-Newtonian Fluid Mech.*, 136, 64-75.

Tandon, G. (2004) *Experimental determination of minimum wetting rates in a falling film evaporator*, University of Canterbury, Christchurch, New Zealand.

TheDairySite (2010) Australian commodities: Global Dairy. Retrieved from http://www.thedairysite.com/articles/2518/australian-commodities-global-dairy.

Trela, M. and Kornecki, I. (1997) Heat transfer and minimum wetting rate for a falling laminar liquid film, *Trans. IFFM*, 103, 29-49.

Trinh et al. (2007) Rheological characterisation of age thickening with special reference to milk concentrates, *Journal of Dairy Research*, 74, 106-115.

Tuzla, K., Palmer, T. R. & Chen, J. C. (2000) Experimental study of heat transfer in laminar falling films at high Prandtl numbers, *Multiphase Science and Technology*, 12(3-4), 145-160.

Uche, J., Artal, J. and Serra, L. (2003) Comparison of heat transfer coefficient correlations for thermal desalination units, *Desalination*, 153(1-3), 195-200.

Vélez-Ruiz, J.F. & Barbosa-Cánovas, G.V. (1998) Rheological properties of concentrated milk as a function of concentration, temperature and storage time, *Journal of Food Engineering*, 35, 177-190.

Vélez-Ruiz, J. F. and Barbosa-Cánovas, G.V. (2000) Flow and structural characteristics of concentrated milk, *Journal of Texture Studies*, 31, 315-333.

Wadekar, V. V. (2000) *Heat transfer to falling liquid films with high Prandtl numbers*, Proceedings of 3rd European Thermal Sciences Conference, Heidelberg

Wadekar, V. V. & Hills, P. D. (2001) Evaporative heat transfer to solutions containing dissolved solids: Effect of vapour-liquid equilibrium and mass transfer, *Chemical Engineering Research and Design*, 79(4), 477-483.

Weise, F. & Scholl, S. (2009) Evaporation of pure liquids with increased viscosity in a falling film evaporator, *Heat Mass Transfer*, 45, 1037-1046.

Westergaard V. (2004) *Milk Powder Technology - Evaporation and Spray Drying*, Retrieved from http://www.niro.com/niro/cmsdoc.nsf/WebDoc/ndkw5y4brlLibrary.

Wiegand, J. (1971) Falling-film evaporators and their applications in the food industry, *J. Appl. Chem. Biotechnol., 21*, 351-358.

Yang, T. M. T. and Yarbrough, D. W. (1980) Laminar flow of non-Newtonian liquid films inside a vertical pipe, *Rheol. Acta*, 19, 432-436.

Yih, S-M. (1986) Modeling heat and mass transport in falling liquid films. In N.P.Cheremisinoff (Ed.) *Handbook of Heat and Mass Transfer Volume 2: Mass Transfer and Reactor Design* (pp.111-210). Houston, Texas: Gulf Publishing Company.

Zhang, F., Tang, D.-L., Geng J., Wang, Z.-X., Zhang, Z.-B. (2008) Study on the temperature distribution of heated falling liquid films, *Physica D: Nonlinear Phenomena*, 237(7), 867-872.

12. Appendices

Appendix A. Analytical Derivations

This includes derivations involving Newtonian and non-Newtonian film flow.

Newtonian Film Flow

The standard equations for Newtonian film flow (Bird et al., 2001) are re-derived here to provide the basis for the non-Newtonian derivations.

i. Film velocity profile

$$\rho g + \mu \frac{\partial^2 v}{\partial x^2} = 0 \qquad \text{(A.1)}$$

$$x = 0,\ \frac{\partial v}{\partial x} = 0 \qquad \text{(A.2)}$$

$$x = \delta,\ \ v = 0 \qquad \text{(A.3)}$$

Equation (A.1) was solved together with its boundary conditions above to obtain the film velocity profile.

$$\mu \frac{\partial^2 v}{\partial x^2} = -\rho g$$

$$\frac{\partial v}{\partial x} = -\frac{\rho g}{\mu} x + C$$

From equation (A.2), $C = 0$

$$\frac{\partial v}{\partial x} = -\frac{\rho g x}{\mu}$$

Continue integrating,

$$v = -\frac{\rho g x^2}{2\mu} + C$$

From equation (A.3), $C = \frac{\rho g \delta^2}{2\mu}$

$$v = -\frac{\rho g x^2}{2\mu} + \frac{\rho g \delta^2}{2\mu}$$

$$= \frac{\rho g \delta^2}{\mu}\left[-\frac{1}{2}\left(\frac{x}{\delta}\right)^2 + \frac{1}{2}\right]$$

$$= \frac{\rho g \delta^2}{2\mu}\left[1 - \left(\frac{x}{\delta}\right)^2\right] \qquad \text{(A.4)}$$

ii. Maximum velocity

From the velocity profile, as $x \to 0$,

$$v \to \frac{\rho g \delta^2}{2\mu}$$

$$v_{\max} = \frac{\rho g \delta^2}{2\mu} \qquad \text{(A.5)}$$

iii. Average velocity

$$v_{av} = \frac{1}{\delta}\int_0^{\delta} v\,dx$$

$$= \frac{1}{\delta}\int_0^{\delta} \frac{\rho g \delta^2}{2\mu}\left[1 - \left(\frac{x}{\delta}\right)^2\right]dx$$

$$= \frac{\rho g \delta}{2\mu}\left[x - \frac{x^3}{3\delta^2}\right]_0^{\delta}$$

$$= \frac{\rho g \delta}{2\mu}\left[\frac{2\delta}{3}\right]$$

$$v_{av} = \frac{\rho g \delta^2}{3\mu}$$

iv. Wetting rate

$$\Gamma = \int_0^\delta \rho v dx$$

$$= \rho \int_0^\delta v dx$$

$$= \rho v_{av} \delta$$

$$= \rho \frac{\rho g \delta^2}{3\mu} \delta$$

$$= \frac{\rho^2 g \delta^3}{3\mu} \qquad \text{(A.6)}$$

v. Film thickness

From equation (A.6) derived for the wetting rate, the film thickness is thus,

$$\delta = \left(\frac{3\mu\Gamma}{\rho^2 g} \right)^{1/3} \qquad \text{(A.7)}$$

This equation is normally attributed to Nusselt.

Non-Newtonian Film Flow

i. Film velocity profile

Based on the book 'Transport Phenomena' by Bird et al. (2001), equation (A.8) was obtained.

The x-axis is defined as being the distance from the liquid/gas interface into the film.

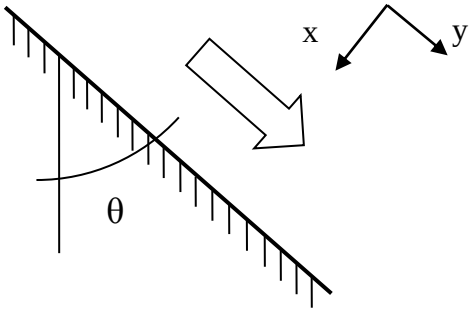

Figure A.1: Falling film on an inclined plane.

$\frac{\partial \tau}{\partial x} = \rho g \cos\theta$ with angle, θ from vertical as in Figure A.1 (A.8)

For vertical plane, $\theta = 0^\circ$ and $\cos\theta = 1$

$$\frac{\partial \tau}{\partial x} = \rho g$$

$$\tau = \rho g x + C$$

Boundary condition i) $x = 0$, $\tau = 0$ (no drag at the film interface)

$$C = 0$$

$$\tau = \rho g x \quad \text{(A.9)}$$

The same derivation can be done for a Herschel-Bulkley fluid. This was derived and was subsequently confirmed when the work of Sutalo et al. (2006) was found.

Using the Herschel-Bulkley equation,

$$\tau = \tau_y + K\dot{\gamma}^n$$

Equation (A.9) becomes (A.10),

$$\tau_y + K\dot{\gamma}^n = \rho g x \qquad \text{(A.10)}$$

$$\dot{\gamma}^n = \frac{\rho g x - \tau_y}{K}$$

$$\dot{\gamma} = \left(\frac{\rho g x - \tau_y}{K} \right)^{\frac{1}{n}} \qquad \text{(A.11)}$$

$$-\frac{\partial v}{\partial x} = \left(\frac{\rho g x - \tau_y}{K} \right)^{\frac{1}{n}}$$

$$\frac{\partial v}{\partial x} = -\left(\frac{\rho g x - \tau_y}{K} \right)^{\frac{1}{n}} \quad \text{and} \quad \frac{\partial v}{\partial x} = 0 \quad \text{when} \quad \rho g x < \tau_y$$

$$v = -\frac{n}{n+1}\frac{K}{\rho g}\left(\frac{\rho g x - \tau_y}{K} \right)^{\frac{n+1}{n}} + C \qquad \text{for} \quad \rho g x > \tau_y$$

Boundary condition ii) $x = \delta_2$ (at the wall), $v = 0$ (no slip phenomena)

$$C = \frac{n}{n+1}\frac{K}{\rho g}\left(\frac{\rho g \delta_2 - \tau_y}{K} \right)^{\frac{n+1}{n}}$$

The film velocity profile becomes,

$$v = \frac{n}{n+1}\frac{K}{\rho g}\left[\left(\frac{\rho g \delta_2 - \tau_y}{K} \right)^{\frac{n+1}{n}} - \left(\frac{\rho g x - \tau_y}{K} \right)^{\frac{n+1}{n}} \right] \qquad \text{(A.12)}$$

It can be seen from the film velocity profile that two thicknesses exist where the velocities are different.

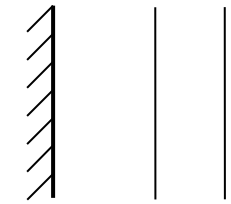

Figure A.2: Two types of film thicknesses.

$x = \delta_1$ from Figure A.2 occurred when $\rho g x = \tau_y$

$$\delta_1 = \frac{\tau_y}{\rho g} \tag{A.13}$$

The velocity profile for non-Newtonian falling film is thus,

For $\delta_1 < x < \delta_2$

$$v = \frac{n}{n+1}\frac{K}{\rho g}\left[\left(\frac{\rho g \delta_2 - \tau_y}{K}\right)^{\frac{n+1}{n}} - \left(\frac{\rho g x - \tau_y}{K}\right)^{\frac{n+1}{n}}\right] \tag{A.14}$$

For $x \le \delta_1$,

$$v = v(\delta_1) \qquad v = \frac{n}{n+1}\frac{K}{\rho g}\left[\left(\frac{\rho g \delta_2 - \tau_y}{K}\right)^{\frac{n+1}{n}}\right] \tag{A.15}$$

ii. <u>Average velocity</u>

$$v_{av} = \frac{1}{\delta_2}\int_0^{\delta_2} v\,dx$$

$$= \frac{1}{\delta_2}\left[\int_0^{\delta_1} v\,dx + \int_{\delta_1}^{\delta_2} v\,dx\right]$$

$$= \frac{1}{\delta_2}\left[\int_0^{\delta_1} \frac{n}{n+1}\frac{K}{\rho g}\left(\frac{\rho g \delta_2 - \tau_y}{K}\right)^{\frac{n+1}{n}} dx + \int_{\delta_1}^{\delta_2} \frac{n}{n+1}\frac{K}{\rho g}\left[\left(\frac{\rho g \delta_2 - \tau_y}{K}\right)^{\frac{n+1}{n}} - \left(\frac{\rho g x - \tau_y}{K}\right)^{\frac{n+1}{n}}\right] dx\right]$$

$$= \frac{1}{\delta_2}\left[\frac{n}{n+1}\frac{K}{\rho g}\left(\frac{\rho g \delta_2 - \tau_y}{K}\right)^{\frac{n+1}{n}} \delta_1 + \right.$$

$$\left. \frac{n}{n+1}\frac{K}{\rho g}\left[\left(\frac{\rho g \delta_2 - \tau_y}{K}\right)^{\frac{n+1}{n}}(\delta_2 - \delta_1) - \frac{n}{2n+1}\frac{K}{\rho g}\left[\left(\frac{\rho g \delta_2 - \tau_y}{K}\right)^{\frac{2n+1}{n}} + \left(\frac{\rho g \delta_1 - \tau_y}{K}\right)^{\frac{2n+1}{n}}\right]\right]\right]$$

= 0

$$= \frac{1}{\delta_2}\left[\frac{n}{n+1}\frac{K}{\rho g}\left(\frac{\rho g\delta_2 - \tau_y}{K}\right)^{\frac{n+1}{n}}\delta_2 - \frac{n}{2n+1}\frac{K}{\rho g}\frac{n}{n+1}\frac{K}{\rho g}\left(\frac{\rho g\delta_2 - \tau_y}{K}\right)^{\frac{2n+1}{n}}\right]$$

$$\mathrm{v}_{ave} = \frac{1}{\delta_2}\frac{n}{n+1}\frac{K}{\rho g}\left[\left(\frac{\rho g\delta_2 - \tau_y}{K}\right)^{\frac{n+1}{n}}\delta_2 - \frac{n}{2n+1}\frac{K}{\rho g}\left(\frac{\rho g\delta_2 - \tau_y}{K}\right)^{\frac{2n+1}{n}}\right]$$

iii. Wetting rate

$$\dot{m} = \rho v_{av} A$$

$$= \rho v_{av}\delta_2 W \quad (W \text{ is the width})$$

and with $\frac{\dot{m}}{W} = \Gamma$,

$$\Gamma = \rho v_{av}\delta_2$$

$$= \rho\frac{n}{n+1}\frac{K}{\rho g}\left[\left(\frac{\rho g\delta_2 - \tau_y}{K}\right)^{\frac{n+1}{n}}\delta_2 - \frac{n}{2n+1}\frac{K}{\rho g}\left(\frac{\rho g\delta_2 - \tau_y}{K}\right)^{\frac{2n+1}{n}}\right] \quad \text{(A.16)}$$

iv. Film thickness

To find δ_2 from Γ using equation (A.16) an iterative solution method is required. Newton's method was implemented and is included here in Appendix B.

Appendix B. Newton's Method For Finding Film Thickness

The code written in Visual Basic for Applications for finding film thickness, δ_2:

```
Option Explicit

Function FindDelta2(Wettingrate As Double, Density As Double, Ty As Double, k As
Double, n As Double, delta1 As Double) As Double
' Use Newton's method to find delta2 for Herschel-Bulkley flow in a tube
Dim icount As Integer
Dim dDelta2 As Double
Dim dDeltadelta2 As Double          ' perturbation for numerical derivative
Dim dTemp As Double, dF0 As Double, dF1 As Double, dDeriv As Double
' guess delta2
dDelta2 = delta1 + 0.001  ' film thickness m



Do
   dF0 = functionvalue(Wettingrate, Density, Ty, k, n, delta1, dDelta2)   '
   ' numerical derivative
   dTemp = dDelta2
   dDeltadelta2 = dDelta2 * 0.0000001
   If dDeltadelta2 < 0.0000000001 Then dDeltadelta2 = 0.0000000001
   dDelta2 = dDelta2 + dDeltadelta2
   dF1 = functionvalue(Wettingrate, Density, Ty, k, n, delta1, dDelta2)

   dDeriv = (dF1 - dF0) / dDeltadelta2     ' numerical derivative by pertubation
   dDelta2 = dTemp                         ' restore value of delta2

   dDelta2 = dDelta2 - dF0 / dDeriv
   If dDelta2 < 0.0000001 Then dDelta2 = 0.0000001

   icount = icount + 1
Loop Until icount > 100 Or Abs(dF0 / dDeriv) < 0.0000000001

FindDelta2 = dDelta2

End Function


Function functionvalue(Wettingrate, Density, Ty, k, n, delta1, delta2) As Double
' returns residual value for the integral  in form f(x)=0
Dim dTerm1 As Double, dTerm2 As Double, dTerm3 As Double
Dim dG As Double
dG = 9.81   ' gravity
```

```
dTerm1 = delta2 * ((Density * dG * delta2 - Ty) / k) ^ ((n + 1) / n)
dTerm2 = ((Density * dG * delta2 - Ty) / k) ^ ((2 * n + 1) / n)
' dTerm3 = ((Density * dG * delta1 - Ty) / K) ^ ((2 * n + 1) / n)

functionvalue = Wettingrate - k * n / (n + 1) / dG * (dTerm1 - k * n / (Density * dG *
(2 * n + 1)) * (dTerm2))

End Function
```

Appendix C. VBA Codes For Physical Properties

These codes were developed by Dr. Ken Morison.

Milk Density

```
Function MilkDensity(Temp As Double, NFS As Double, Fat As Double)
' Density of milk based on Jan Pisecky, Handbook of Milk Powder Manufacture, 1997
' Temp in deg C, NFS and Fat are mass fractions of non fat solids and fat

Dim sRhoFat As Double, sRhoNFS As Double, sRhoWater As Double

sRhoFat = 966.665 - 1.334 * Temp
sRhoNFS = 1635 - 2.6 * Temp + 0.02 * Temp ^ 2
sRhoWater = WaterDensity(Temp)

MilkDensity = 1 / (Fat / sRhoFat + NFS / sRhoNFS + (1 - Fat - NFS) / sRhoWater)

End Function
```

Milk Heat Capacity

```
Function MilkCp(Temp As Double, Protein As Double, _
  Lactose As Double, Fat As Double, Ash As Double) As Double
' Specific heat capacity based on Choi and Okos
Dim sProteinCp As Double
Dim sLactoseCp As Double
Dim sFatCp As Double
Dim sAshCp As Double

sProteinCp = 2008.2 + 1.2089 * Temp - 0.0013129 * Temp ^ 2
sLactoseCp = 1548.8 + 1.9625 * Temp - 0.0059399 * Temp ^ 2
sFatCp = 1984.2 + 1.4733 * Temp - 0.0048008 * Temp ^ 2
sAshCp = 1092.6 + 1.8896 * Temp - 0.0036817 * Temp ^ 2

MilkCp = Protein * sProteinCp + Lactose * sLactoseCp + _
      Fat * sFatCp + Ash * sAshCp + _
      (1 - Protein - Lactose - Fat - Ash) * WaterCp(Temp)

End Function
```

Milk Thermal Conductivity

```
Function MilkThermalConductivity(Temp As Double, Protein As Double, _
 Lactose As Double, Fat As Double, Ash As Double) As Double
' Thermal conductivity of milk based foods
' Based on Choi and Okos
Dim sVolWater As Double, sVolProtein As Double, sVolLactose As Double
Dim sVolAsh As Double, sVolFat As Double
```

```
sVolProtein = Protein / ProteinDensity(Temp)
sVolLactose = Lactose / LactoseSolidDensity(Temp)
sVolFat = Fat / FatDensity(Temp)
sVolAsh = Ash / AshDensity(Temp)
' Assume all the remainder is water
sVolWater = (1 - Protein - Lactose - Fat - Ash) / WaterDensityChoi(Temp)

MilkThermalConductivity = (sVolWater * WaterThermalConductivity(Temp) + _
      sVolProtein * ProteinThermalConductivity(Temp) + _
      sVolLactose * LactoseThermalConductivity(Temp) + _
      sVolFat * FatThermalConductivity(Temp) + _
      sVolAsh * AshThermalConductivity(Temp)) / _
      (sVolWater + sVolProtein + sVolLactose + sVolFat + sVolAsh)

End Function


Function WaterDensityChoi(Temp As Double) As Double
WaterDensityChoi = 997.2 - 0.00314 * Temp - 0.00376 * Temp ^ 2
End Function

Function ProteinDensity(Temp As Double) As Double
ProteinDensity = 1329.9 - 0.5184 * Temp
End Function

Function FatDensity(Temp As Double) As Double
FatDensity = 925.59 - 0.41757 * Temp
End Function

 Function LactoseSolidDensity(Temp As Double) As Double
LactoseSolidDensity = 1599.1 - 0.31046 * Temp
End Function

 Function AshDensity(Temp As Double) As Double
AshDensity = 2423.8 - 0.28063 * Temp
End Function

Function WaterThermalConductivity(Temp As Double) As Double
' Thermal conductivity from data in A J Chapman curve by KRM
' WaterThermalConductivity = 0.56561 + 0.0018379 * Temp - 0.000007109 * Temp ^
2
' From NBS/NRC Steam tables

WaterThermalConductivity = 0.5603 + 0.002124 * Temp - 0.000009374 * Temp ^ 2
End Function

Private Function ProteinThermalConductivity(Temp As Double) As Double
ProteinThermalConductivity = 0.17881 + 0.0011958 * Temp - 0.0000027178 * Temp
^ 2
End Function
```

```
Private Function LactoseThermalConductivity(Temp As Double) As Double
LactoseThermalConductivity = 0.20141 + 0.0013874 * Temp - 0.0000043312 * Temp
^ 2
End Function

Private Function FatThermalConductivity(Temp As Double) As Double
FatThermalConductivity = 0.18071 - 0.0027604 * Temp - 0.00000017749 * Temp ^ 2
End Function

Private Function AshThermalConductivity(Temp As Double) As Double
AshThermalConductivity = 0.32962 + 0.0014011 * Temp - 0.0000029069 * Temp ^ 2
End Function
```

Appendix D. Matlab Code For Film Temperature Distribution

This code was developed by Dr. Alex James.

```
function mypdex1

for i=1:20
    delete(gcf)  % deletes figures from last run
end
% We are working in ordinary Cartesian coordinates
m = 0;

% A grid from x=x0 to x=x1 in Npts
% These are the points we want to see the solution at
x0 = 0;
x1 = 1;
Npts = 100;   % points away from the wall, horizontally
x = linspace(x0,x1,Npts);  % x in Matlab in y in Saouli et al, i.e.
distance from wall
,
% and the interval we want to see the soln at
% from T0 to T1 in steps of dT

% T or t is distance down the tube (x in Saouli et al)
T0 = 0;
T1 = 1;
dT = 0.1;
t = [T0:dT:T1];

% solve the PDE!
sol = pdepe(m,@pde_eqn,@ics,@bcs,x,t);

% Extract the first solution component as u. u is temperature
u = sol(:,:,1);
% each row of u is the temperature variation away from the wall at a
% particular position down the tube

% A solution profile can also be illuminating.
for I = 1:length(t)  % ie for different positions down the tube
    analyt = 3*t(I)/2 + 3*(x/2-1).*x/2 - (1-x).^4./8 + 63/120;
    analyt2=1/(exp(-1)-exp(0.5))*(exp(-t(I)-0.5*x.^2+x)-exp(0.5));
    % figure(1)
    figure
    plot(x,u(I,:),'b',x,analyt,'r', x,analyt2,'g')
    str = strcat('Solution at distance down = ',num2str(t(I)),'{ }
Red:analytical-1, Green:analytical-2, Blue:numerical');
    title(str)
    axis([x0 x1 -0.3 5.0]);
    xlabel('Thickness of film from wall')
    ylabel('Theta')
    drawnow
    %pause(0.1)
    % reply=input('Pause');
end

end
```

```
%%%%%%%%%%%%%%%%%%%%%%%%%%%%%%%%%%%%%%%%%%%%%%%%%%%%%%%%%%%%%%%%%%%%%%%%%%%%%%%%

function [c,f,s] = pde_eqn(x,t,u,DuDx)

% If m = 0
% c du/dt = df/dx + s
% f = f(x,t,u,du/dx)

c = 1-(1-x).^2;
f = DuDx;

% and external heat loss
s = 0;

end

%%%%%%%%%%%%%%%%%%%%%%%%%%%%%%%%%%%%%%%%%%%%%%%%%%%%%%%%%%%%%%%%%%%%%%%%%%%%%%%%

function u0 = ics(x)

% The initial condition
u0 = 0;

end

%%%%%%%%%%%%%%%%%%%%%%%%%%%%%%%%%%%%%%%%%%%%%%%%%%%%%%%%%%%%%%%%%%%%%%%%%%%%%%%%

function [pl,ql,pr,qr] = bcs(xl,ul,xr,ur,t)

% p + q*f = 0
% NB f is defined in pde_eqn

%The left end
pl = 1;
ql = 1;

% for Zhang left end it pl=ul-1, ql=0 which forces T=Tw at the wall

% The right end
pr = 0;
qr = 1;

end
```

Appendix E. vaporator

Expected masses for various TS in Rotary Evaporator

Initial TS	0.0977		
Initial milk mass	500	g	
Mass solids	48.85	g	
Amount of sampling	13	g	
Evaporation rate	2.5	g/min	

Evaporation to desired concentration (*TS*)	Milk left in flask (*g*)	Mass of solids (*g*)	Mass condensate (*g*)	Sample mass (*g*)	Solids removed (*g*)	Mass after sampling (*g*)	Solids after sampling (*g*)	Time taken (*min*)
0.350	139.6	48.9	360.4	13	4.6	126.6	44.30	144.2
0.400	110.8	44.3	376.3	13	5.2	97.8	39.10	
0.450	86.9	39.1	387.1	13	5.9	73.9	33.25	
0.500	66.5	33.3	394.5	13	6.5	53.5	26.75	
0.550	48.6	26.8	399.4	13	7.2	35.6	19.60	
0.600	32.7	19.6	402.3	13	7.8	19.7	11.80	

Figure E1: A sample calculations in Excel for approximating masses in rotary evaporator.

Calculations were done in Excel as shown in Figure E1. The cells C3, C4, C6 and C7 were entries to be entered. The desired concentrations to be achieved were entered in column B in cells B13 to B18. Calculations for the cells in row 13 from column B to J were done using formulae as listed in Table E1 and later copied down except cell J13.

Table E1: Corresponding formulae used in Figure E1.

Cell	Formula
C5	=C3*C4
C13	=D13/B13
D13	=C5
E13	=$C$4-C13
F13	=C6
G13	=F13*B13
H13	=C13-F13
I13	=D13-G13
J13	=(C4-C13)/C7

Appendix F. The Spreadsheet

Scenario

A single tube of 15 m long was divided into 0.1 m elements. Calculations were then done on each element as the milk enters from the top of the tube and downward. The basis for the calculations was that the milk is flowing as a thin film under steady state and completely wet the inside of the tube.

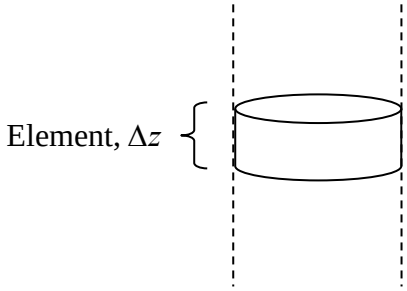

The type of milk to be used is skim milk and it is assumed to have total solids of **9.7 %** before being concentrated to 45 % total solids. Its initial compositions are assumed to be as follows:

Lactose, 5.0 %

Ash, 0.07 %

Protein, 3.5 %

Fat, 0.5 %

For the spreadsheet calculations, milk's concentration is 45 % total solids (being pre-concentrated from 9.7 % total solids) and immediately enters as a film at the top of the tube without the aid of any distribution system.

The milk flow is also subjected to vacuum pressure of **15 kPa**.

Calculations were done starting from the top of the tube and subsequently moving downwards by an element, Δz.

Assumptions

Some assumptions were made throughout the study:

1. The film flow is *smooth* laminar.
2. The film surface is non wavy.
3. No nucleate boiling occurs.
4. Evaporation occurs at the free surface only.
5. The fluid is incompressible.
6. The tube wall is isothermal.
7. The vapour pressure is constant

Specifications

	Values	**In Spreadsheet**
Outer tube diameter, D_o	0.0508 m	C9
Inner tube diameter, D_i	0.0478 m	C10
Total solids upon entrance, TS_{in}	0.45	C7
Element, Δz	0.1 m	C8
Enthalpy of vaporization, ΔH	2383 kJ/kg	C21
Wetting rate, Γ	0.3 $kg \cdot m^{-1} \cdot s^{-1}$	C11
Gas constant, R	8.314 $J \cdot mol^{-1} \cdot K^{-1}$	C13
Temperature water boiling, T_{wb}	373.15 K	C14
Latent heat of vaporization, ΔH_v	40691.455 $J \cdot mol^{-1}$	C15
Overall heat transfer coefficient, U_{50}	1 $kJ/m^2s°C$	C16
Overall heat transfer coefficient, U_{60}	0.5 $kJ/m^2s°C$	C17
Total solids 50 %	0.5	C18
Total solids 60 %	0.6	C19
Temperature difference, ΔT	6 °C	C20
Gravity, g	9.81 $m \cdot s^{-2}$	C23
Length of tube, L	15 m	C24
Yield stress (Maximum total solids), TS_{max}	0.653	C25
Yield stress constant, a_{yield}	0.15	C26

Yield stress constant, b_{yield}	1.2	C27
Consistency Factor constant, a_k	4.93	C28
Flow behavior index constant, b_{index}	-1.9	C29
Flow behavior index constant, a_{index}	1.88	C30
Flow behavior index constant, c_{index}	15	C31
Heat flux,	2000 $W \cdot m^{-2}$	B52

Note: 1) Some of the calculations below were truncated and may not be the same as in the spreadsheet.

2) The samples included were from length, L = 0m.

Calculation of Surface Area, A/m^2

The available surface area, $A = \pi \times D_i \times \Delta z$

$= 3.14159 \times 0.0478 \times 0.1$

$= 0.0150\ m^2$

In spreadsheet:

The available surface area, A = PI()*C11*C18

Calculation of Mole Fraction of Water, x_{water}

The composition of milk upon entering the top of the tube after concentrated to 45 % total solids from 9.7 % total solids:

	9.7 % TS	**45 % TS**	**45 % TS**
	Mass fraction	Mass fraction	w_i/M_i
	(w_i)	(w_i)	
Lactose	$w_{lact} = 0.05$	$w_{lact} = 45 \times \left(\frac{0.05}{9.7}\right)$ $= 0.232$	Molecular mass of Lactose, M_{lact} : 0.342 kg/mol $w_{lact}/M_{lact} = 0.23196/0.342$

		In spreadsheet: $H7/$B$50*$B$45	= 0.678
Ash	w_{ash} = 0.007	$w_{ash} = 45 \times \left(\frac{0.007}{9.7} \right)$ = 0.0325 In spreadsheet: $H7/$B$50*$B$46	Molecular mass of Ash, M_{ash} : 0.067 kg/mol w_{ash}/M_{ash} = 0.03247/0.067 = 0.485
Protein	$w_{protein}$ = 0.035	$w_{protein} = 45 \times \left(\frac{0.035}{9.7} \right)$ = 0.162 In spreadsheet: $H7/$B$50*$B$47	
Fat	w_{fat} = 0.005	$w_{fat} = 45 \times \left(\frac{0.005}{9.7} \right)$ =0.0232 In spreadsheet: $H7/$B$50*$B$48	

Molecular mass of water, M_{H20} : 0.01801528 kg/mol

For water, w_{H20}/M_{H20} = (1- TS_{in}) / M_{H20}

= (1 - 0.45) / 0.01801528

= 30.53

Because Proteins and Fat have very high molecular masses and therefore low mole fractions, they are negligible (Morison and Hartel 2007).

Mole fraction of water, $x_w = \frac{w_w / M_w}{\sum w_i / M_i}$

$$= \frac{30.5296}{0.67824 + 0.48462 + 30.5296}$$

= 0.963

Calculation of Boiling Point Elevation (BPE), ΔT_b/K

From the equation, $\Delta T_b = \frac{-RT_{wb}^2 \ln x_w}{\Delta h_v}$

Where, R = 8.314 $J \cdot mol^{-1} \cdot K^{-1}$

T_{wb} = 373.15 K

Δh_v = 57 222 – 44.3T_{wb} $J \cdot mol^{-1}$

= 57 222 – 44.3(373.15) $J \cdot mol^{-1}$

= 40 691.5 $J \cdot mol^{-1}$

The Boiling Point Elevation (BPE), $\Delta T_b = \frac{-8.314 \times 373.15^2 \ln 0.963308}{40691.455}$ K

= 1.06 K

In spreadsheet:

The Boiling Point Elevation (BPE), ΔT_b = (-$C$13*$C$14*$C$14*LN(P7))/$C$15

Calculation of Milk Temperature, T_{milk}/K

From Antoine equation, $\ln P^{sat} = A - \frac{B}{T + C}$

Vacuum pressure = 15 000 Pa

With the values of the constants as,

A= 16.262

B= 3799.89

C= 226.35

Temperature, T= $\frac{B}{A - \ln(15000)} - C$

$$= \frac{3799.89}{16.262 - \ln(15000)} - 226.35$$

$= 54\ ^{0}C$

$= 327.15$ K

In spreadsheet:

Temperature, T= B57/(B56-LN((B55)/1000))-B58

The Milk Temperature, $T_{milk} = T_{sat} + \Delta T_b$

$= 327.15 + 1.063$

$= 328.213$ K

In spreadsheet:

The Milk Temperature, T_{milk} = $B$59+Q7

Calculation of Overall Heat Transfer Coefficient, *U*/kJ·m^{-2}·s^{-1}·°C^{-1}

The overall heat transfer coefficient was calculated based on this data:

Overall heat transfer coefficient at 50% TS	1 kJ·m^{-2}·s^{-1}·°C^{-1}
Overall heat transfer coefficient at 60% TS	0.5 kJ·m^{-2}·s^{-1}·°C^{-1}

In order to determine the value of the overall heat transfer coefficient at any total solids, the function 'Forecast' in Excel was used.

The function 'Forecast' is:

FORECAST(x, known_y's, known_x's)

x : the total solids to determine the value of its overall heat transfer coefficient

known_y's : the values 1 and 0.5

known_x's : the values 0.5 and 0.6

In spreadsheet:

The U = FORECAST(H7,$C$16:$C$17,$C$18:$C$19)

Calculation of Temperature difference, ΔT/°C

The temperature difference, ΔT is an arbitrary value. The value used in the sample calculation was ΔT = 6 °C.

Calculation of Enthalpy of vaporization, ΔH/KJ·Kg^{-1}

The enthalpy of vaporization was predetermined to be 2383 KJ·Kg^{-1}.

Calculation of Evaporation rate, M_{evap}/kg·s^{-1}

From, $Q=UA\Delta T=M_{evap}\Delta H$

The evaporation rate, $M_{evap} = \frac{UA\Delta T}{\Delta H}$

With the surface area, A = 0.015 m^2

ΔT = 6 °C

ΔH = 2383 kJ/kg

At 45% total solids,

Overall heat transfer coefficient, U = 1.3 kW·m^{-2}·K^{-1}

The evaporation rate, M_{evap} = 0.000039 kg·s^{-1}

In spreadsheet:

The evaporation rate, M_{evap} = (T7*$C$22*($C$20-Q7))/$C$21

Calculation of Mass Flowrate In, M_{in}/kg·s^{-1}

From the formula, $\Gamma = \frac{\dot{m}}{\pi D}$

With the wetting rate, Γ= 0.3 kg·m^{-1}·s^{-1}

π= 3.14159

D= 0.0478 m

The Mass Flowrate In, M_{in}= 0.3 × 3.14159 × 0.0478

= 0.04505 kg·s^{-1}

In spreadsheet:

The Mass Flowrate In, M_{in}= C23*PI()*C11

Calculation of Mass Flowrate Solids, M_{solids}/kg·s^{-1}

With the initial total solids entering = 0.45

The Mass Flowrate Solids, M_{solids}= 0.45 × M_{in}

= 0.45 × 0.04505

= 0.02027 kg/s

In spreadsheet:

The Mass Flowrate Solids, M_{solids}= H7*G7

Calculation of Total Solids, *TS*

The Total Solids, *TS* = M_{solids} / M_{in} = 0.45

In spreadsheet:

The Total Solids, *TS* = $C$12/G8

Calculation of Flow behavior index, *n*

The Flow behavior index, n was calculated from an equation determined from experimental measurements of milk viscosity at different total solids. This equation is a function of total solids.

$$n = \left(\left(\frac{1}{a_{index} - b_{index} TS} \right)^{c_{index}} + 1 \right)^{-1/c_{index}}$$

a_{index} = 1.88

b_{index} = -1.9

c_{index} = 15

At 45% total solids, n = 0.966

In spreadsheet:

The Flow behavior index, n = ((1/($C$30+$C$29*H7))^$C$31+1)^(-1/$C$31)

Calculation of Yield stress, τ_y/Pa

The Yield stress, τ_y was calculated from an equation determined from experimental measurements of milk viscosity at different total solids. This equation is a function of total solids.

An Excel function, 'MAX' was incorporated into the equation.

$$\tau_y = MAX\left[0, \frac{a_{yield}}{\left(1-\frac{TS}{TS_{\max}}\right)^{b_{yield}}} - 0.5\right]$$

a_{yield} = 0.15

TS_{max} = 0.653

b_{yield} = 1.2

At 45% total solids, τ_y = 0.11

In spreadsheet:

The yield stress , τ_y = MAX(0,$C$26/(1-H7/$C$25)^$C$27-0.5)

Calculation of Consistency factor, *K*/Pa·s^n

The Consistency factor, K was calculated from an equation determined from experimental measurements of milk viscosity at different total solids. This equation is a function of total solids and milk temperature.

$$K = e\left(\frac{a_k TS}{1-TS}\right)\mu(T_{milk})$$

ak = 4.93

At 45% total solids, K = 0.028

In spreadsheet:

The consistency factor, K = EXP($C$28*H7/(1-H7))*WaterViscosity(R7)

Calculation of Density, ρ/kg·m^{-3}

The function MilkDensity was used.

Calculation of Thermal Conductivity, k/J·s^{-1}·m^{-1}·K^{-1}

The function MilkThermalConductivity was used.

Calculation of Heat Capacity, C_p/J·kg^{-1}·K^{-1}

The function MilkCp was used.

Calculation of Film thickness, δ_1/m

From $\delta_1 = \dfrac{\tau_y}{\rho g}$

The film thickness, $\delta_1 = \dfrac{0.10953}{1164.3 \times 9.81}$

$\delta_1 = 9.589E-06$ m

In spreadsheet:

The film thickness, δ_1 = W7/($C$23*AJ7)

Calculation of Film thickness, δ_2/m

The function FindDelta2 was used.

Calculation of Wetting rate into each elements, Γ/kg·m^{-1}·s^{-1}

From $\Gamma = \frac{\dot{m}_{in}}{\pi D}$

The wetting rate, $\Gamma = \frac{0.04505}{PI \times 0.0478}$

$= 0.300$ kg·m^{-1}·s^{-1}

In spreadsheet:

The wetting rate, Γ = G7/(PI()*$C$10)

Calculation of Time

The time in each segment, t = $\frac{\Delta z}{v_{ave}}$, where $v_{ave} = \frac{\dot{m}}{\rho A}$ and $A = \frac{\pi}{4}\left(D^2 - \left(D - 2\delta_2\right)^2\right)$

Element, $\Delta z = 0.1$ m

Mass flow rate, $\dot{m} = 0.04505$ kg/s

Density, $\rho = 1164.3$ kg/m^3

Area, $A = 0.0001707$ m^2

Film thickness, $\delta_2 = 0.001165$ m

Diameter, $D = 0.0478$ m

The time, $t = 0.1 \times \frac{1164.3 \times 0.0001707}{0.04505} = 0.44$ s

In spreadsheet:

The time, t = $C$8*PI()/4*($C$10^2-($C$10-2*Z7)^2)*AJ7/G7

Calculation of Shear stress, τ_w

From, $\tau_w = \rho g \delta_2$

The shear stress, $\tau_w = 1164.289 \times 9.81 \times 0.00116526$

$= 13.3$ Pa

In spreadsheet:

The shear stress, τ_w = AJ7*$C$23*Z7

Calculation of Shear rate

From $\dot{\gamma} = \left(\frac{\rho g x - \tau_y}{K} \right)^{\frac{1}{n}}$

The shear rate, $\dot{\gamma} = \left(\frac{(1164.28 \times 9.81 \times 0.001165) - 0.1095254}{0.02839} \right)^{\frac{1}{0.96561}}$

$= 578\ s^{-1}$

In spreadsheet:

The shear rate, $\dot{\gamma}$ = ((AJ7*$C$23*Z7-W7)/X7)^(1/V7)

Calculation of Viscosity

From $\eta = \frac{\tau}{\dot{\gamma}}$

The viscosity, $= \frac{13.30922}{578.49}$

$= 0.023$ Pa·s

In spreadsheet:

The viscosity,= AA7/AD7

Calculation of Surface tension

Based on Tim Reily's work via Dr. Ken Morison, $\sigma = \frac{\left(-0.17T_{milk}\right)+55}{1000}$

The surface tension, σ $= \frac{\left(-0.17\times 55.07\right)+55}{1000}$

$= 0.046$ N·m^{-1}

In spreadsheet:

The surface tension, σ = (-0.17*R7+55)/1000

Calculation of Reynolds number

From $\mathrm{Re} = \frac{4\Gamma}{\mu}$

$= \frac{4\times 0.300}{0.023}$

$= 52.17$

In spreadsheet:

The Reynolds number, = 4*S7/AE7

Calculation of Prandtl number

From $\Pr = \frac{\mu C_p}{k}$

The Prandtl number, $Pr = \frac{0.023006828 \times 3102.595}{0.50249}$

$= 142.05$

In spreadsheet:

The Prandtl number, = (AE7*AI7)/AH7

Calculation of Kapitza number

From $Ka = \frac{\mu^4 g}{\rho \sigma^3}$

The Kapitza number, $Ka = \frac{0.023006828^4 \times 9.81}{1164.28903 \times 0.0456381^3}$

$= 0.0000248$

In spreadsheet:

The Kapitza number, Ka = (($C$23*AE7^4)/AJ7)/AK7^3

Calculation of Boiling number

$$Bo = \frac{\Phi}{G\Delta H_v} \text{ where, } G = \frac{\dot{m}}{\pi D\delta} = \frac{\Gamma}{\delta}$$

The Boiling number, $Bo = \frac{2000 \times 0.001165}{2383 \times 1000 \times 0.3}$

$= 3.26 \times 10^{-6}$

In spreadsheet:

The Boiling number, = $B$52/(($C$21*1000)*(S7/Z7))

Calculation of $Bo \times Ka^{1/11}$

The $Bo \times Ka^{1/11}$ can be calculated using the two calculations from above.

The $Bo \times Ka^{1/11} = (3.26 \times 10^{-6}) \times (0.00002483)^{1/11}$

$= 1.24 \times 10^{-6}$

In spreadsheet:

The $Bo \times Ka^{1/11}$ = AL7*AO7^0.090909

Calculation of mass transfer coefficient β/m·s^{-1}

Based on the paper from Wadekar (2002), the mass transfer coefficient is given by

$$\beta = 2 \times 10^{-6} \, \mathrm{Re}^{0.8}$$

From the calculated Reynolds number, $\beta = (2 \times 10^{-6}) \times 52.151^{0.8}$

$= 4.73 \times 10^{-5}$ m·s^{-1}

In spreadsheet:

The mass transfer coefficient, β = 0.000002*AM7^0.8

Calculation of θ

From Wadekar (2002), $\theta = \frac{\dot{q}}{\Delta h_v \rho \beta}$. This equation was modified into,

$$\theta = \frac{\dot{q}}{\Delta h_v \rho\left(\omega_{\mathrm{H20}}/\mathrm{M}_{\mathrm{H20}} + \omega_{lactose}/\mathrm{M}_{\mathrm{lactose}} + \omega_{ash}/\mathrm{M}_{\mathrm{ash}}\right)\beta}$$

β = 4.729×10^{-5} m·s^{-1}

$\dot{q}$ = 2000 W·m^{-2}

ρ = 1164.289 kg·m^{-3}

ω_{H20}/M_{H20} = 30.53

$\omega_{lactose}/M_{lactose}$ = 0.678

ω_{ash}/M_{ash} = 0.485

Δh_v = 40691.455 J·mol^{-1}

With the mass transfer coefficient, β, as calculated before, θ = 0.028

In spreadsheet:

The θ = $B$52/($C$15*AJ7*(M7+N7+O7)*AQ7)

Calculation of $\omega_{water,i}$

Based on Wadekar and Hills (2001) where $x_i = (1+\theta)x_b - \theta$ and

$x_b = \omega_{water,b}$ (water at the bulk) = 1 – TS = 1 - 0.45 = 0.55

$x_i = \omega_{water,i}$ (water at the interface) = [(1+0.0282)×(1-TS)] - 0.0282

= 0.537

In spreadsheet:

(1+AR7)*(1-H7)-AR7

Calculation of TS_i

The total solids at the interface, $TS_i = 1 - \omega_{water,i}$

$= 0.4626$

In spreadsheet:

The total solids at the interface, TS_i = 1-AS7

Calculation of $\omega_{lactose,i}$

Mass fraction of lactose at the interface, $= \frac{TS_i}{TS_{9.7}} \times \text{Percentage lactose in 9.7\% TS}$

Percentage lactose in 9.7% TS = 0.05

$TS_{9.7}$ = 0.097 (Total solids in mass fraction at 9.7%)

The $\omega_{lactose,i} = \frac{0.4626}{0.097} \times 0.05$

$= 0.238$

In spreadsheet:

The $\omega_{lactose,i}$ = AT7/$B$50*$B$45

Calculation of $\omega_{ash,i}$

Mass fraction of ash at the interface, $= \frac{TS_i}{TS_{9.7}} \times \text{Percentage ash in 9.7\% TS}$

Percentage lactose in 9.7% TS = 0.007

$TS_{9.7}$ = 0.097 (Total solids in mass fraction at 9.7%)

The $\omega_{lactose,i} = \frac{0.4626}{0.097} \times 0.007$

$= 0.0338$

In spreadsheet:

The $\omega_{ash,i}$ = AT7/$B$50*$B$46

Calculation of $\omega_{H20,i}/M_{H20,i}$

With $\omega_{H20,i}$ as calculated above and the molecular mass of water = 0.01801

The $\omega_{H20,i}/M_{H20,i}$ = 0.53731/0.01801
= 29.83

In spreadsheet:

The $\omega_{H20,i}/M_{H20,i}$ = (1-AT7)/$B$38

Calculation of $\omega_{lactose,i}/M_{lactose,i}$

With $\omega_{lactose,i}$ as calculated above and the molecular mass of lactose = 0.342

The $\omega_{lactose,i}/M_{lactose,i}$ = 0.238/0.342
= 0.696

In spreadsheet:

The $\omega_{lactose,i}/M_{lactose,i}$ = AU7/$B$36

Calculation of $\omega_{ash,i}/M_{ash,i}$

With $\omega_{H20,i}$ as calculated above and the molecular mass of water = 0.067

The $\omega_{ash,i}/M_{ash,i}$ = 0.0338/ 0.067
= 0.5

In spreadsheet:

The $\omega_{ash,i}/M_{ash,i}$ = AV7/$B$37

Calculation of mole fraction water, $x_{water,i}$

Mole fraction of water at interface, $x_{water,i} = \frac{w_{H20,i} / M_{H20,i}}{\sum w_i / M_i}$

$$= \frac{29.83}{0.696 + 0.5 + 29.83}$$

$$= 0.96$$

In spreadsheet:

Mole fraction of water at interface = AW7/(AW7+AX7+AY7)

Calculation boiling point elevation at interface $\Delta T_{b,i}$

From the equation, $\Delta T_{b,i} = \frac{-RT_{wb}^2 \ln x_{water,i}}{\Delta h_v}$

Where, R = 8.314 $J \cdot mol^{-1} \cdot K^{-1}$

T_{wb} = 373.15 K

Δh_v = 57 222 – 44.3T_{wb} $J \cdot mol^{-1}$

= 57 222 – 44.3(373.15) $J \cdot mol^{-1}$

= 40 691 $J \cdot mol^{-1}$

The Boiling Point Elevation at interface, $\Delta T_{b,i} = \frac{-8.314 \times 373.15^2 \ln 0.96145}{40691.455}$ K

= 1.118 K

In spreadsheet:

The Boiling Point Elevation at interface = (-$C$13*$C$14*$C$14*LN(AZ7))/$C$15

Calculation of milk temperature at interface, T_i

From previous calculation, milk temperature = 54 °C

The milk temperature at interface, T_i = T_{milk} (without BPE) + $\Delta T_{b,i}$

= 54 + 1.118

= 55.118 °C

In spreadsheet:

The milk temperature at interface = $B$59+BA7

Calculation of Interfacial Temperature Rise, ΔT_m

From Wadekar and Hills, (2001) $\Delta T_m = \left(T_{bub(x_i)} - T_{(x_b)}\right)$

= 55.118 - 55.063 = 0.055

In spreadsheet:

The interfacial temperature rise = ABS(BB7-R7)

Calculation of Heat Transfer Coefficient

1) Alhusseini et al.'s equation

$$h_l^+ = 2.65\,\mathrm{Re}^{-0.158}\,Ka^{0.0563}$$

In spreadsheet:

(((2.65*AM7^-0.158)*AO7^0.0563)*AH7)/(((AE7/AJ7)^2/$C$23)^0.33333)

2) Chun and Seban's equation

$$h^+ = 0.821\mathrm{Re}^{-0.22}$$

In spreadsheet:

((0.821*(AM7^-0.22))*AH7)/(((AE7/AJ7)^2/$C$23)^0.33333)

3) Wadekar and Hills equation

$$\alpha_{lm} = \alpha_{epf}\left(1 - \frac{\Delta T_m}{T_w - T_{bub(x_b)}}\right)$$

In spreadsheet:

BF7*(1-BC7/($B$53-R7))

4) Ahmed and Kaparthi's equation

$$Nu = 0.0911\,\mathrm{Re}^{0.33}\,\mathrm{Pr}^{0.4}\left(\mu/\mu_w\right)^{0.25}$$

In spreadsheet:

((0.0911*AM7^0.33*AN7^0.4*(AF7/AG7)^0.25)*AH7)/Z7

Appendix G. Sample spreadsheet

	A	B	C	D	E
6					
7	Total solids initial	TS_{In}	0.45		
8	Element	Δz	0.1	m	
9	Outer tube diameter	D_o	0.0508	m	
10	Inner tube diameter	D_i	0.0478	m	
11	Wetting rate	Γ	0.3	$kg \cdot m^{-1} \cdot s^{-1}$	
12	Mass flow rate (solids)	M_{solids}	0.020273	kg/s	
13	Gas constant	R	8.314	$J \cdot mol^{-1} \cdot K^{-1}$	
14	Temperature water boiling	Twb	373.15	K	
15	Latent heat of vaporization	ΔHv	40691.46	$J \cdot mol^{-1}$	
16	Overall heat transfer coefficient	U_{50}	1	$kJ/m^2s°C$	
17	Overall heat transfer coefficient	U_{60}	0.5	$kJ/m^2s°C$	
18	Total solids 50%	TS_{50}	0.5		
19	Total solids 60%	TS_{60}	0.6		
20	Temperature difference	ΔT	6	°C	
21	Enthalpy of vaporization	ΔH	2383	kJ/kg	
22	Tube surface area	A	0.015017	m^2	
23	Gravity	g	9.81	$m \cdot s^{-2}$	
24	Length of tube	L	15	m	
25	Yield Stress Maximum total solids	TS_{max}	0.653		
26	Yield Stress Constant	a_{yield}	0.15		
27	Yield Stress Constant	b_{yield}	1.2		
28	Consistency Factor Constant	a_K	4.93		
29	Flow Behaviour Index Constant	b_{index}	-1.9		
30	Flow Behaviour Index Constant	a_{index}	1.88		
31	Flow Behaviour Index Constant	c_{index}	15		
32					

Figure G1: A sample spreadsheet.

	A	B	C	D	E
33					
34	**Individual molecular mass, M in skim milk's composition**				
35	**Component**	**kg/mol**			
36	Lactose	0.342			
37	Ash	0.067			
38	Water	0.01801528			
39	Protein	-			
40	Fat	-			
41					
42					
43	**Composition of skim milk at 0.097 TS and its corresponding mass flow rate**				
44	**Component**	**ω**	**kg/s**		
45	Lactose	0.05	0.01045		
46	Ash	0.007	0.00146		
47	Protein	0.035	0.00731		
48	Fat	0.005	0.00104		
49			0.02027		
50	Total TS	**0.097**	0.45		
51					
52	Say q(wall) in heat flux form	2000	$W \cdot m^{-2}$		
53	Temp. Wall	61	^0C		
54					
55	Setting vacuum pressure	15000	Pa abs		
56	Antoine eqn constant A	16.262			
57	Antoine eqn constant B	3799.89			
58	Antoine eqn constant C	226.35			
59	Fr Antoine eqn, Temp. of vapour	54.00	^0C		
60					
61	**Wall conduction**				
62	Wall thickness	0.0015	m		
63	SS Thermal conductivity	17	$W \cdot m^{-1} \cdot K^{-1}$		
64	dx/k	0.000088	$m^2 \cdot K \cdot W^{-1}$		
65					

Figure G2: A sample spreadsheet (continued).

	F	G	H	I	J	K	L	M	N
3									
4									
5									
6	L/m	M_{in}/kg·s^{-1}	TS	$\omega_{Lactose}$	ω_{Ash}	$\omega_{Protein}$	ω_{Fat}	ω_{H20}/M_{H20}	$\omega_{lactose}/M_{lactose}$
7	0	0.04505	0.45	0.232	0.032	0.162	0.023	30.530	0.678
8	0.1	0.04501	0.450	0.232	0.033	0.163	0.023	30.508	0.679
9	0.2	0.04497	0.451	0.232	0.033	0.163	0.023	30.486	0.679
10	0.3	0.04493	0.451	0.233	0.033	0.163	0.023	30.465	0.680
11	0.4	0.04490	0.452	0.233	0.033	0.163	0.023	30.443	0.681
12	0.5	0.04486	0.452	0.233	0.033	0.163	0.023	30.422	0.681
13	0.6	0.04482	0.452	0.233	0.033	0.163	0.023	30.400	0.682
14	0.7	0.04478	0.453	0.233	0.033	0.163	0.023	30.379	0.682
15	0.8	0.04474	0.453	0.234	0.033	0.163	0.023	30.357	0.683
16	0.9	0.04470	0.453	0.234	0.033	0.164	0.023	30.336	0.684
17	1	0.04466	0.454	0.234	0.033	0.164	0.023	30.314	0.684

Figure G3: A sample spreadsheet (continued).

	O	P	Q	R	S	T	U	V	W
3									
4									
5									
6	ω_{ash}/M_{ash}	χ_{water}	BPE, ΔT_b/K	Milk Temp., T/°C	Γ/kg·m^{-1}·s^{-1}	U/kW·m^{-2}·K^{-1}	M_{evap}/kg·s^{-1}	n	τ_y/Pa
7	0.485	0.963	1.064	55.07	0.300	1.3	0.000039	0.966	0.110
8	0.485	0.963	1.065	55.07	0.300	1.2	0.000039	0.965	0.111
9	0.486	0.963	1.067	55.07	0.299	1.2	0.000039	0.965	0.112
10	0.486	0.963	1.068	55.07	0.299	1.2	0.000039	0.965	0.114
11	0.486	0.963	1.070	55.07	0.299	1.2	0.000039	0.964	0.115
12	0.487	0.963	1.072	55.07	0.299	1.2	0.000039	0.964	0.117
13	0.487	0.963	1.073	55.08	0.298	1.2	0.000038	0.964	0.118
14	0.488	0.963	1.075	55.08	0.298	1.2	0.000038	0.964	0.119
15	0.488	0.963	1.077	55.08	0.298	1.2	0.000038	0.963	0.121
16	0.488	0.963	1.078	55.08	0.298	1.2	0.000038	0.963	0.122
17	0.489	0.963	1.080	55.08	0.297	1.2	0.000038	0.963	0.124

Figure G4: A sample spreadsheet (continued).

	X	Y	Z	AA	AB	AC	AD	AE	AF
3									
4									
5									
6	K/Pa·s^n	δ_1/m	δ_2/m	τ_w/Pa	v/m·s^{-1}	t/s	γ_w/s^{-1}	η/Pa·s	η/Pa·s
7	0.028	9.589E-06	0.001165	13.309	0.328	0.441	578.5	0.023	0.02208
8	0.029	9.711E-06	0.001167	13.331	0.328	0.442	576.7	0.023	0.02228
9	0.029	9.832E-06	0.001169	13.354	0.327	0.443	575.0	0.023	0.02249
10	0.029	9.955E-06	0.001171	13.376	0.327	0.445	573.3	0.023	0.02269
11	0.029	1.008E-05	0.001172	13.398	0.326	0.446	571.5	0.023	0.02290
12	0.029	1.020E-05	0.001174	13.421	0.326	0.447	569.8	0.024	0.02312
13	0.029	1.032E-05	0.001176	13.443	0.325	0.448	568.1	0.024	0.02333
14	0.030	1.045E-05	0.001178	13.465	0.324	0.449	566.4	0.024	0.02354
15	0.030	1.057E-05	0.001179	13.488	0.324	0.450	564.7	0.024	0.02376
16	0.030	1.070E-05	0.001181	13.510	0.323	0.451	563.0	0.024	0.02398
17	0.030	1.082E-05	0.001183	13.533	0.323	0.452	561.3	0.024	0.02420

Figure G5: A sample spreadsheet (continued).

	AG	AH	AI	AJ	AK	AL	AM	AN	AO
3									
4									
5									
6	η_w/Pa·s	K/J·s^{-1}·m^{-1}·K^{-1}	C_p/J·kg^{-1}·K^{-1}	ρ/kg·m^{-3}	σ/N·m^{-1}	Bo	Re_{film}	Pr	Ka
7	0.01993	0.502	3102.6	1164.3	0.046	3.26E-06	52.2	142.1	0.00002483
8	0.02012	0.502	3101.7	1164.5	0.046	3.27E-06	51.9	142.7	0.00002530
9	0.02030	0.502	3100.7	1164.7	0.046	3.28E-06	51.6	143.4	0.00002578
10	0.02049	0.502	3099.8	1164.8	0.046	3.28E-06	51.3	144.1	0.00002626
11	0.02068	0.502	3098.9	1165.0	0.046	3.29E-06	51.0	144.7	0.00002675
12	0.02087	0.502	3097.9	1165.2	0.046	3.30E-06	50.7	145.4	0.00002726
13	0.02107	0.502	3097.0	1165.4	0.046	3.31E-06	50.4	146.1	0.00002777
14	0.02126	0.501	3096.1	1165.6	0.046	3.31E-06	50.2	146.8	0.00002829
15	0.02146	0.501	3095.1	1165.7	0.046	3.32E-06	49.9	147.5	0.00002882
16	0.02166	0.501	3094.2	1165.9	0.046	3.33E-06	49.6	148.2	0.00002936
17	0.02186	0.501	3093.3	1166.1	0.046	3.34E-06	49.3	148.9	0.00002991

Figure G6: A sample spreadsheet (continued).

	AP	AQ	AR	AS	AT	AU	AV	AW	AX
3									
4									
5									
6	$Bo \times Ka^{1/11}$	β/m·s^{-1}	θ	$W_{water,i}$	TS_i	$W_{lactose,i}$	$W_{ash,i}$	$w_{H20,i}/M_{H20,i}$	$w_{lactose,i}/M_{lactose,i}$
7	1.24E-06	0.00004730	0.028	0.537	0.463	0.238	0.033	29.826	0.697
8	1.25E-06	0.00004709	0.028	0.537	0.463	0.239	0.033	29.801	0.698
9	1.25E-06	0.00004688	0.028	0.536	0.464	0.239	0.033	29.775	0.699
10	1.26E-06	0.00004668	0.029	0.536	0.464	0.239	0.033	29.749	0.699
11	1.26E-06	0.00004647	0.029	0.535	0.465	0.239	0.034	29.723	0.700
12	1.27E-06	0.00004626	0.029	0.535	0.465	0.240	0.034	29.698	0.701
13	1.27E-06	0.00004606	0.029	0.535	0.465	0.240	0.034	29.672	0.702
14	1.28E-06	0.00004586	0.029	0.534	0.466	0.240	0.034	29.646	0.702
15	1.28E-06	0.00004565	0.029	0.534	0.466	0.240	0.034	29.620	0.703
16	1.29E-06	0.00004545	0.029	0.533	0.467	0.241	0.034	29.595	0.704
17	1.29E-06	0.00004525	0.030	0.533	0.467	0.241	0.034	29.569	0.704

Figure G7: A sample spreadsheet (continued).

	AY	AZ	BA	BB	BC	BD	BE	BF	BG
3									
4									
5									
6	$w_{ash,i}/M_{ash,i}$	$x_{water,i}$	$\Delta T_{b,i}$/K	T_i/^{0}C	ΔT_m/K	$\Delta T_m \cdot q^{-1}$/W·m^{-2}·K^{-1}	h_{int}/W·m^{-2}·K^{-1}	h_{int}/W·m^{-2}·K^{-1}	h_{int}/W·m^{-2}·K^{-1}
7	0.498	0.961	1.118	55.12	0.055	0.000027	1149.3	506	499.3
8	0.499	0.961	1.120	55.12	0.055	0.000028	1147.7	505	498.2
9	0.499	0.961	1.122	55.13	0.055	0.000028	1146.1	504	497.1
10	0.500	0.961	1.124	55.13	0.056	0.000028	1144.5	503	496.1
11	0.500	0.961	1.126	55.13	0.056	0.000028	1142.9	502	495.0
12	0.501	0.961	1.128	55.13	0.057	0.000028	1141.3	501	493.9
13	0.501	0.961	1.131	55.13	0.057	0.000029	1139.8	500	492.8
14	0.502	0.961	1.133	55.14	0.058	0.000029	1138.2	499	491.8
15	0.502	0.961	1.135	55.14	0.058	0.000029	1136.6	498	490.7
16	0.503	0.961	1.137	55.14	0.058	0.000029	1135.0	497	489.7
17	0.503	0.961	1.139	55.14	0.059	0.000029	1133.5	496	488.6

Figure G8: A sample spreadsheet (continued).

	BH	BI	BJ	BK
3				
4				
5				
6	h_{int}/W·m^{-2}·K^{-1}	h_{int}/W·m^{-2}·K^{-1}	h_{ext}/W·m^{-2}·K^{-1}	U/W·m^{-2}·K^{-1}
7	501.5	1079.0	8000	451
8	500.4	1077.1	8000	450
9	499.4	1075.2	8000	449
10	498.3	1073.3	8000	449
11	497.2	1071.4	8000	448
12	496.1	1069.5	8000	447
13	495.1	1067.6	8000	446
14	494.0	1065.7	8000	445
15	492.9	1063.8	8000	444
16	491.9	1061.9	8000	443
17	490.8	1060.1	8000	442

Figure G9: A sample spreadsheet (continued).